Characterising the activation process for cobalt catalysts used in Fischer-Tropsch synthesis

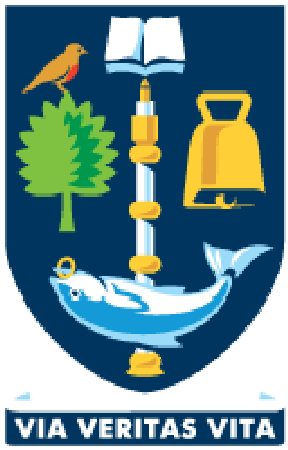

Fiona A. Wigzell

A Thesis Presented to the University of Glasgow for the Degree of Doctor of Philosophy

ABSTRACT

The effects of precursor, support and calcination procedure on the physical and chemical properties of supported cobalt catalysts have been investigated. A multiple characterisation approach of thermogravimetric analysis, differential scanning calorimetry, X-ray diffraction and transmission electron microscopy was employed in order to gain understanding into the calcination and reduction processes. In addition, the catalysts were screened on a purpose built fixed bed reactor, under industrially relevant conditions, to determine effect of catalyst preparation on Fischer-Tropsch activity.

A number of supported cobalt Fischer-Tropsch catalysts were prepared and investigated in this study in addition to an industrially supplied cobalt on zinc oxide catalyst. Data obtained from TGA, XRD and TEM analysis showed that the interaction of the cobalt nitrate complex varied significantly depending on the nature of the support. The cobalt species were found to be less well dispersed on the alumina when compared with the zinc oxide support. The nature of the decomposition of the cobalt nitrate on alumina was more closely related to that of the bulk nitrate, indicating less interaction between support and nitrate complex. This was reflected in the measured crystallite size after calcination, where the average cobalt oxide crystallite was found to be relatively larger.

Precursor effects were examined using cobalt nitrate and cobalt acetate salts on an alumina support. Decomposition on the catalyst prepared via the acetate precursor occurred as a single event, in contrast to the bulk acetate decomposition, suggesting a significant interaction between support and cobalt acetate complex. The highly exothermic nature of the cobalt acetate decomposition, observed from the DSC data, is likely to be responsible for this increased salt-support interaction. Absence of cobalt oxide peaks from the XRD data suggest small or amorphous particles present after calcination on the catalyst prepared from the acetate. The measured cobalt oxide particle size was found to correlate with the extent of cobalt reduction.

The effect of the calcination procedure was examined using differently calcined but otherwise identical cobalt on zinc oxide catalysts; exposing a difference in the measured cobalt oxide crystallite size, and subsequently, a measurable effect on

the extent of reduction. The reduction profiles for the cobalt on zinc oxide catalyst did not exhibit the expected ratio for reduction of cobalt spinel oxide to metallic cobalt, seen with the cobalt nitrate on alumina catalyst; instead it was found that reduction profile was more closely linked to reduction of cobalt zincate.

In terms of FTS results, CO conversion and selectivity were found to be influenced by the nature of the cobalt precursor. Comparison between the zinc oxide and alumina supported catalysts showed little effect on FTS activity. However, cobalt supported on zinc oxide exhibited a shift towards products with higher molecular weight hydrocarbons. It has been postulated that this increased C5+ selectivity is due to decoration of the active cobalt sites with zinc. Catalysts prepared from the cobalt acetate exhibited higher activity than those prepared from the cobalt nitrate; a result of the highly dispersed cobalt present on the cobalt acetate. The formation of higher molecular weight hydrocarbons was favoured over cobalt nitrate on alumina exhibiting high reducibility, while the product distribution shifted towards the formation of lighter hydrocarbons for the less reducible cobalt acetate catalyst.

All catalysts exhibited a two stage deactivation suggesting several modes of deactivation are occurring during time on stream. The nature of the support plays a role in the cause of deactivation. Sintering for the cobalt active phases has been put forward as the likely mechanism responsible for this, however this is only thought to occur during the initial stages of the reaction. It is proposed that no significant sintering occurs on the calcined cobalt on zinc oxide catalyst.

ACKNOWLEDGEMENTS

First and foremost I should like to express my thanks to Professor S. D. Jackson for his constant help and encouragement throughout the course of this research. I would especially like to thank him for the faith he showed in me when providing me with the opportunity to do both my Masters and this PhD.

I would like to thank my industrial supervisors at BP, Ewan Ferguson and Barry Nay who provided valuable assistance at different stages of the project.

Special thanks also go to my second supervisor Dr. Justin Hargreaves, for always having the time to help out even when he didn't have the time.

My thanks are also due to my colleagues and the technical staff, especially Andy Monaghan for many useful discussions and assistance.

Finally I would like to thank my family and friends for their patience and support.

CONTENTS

List of Figures

List of Tables

List of Abbreviations

All abbreviations used in this thesis are listed below.

ASF	Anderson-Schultz-Flory
BET	Brunauer-Emmett-Teller
DSC	Differential scanning calorimetry
FID	Flame ionisation detector
FTS	Fischer Tropsch synthesis
GC	Gas chromatograph
GTL	Gas-to-liquid
LNG	Liquefied natural gas
TEM	Transmission electron microscope
TGA	Thermogravimetric analysis
TOF	Turnover frequency
TOS	Time on stream
WGS	Water-gas-shift
XAFS	X-ray absorption fine-structure
XANES	X-ray adsorption near-edge structure
XPS	X-ray photoelectron spectroscopy
XRD	X-ray diffraction

1. INTRODUCTION

1.1 Gas to liquids

Fischer Tropsch synthesis (FTS) is an industrially important catalytic reaction for the production of hydrocarbons which are synthesised catalytically from synthesis gas (syngas), which is a mixture of carbon monoxide and hydrogen. This can be expressed by the general equation shown below:

$$n\mathrm{CO} + 2n\mathrm{H_2} \rightarrow (\text{-}\mathrm{CH_2}\text{-})_n + n\mathrm{H_2O}$$

Equation 1.1: General overall reaction in Fischer-Tropsch synthesis.

As can be seen from equation 1.1 Fischer-Tropsch synthesis yields a broad mixture of hydrocarbon products, ranging from light gases to heavy wax as well as some oxygenated products. The process was discovered by co-workers Franz Fischer and Hanz Tropsch in Germany in the 1920's and in 1926 they were able to demonstrate the synthesis of a range of hydrocarbons, from ethane to solid paraffin, from syngas over a catalyst surface [1]. Despite being viewed at the time as a major scientific breakthrough, its industrial application as an option for the production of fuel has been strongly linked to the prevalent economic and political conditions in different countries. Interest in the Fischer-Tropsch (FT) process has always had to compete economically with the refining process and the price of crude oil in order to make the process viable. It can be seen from figure 1-1 that the price of crude oil has varied considerably over the last couple of decades [2]. This coupled with political factors such as the drive for energy security by individual nations has led to fluctuations in the level of research and investment into FTS over the last 80 years. However, in recent years there has been a renewed interest in FT technology for a number of reasons [3-5].

The worlds proven reserves of crude oil have stagnated whilst known natural gas reserves have continued to increase to a point where exploitation of natural gas will become of primary importance to the energy sector in the foreseeable future. However the remote or stranded location, of around half of the world gas reserves, is a barrier to the commercial exploitation of this potential resource. This is due to

the lack of infrastructure in these areas rendering the gas reserves not easily or economically transferrable to markets by either pipelines or liquefied natural gas (LNG). The conversion of natural gas to liquid at source enables the use of cheaper, conventional methods of transportation to market as well as the utilisation of existing storage facilities. In contrast, LNG transportation requires the construction of both liquefaction and re-gasification facilities and the use of specially designed tankers. On sites where oil production is already in operation, the significant amounts of flared gas, produced as a by-product, can be converted to liquids with the existing infrastructure employed to transport the product to market [6, 7].

In addition, gas to liquid (GTL) technology can help meet the increasing pressures on the energy industry to provide greener fuels, driven by both changing consumer attitudes and environmentally based government legislation. In comparison to that produced from crude oil, fuel obtained via GTL technology is much cleaner being virtually free from aromatics as well as nitrogen and sulphur compounds [8]. The conversion of previously flared natural gas associated with crude oil has both a positive environmental impact and facilitates the attainment of legislative requirements by utilising gases that would otherwise be wasted.

Increased desire for energy security amongst the worlds leading energy consumers is a further driver for interest into GTL technology. Increasing instability in many of the current major oil producing regions coupled with fractious relations between major consumers and producers of oil have made exploitation of alternative fuel sources out with these regions more desirable.

In light of these factors, it is likely that there will be a shift in the future, resulting in a change from crude oil to natural gas as a feedstock for the production of fuels and chemicals. The price of crude oil has remained at well over $50 per barrel in recent years. However technological developments have lead to increased efficiencies in the FT process which would allow the process to be competitive even if the value of crude oil drops as low as $16 per barrel [7] . Taking all of these factors into consideration, FT is now seen as an attractive and competitive option when considering future energy production.

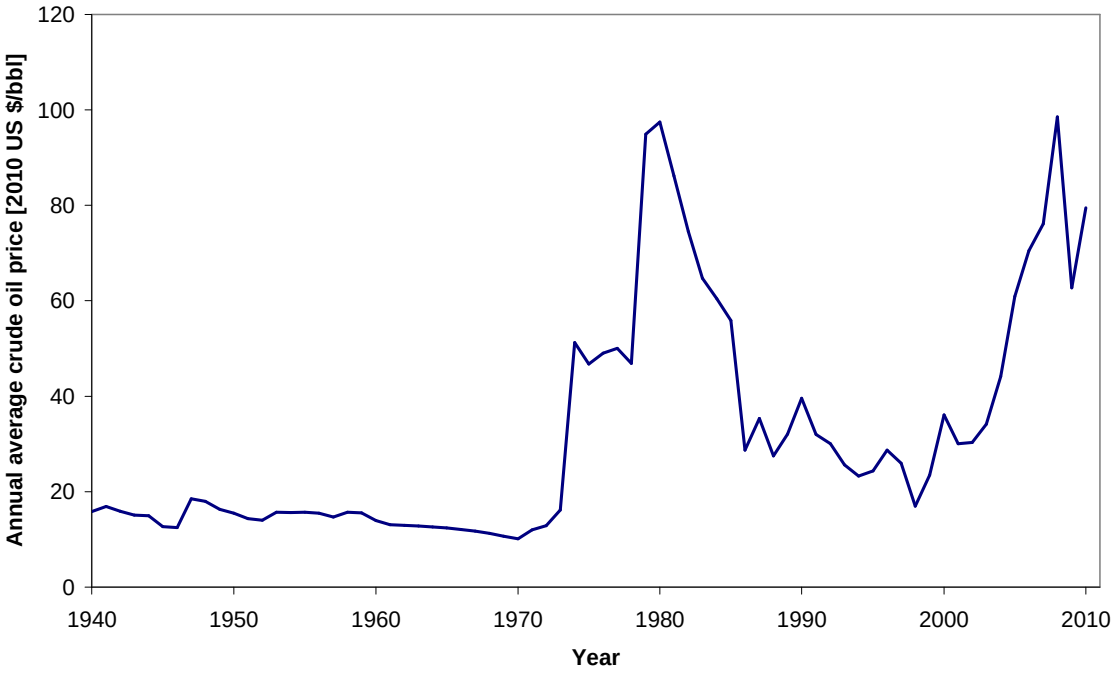

Figure 1-1: Historical variation in crude oil prices. The figures have been corrected for inflation to 2010 US$/bbl [2] .

As a consequence of this, there have been several recent decisions by leading petrochemical companies to drive major investments in the building of large scale FT plants. One of the best examples of these is the Oryx GTL plant in Qatar which is a joint venture between Qatar Petroleum and Sasol. The plant has been operational since 2006 and produces 34,000 bbl/ day of liquid fuels. Another example is Shell's Pearl GTL plant in Qatar, which is set to be fully operational next year with a capacity of 260,000 bbl/day of lubricants, naptha and fuels [9] . With many projects either under construction or at the planning stage it is believed that by the year 2020, 5% of the total production of chemicals could be based on FT technology using methane instead of crude oil refining operations [4, 5, 10, 11].

1.2 Technology

Fischer Tropsch synthesis is just one of three key components that make up the gas to liquid (GTL) technology process. The complete process consists of, the generation of synthesis gas (carbon monoxide and hydrogen), syngas conversion to hydrocarbons via Fischer-Tropsch synthesis and product upgrading [5]. Figure

1-2 shows a block flow diagram of the Oryx GTL plant, which is an example of the complete gas to liquid conversion process [12] .

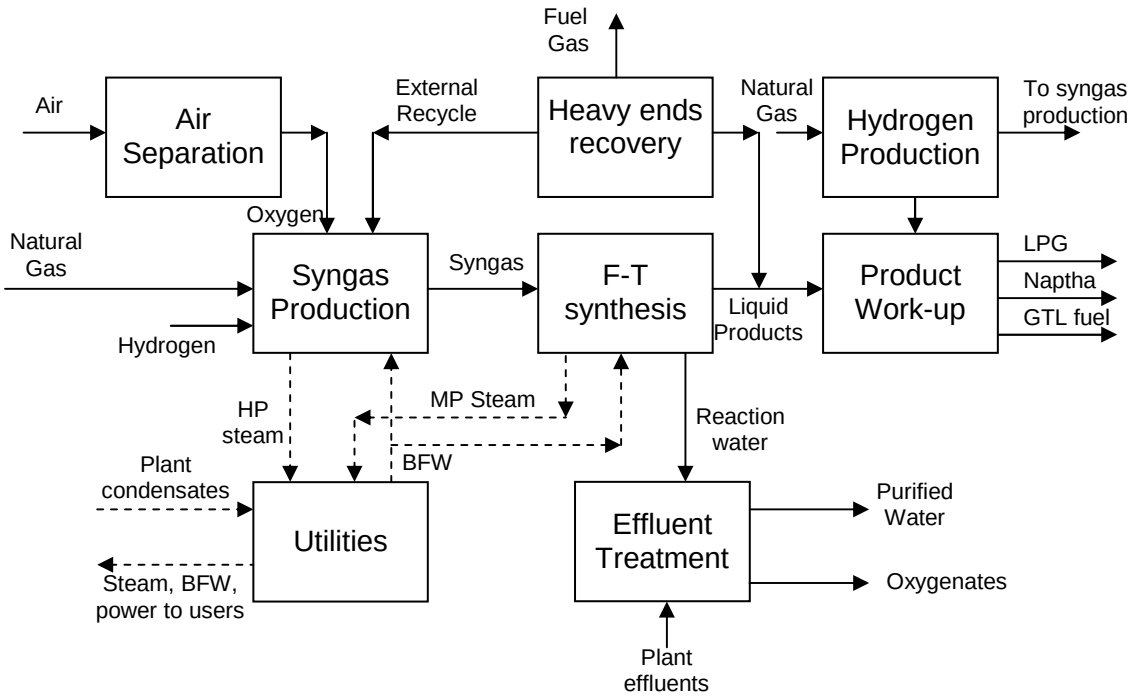

Figure 1-2: Flow diagram for Oryx GTL plant [12]

The first stage involves production of synthesis gas which can be generated from a variety of sources including coal, natural gas and biomass. For natural gas there is a range of processes by which this can be achieved including steam reforming, combined or two step reforming, partial oxidation and autothermal reforming. For the Oryx plant, the synthesis gas is produced from natural gas by autothermal reforming, currently considered to be the most economically attractive option [5].

The produced syngas is used as a feedstock for the FT process, which involves the catalytic conversion of the syngas into hydrocarbons of varying chain lengths. The Fischer-Tropsch component of the process will be the main focus of this thesis.

The final part involves separation and upgrading of the FT products into shippable liquid fuel. Specifically, hydrocracking and fractionation of the long chain hydrocarbons in addition to hydrogenation of olefins and oxygenated products.

From the diagram of the Oryx plant it can be observed that there are several other facilities that supplement the core processes. These are employed to increase the efficiency of the plant and include a heavy end recovery unit which recovers C_{5+} materials that would otherwise be lost in the FTS off-gas and a water treatment unit which separates hydrocarbons and oxygenates from the FT reaction water, enabling the former to be used as fuel.

1.3 Major reactions in FTS

A large number of reactions occur during FTS with the principal ones shown below (equations 1.2 to 1.4) [13, 14]. However FTS is complex and there can also be several side reactions such as water-gas-shift (WGS) where CO and water react to form CO_2 and hydrogen; and the Boudard reaction which results in the deposition of carbon [15]. The ratio of different reactions occurring will vary depending on a variety of factors and is strongly influenced by the type of catalyst used as well as process reaction conditions.

Alkanes $n\mathrm{CO} + (2n+1)\mathrm{H_2} \rightarrow \mathrm{C}_n\mathrm{H}_{2n+2} + n\mathrm{H_2O}$ (1.2)

Alkenes $n\mathrm{CO} + 2n\mathrm{H_2} \rightarrow \mathrm{C}_n\mathrm{H}_{2n} + n\mathrm{H_2O}$ (1.3)

Oxygenates $n\mathrm{CO} + 2n\mathrm{H_2} \rightarrow \mathrm{C}_n\mathrm{H}_{2n+2}\mathrm{O} + (n-1)\mathrm{H_2O}$ (1.4)

Thermodynamically the formation of hydrocarbons is energetically favourable. All the reactions shown above are exothermic therefore the formation of hydrocarbons is favoured at lower temperatures. However, the formation of methane, which is a less desirable product, is favoured over the formation of higher molecular weight hydrocarbons. Consequently, it is important that FTS catalysts and reaction conditions are tailored to minimise production of methane [16].

1.4 Cobalt catalysts

It is well known that iron, nickel, ruthenium and cobalt metals are active for hydrogenation of carbon monoxide [4].

Despite being the most active, the high cost and limited availability of ruthenium negates its use as a commercial catalyst for Fischer-Tropsch synthesis. On an equivalent metal basis, ruthenium is orders of magnitude more expensive than both iron and cobalt [6]. However, supported ruthenium catalysts have been widely employed in academic studies, particularly with those relating to mechanistic study [17, 18].

Nickel is also very active for CO hydrogenation; however, it has two main disadvantages. It has a high hydrogenating power resulting in the production of too much methane. Also, under realistic FT operating conditions Ni forms volatile carbonyls and as a consequence is gradually lost from the reactor. These factors render Ni unviable as an option for FTS [6] .

This leaves iron and cobalt as the only practical metals for FTS catalysts for industrial application. Due to the significantly lower price of iron in relation to cobalt, around 1000 times cheaper, the initial investment costs in production of iron catalysts for FT synthesis are substantially lower than those for cobalt catalysts. The low cost and abundance of iron allows for the catalysts to be prepared in the bulk form. In contrast to this, the cost associated with cobalt dictates that the metal must be highly dispersed on a high surface area oxide support, such as alumina or silica, to maximise available metal surface area. The use of these supports also serves to provide a robustness that iron catalysts do not have in the unsupported state [6, 19]. The initial higher outlay associated with cobalt is offset by the numerous performance advantages cobalt has over iron. These include higher activity, higher selectivity to longer chain paraffin's, lower water gas shift activity and longer lifetime.

Besides cost, the choice between iron and cobalt catalysts can also be influenced by the feedstock. The H_2/CO ratio will vary considerably depending on the source of carbon for production of synthesis gas. Cobalt catalysts have a low water gas shift activity which means the syngas feed needs to have a high H_2/CO ratio, usually of ~2, to ensure high conversions. This makes cobalt the ideal choice when syngas is produced from natural gas. In contrast, iron's water gas shift activity is ideal for feedstocks such as coal that produce a very low H_2/CO ratio, usually around 0.7. The iron catalysts WGS activity internally adjusts the low H_2/CO ratio to that required for FT synthesis reaction [19, 20] .

Although iron based FT catalyst are still currently used in industrial FT applications, the far greater advantages of cobalt mean that future plants for the production of diesel fuel will most likely use cobalt catalysts. This is reflected in the literature where the largest body of papers and patents in the last three decades have dealt with Co-based FT catalysts. This is in an attempt to make more active catalysts, with high wax selectivities (the waxy product then being the feed for hydrocracking) and low water-gas shift activity. Typical metal loadings of cobalt are between 10-30g of cobalt for 100g of support. Cobalt based catalyst compositions contain the following components [21]:

1. Co as the primary FT metal
2. A second metal (e.g. Ru, Re)
3. An oxcidic promoter element (e.g. Zirconia)
4. A high surface area oxide support

1.5 Anderson-Schultz-Flory (ASF)

As previously stated, FTS produces a broad spectrum of products, mainly consisting of alkanes and alkenes with carbon numbers ranging from C_1 to C_{50}. FTS is essentially a polymerisation reaction in which a monomer produced on the surface is added stepwise to a growing aliphatic chain. Hydrocarbon product selectivities are determined by surface-catalyzed chain propagation and rate relative to chain termination rate. The carbon number distribution of FT products is described in part by a chain polymerization kinetics model, Anderson-Schulz-Flory (ASF) distribution, which is mathematically represented by equation 1.5:

$$W_n/n = (1 - \alpha)^2 \alpha^{n-1} \qquad (1.5)$$

Where W*n* is the weight fraction of the product containing n carbon atoms and α is the chain growth probability.

Figure 1-3 shows how the theoretical product distributions depend on the chain growth probability (α). It is clear that only methane can be produced at 100% selectivity, and for all other values of alpha a broad range of products are formed. Deviations from the ASF model have been shown to occur, these usually include

higher than predicted methane selectivities, relatively low selectivity of C_2 and increased selectivities for heavier products.

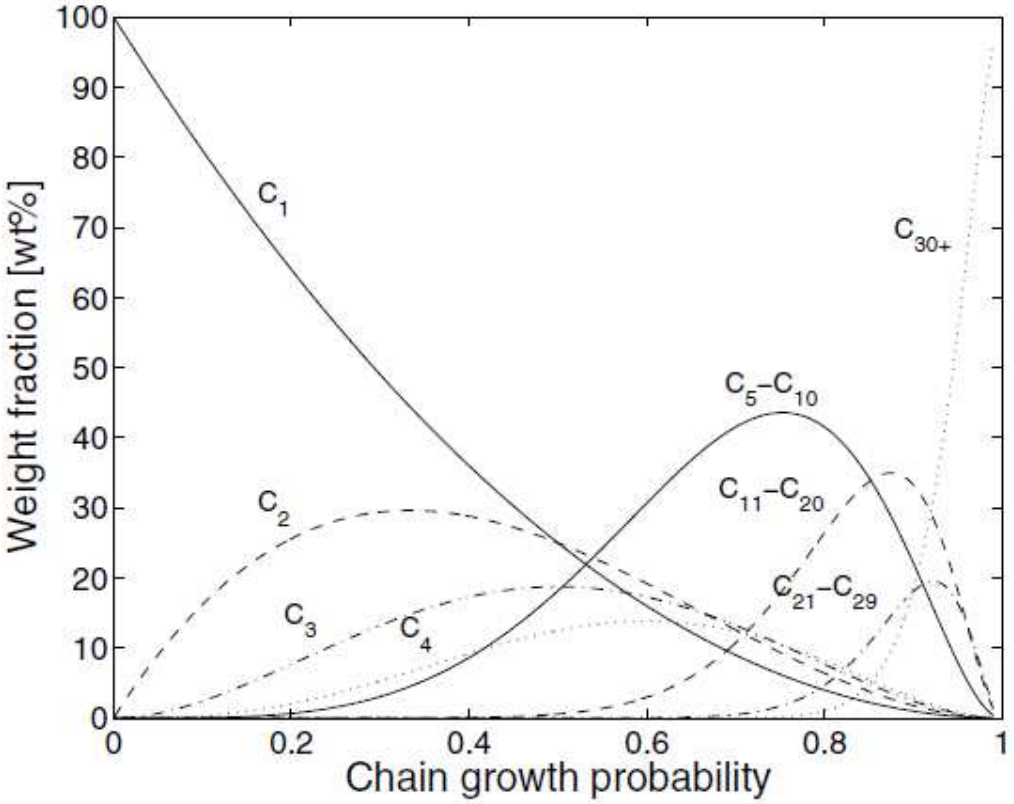

Figure 1-3 Selectivity of hydrocarbon fractions as a function of chain growth probability

A low alpha value implies a greater production of methane and light hydrocarbons whereas a high alpha value will indicate production of heavier hydrocarbons such as waxes. For the FTS process to be economical it is now considered desirable for catalysts to produce products with an alpha value of greater than 0.9. At this high value of alpha, the products will contain a large percentage of high chain hydrocarbons, such as waxes. These can subsequently be upgraded via hydrocracking to produce products with the desired chain length, usually high quality diesel fuels. There are many factors that can have an effect on the chain growth probability. These include the type of catalyst, use of promoters, operating temperature and the partial pressure of gases in contact with the catalyst. Today catalysts and reaction conditions are optimised towards the desired, relatively more valuable heavy hydrocarbons. Currently, promoted cobalt catalysts can

produce waxes with greater than 70% selectivity and therefore alpha values of 0.90-0.95.

1.6 Mechanism

Since the beginning of FTS in the 1920's, the elucidation of the mechanistic pathway for products formed has received considerable study with a variety of mechanistic schemes being postulated. Despite debate as to the exact mechanism there is a general acceptance that the formation of products involves a step wise chain growth of $–CH_2-$ groups on the catalyst's surface regardless of the products formed being alkanes, alkenes or alcohols. The main key steps are given below [10, 15]:

1. The adsorption and possible dissociation of CO
2. The adsorption and dissociation of H_2
3. Surface reactions leading to the formation of H_2O and CO_2
4. Surface reactions of adsorbed carbon and hydrogen leading to formation of alkyl chains of varying lengths. These are terminated by either addition or elimination of hydrogen to yield alkane or alkene products.
5. Desorption of final FT products
6. Secondary reactions taking place on the primary products formed, for example olefin readsorption followed by hydrogenation.

Although there is still a certain amount of debate as to the exact mechanism, most mechanistic proposals can be grouped into three principal types [22].

1. Carbene mechanism which proceeds via insertion of CH_x monomers, which are generated by dissociative chemisorption of CO followed by partial hydrogenation, into the metal-carbon bond of an adsorbed carbon chain. This is similar to the original mechanism postulated by Fischer and Tropsch in the 1920s [1].
2. The hydroxyl-carbene mechanism entailing partial hydrogenation to form CH bonds before the breaking of the CO bond, which produces a hydroxylmethylene intermediate (HCOH). This structure then grows by a

combination of condensation and water elimination steps using adjacent groups.

3. The CO insertion mechanism proposed by Pichler and Schultz [23] which involves insertion of adsorbed CO into the metal alkyl groups at the surface of the catalyst.

Although there is still much debate over the details of the mechanism, the carbene mechanism is now believed to be the most valid for the FT reactions [18, 24, 25] . However other proposed mechanisms such as CO insertion are still thought to be possible routes accounting for the formation of alcohols and other oxygenated products [26].

1.7 Characterisation

There is a huge amount of literature available in the scientific press citing the characterisation of cobalt catalysts. There have been many studies examining the structural, chemical as well as electronic properties of these catalysts. These results were obtained using a combination of different methods, the majority of which make use of techniques such as temperature-programmed reduction and oxidation (TPR/TPO), transmission electron microscopy (TEM), X-ray diffraction (XRD), thermogravimetric analysis and differential scanning calorimetry (TGA-DSC). It has been well documented that the different preparation variables influence the catalyst's structure and morphology. The following sections aim to look at the literature concerned with the effect of some of these variables.

1.7.1 Cobalt precursor

In FT synthesis the choice of precursor used to prepare supported cobalt catalysts can have a great impact on the resulting catalytic properties. There are a variety of precursors used for the preparation of cobalt supported catalysts, these include cobalt EDTA, ammonium cobalt citrate, cobalt acetylacetonate and cobalt chloride [27]. The majority of the literature however is concerned with the cobalt nitrate and cobalt acetate salts. Giradon *et al.* [28] examined the effect of cobalt silica-supported catalysts prepared from acetate and nitrate salts using a combination of characterisation techniques including TGA-DSC. They found that the precursor used, strongly influences the structure of the supported cobalt species formed.

The highly exothermic nature of the acetate decomposition was found to react with the silica to produce barely reducible cobalt silicate. On the other hand, the decomposition of the nitrate was found to be endothermic, yielding larger Co_3O_4 crystallites. Therefore depending on the exothermicity of cobalt precursor decomposition, the supported cobalt ions either agglomerated to form Co_3O_4, or reacted with the silica support to yield amorphous cobalt silicate. Martinez *et al.* [29] studied the effect of cobalt precursors on the catalytic properties of mesoporous Co/SBA-15 catalysts for FT synthesis. At similar cobalt loadings, catalysts prepared from organic precursors such as acetate and acetylacetone gave a much better dispersion when compared with those prepared from the nitrate. However, these well dispersed cobalt particles subsequently interacted strongly with the support, producing cobalt silicates which are only reducible at temperatures above 1000 K. Similar results have been reported in a number of other studies [30, 31] .

Investigations using XRD and TEM confirmed a greater degree of cobalt species dispersion on catalysts prepared via acetate [32]. From XPS data in the same study, it was shown that after calcination Co_3O_4 is the dominant cobalt species on the catalysts prepared via the nitrate, whilst Co^{2+} dominate on the acetate catalysts. They proposed that the differences are due to oxidation of Co^{2+} to Co^{3+} during calcinations by residual NO_3^- anions from the cobalt nitrate precursor.

Studies into the effect of cobalt precursor on the cobalt reducibility have shown that the TPR profile is strongly influenced by the nature of the starting cobalt precursor. For catalysts prepared via the nitrate the TPR profile contains two reduction peaks, usually assigned to the stepwise reduction of cobalt oxide via $Co^{3+} \rightarrow Co^{2+} \rightarrow Co$. For catalysts prepared using organic precursors the reduction occurs as a single event. It was suggested that this one broad peak could be the result of an overlap of both reduction steps [30].

More recent studies have examined cobalt catalysts prepared from a mixture of cobalt nitrate and cobalt acetate salts for use in Fischer Tropsch synthesis[33]. These catalysts displayed higher activity than those prepared from either mono precursor [33-35].

The influence of the precursor can also be explained in terms of its effect on the pH of the impregnating solution [36, 37] . Van Steen *et al.* [37] studied the influence of the pH of the impregnating solution on cobalt on silica FT catalysts. They reported that the silanol groups can exist as different species depending on the pH of the impregnating solution, resulting in varying interactions between the cobalt and the silica support. It was found that using an impregnating solution with a pH of above 5, in this case acetate, leads to a higher concentration of cobalt silicate species formed after impregnation and calcination. This is thought to be due to the high pH causing the partial dissociation of the silanol groups, leading to increased interaction between these and the cobalt complexes. Similar results have been found by Ming *et al.* [36].

A recently published example of controlling the pH of the precursor solution is described by Lok [38]. The High Dispersion Catalyst (HDC) method uses a controlled pH precipitation of cobalt ammine to produce very small, uniformly dispersed cobalt crystallites on a γ-Al_2O_3 support.

1.7.2 Support

A variety of supports are used to prepare cobalt catalysts for FT synthesis depending on the properties required; however the bulk of the literature is concerned with high surface area oxide supports, in particular silica, alumina and titania. The use of supports such as zeolites [39-41] and carbon [42, 43] are also widely reported in the literature.

Cobalt FT catalysts prepared using different supports were studied by Vob *et al*. [44] using a variety of characterisation techniques. A strong Co-support oxide interaction, as seen in the case of alumina and titania, was observed to stabilise small clusters. This favours dispersion but in turn decreases reducibility. On the other hand, a much weaker interaction leading to higher reducibility occurs for the silica supported cobalt catalysts. In this case the cobalt particles tend to appear as large clusters on the support surface, resulting in relatively low cobalt dispersion. Similarly Jacobs *et al*. [45] found that support interactions during the reduction of cobalt oxide species were observed in the order Al_2O_3 > TiO_2 > SiO_2. The interaction between the cobalt surface species and support was increased for supports that stabilised smaller clusters.

There has also been considerable research examining the effect of the support pore size distribution on both the resulting Co_3O_4 particle size and the extent of agglomeration. The relationship between pore diameter and cobalt particle size has been reported for various silica supports. It has been well documented that larger pore size leads to the formation of larger cobalt particles [46-48] . Saib *et al.* [46] investigated the average cobalt crystallite size produced when cobalt nitrate was impregnated on silicas with a range of mean pore diameters. The size of the cobalt crystallite was found to depend on the average pore diameter of the silica support; with the crystallite size found to increase with increasing average pore diameter above 2nm. The same conclusion has been reached by Khodakov *et al.* [47, 49] investigating cobalt catalysts supported by mesoporous silicas, with larger Co_3O_4 particles being observed in silicas with larger pores. Figure 1-4 shows that the Co_3O_4 particle size increased with an increase in the pore diameter and can also be correlated to the reducibility.

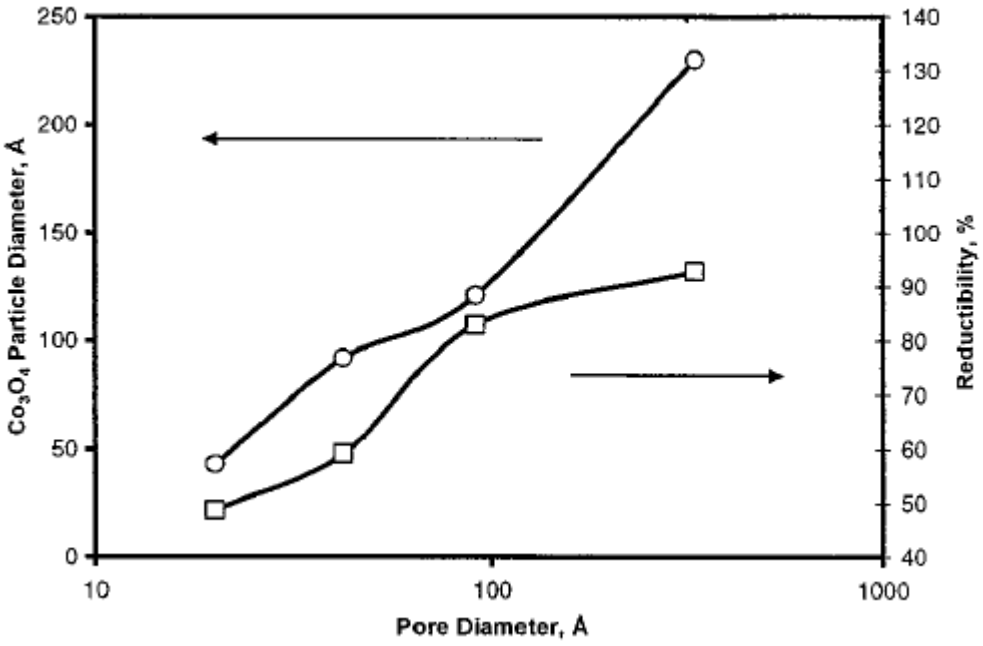

Figure 1-4: Dependences of Co_3O_4 particle sizes and extents of cobalt reduction on the pore diameter of mesoporous silicas [49].

Similar correlations have been found for alumina supported cobalt [50]. As a consequence of this positive correlation, Khodakov *et al*. [47, 49] postulated that the cobalt crystallites were located in the silica pores rather than located on the exterior surface of the support. In contrast, research by Dalai *et al.* [51] examined

20% cobalt supported on wide and narrow pore silicas and found in both cases that the average cobalt crystallite size was larger than the average pore diameters. As a result, they propose that the cobalt resides predominantly on the exterior surface of the support.

The majority of studies linking Co_3O_4 crystallite size to catalyst pore diameter involve catalyst preparation by incipient wetness impregnation. Where other preparation techniques have been employed, such as 'high dispersion catalyst' (HDC) technology it was found that small, highly dispersed cobalt particles were produced regardless of the support pore sizes [38].

As well as a correlation between pore structure of the support and Co_3O_4 particle size, the pore size distribution also influences whether the Co_3O_4 crystallites occur as single crystals or as aggregates of many crystallites following calcination. For instance, Storsaeter *et al.* [52] used a variety of characterisation techniques to investigate the effect the support had on the size, appearance and shape of the cobalt particles. They reported that larger Co_3O_4 aggregates were found on silica and γ-Al_2O_3 supports. On the other hand, on TiO_2 which has a relatively large average pore size, Co_3O_4 exists as larger single discrete particles. It was concluded that the agglomerates of Co_3O_4 particles increase with increasing pore diameter of the support up to a point at which no agglomeration will occur. Similar effects have been observed for cobalt catalysts supported on silicas with increasing mean pore diameters [46]. Also, Jablonski *et al.* [53] found that on high surface area silica, the Co_3O_4 particles exist in agglomerates whereas for low surface area silica, with larger pores, the Co_3O_4 phase is distributed relatively evenly over the support. Storsaeter *et al*. [52] speculated that this effect was explained by the fact that, for the smaller pore diameter supports, the Co_3O_4 crystallite size was larger than the average pore diameter. In turn, a large fraction of the particle is not located within the pore but instead situated on the outside or occupying adjacent, interconnecting pore cavities. On the higher surface area supports, it is likely that the pores are more closely connected. This may enhance the possibility of diffusion of the cobalt precursor into adjacent pores during drying and calcination and in turn increase the probability of cluster growth. In supports with lower surface area and larger pores, the average Co_3O_4 particle size is smaller than the average pore diameter suggesting that the cobalt particles are

located within the pores. The larger particles do not easily migrate on the support surface and hence no agglomeration will take place.

It has also been shown that modification of the support, through heating or chemical treatment, prior to impregnation can be employed to influence the FT activity through changes in reducibility and dispersion. It is widely accepted that calcination of the support prior to impregnation can moderate the interaction between the support and the metal precursor [54, 55]. In addition, modification of the support through the use of various organic groups has been shown to lead to changes in the interaction between the cobalt species and support, and hence the reducibility [56, 57].

1.7.3 Drying and calcination

When preparing catalysts via impregnation, drying and calcination are important steps and can have a significant influence on the final catalyst [28, 37, 58, 59]. Many articles have been published on the effect of the temperature of calcination. The size of Co_3O_4 crystallites formed after calcination has been found to increase with the temperature of calcination. For instance, Giradon *et al*. [28] found a low calcination temperature produced small and therefore difficult to reduce, cobalt oxide particles. In contrast, at higher calcination temperatures much larger cobalt oxide crystallites were formed, however these did not yield a high concentration of cobalt metal sites. Therefore it has been suggested that there is an optimum calcination temperature to produce catalysts with good FT performance.

The TPR profiles have been shown to be affected by the temperature at which the catalyst has been calcined. Lower temperature calcinations have been shown to produce TPR profiles that exhibit a higher intensity of lower temperature peaks [28, 37] . In all cases these have been assigned to the decomposition of residual nitrate species in hydrogen. Lapidus *et al.* [59] investigated properties of impregnated cobalt catalysts with varying temperatures of calcination. Their results showed that the degree of reduction also decreases with increasing calcination temperature.

During calcination the heating rate and air-space velocity have been correlated to the catalysts FT performance [60, 61]. Increasing the air-space velocity or

decreasing the heating rate was shown to increase the final catalyst's FT performance. Van de Loosdretch *et al.* [60] found that a slower heating rate led to higher dispersed cobalt catalysts. An increase in the air-space velocity has also been correlated with an increase in cobalt metal surface area. This positive effect is thought to be due to both of these factors decreasing the concentration of water and NO_x. This effect has also been explained in terms of cobalt species formed, with the valency of cobalt depending on the concentration of NO_2 present during calcination. The valency will effect the final dispersion, when only Co^{2+} ions are present, wide distribution of the cobalt ions occur whereas in the presence of Co^{3+} ions sintering to form Co_3O_4 crystallites takes place [58].

Coulter and Sault [62] also attributed the nature of the cobalt surface species formed to the concentration of gas phase NO_x near the surface during the decomposition of the nitrate precursor. They also concluded that large concentrations of NO_x oxidise the intermediate Co^{2+} ions to form large Co_3O_4 particles, whereas in the absence of NO_x the cobalt ions react with the support. This is in agreement with van Steen *et al.* [37] who found that an increase in drying time and temperature both resulted in a decrease in the amount of cobalt species which are reduced at high temperatures.

1.7.4 Reduction

Reduction is a vital step in the pre-treatment of catalysts for FTS since it is the cobalt metal that is the active phase. The hydrogen reduction properties of particles of cobalt oxide have been found to depend on the size of the Co_3O_4 crystallites. Khodakov *et al.* [63] using *in-situ* X-ray diffraction studied the reducibility of Co species in silica supported catalysts with varying diameters of Co_3O_4 particles. It was found that reduction of Co_3O_4 to the CoO phase takes place in the same temperature range for all catalysts and is therefore independent of the average Co_3O_4 particle size. However the percentage reduced to cobalt metal is observed to be greater in catalysts with larger Co_3O_4 particles, suggesting that this second reduction step is dependant on the size of these particles. With samples consisting of smaller cobalt oxide particles, considerable concentrations of CoO were observed even after reduction at 723 K. Hence, the ease of reduction to metallic cobalt decreased from larger (20-70 nm) to smaller particles (6 nm). Similar results have been found with studies into the reduction properties of cobalt

catalysts supported on small and large pore silica [64]. Again it was observed that the difficulty of the reduction step CoO to Co increases with decreasing cobalt oxide particle size. Khodakov *et al.* [63] explained that these results are likely to be due to the smaller particles having a stronger interaction with the support and hence greater stability leading to a decrease in reducibility. Castner *et al.* [64] on the other hand correlated this effect to the ease of water removal during the CoO to metallic cobalt reduction step.

1.8 Fischer Tropsch

1.8.1 Activity

As mentioned previously, the majority of supports employed for FTS are high surface area oxide supports, namely silica, alumina and titania. Earlier studies of Fischer-Tropsch synthesis had suggested that the identity of the support was an important factor in determining the activity of an FT catalyst. For example Reuel *et al.* [65] found that the activity and selectivity of supported cobalt catalysts varied with support. A trend of increasing activity in the series Co/Al_2O_3 > Co/SiO_2 > Co/TiO_2 was observed. This observation was consistent with other findings such as the work by Vannice *et al.* [66] that found cobalt supported on alumina had a lower FTS activity compared to cobalt on silica.

However it is now widely accepted that FT activity is independent of the chemical identity of the metal oxide support. Instead there is thought to be a strong correlation between the cobalt metal area and the FT activity, in other words, the support has no chemical effect on the turnover frequency of Co sites. There are many studies relating to cobalt based FT catalysts, all of which indicate that the number of available surface Co metal atoms determine the catalytic activity.

Iglesia *et al.* [67] investigated cobalt supported on silica, alumina and titania under FT conditions that favour the formation of C5+ hydrocarbons. They showed that the cobalt-time yields increase linearly with increasing dispersion of the cobalt crystallites, regardless of the catalytic support. Investigations by Johnson *et al.* [54] again found that differences in the specific activity appeared to be more closely related to the extent of reduction of the catalysts. Similarly, Bessell [68] found that catalysts with high cobalt dispersions tended to produce highly active

FT catalysts as long as the reducibility was not hindered by the metal-support interactions.

CO hydrogenation activity was also shown to be independent of particle size in the range 6-20% dispersion. It was shown that the turn over frequency (TOF) was constant in the cobalt dispersion range studied. These results again are in contrast to the formerly discussed study by Reuel and Bartholomew [65] which reported an increase in the TOF by a factor of three when decreasing the dispersion from 20 to 10% under similar conditions with a similar SiO_2 supported catalyst.

However it is not certain as to whether these findings can be extrapolated to smaller more highly dispersed crystallites. Bezemer *et al.* [69] studied the effect of particle size on Fischer-Tropsch activity in 2.6 to 27nm range for cobalt supported on inert carbon nanofibre support. Similar to previous findings they reported that the surface-specific activity was constant and unaffected by the particle size in the range 7-27nm. However at particle sizes smaller than this there was found to be a sharp decrease in the turnover frequency. Several studies are in agreement with these findings with a similar relationship between the cobalt particle size and TOF being obtained [43, 70]. For particles smaller than 10 nm the TOF is found to increase linearly with increasing Co particle size.

It has been speculated that the dependence of FT turnover frequencies on cobalt particle sizes less than 10nm could be ascribed to reoxidation of smaller cobalt particles under FT reaction conditions or structural sensitivity of FT synthesis.

Bezemer *et al*. [69] however discarded the theory that this effect might be due to classical structure sensitivity, since this would only become apparent when the particle size is reduced to typically below 3-4 nm. The effect they observed was present for catalysts with particle sizes of up to 8nm. Instead, they attributed the cobalt particle size effect on FT performance to non classical particle size effects as well as surface reconstruction due to CO. They pointed out that FT reaction involves a large number of elementary steps, such as dissociation, hydrogenation and insertion and that a variety of sites may be needed. It was postulated, that on smaller cobalt crystallites the domains that combine these different active sites are not stable or they contain a non-optimum ratio of the different sites.

1.8.2 Selectivity

In contrast to their effect on activity, the size of cobalt crystallites have been shown to influence the C5+ selectivity. Using cobalt supported on carbon nanotubes, Borg and co-workers [71] examined the effect particle size had on selectivity and observed a positive correlation between cobalt particle size and C5+ selectivity. A similar correlation has been observed in several other studies [43, 72, 73]. Xiong *et al.* [43] postulated that this effect was due to bridged type adsorbed CO. This is thought to be more active because of the weaker CO bond being more likely to form on larger cobalt particles.

In addition, the nature of the oxide support has been shown to influence the chain growth selectivity of FT products. Carbon number product distributions have been shown to be significantly different on catalysts with similar loadings and dispersion on several different supports [74]. Borg *et al.* [75] showed that the C5+ selectivity was different for cobalt supported on two different types of alumina support in a range of particles size. This again suggests that the selectivity is not only related to the size of the cobalt particles but also the nature of the support. The authors also suggested that maximum selectivity was found with cobalt particles in the 7-8 nm particle range.

While investigating the effect of support, loading and preparation on FT selectivity, Reuel *et al.* [65] found that one of the most dramatic correlations was in its relationship with dispersion. They found that the average carbon chain length increased with decreasing dispersion. It is postulated that this effect is due to highly dispersed catalysts having an abundance of unreduced oxide surface species which are capable of catalysing the water gas shift reaction and as a consequence increasing the H_2/CO ratio. Therefore by decreasing the dispersion of the catalyst the production of higher molecular weight hydrocarbons was observed. Song et *al.* [76] reported that the pore size of silica support had a significant effect of FT catalytic performance. It was shown that with increasing mean pore diameter of the support, both the activity and selectivity pass through a maximum. They found silica supported catalysts that had an average pore diameter of between 6 to 10 nm exhibited the best performance for FT synthesis in terms of both conversion and selectivity for hydrocarbon formation.

1.9 FT deactivation

In Fischer-Tropsch synthesis, deactivation of supported cobalt catalysts is one of the main problems faced during practical application. Some of the suggested mechanisms of deactivation of cobalt catalysts during FTS include re-oxidation, sintering and solid-state reactions yielding inactive cobalt.

Oxidation by water produced from the Fischer-Tropsch reaction has been widely studied as a cause of catalyst deactivation. It has been shown that bulk oxidation of cobalt to cobalt oxide is unable to occur thermodynamically under the usual conditions employed during FTS [77]. In spite of this, there is evidence for the oxidation of smaller cobalt crystallites, which deviate from the bulk like behaviour and are therefore more susceptible to re-oxidation in the presence of water under realistic FT conditions [78].

Schanke *et al.* [79] using XPS and gravimetric analysis concluded that surface oxidation or oxidation of highly dispersed cobalt phases are responsible for the observed deactivation on the Co/Al_2O_3 catalysts studied. Jacobs *et al.* [78] showed by XANES and EXAFS analysis that again re-oxidation occurred for a small fraction of the cobalt, with evidence for either Co_3O_4 or cobalt aluminate being formed. Van Steen *et al.* [80] found that the re-oxidation of cobalt was dependant on the size of the crystallite. As a model for catalyst deactivation during FTS they investigated the oxidation of small cobalt crystallites in the presence of water and hydrogen as a function of crystallite diameter. It was found that cobalt crystallites smaller than 4-5 nm were likely to be re-oxidised under realistic FTS conditions. This is in agreement with Saib *et al.* [81] who ruled out oxidation as a mechanism for deactivation in a study using a supported cobalt on alumina catalyst with cobalt metal crystallite of about 6 nm. XANES measurements were performed on wax covered spent catalysts which were taken from the FT reactor at various times on stream. It was thought that the wax coating would prevent re-oxidation of the catalyst prior to characterisation. XANES data of samples withdrawn at increasing times on stream indicate that no oxidation of the cobalt occurred and in fact a gradual reduction of the cobalt oxide was observed with time on stream under FTS conditions. The conclusion was that oxidation does not occur on cobalt metal crystallites of 6nm under realistic FT conditions. Similarly crystallite size correlations have been reported showing that under realistic FTS conditions only

small cobalt crystallites (less than 5-6 nm) will re-oxidise and deactivate rapidly under industrially relevant FTS conditions. The cobalt oxidation was not significant, if at all present, for metal crystallites larger than 5 nm [82] . A recent study has even ruled out oxidation as a mechanism for deactivation of cobalt particles with a crystallite size of larger than 2 nm [83].

A further factor influencing the extent of oxidation is the P_{H_2}/P_{H_2O} ratio. Reducible and less reducible cobalt oxide species will be formed depending on the severity of the oxidant conditions [77]. Schanke *et al.* [84] found that even at high H_2O/H_2 ratios, only a small amount of re-oxidation of cobalt could be observed when H_2 was present. Li and co-workers [85] studied the deactivation of cobalt catalysts by varying the partial pressures of water in a continuously stirred tank reactor. It was shown that low space velocity, hence higher water partial pressures, resulted in higher deactivation rates when compared with higher space velocities. Furthermore it was shown that the addition of small amounts of water resulted in only a small decrease in conversion. This effect was transient with conversion returning to the expected value after the addition of water had terminated. However, when large amounts of water, greater than 28% volume were added, the result was a severe and irreversible deactivation of the catalyst. Similarly Jacobs *et al.* [86] found that the addition of water, of less than 25% by volume, had only a slight effect on the conversion which was reversible and hence thought to be due to a kinetic effect. Again addition of water above 28% by volume caused irreversible deactivation which was concomitant with changes in the cobalt structure observed by XANES analysis. It was suggested that cobalt aluminate type species had been formed.

Cobalt crystal growth or cobalt sintering during the reaction has been suggested by several authors as a possible cause of FT catalyst deactivation. Karaca *et al.* [82] studied alumina supported cobalt catalyst using *in-situ* time resolved XRD under realistic reaction conditions. They found that with time on stream there was narrowing of the XRD peaks attributed to metallic cobalt phase, indicating the sintering of the cobalt crystallites. This occurred during the first 3-4 hours of reaction and was concurrent with a drop in CO conversion. This data is consistent with Saib et al. [87] who, using HADDF-TEM analysis of spent catalysts observed that sintering appears to dominate the deactivation in the early stages of the reaction with sintering of the cobalt crystallite from around 9 nm to 15 nm after 20

days of FTS. Das *et al.* [88] also cited sintering of cobalt as the main cause of deactivation in cobalt on alumina catalysts with cobalt crystallites of 7-8nm during FTS. Using EXAFS, a substantial increase in coordination number for the first Co-Co shell of the metallic phase was evident indicating significant cluster growth in the early part of the deactivation period. Similar results have been observed on silica supported cobalt catalysts with growth of cobalt crystallite during FTS observed at temperatures of 200 ^{o}C and 240 ^{o}C. It was found that sintering was much more pronounced at higher temperatures, with smaller cobalt particles aggregation more significant compared with larger ones.

In addition to re-oxidation, Jacobs *et al.* [78] concluded from XAFS and XANES studies of Al_2O_3 supported cobalt catalysts that significant cluster growth during the initial period of deactivation occurs.

A further cause of catalyst deactivation is solid state reactions between cobalt species and the support producing, for example, inactive cobalt aluminates. A study using cobalt on silica catalyst found that deactivation, at high CO conversion and therefore high water partial pressures, was due to cobalt-silica mixed oxide formation [89]. Similarly, Moodley *et al*. [90] cited solid state interactions as a cause of deactivation during FTS. They proposed that cobalt aluminate formation was due to the interaction of unreduced CoO and the alumina support. However they concluded that the formation of cobalt aluminate, despite occurring was not a major deactivation mechanism.

1.10 Project aims

Currently a vast amount of literature exists relating to the characterisation of supported cobalt catalysts for Fischer-Tropsch synthesis. Despite this many questions remain on the effect that the choice of precursor, support, and activation procedure have in determining the effectiveness of the final supported cobalt catalyst.

The overall aim of this project was to investigate the effects of (i) precursor (ii) support (iii) calcination procedure on the physical and chemical properties of supported cobalt catalysts. A multiple characterisation approach of thermogravimetric analysis, differential scanning calorimetry, X-ray diffraction and transmission electron microscopy was employed in order to gain understanding into the calcination and reduction processes. In addition, the catalysts were screened on a purpose built fixed bed reactor, under industrially relevant conditions, to determine effect of catalyst preparation on Fischer-Tropsch activity.

The scope of this thesis will involve three catalysts: BP supplied cobalt nitrate on zinc oxide, which is of particular interest to the projects industrial sponsors; a cobalt nitrate on alumina, a typical FT catalyst, to act as a standard for comparison; and a cobalt acetate catalyst to aid investigation into the effect of cobalt precursor.

2. EXPERIMENTAL

In this study both university and industrially produced catalysts were examined. The preparation method described in section 2.2 relates to the university produced catalysts only. The industrial catalyst, cobalt on zinc oxide, was supplied by BP chemicals in both the calcined and uncalcined form.

2.1 Materials

The chemicals used in the project were as follows with no further purification:

Table 2-1: Chemicals used, supplier and purity.

Chemical	Manufacturer	Purity
Cobalt nitrate hexahydrate	Avocado	98%
Cobalt acetate tetrahydrate	Sigma-Aldrich	99.995%
N_2	BOC	99.998%
Ar	BOC	99.998%
He	BOC	99.996%
H_2	BOC	99.995%

2% O_2/Ar	BOC	99.96% / 99.998%
2%H_2-N_2	BOC	99.995% / 99.98%
CO	BOC	99.9%
Toluene	Fischer	99.99%
Dichloromethane	Fischer	99.99%
Cobalt on Zinc Oxide	BP Chemicals	-
Alumina Support	Engelhard Al-3992	-
Alkane Standard C_{10}-C_{40} (even)	Aldrich	-

2.2 Catalyst Preparation

Catalysts containing 20 weight % cobalt were prepared by incipient wetness of alumina support with aqueous solutions of cobalt nitrate hexahydrate {$Co(NO_3)_2.6H_2O$} and cobalt acetate tetrahydrate {$Co(CH_3CO_2)_2.4H_2O$}.

Prior to impregnation, the support was dried in an oven at 100 ^oC overnight. To ensure uniform metal dispersion, the precursor salt was dissolved in a volume of water equal to that of the support pore volume. For the alumina, the pore volume was found to be 1 $cm^3\ g^{-1}$.

The metal precursor, cobalt acetate tetrahydrate (52.831g) or cobalt nitrate hexahydrate (61.730g), was dissolved in 50ml of deionised water and added to the support (50g). This was mixed on a rotary evaporator for 1 hour at room temperature, followed by 30 minutes at 80 ^{o}C to remove water. The catalyst was then dried in an oven at 100 ^{o}C overnight.

The following table shows the catalysts that were included in the study:-

Table 2-2:Table of catalysts used in study

Code	Catalyst/Support	Precursor	Make of support
CoNZ	Co/ZnO uncalcined	Nitrate salt	BP
CoNZC	Co/ZnO calcined	Nitrate salt	BP
CoNA	Co/Alumina	Nitrate salt	Engelhard Al-3992
CoAA	Co/Alumina	Acetate salt	Engelhard Al-3992

2.3 Catalyst Characterisation

2.3.1 Surface Area Determination

Physisorption of an inert gas (generally nitrogen at -196 ^{o}C) onto a surface and the subsequent plotting of the volume absorbed as a function of equilibrium pressure allows for the construction of an isotherm. The approach most commonly used was devised by Brunauer, Emmett and Teller, giving the expression:

Equation 2.1: The BET equation

$$\frac{P}{V(P_0-P)} = \frac{1}{V_M C} + \frac{(C-1)P}{V_M C P_0}$$

Where V = volume of gas adsorbed at equilibrium pressure P

V_M = volume necessary to form a monolayer

P_0 = saturated vapour pressure of the adsorbent gas at the temperature of measurement

C = a constant related experimentally to the heats of adsorption and liquefaction of the gas

$C = e^{(q1-qL)/RT}$

Where q1 = heat of adsorption of the first layer

qL = heat of liquefaction of adsorbed gas on all other layers

R = gas constant

Plotting $P/V(P_0-P)$ against P/P_0 yields a straight line, with the slope given by $(C-1)/V_M C$ and the intercept by $1/V_M C$.

The samples were initially out gassed at 110 ^oC in flowing nitrogen overnight to remove any adsorbed species from the surface. Measurements were performed using a Micromeritics Gemini III 2375 Surface Area Analyzer with helium being used as a calibrant and nitrogen as the adsorbent at -196 ^oC. Surface areas were calculated assuming the average cross sectional area of a nitrogen molecule to be 0.162 nm^2. Approximately 0.04 g of sample was weighed into a glass tube, with measurements taken of both the support material and the prepared catalysts.

2.3.2 Thermo-gravimetric Analysis-Differential Scanning Calorimetry (TGA-DSC)

Thermo-gravimetric analysis (TGA) was performed using a combined TGA/DSC SDT Q600 thermal analyser coupled to an ESS mass spectrometer for evolved gas analysis. Fresh sample (10-15mg) was heated to a maximum temperature of 1000 ^oC at a typical ramp rate of 10 $^oC\ min^{-1}$. Temperature parameters and gas

atmospheres that the samples were subjected to are outlined in the following treatments. The flow rate for the gases was 100ml min^{-1}. For mass spectrometric analysis, mass fragments with m/z = 2, 14, 16, 17, 18, 28, 30, 32, 40, 44 and 46 (amu) were followed.

Treatment 1: Sample was heated at 10 $^{o}C\ min^{-1}$ to 1000 ^{o}C in Argon.

Treatment 2: Sample was heated at 10 $^{o}C\ min^{-1}$ to 1000 ^{o}C in 2% Oxygen-Argon

Treatment 3: Sample was heated at 10 $^{o}C\ min^{-1}$ to 1000 ^{o}C in 5% Hydrogen-Nitrogen

Treatment 4: Sample was heated to 500 ^{o}C in 2% Oxygen-Argon. Sample was then cooled to room temperature in flowing Argon before being heated to 1000 ^{o}C in 5% Hydrogen-Nitrogen.

To calculate the degree of reduction of the catalyst, each sample was heated to the desired temperature and held for 10 hours in 5% Hydrogen-Nitrogen, with the weight loss monitored as a function of time.

2.3.3 X-ray Diffraction (XRD)

To obtain information concerning phase composition of the catalyst and crystallite size distribution, XRD studies were performed on a Siemens D5000 X-ray diffractometer (40kV, 40mA) using monochromatic CuKα X-ray source (1.5418 Å). The scanning range employed was $15^{o} < 2\theta < 75^{o}$ with a step size of 0.02^{o} and a counting time of between 1 and 15 seconds per step. All X-ray diffraction analysis was carried out using the Bragg-Brentano geometry. For sample preparation the catalysts were ground using an agate pestle and mortar to help ensure random orientation of crystallites. The material was subsequently placed into a circular depression on a sample holder and compressed with a glass slide until the level of the sample was aligned with the surface of the holder.

Hot-stage analysis was carried out using an Anton-Paar XRK reaction cell. The set up consisted of a water cooled, vacuum tight, stainless steel chamber with a beryllium window. Figure 2-1 shows a schematic of the main features associated with the cell :

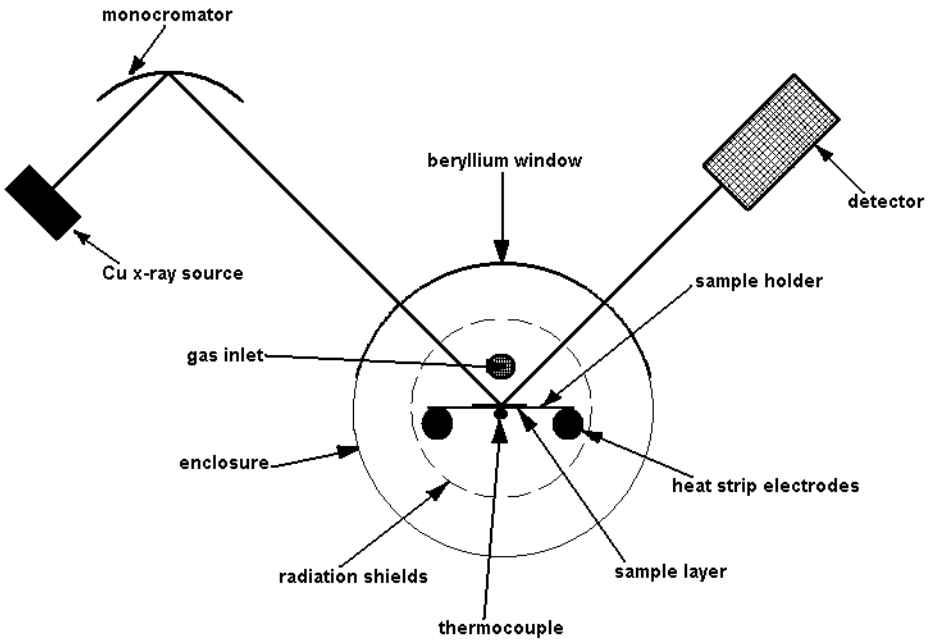

Figure 2-1: Schematic of hot-stage XRD chamber [91]

The samples were heated at 12 ^{o}C min^{-1} and scans taken at 30 ^{o}C, 100 ^{o}C and at 100 ^{o}C increments thereafter to 900 ^{o}C. At each stage the sample was held for 15 minutes at the desired temperature before the scan was taken. For each catalyst this temperature profile was carried out in a number of atmospheres.

Average crystallite sizes were obtained by measuring the full width at half maximum (FWHM) of a peak and applying the Scherrer equation:

Equation 2.2: The Scherrer equation

$$d = \frac{K \lambda}{B \cos\theta}$$

where d = particle size diameter / Å

k = constant = 57.29578^{o}

λ = wavelength of X-ray source = 1.5418 Å

B = full width at half maximum / degrees

θ = diffraction angle / degrees

This is only an approximate method since the results can be influenced by various factors such as micro strain as well as instrumental parameters. For crystallite size calculations only one peak was used, which will give only a lower limit to the size. Unfortunately there was no opportunity for a more detailed analysis to calculate broadening contribution from either micro strain or instrumentation. Based on independent runs for a selection of catalysts, the experimental error (+/- 2σ) for the cobalt particle sizes calculated from X-ray diffraction is less than +/- 1 nm.

2.3.4 High Resolution Transmission Electron Microscopy (HRTEM)

High-Resolution Transmission Electron microscopy (TEM) was performed on a FEI Technai T20 instrument equipped with a LaB_6 source, at 200 kV, with a point to point resolution of 0.24 nm. Samples were mixed with an appropriate solvent before being deposited, using a pipette, on copper grids with a holey-carbon-film support. Magnification and camera constants were calibrated using appropriate standards in the same electrical-optical conditions.

To conduct the electron microscopy studies with the catalyst in the reduced state, the catalyst was reduced and then passivated using 2% Oxygen-Argon before exposure to air. XRD studies of the sample after the passivation procedure showed that the major part of the cobalt oxidised rapidly to CoO with no traces of metallic cobalt found. *In-situ* reduction was not possible with the available equipment and thus the electron microscopy studies were carried out with the catalysts in their calcined state.

2.3.5 Metal Area Determination (CO Chemisorption)

CO chemisorptions were carried out on a pulse-flow glass microreactor (figure 2-2) composed of a series of glass bulbs connected to a manifold, which could be evacuated by rotary pump (Edwards Rotary Pump, Max vacuum ~ 10^{-2} torr). A bulb (2 litres) was used to store the carbon monoxide at just above atmospheric pressure. From this, aliquots of adsorbate gas could be inserted into a carrier gas flow through a sample loop (8.62 cm^3) and passed over catalyst contained in a U shaped reactor (figure 2-3).

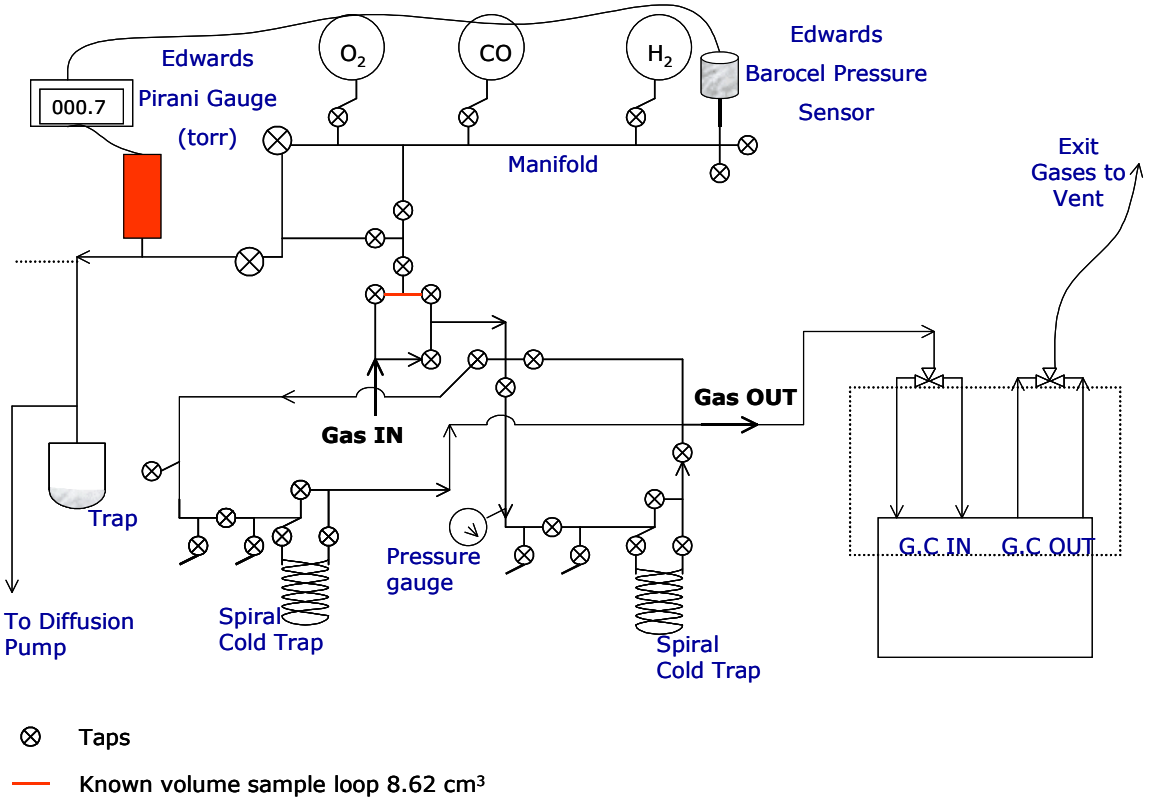

Figure 2-2: Glass rig line diagram

Temperature was controlled by a WEST temperature controller and was measured with a thermocouple located at the top of the catalyst bed, as shown in figure 2-3. The granules of catalyst (250-425 microns) were loaded into the reactor and placed on a fine sinter. The reactor was attached to the rig using black wax to seal the cone and socket connections.

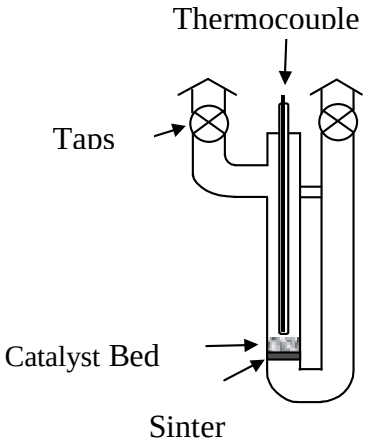

Figure 2-3: Reactor tube diagram

An on-line gas chromatograph (GC) was used to analyse the exit gases. The GC had a Thermal Conductivity Detector (TCD) and was fitted with a molecular sieve, 60-80 mesh column.

The catalyst (~0.5g) was reduced in flowing hydrogen at 40 cm^3 min^{-1} at 260 ^oC (for BP catalysts) and 300 ^oC (for cobalt on alumina catalysts) and held at the desired temperature for 10 hours before being cooled to room temperature. The gas was changed to flowing argon at 40 cm^3 min^{-1}. The sample was then heated in argon to the catalyst reduction temperature and held for 1 hour to desorb any chemisorbed hydrogen. A pulse of carbon monoxide (~30 torr) was introduced to the argon carrier gas from the sample loop. This bypassed the reactor and went directly to the GC. This was repeated several times to give a series of GC responses that acted as calibration peaks. From the volume and pressure of the gas the number of moles in the sample loop was calculated (equation 2.3). The sample loop was filled with a known quantity of gas as before. The pulse was injected into the flowing argon stream and passed over the catalyst and recorded by TCD. Aliquots of CO were continually passed through the catalyst bed until saturation occurred. The number of moles adsorbed by the catalyst for each pulse was obtained, with the sum being the total moles of gas required for complete chemisorption. From the results, catalyst dispersions and average metal particle sizes were calculated. Dispersions were calculated using equation 2.4.

Equation 2.3: Ideal gas equation

$$PV = nRT$$

P = pressure of gas

V = volume of gas

n = number of moles

R = gas constant

T = temperature

Equation 2.4: Catalyst dispersion calculation

$$\text{Dispersion (\%)} = \frac{\text{moles of surface metal}}{\text{total moles of metal}}$$

$$= \frac{\left[\text{Total number of molecules adsorbed}\right]}{\left[\frac{\left[\frac{\text{metal loading}}{100}\right]}{\text{MWt}}\right]}$$

MWt = moleculare weight of metal, Co = 58.93

2.4 Catalyst Testing

2.4.1 Apparatus

Catalytic tests were carried out in a purpose-built single-tube fixed-bed high pressure reactor, constructed from 316 stainless steel (figure 2-4).

The section of the rig, from the gas inlet through to and including the reactor tube, was silica lined to minimise the possible formation of iron or nickel carbonyls, a potential source of deactivation. Gases were fed into the reactor via programmable mass flow controllers, with a back pressure regulator allowing pressures of up to 20 barg to be achieved. The major part of the rig, from the vaporiser through to the first knock out pot, was contained within a purpose built oven heated to 170 ^{o}C. This was done in order to prevent the build up of products, such as high molecular weight hydrocarbons, which could impede the flow of gas through the reactor.

The reactor consisted of a 0.455 cm inside-diameter glass lined metal reactor tube positioned within an aluminium/bronze heater block. The temperature of the

catalyst bed was controlled by a thermocouple positioned in a groove in the heating block directly behind the reactor. An additional thermocouple, within the heating block, acted as a safety trip in the event of overheating.

Due to the wide range of products formed during FT synthesis, two individual traps, each maintained at different temperatures were employed to knock out desired reaction products. The first knockout pot was heated to 170 ^{o}C and was used to collect wax products (as defined below). An external tap was fitted to an internal needle valve allowing for sampling of heavy hydrocarbons throughout a reaction. The second knockout pot was chilled to 5 ^{o}C to collect lighter hydrocarbon products (defined below) as well as water. This was fitted with a two way valve for sampling during each reaction.

Hydrocarbons between C_6-C_{40} were analysed with wax products defined as heavy hydrocarbons, in the range of C_{10} to C_{40}. Liquid hydrocarbons products are defined as hydrocarbons in the range C_7 to C_{22}.

There was no set up in place for analysis of gaseous products. Online gas analysis would have allowed for determination and quantification of light hydrocarbon gases as well as H_2, CO and CO_2. Unfortunately due to problems with the equipment, it has not been possible to analyse this fraction of products and reactants. Analysis of lighter hydrocarbon products would have given us a complete analysis of all hydrocarbon products, allowing for calculation of C5+ selectivity. The analysis of CO_2 and CH_4 would have been of particular interest. Methane selectivity is an especially important index for FTS, for the process to be economical it is very important to have a very low selectivity towards methane production.

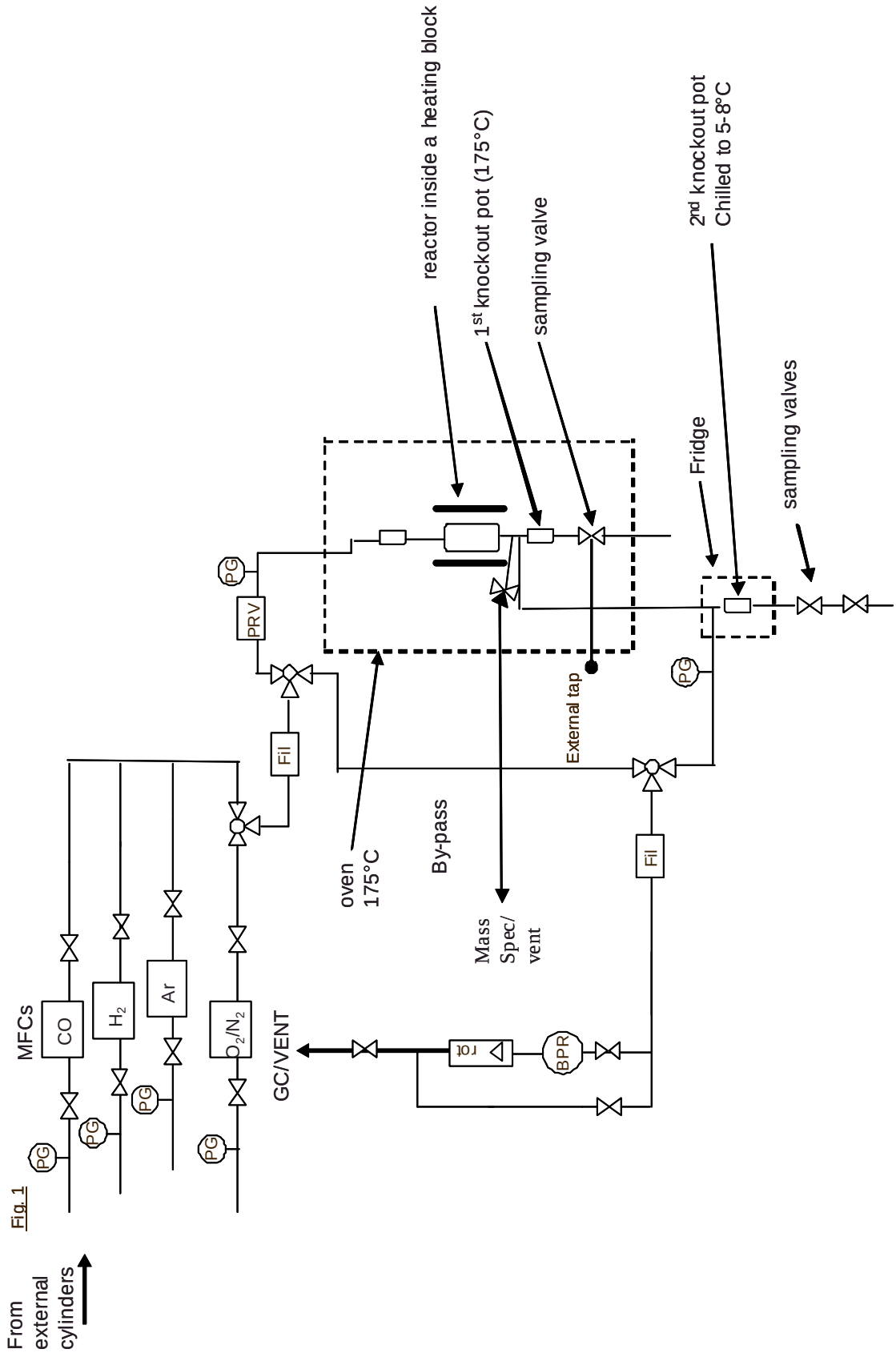

Figure 2-4: Process and instrumentation diagram of Fischer-Tropsch rig

2.4.2 Reaction Procedure

Catalyst, typically 0.4 g, was sieved to between 250 and 425 microns and placed in the reactor tube. To ensure the catalyst bed was centrally positioned within the tube, alumina was packed on either side. Prior to the reaction the catalyst was reduced *in-situ* at 260 ^{o}C (for the cobalt on zinc oxide catalysts) and 300 ^{o}C (for the cobalt on alumina catalysts) for 10 hours in a flow of hydrogen at atmospheric pressure. Subsequently, the temperature was decreased to the reaction temperature of 220 ^{o}C. CO was introduced and the flow rates adjusted to give a H_2:CO ratio of 2:1 and the pressure increased to 20 barg. A Gas Hourly Space Velocity (GHSV) of 10, 000 was employed. In order to achieve this, the weight of catalyst was kept consistent and total gas flow rates adjusted accordingly. These are shown in table 2-3 below. Once all desired parameters had been reached, the analysis was started and both liquid and wax samples were taken at 24 hour intervals.

Table 2-3: Total gas flow for each catalyst for Fischer-Tropsch reaction

Catalyst	Total Gas Flow (ml min^{-1})
CoNA	87.5
CoAA	119.1
CoNZ calcined	112.2
CoNZC	63.12
CoNZ no calcination	113.3

Prior to catalyst testing the alumina packing material was tested under identical conditions with no reaction found to occur.

2.4.3 Gas Chromatography (GC)

Product analysis was carried out offline by a Thermo Finnigan Trace GC fitted with a Varian CP-Sil 8 CB column (50m length x 0.32 mm I.D, 0.45 mm O.D, 5.0 µm film thickness).

2.4.3.1 Column Conditions

The carrier gas was Helium with a flow rate of 1.5 cm^3 min^{-1}. The injection temperature was 375 ^oC. For the waxes the column heating program was held at room temperature for 3 minutes before being heated at 20^{o}C to 300^{o}C and held for 240 minutes. The GC program for the lights is shown below in figure 2-5.

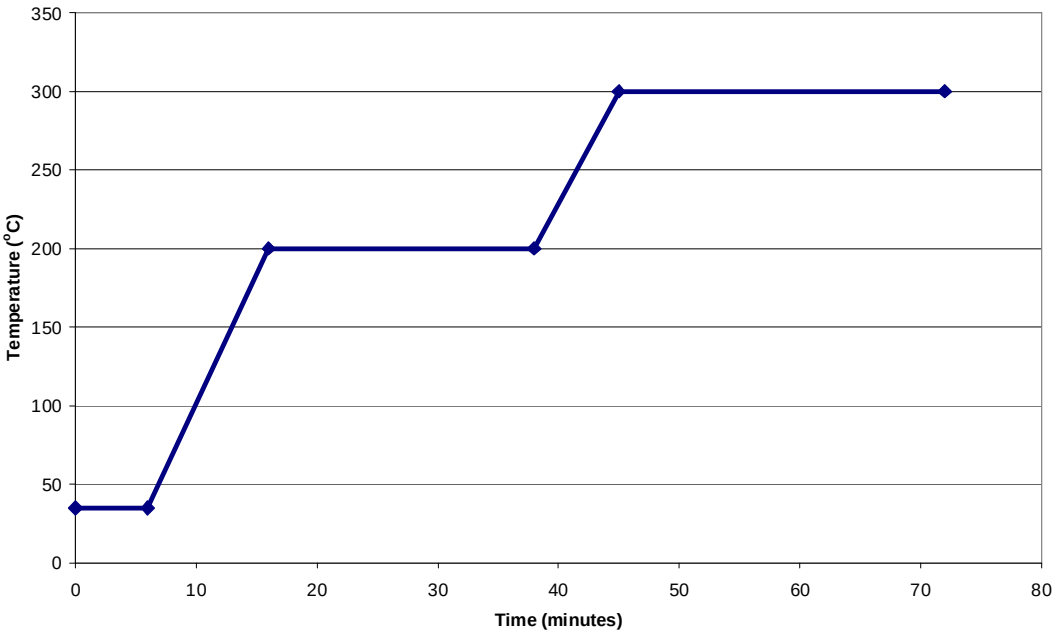

Figure 2-5: GC temperature ramp profile for lights

2.4.3.2 Calibrations

Quantification of results was carried out using a bought preset mixture of calibration standards for carbon even numbered hydrocarbons from C_{10} to C_{40}. These were prepared in a range of concentrations. The lower molecular weight hydrocarbons (C_6, C_7 and C_8) were prepared separately, again in a range of concentrations. For each component a known molar quantity was prepared in 10 mL solution of toluene. Solutions were prepared at theoretical 50, 75 and 100%

and from the peak responses linear calibration plots were obtained. This then allowed for GC response factors to be generated. From the peak responses, linear calibration plots were obtained. An example of the C_{34} calibration graph is shown in figure 2-6. The analogous nature of the hydrocarbons being studied allowed for determination of the odd numbered hydrocarbons. These were then used to work out the total number of moles produced in the whole sample. The standards were rerun at various stages throughout the research programme.

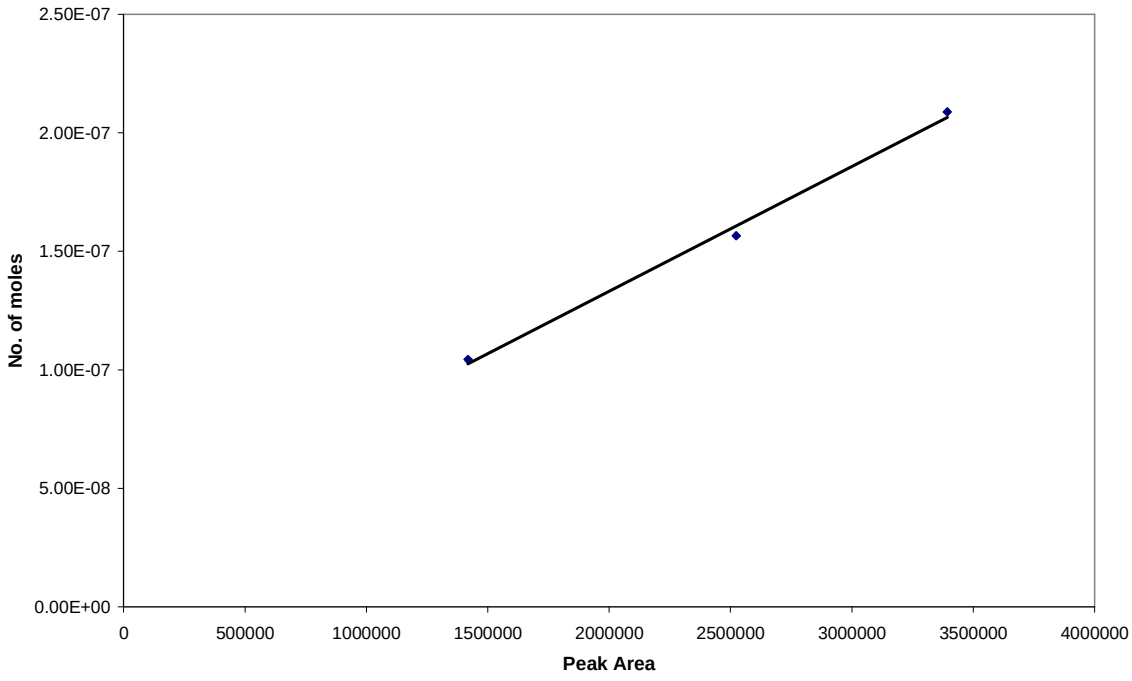

Figure 2-6: Calibration graph for C_{34} alkane

2.5 Calculations

2.5.1 Conversion

Due to water being the principle oxygenate product when using cobalt catalysts for FT synthesis it is possible to calculate the conversion from the amount of water formed. Specifically, each mole of oxygen from the reacted CO equates to one mole of oxygen in the water produced. Therefore the conversion was calculated as show in equation 2.5.

Equation 2.5: Conversion

$$\text{Conversion} = [\text{moles of water out} / \text{moles of CO in}] \times 100$$

As a consequence of calculating conversion in this way, experimental errors will arise from the measured amount of water, as despite being cooled to 5 ^{o}C, loss of water vapour from the knock out pot is possible. In addition, water was found from analysis to be the only oxygen containing reaction product, however, the lack of gaseous product analysis means we cannot rule out the production of CO_2 from CO. Therefore experimental errors of +/- 5% was assumed for all conversion data.

2.5.2 Deactivation

To calculate deactivation equation 2.6 was used:

Equation 2.6: Deactivation equation

$$\ln[C_{A0}/C_A)-1] = \ln(k\tau w) - kdt$$

Since our data is in the form of conversion we can transform equation 2.6 to one relating conversion with time as follows:

Since $C_A/C_{Ao} = 1-Xa$ (2.7)

$C_{Ao}/C_A-1 = [1/(1-X_A)]-1 = X_A/(1-X_A)$ (2.8)

By utilising Equation 2.8, the rate constant for deactivation, k_d, was calculated by plotting ln [Xa/1-Xa] versus time which yields a straight line with the gradient equal to $-k_d$. This equation assumes first order, irreversible kinetics for the main reaction and concentration independent, first order deactivation.

2.5.3 Alpha Values

The distribution of hydrocarbon products in FT synthesis is generally described by a chain polymerisation kinetics model referred to as the Anderson-Schulz-Flory (ASF) model which is mathematically represented by equation 2.9:

Equation 2.9: ASF equation

$$W_n/n = a^{n-1}(1-a)^2$$

This can be derived as follows:

The probability of forming a polymer = $P^{x-1}(1-P)$ (2.10)

If we define:

M = number of functional groups remaining
Mo = number of functional groups initially
Mx = number of polymers

Then we can say that $M_x = M\,P^{x-1}(1-P)$ (2.11)

Extent of Reaction

Following Carother's theory where P = extent of reaction

$$Mx = (M_o - M)/ M_o \quad (2.12)$$

Re-arranging gives

$$M = M_o(1-P) \quad (2.13)$$

Substituting equation (2.13) into (2.11)

$$M_x = M_o P^{x-1}(1-P)^2 \quad (2.14)$$

Number Distribution Fuction (Y_x)

$$Y_x = M_x / M \qquad (2.15)$$

i.e divide equation (2.14) with equation (2.13)

$$=P^{x-1}(1-P) \qquad (2.16)$$

⇨ Number distribution function = Probability of forming a polymer = $P^{x-1}(1-P)$

Weight Distribution Function (W_x)

If we define:

(FW) = the formula weight of a monomer unit

$W_{polymer}$ = weight of polymer present

$$W_{polymer} = x.(FW).M_x \qquad (2.17)$$

substitute M_x from (2.14)

$$W_{polymer}=x.(FW).M_oP^{x-1}(1-p)^2 \qquad (2.18)$$

Weight of material before reaction = $(FW).M_o$

If we divide equation (2.17) by equation (2.18)

$$W_{polymer} = x.P^{x-1}(1-P)^2 \qquad (2.19)$$

Alpha plots for FT

Rearranging equation (2.19) and changing x to n and changing P to α, gives

$$Wn/n = an\text{-}1(1\text{-}a)^2 \qquad (2.20)$$

Where:

n = carbon chain length
α = chain growth probability

An ln version used to calculate alpha values is shown below.

$$\ln(Wn/n) = (n-1)\ln a + \ln(1-a)^2 \qquad (2.21)$$

Rearranging gives

$$\ln (Wn/n) = n\ln a + \ln [(1-a)2/a] \qquad (2.22)$$

The Anderson-Schultz-Flory (ASF) chain growth probabilities were then calculated from the slope of the curve ln(Wn/n) versus n, where n is the carbon chain length and Wn is the selectivity for the C_n hydrocarbon. The chain growth probability was calculated for the C_{25}-C_{35} hydrocarbon range.

3. RESULTS

3.1 Surface area determination

Nitrogen adsorption at -196 ^{o}C was carried out on all catalysts and supports as described in section 2.3.1 with the data obtained presented in Table 3-1.

Table 3-1: BET data for the alumina support, and as prepared and calcined catalysts.

Catalysts	Surface Area (m^2/g)	Average pore diameter (Å)	Pore volume (cm^3/g)
Alumina	205	155	0.79
CoNA	132	127	0.42
CoNA calcined	146	125	0.46
CoAA	92	143	0.33
CoAA calcined	187	117	0.55
CoNZ	11	261	0.07
CoNZ calcined	28	253	0.17
CoNZC	8	221	0.048

It is clear from the results that, after deposition of the cobalt species on the alumina support, the surface area, pore volume and average pore diameter have all decreased. For the alumina, the surface area decreases from 205 m^2/g to 132 m^2/g and 92 m^2/g for the CoNA and CoAA samples, respectively.

It can be seen that the zinc oxide supported catalysts have a much smaller surface area and larger average pore diameter than the alumina supported catalysts. The

CoNZ catalyst has a surface area of 11 m^2/g, and a pore volume and average pore diameter of 0.07 cm^3/g and 261 Å, respectively. Depending on the calcination, the surface area and pore volume of the CoNZ catalyst are dramatically different. For the CoNZC catalyst the surface area, average pore diameter and pore volume all decreased. The CoNZ calcined catalyst showed an increased surface area and pore volume compared with the uncalcined CoNZ catalyst.

3.2 Supports

TGA-DSC profiles of the supports were collected as described in section 2.3.2. This was done in order to ascertain what role the support played in the catalyst characterisation results.

3.2.1 Alumina

TGA-DSC measurements were carried out and reported previously for the alumina support [92] . For all gas atmospheres it was found that, with the exception of the loss of water before 100 ^oC, there were no other significant weight losses.

A reaction was performed in the Fischer Tropsch rig as described in section 2.4, using alumina with no cobalt supported catalyst present. It was found that no reaction occurred.

3.2.2 Zinc Oxide

The Zinc Oxide was a proprietary BP support and characterisation was not within the scope of the PhD.

3.3 Cobalt nitrate

TGA-DSC analysis was carried out on the bulk cobalt nitrate salt as described in section 2.3.2 with the data shown in figures 3.1 and 3.2.

3.3.1 Thermogravimetric analysis-differential scanning calorimetry

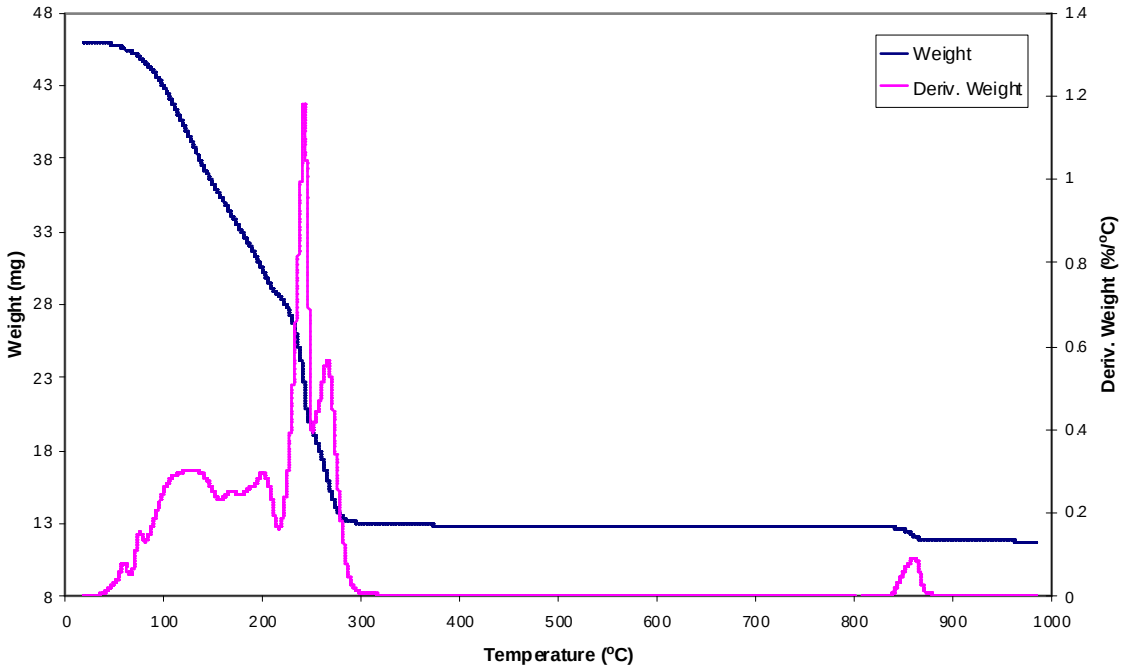

Figure 3-1: TGA weight and derivative weight profiles for cobalt nitrate hexahydrate in oxygen

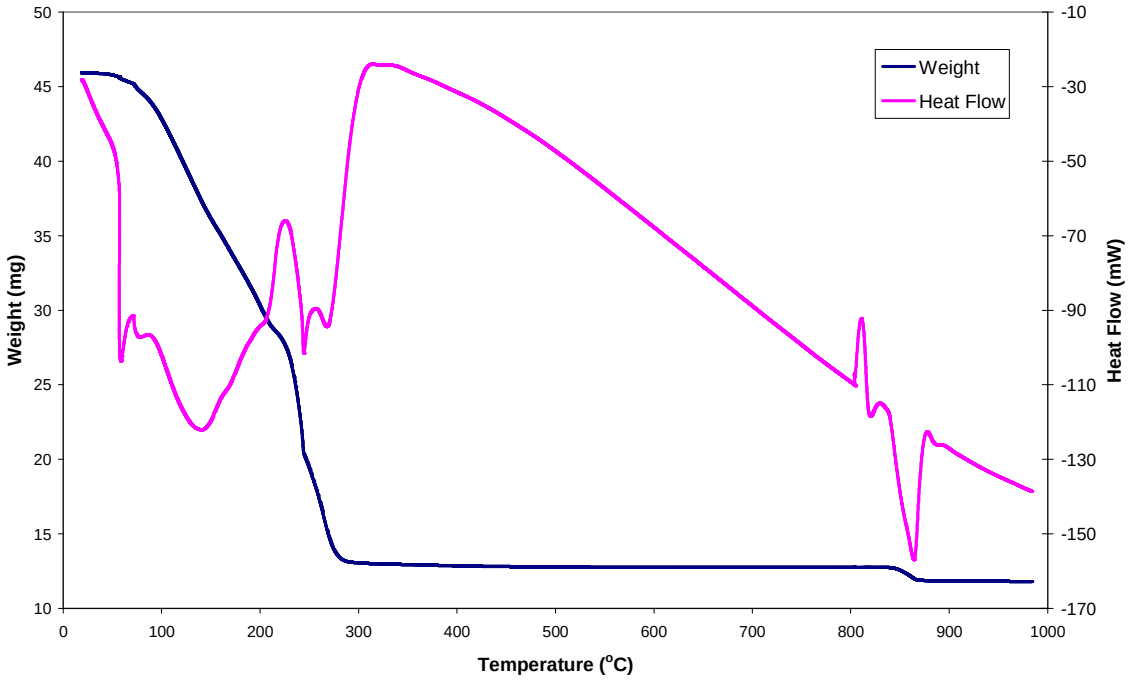

Figure 3-2: TGA-DSC weight and heat flow profiles for cobalt nitrate hexahydrate in oxygen

From the weight and derivative weight profiles, the cobalt nitrate decomposition in oxygen mainly occurs as several overlapping events before 400 ^{o}C. There is a further high temperature weight loss at 862 ^{o}C. From the heat flow data (figure 3-2) it can be seen that all the weight losses were endothermic events apart from a small exothermic peak around 850 ^{o}C.

3.3.2 Mass spectrometric analysis

The mass spectrometric data shows the decomposition in oxygen occurs via the evolution of water, oxygen, nitrogen monoxide and nitrogen dioxide. Above 500 ^{o}C, the evolution of oxygen and nitrogen monoxide is detected.

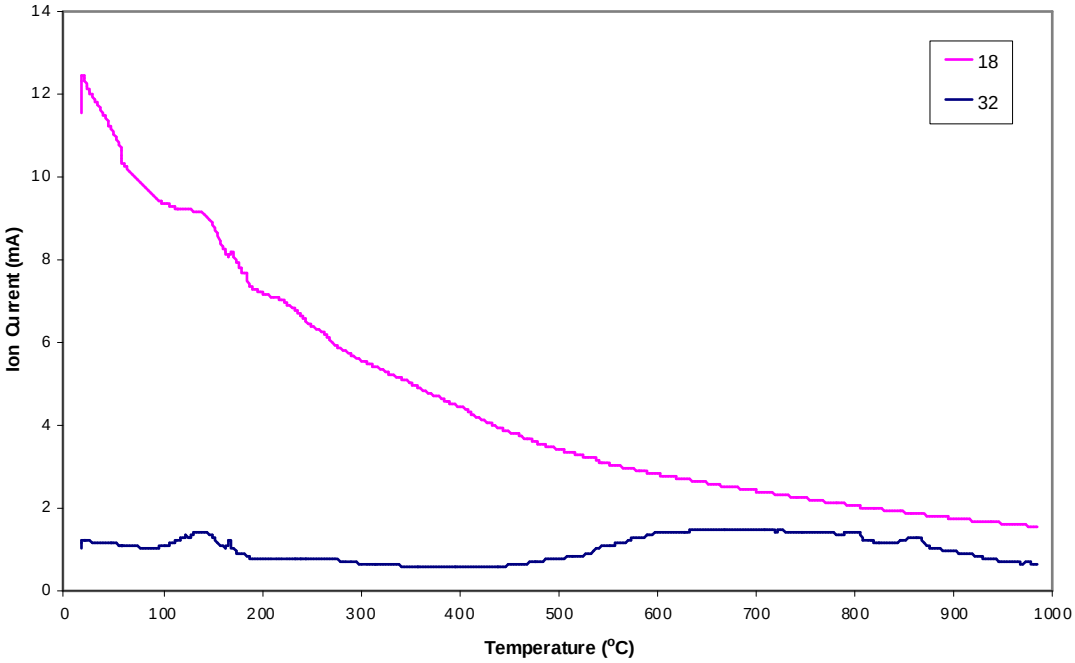

Figure 3-3: Mass spectrometric data of H_2O (m/z=18) and O_2 (m/z=32) for cobalt nitrate hexahydrate in oxygen

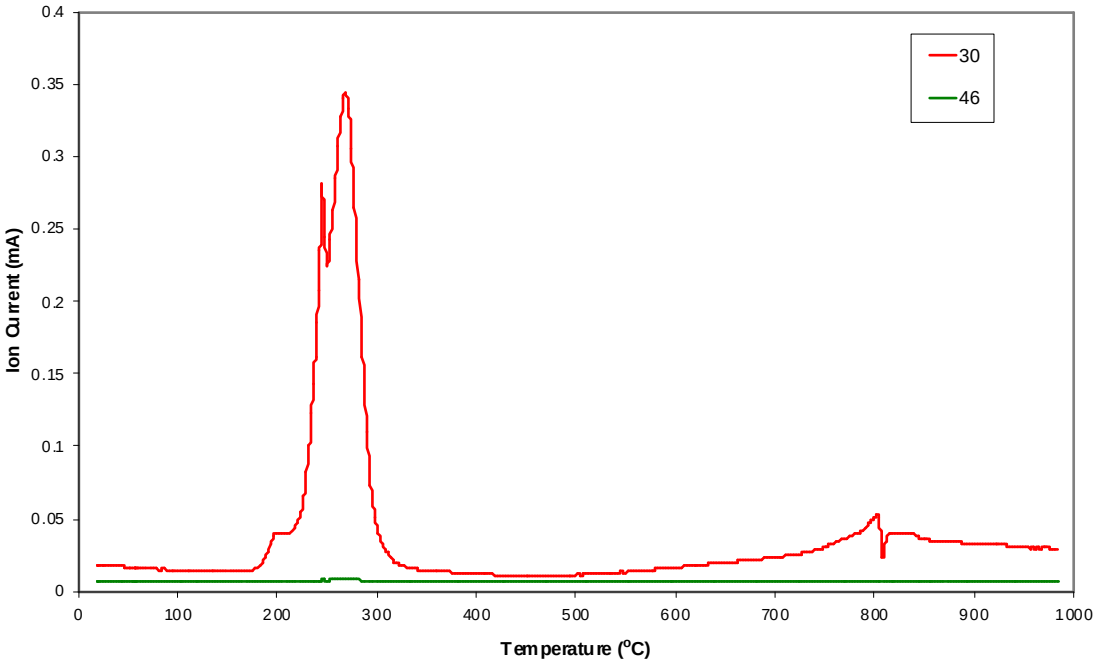

Figure 3-4: Mass spectrometric data of NO (m/z=30) and NO_2 (m/z=46) for cobalt nitrate hexahydrate in oxygen

3.4 Cobalt acetate

3.4.1 Thermogravimetric analysis-differential scanning calorimetry

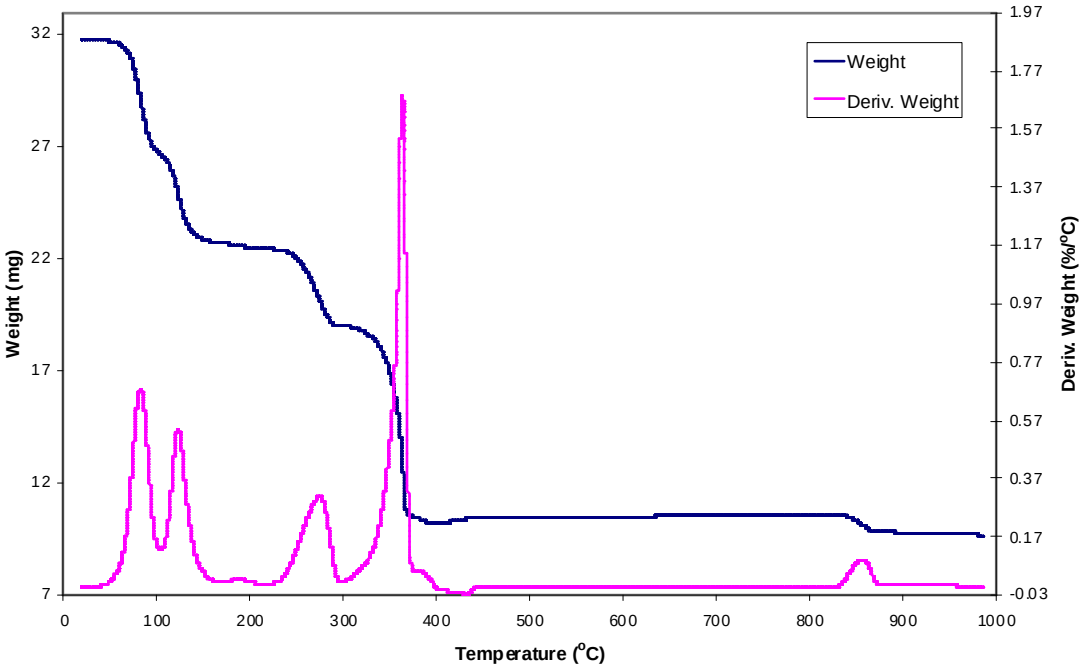

Figure 3-5: TGA weight and derivative weight profiles for cobalt acetate tetrahydrate in oxygen

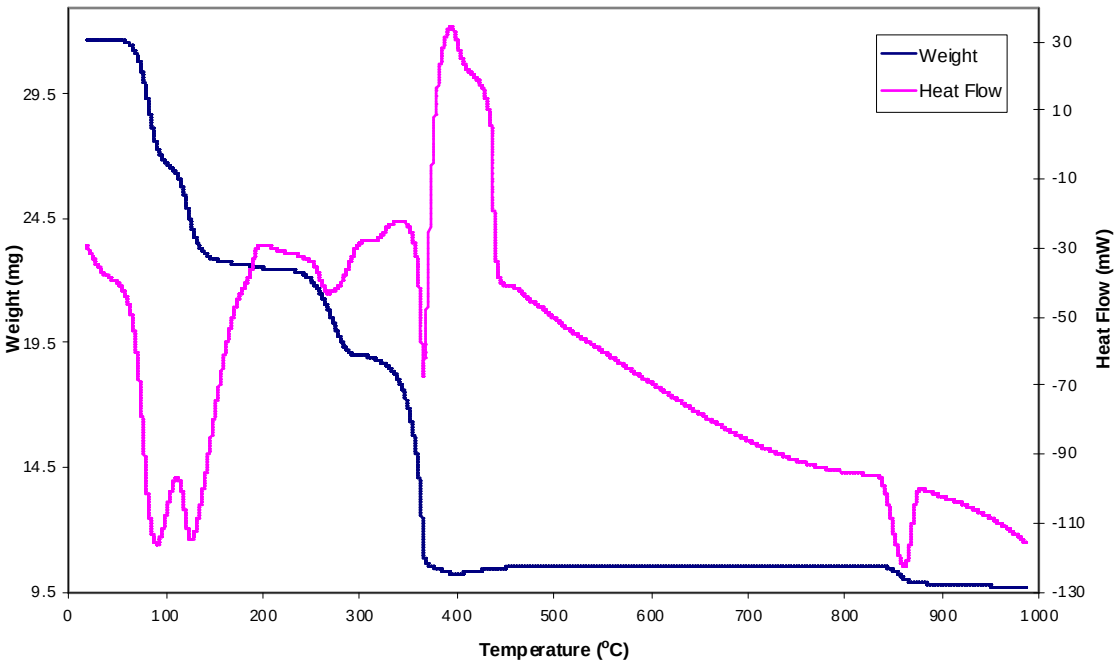

Figure 3-6: TGA-DSC weight and heat flow profiles for cobalt acetate tetrahydrate in oxygen

From the weight loss and derivative weight profiles in figure 3-5 it can be seen that there are four main weight loss events before 385 ^{o}C. Between 388-447 ^{o}C, weight loss and derivative weight profiles suggest a weight gain. There is an additional weight loss event at higher temperatures around 860 ^{o}C. The heat flow profile in figure 3-6 shows that all the weight losses correspond to an endothermic event. In contrast to this, from the heat flow profile, it can be seen that the observed weight gain is highly exothermic.

3.4.2 Mass spectrometric analysis

Mass spectrometric data confirms that the cobalt acetate tetrahydrate decomposition in oxygen occurs via the evolution of water, oxygen, hydrogen, carbon monoxide and carbon dioxide.

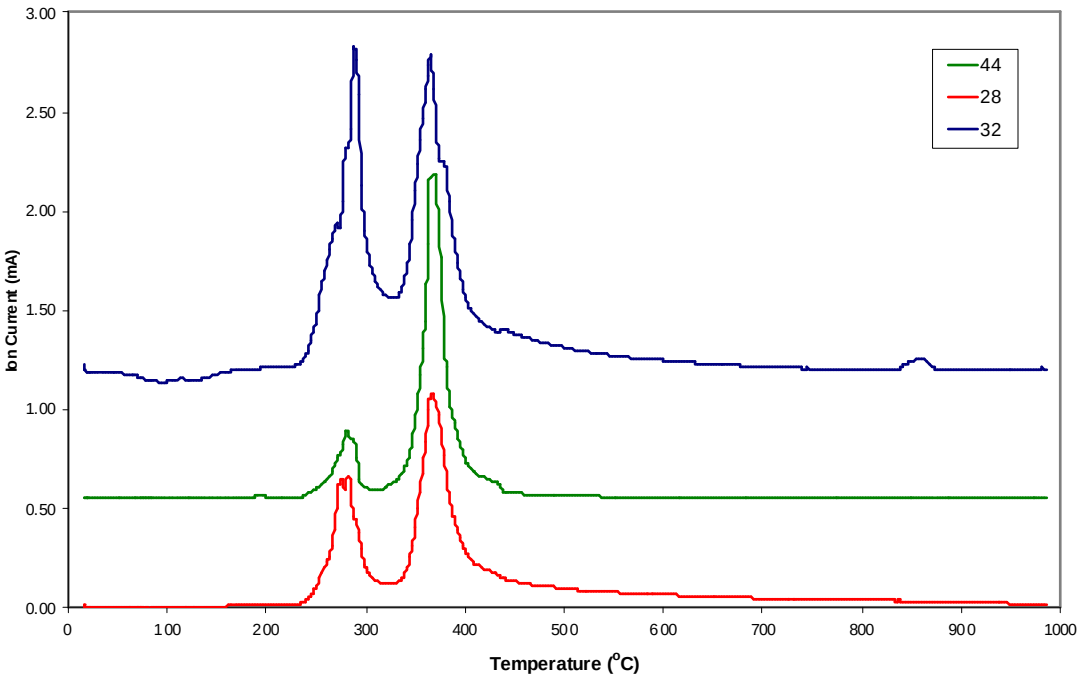

Figure 3-7: Mass spectrometric data of CO (m/z= 28), O_2 (m/z=32) and CO_2 (m/z=44) for cobalt acetate tetrahydrate in oxygen

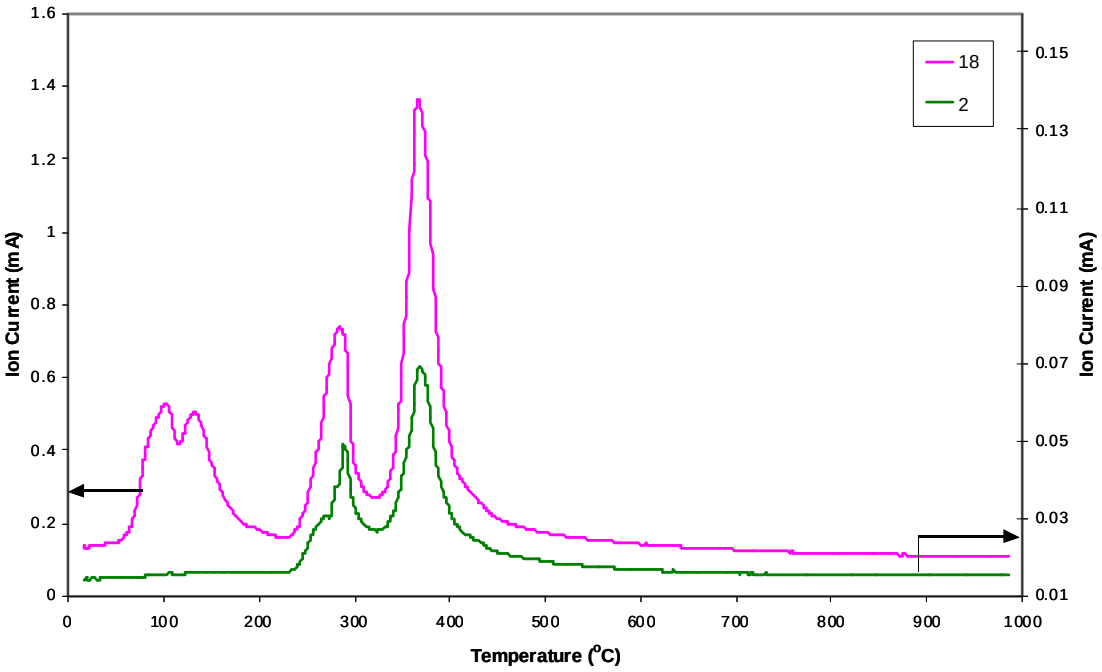

Figure 3-8: Mass spectrometric data of H_2 (m/z=2), H_2O (m/z=18) for cobalt acetate tetrahydrate in oxygen

3.5 Cobalt nitrate on Alumina

In sections 3.5.1.1 to 3.5.1.3, 3.5.2.1 to 3.5.2.2 and 3.5.2.5 the TGA-DSC, XRD and mass spectrometric data for the cobalt nitrate on alumina catalyst are taken from previous work [92]. This was done in order to aid interpretation of the other results.

3.5.1 Oxygen treatment

3.5.1.1 Thermogravimetric analysis-differential scanning calorimetry

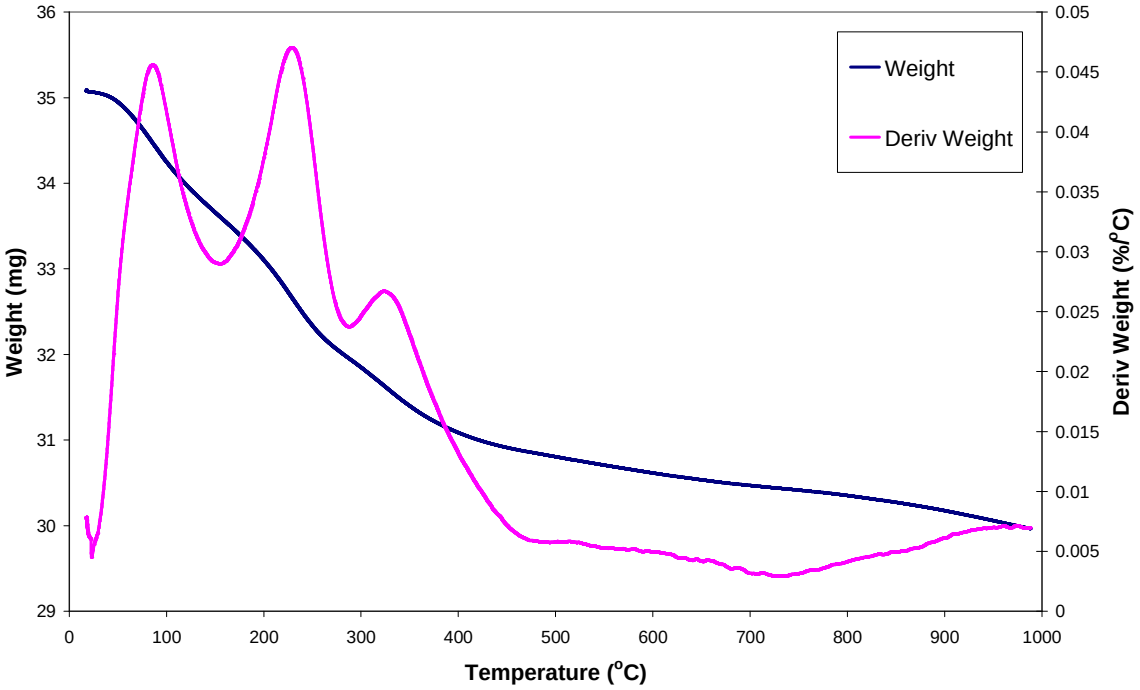

Figure 3-9: TGA weight and derivative weight profiles in oxygen for cobalt nitrate on alumina

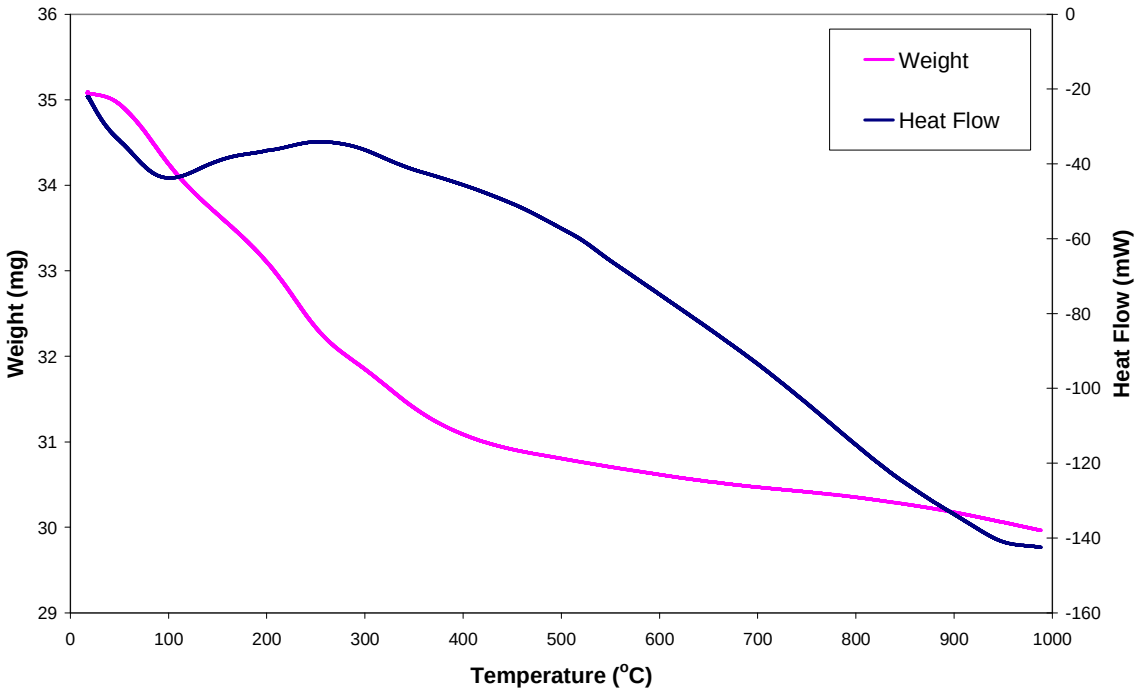

Figure 3-10: TGA-DSC weight and heat flow profiles in oxygen for cobalt nitrate on alumina

Figures 3-9 and 3-10 present the TGA-DSC data in oxygen for the cobalt nitrate on alumina catalyst. The derivative weight profile exhibits three peaks before 500 ^{o}C. These are thought to be due to desorption of water molecules in the cobalt hydrate shell and to the decomposition of the nitrate anion. From the heat flow profile in figure 3-10, an endothermic event can clearly be seen before 100 ^{o}C, indicating desorption of hydrate water molecules.

3.5.1.2 Mass spectrometric analysis

Mass spectrometric data shown in figure 3-11 shows that decomposition of the nitrate precursor in oxygen takes place as two distinct events, occurring at 245 ^{o}C and 340 ^{o}C.

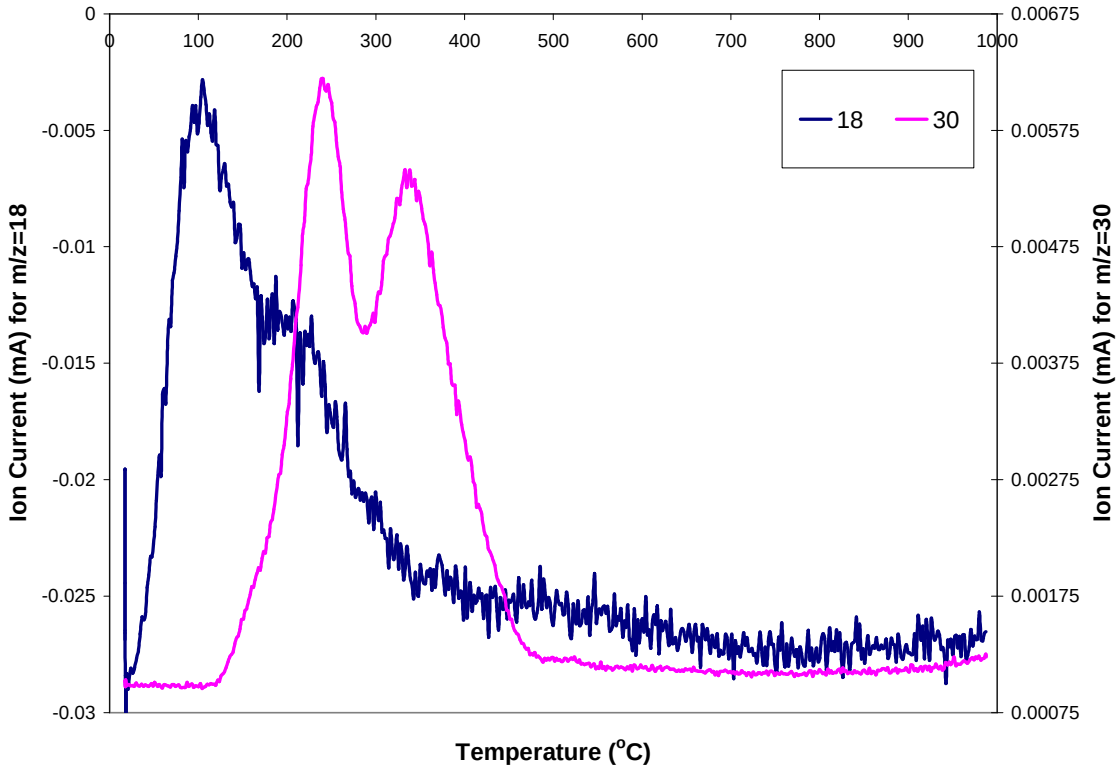

Figure 3-11: Mass spectrometric data of H_2O (m/z=18) and NO (m/z=30) in oxygen for cobalt nitrate on alumina

3.5.1.3 Hot-stage X-Ray diffraction analysis

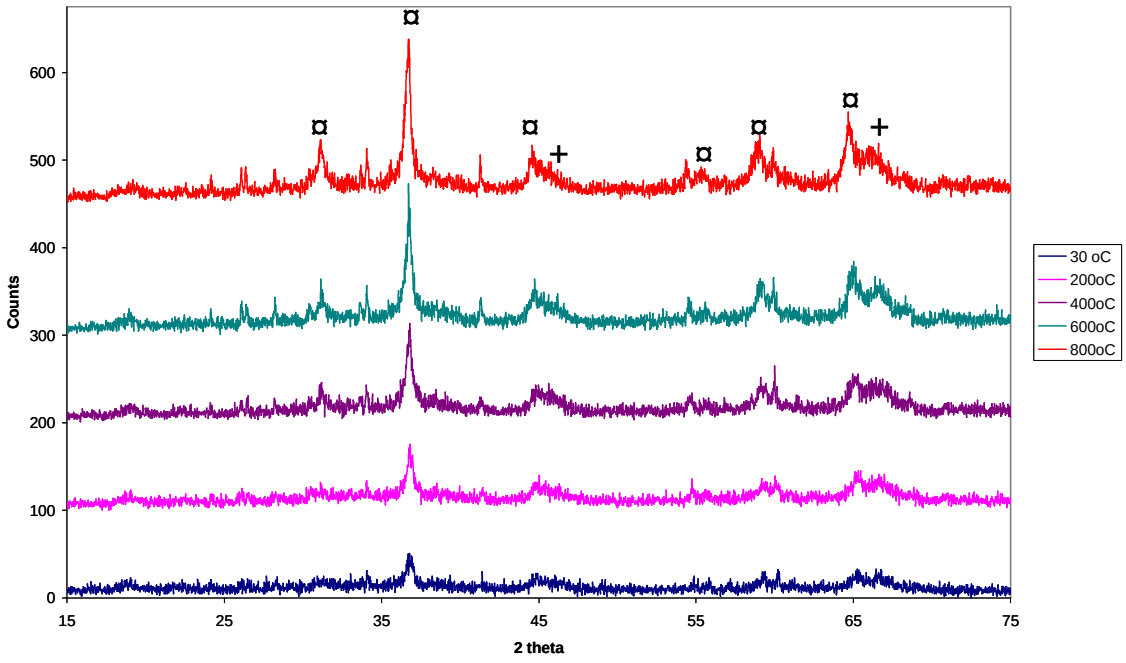

Figure 3-12: Hot-stage XRD pattern in oxygen for cobalt nitrate on alumina. The phases denoted are (¤) Co_3O_4 and (+) alumina.

Figure 3-12 shows the hot-stage XRD pattern for the cobalt nitrate on alumina. The locations of the peaks confirm that Co_3O_4 was the only crystalline phase of cobalt present. Except for Co_3O_4, only peaks indicating alumina were detected. The full width at half maximum of the most intense Co_3O_4 peak, in this case at $2\theta = 36.9^o$ was used to calculate the Co_3O_4 particle sizes. The average particle size calculated for all the temperatures from the Scherrer equation is given in table 3-2. There is little variation in the Co_3O_4 particle sizes, with the exception of the value at 600 ^{o}C which appears slightly larger.

Table 3-2: Average Co_3O_4 crystallite size as determined by hot-stage XRD, in oxygen, of cobalt nitrate on alumina. The experimental error for Co_3O_4 sizes calculated from X-ray diffraction is less than +/- 1 nm.

Temperature (^{o}C)	Co_3O_4 crystallite size (nm)
30	16
100	-
200	20
300	16
400	20
500	18
600	26
700	20
800	20

3.5.1.4 Effect of heating rate

Figure 3-13 shows the TGA data in oxygen for CoNA catalyst at a ramp rate of 1 ^{o}C min^{-1}. From the derivative weight profile it can be seen that decreasing the ramp rate to 1 ^{o}C min^{-1} results in a decrease in the temperature of the decomposition peak maxima.

From the characterisation data it was determined that a suitable calcination procedure for the cobalt nitrate on alumina catalyst was as follows:

- Ramp 1 ^{o}C min^{-1} to 350 ^{o}C and hold for 120 minutes in 2% Oxygen-Argon at 40 ml min^{-1}.

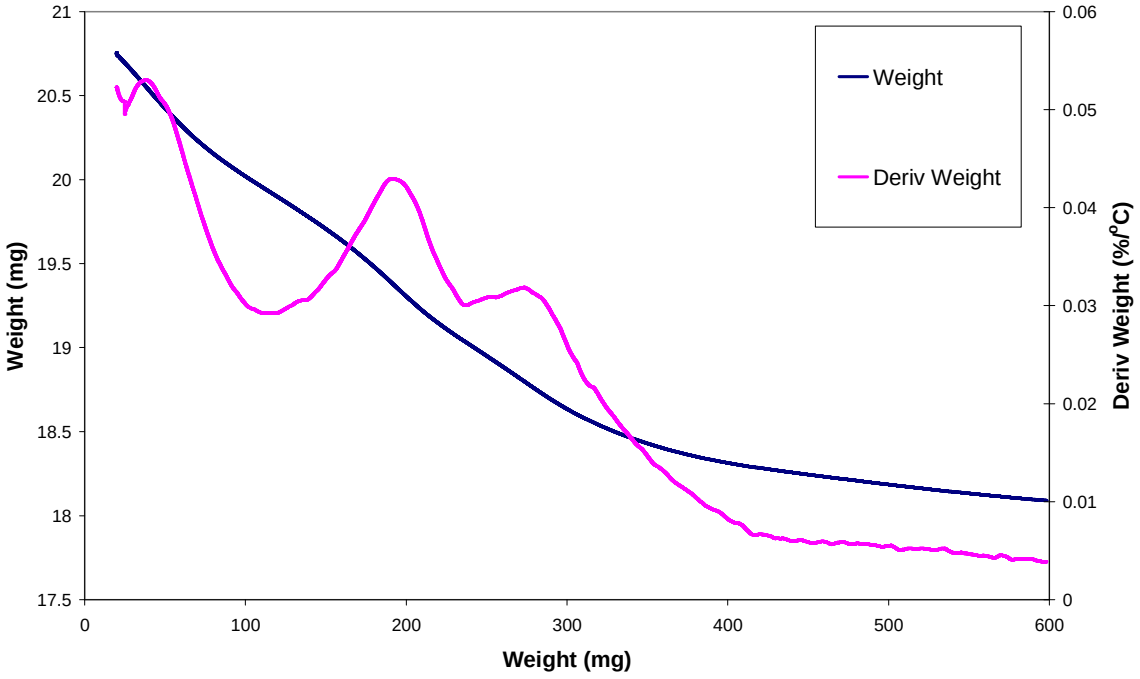

Figure 3-13: TGA weight and derivative weight profiles in oxygen for cobalt nitrate on alumina at a heating rate of 1 ^{o}C min^{-1}

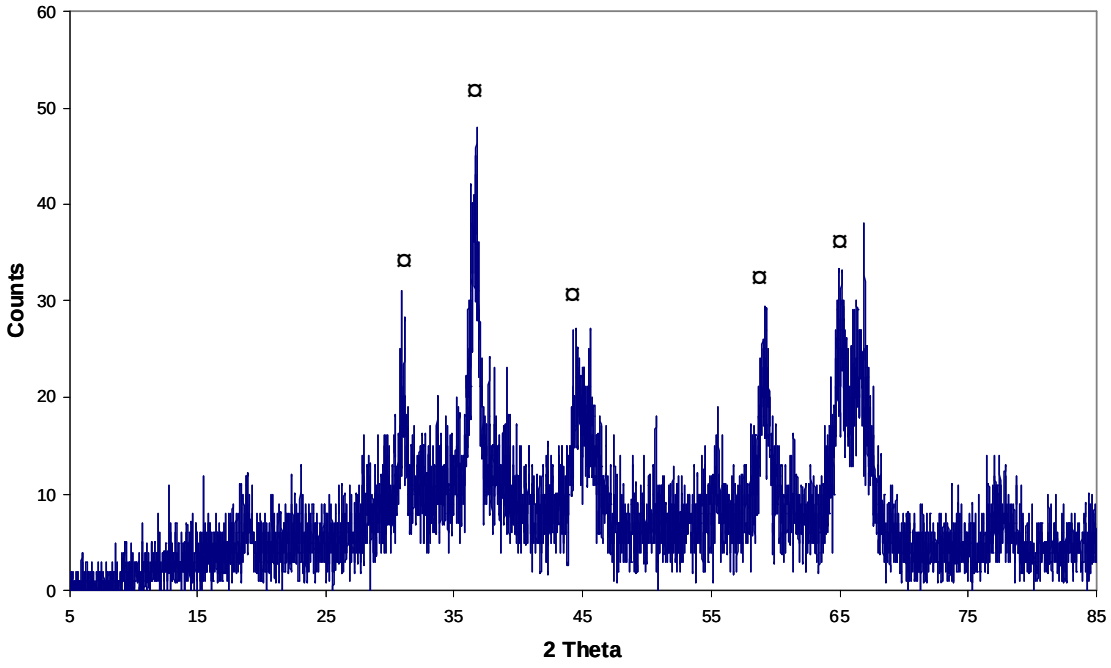

Figure 3-14: X-ray diffraction pattern for calcined cobalt nitrate on alumina catalyst. Phases denoted are (¤) Co_3O_4. The experimental error for Co_3O_4 size calculated from X-ray diffraction is less than +/- 1 nm.

The XRD pattern of the CoNA catalyst, calcined as outlined previously, is shown in figure 3-14. There are reflections present at 2θ = 30.9^o, 36.4^o, 45^o, 59^o and 65.4^o indicating the presence of the Co_3O_4 spinel phase. The mean cobalt oxide crystallite size was calculated from line broadening and found to be 15 nm.

3.5.1.5 Transmission electron microscopy

TEM analysis was carried out as described in section 2.3.4 on the cobalt nitrate on alumina catalyst, calcined as outlined in section 3.5.1.4. Figure 3-15a shows a low magnification image of the calcined CoNA catalyst. Several dark clusters of around 150-200 nm can clearly be observed. The higher magnification image in figure 3-15b shows that each of these clusters appear to consist of many smaller particles. At higher resolution, lattice fringe spacing can be observed corresponding to Co_3O_4 (figure 3-15c). In the dark area in figure 3-15d lattice spacing around 2.4 nm can be seen, corresponding to the alumina support. This suggests that for this sample the brightness or darkness of an item in the TEM is due to its orientation and thickness rather than being indicative of the presence of cobalt oxide crystallites.

Figure 3-15: TEM micrographs of the calcined cobalt nitrate on alumina catalyst

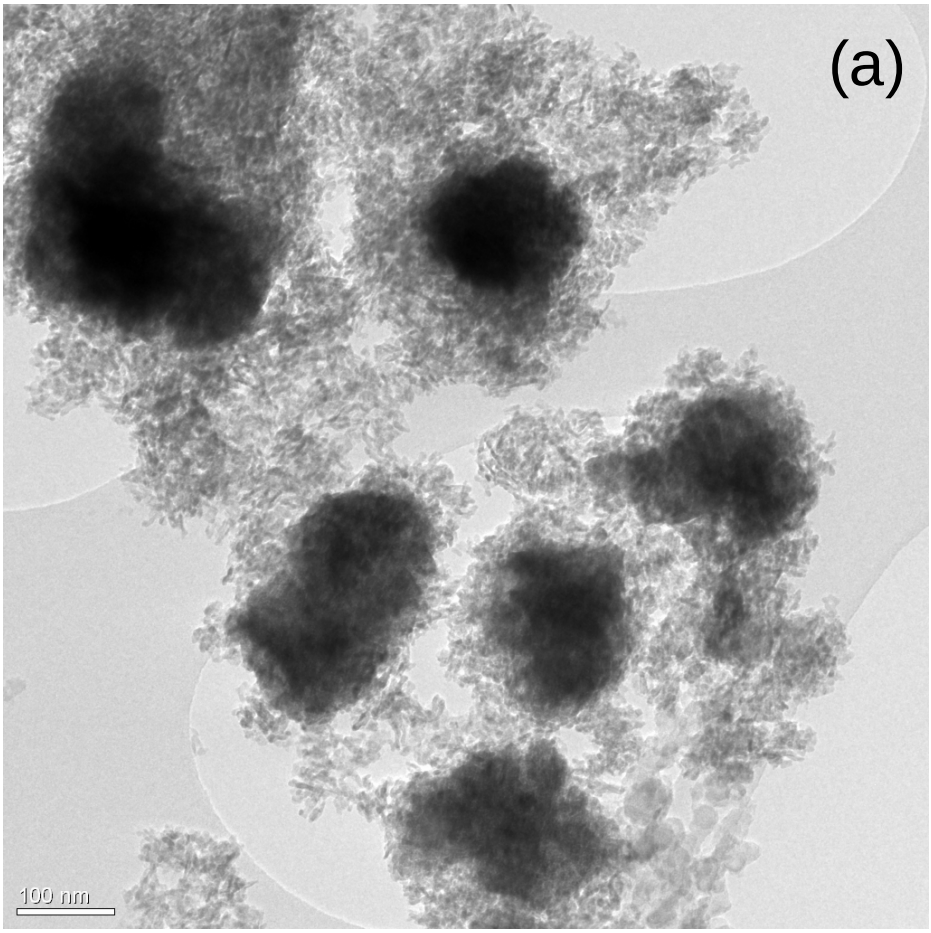

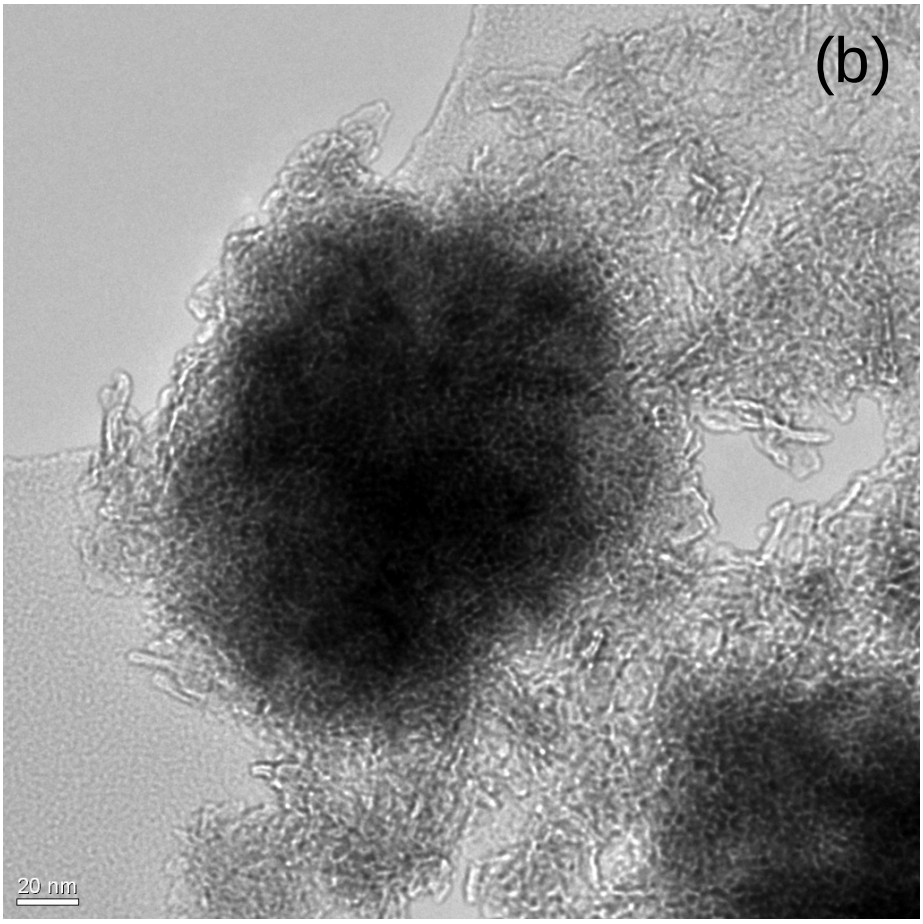
(b)
20 nm

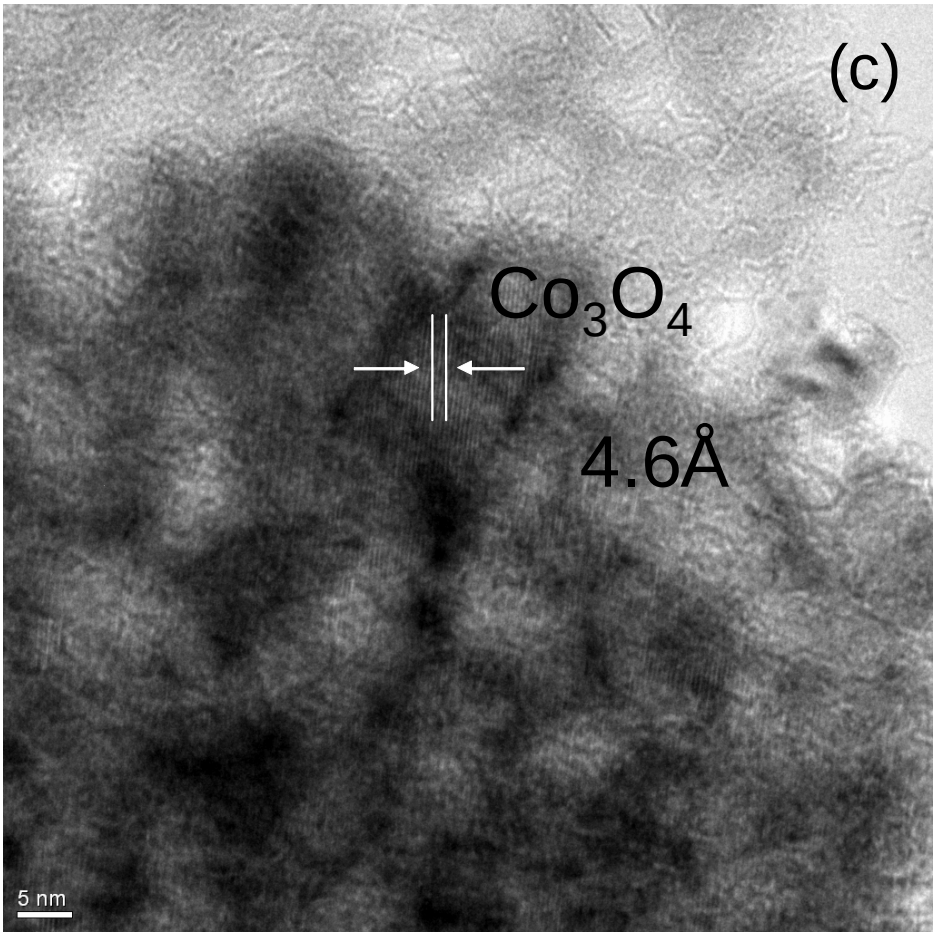
(c)
Co_3O_4
4.6Å
5 nm

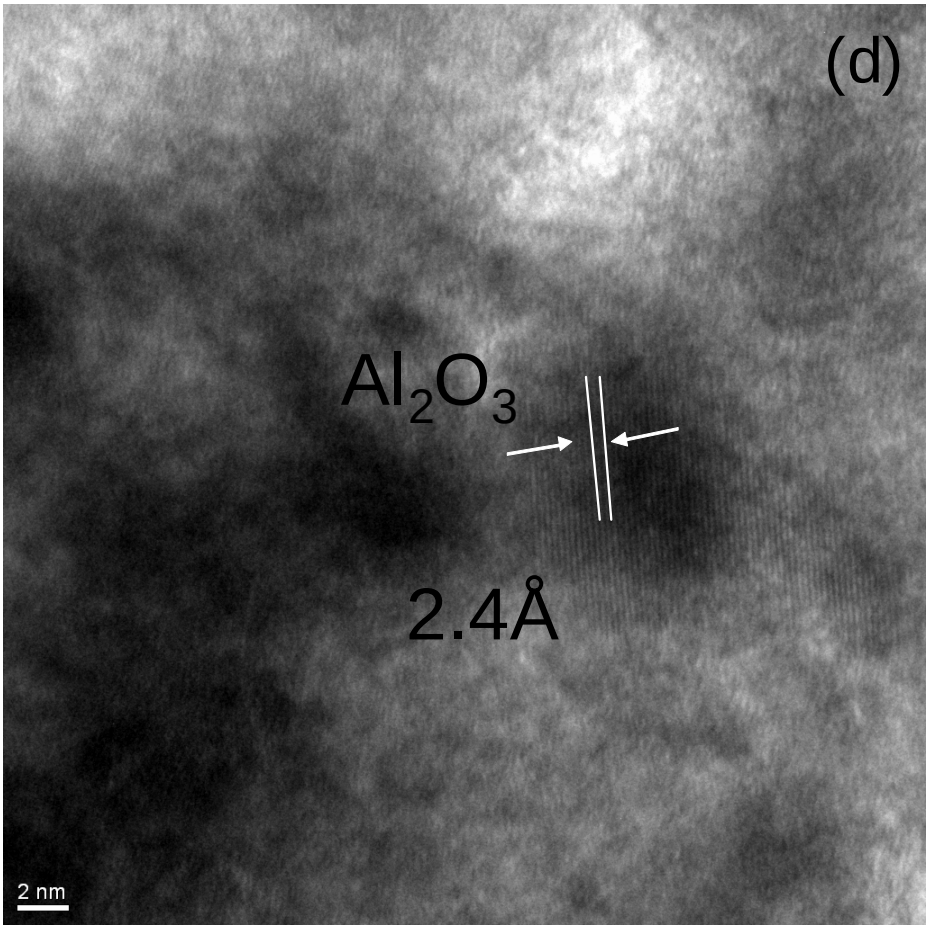
(d)
Al_2O_3
2.4Å
2 nm

3.5.2 Hydrogen treatment (after calcination in oxygen)

3.5.2.1 Thermogravimetric analysis-differential scanning calorimetry

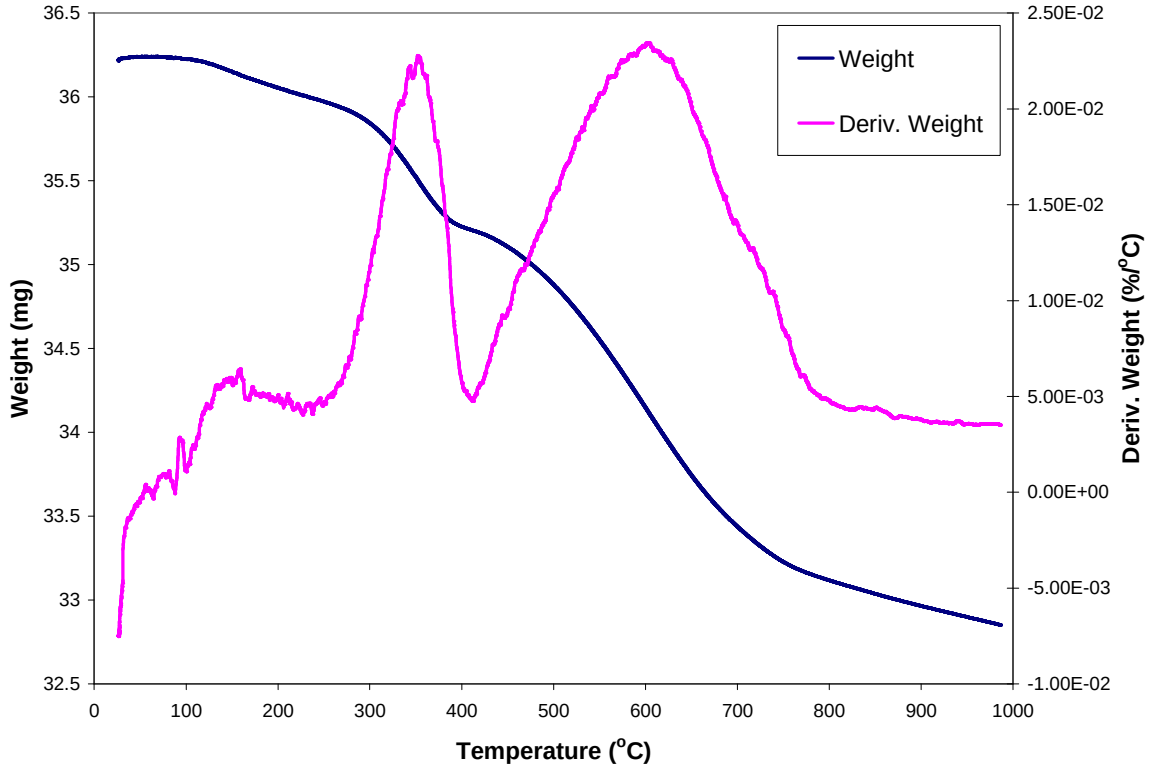

Figure 3-16: TGA weight and derivative weight profiles in hydrogen (after calcination in oxygen) for cobalt nitrate on alumina

Figures 3-16 and 3-17 present the TGA-DSC curves in hydrogen for the calcined cobalt nitrate on alumina catalyst. The derivative weight profile exhibits a small peak before 200 ^{o}C which can be assigned to desorption of water molecules. Two main peaks are apparent with maximums at 355 ^{o}C and 605 ^{o}C. These correspond to weight losses of 0.81 mg and 2.32 mg and are probably due to the reduction of the supported cobalt oxide species.

Apart from the initial endothermic desorption of water, the heat flow curves for the CoNA catalyst in hydrogen are relatively featureless. However, there is a broad exotherm spread over 200 ^{o}C, ending around 400 ^{o}C, with a possible subsequent exotherm above this temperature.

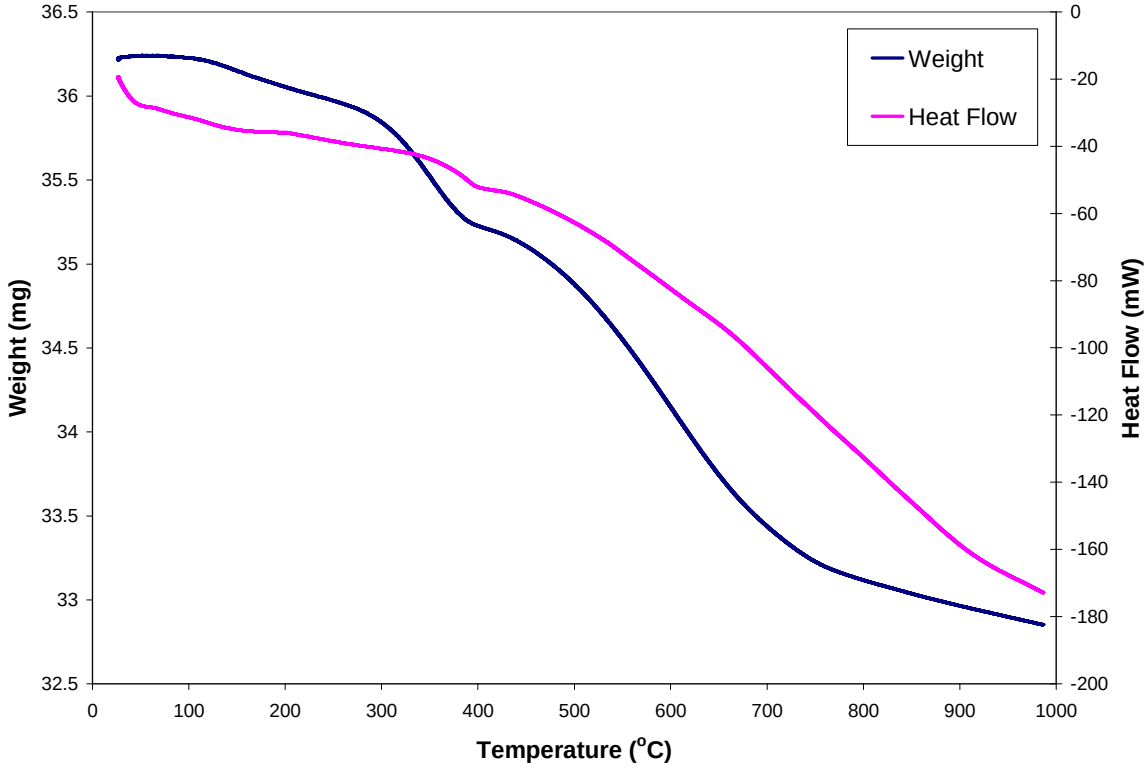

Figure 3-17: TGA-DSC weight and heat flow profiles in hydrogen (after calcination in oxygen) for cobalt nitrate on alumina.

3.5.2.2 Mass spectrometric analysis

Figure 3-18 shows the uptake of hydrogen gas and corresponding production of water for the CoNA catalyst. The uptake of hydrogen is clearly seen to occur as two distinct events.

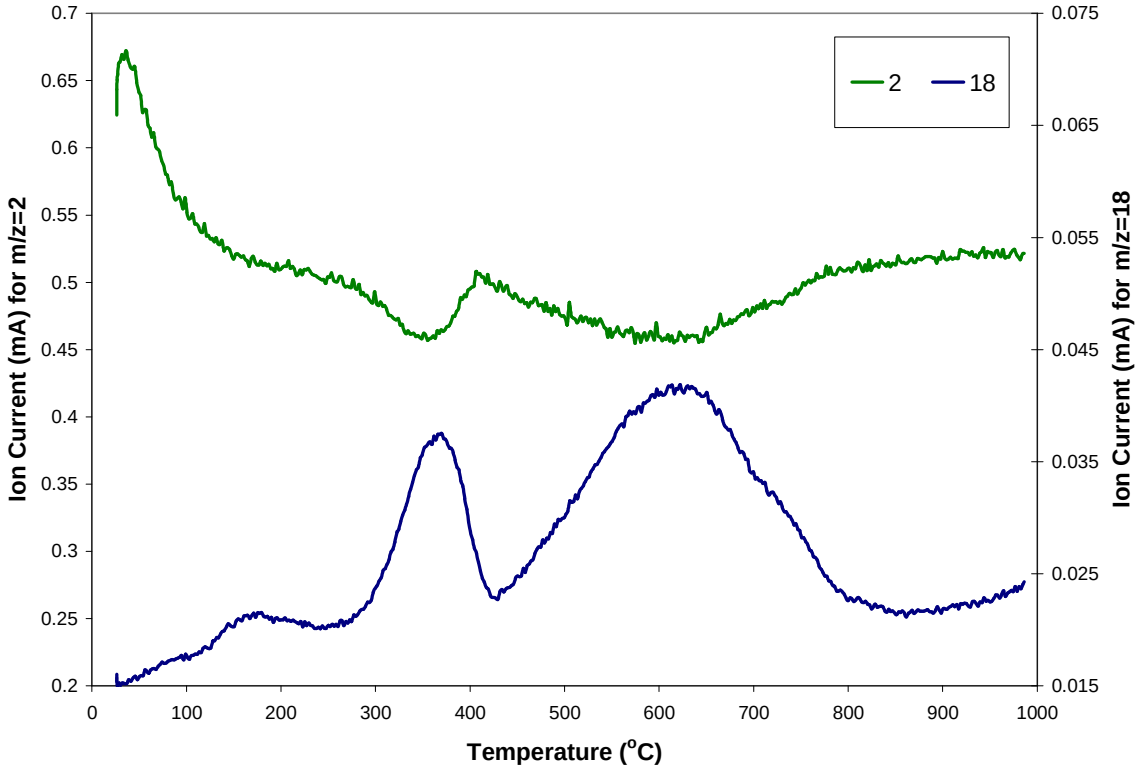

Figure 3-18: Mass spectrometric data of H_2 (m/z=2) and H_2O (m/z=18) in hydrogen (after calcination in oxygen) for cobalt nitrate on alumina.

3.5.2.3 Effect of heating rate

Figures 3-19 and 3-20 show a series of TGA weight and derivative weight profiles of calcined CoNA catalyst in hydrogen, obtained at various temperature ramp rates of 1, 3, 5 and 7 $^{o}C\ min^{-1}$. By decreasing the heating rate from 7 to 1^{o}C, the location of the derivative weight peak maxima for the 1st and 2nd reduction peaks decreased by around 55 and 115^{o}C respectively. However, it can be seen from figure 3-19 that this did not affect the total weight loss which was consistently 9% for each of the heating rates.

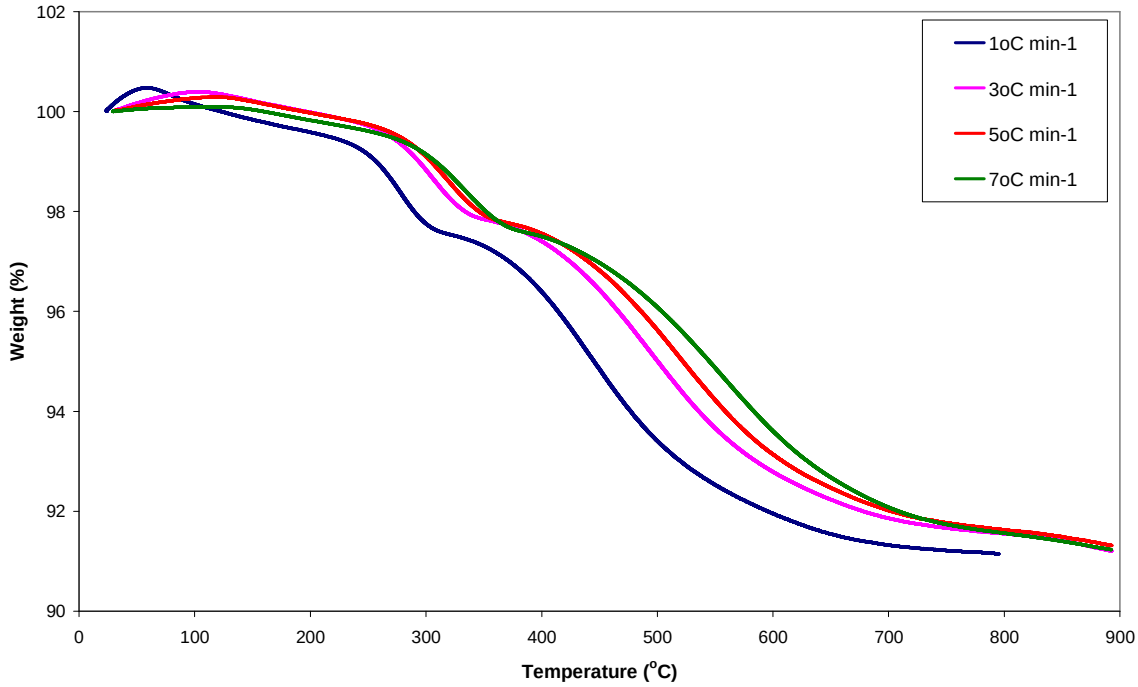

Figure 3-19: TGA weight profiles in hydrogen for calcined cobalt nitrate on alumina at different heating rates.

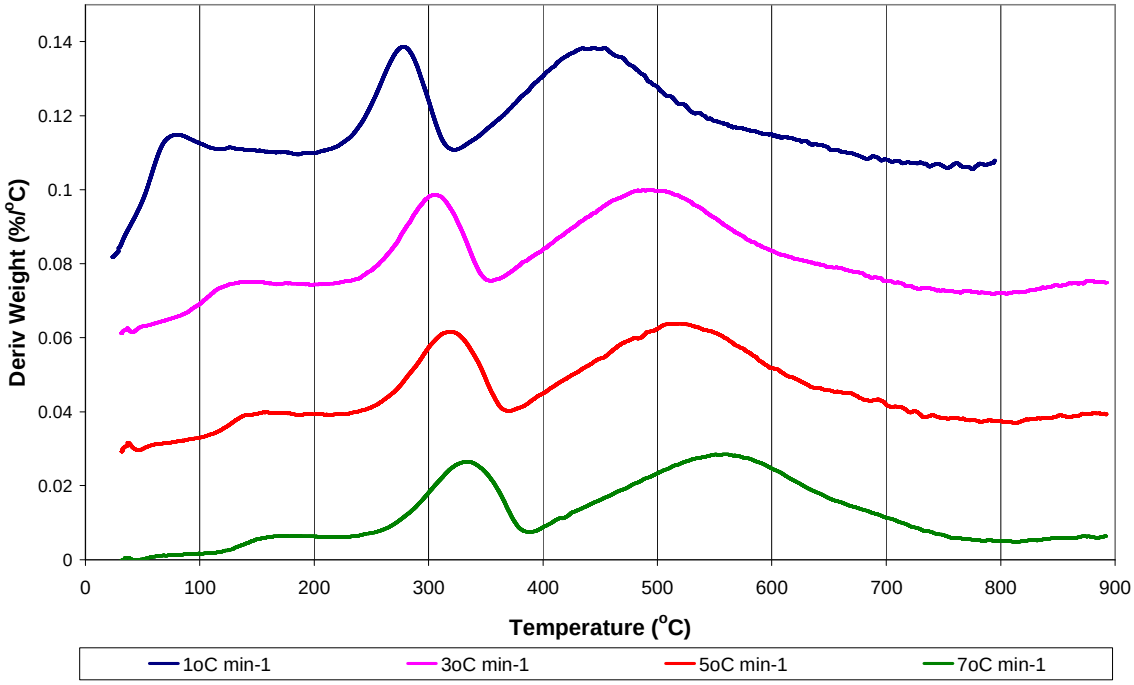

Figure 3-20: TGA derivative weight profiles in hydrogen for calcined cobalt nitrate on alumina at different heating rates.

3.5.2.4 Extent of reduction

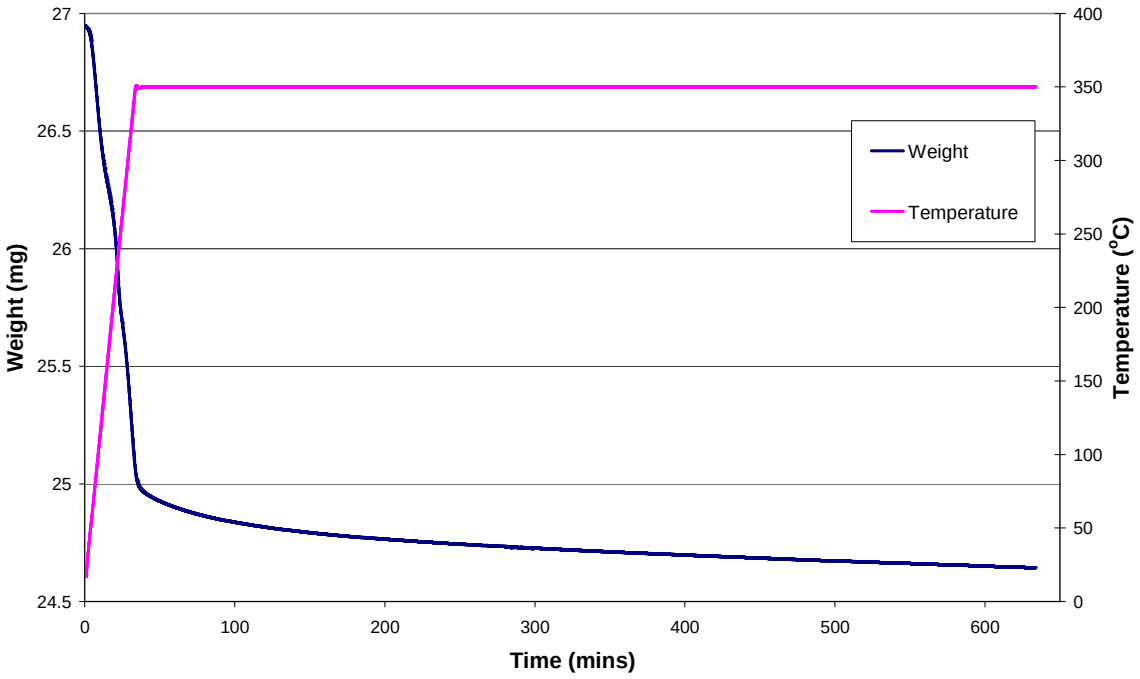

Figure 3-21: TGA weight profile as a function of time in hydrogen for calcined CoNA catalyst.

In order to determine the extent of reduction of the CoNA catalyst, the calcined catalyst was followed by TGA in hydrogen, as described in section 2.3.2, with the resulting weight loss versus time curve shown in figure 3-21. Following desorption of water, the weight loss observed due to the reduction of the Co_3O_4 to metallic cobalt was 1.57336 mg. This corresponds to a weight loss of 25.1% of the cobalt oxide present which, when compared with a calculated value of 26.6% predicted for the decomposition of Co_3O_4 to cobalt metal gives a percentage extent of reduction of 94%.

3.5.2.5 Hot-stage X-Ray diffraction

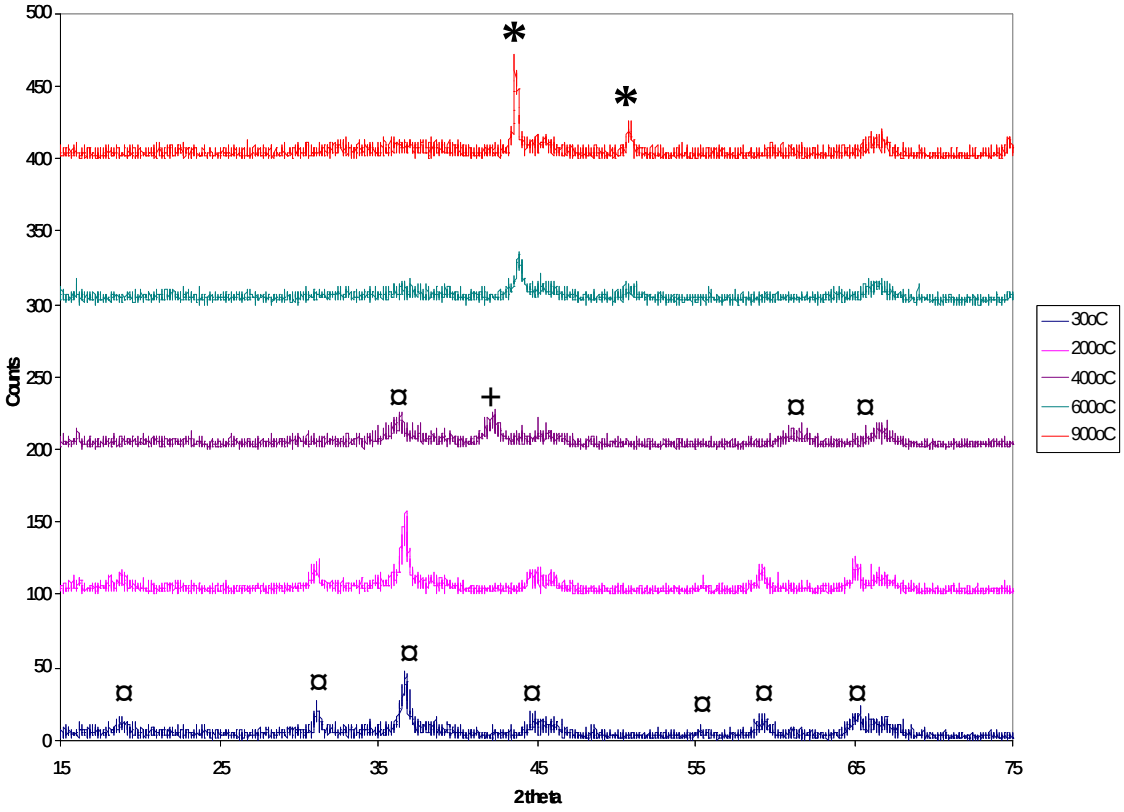

Figure 3-22: Hot-stage XRD patterns in hydrogen (after calcination in oxygen) for cobalt nitrate on alumina. The phases denoted are (¤) Co_3O_4, (+) CoO and (*) metallic Co. The XRD pattern is offset for clarity.

The *in-situ* hot-stage XRD patterns in figure 3-22 show the reduction of Co_3O_4 and the appearance of Co metal. During the reduction, Co_3O_4 is present to around 400 ^oC. Signals confirm the presence of CoO species between 300 ^oC and 400 ^oC, with metallic cobalt appearing at 500 ^oC. It should be noted that the hot-stage XRD results are consistent with the peaks in the mass spectrometric data attributed to the reduction of Co_3O_4 to CoO, which then reduces at higher temperatures to metallic cobalt. The cobalt crystallite size after reduction was calculated at each temperature and is shown in table 3-3. The smallest cobalt crystallite size was 20 nm occurring at 600 ^oC.

Table 3-3: Average cobalt metal crystallite size as determined by hot-stage XRD in hydrogen (after calcination in oxygen) for cobalt nitrate on alumina catalyst. The experimental error for cobalt sizes calculated from X-ray diffraction is less than +/- 1 nm.

Temperature (^{o}C)	Co metal crystallie size (nm)
500	27
600	20
700	32
800	23
900	32

3.5.2.6 CO chemisorption

CO chemisorption was performed on the calcined cobalt nitrate on alumina catalyst as described in section 2.3.5. The number of moles of CO adsorbed was found to be 49.9 µmol/g_{cat}. Dispersion was calculated using equation 2.4 and assuming a ratio between CO and cobalt of 1:1 was found to be 2.9%, giving an average crystallite size of 33 nm.

3.5.3 Fischer Tropsch reaction

3.5.3.1 Conversion

The results for the CO conversion for cobalt nitrate on alumina catalyst are presented in figure 3-23. In the initial stages of the reaction, there was a rapid increase in conversion from 15 % at 24 hours to 21% at 48 hours time on stream (TOS). The conversion then decreased and reached steady state after around 312 hours TOS at a CO conversion level of 5-6%.

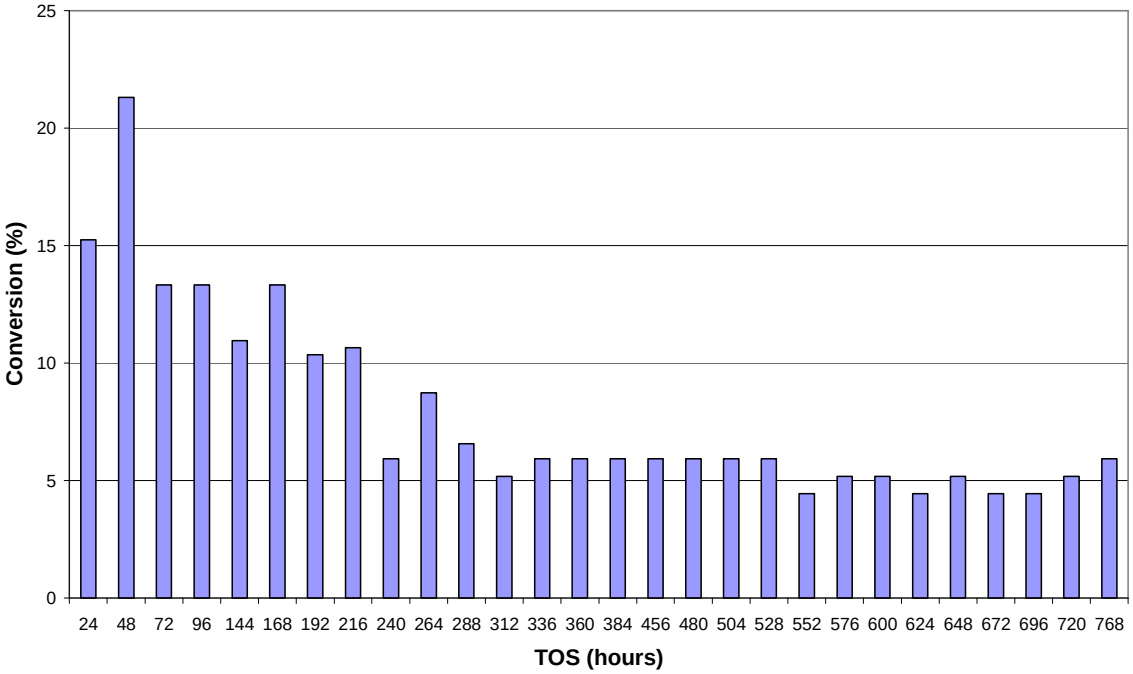

Figure 3-23: Conversion as a function of time-on-stream for CoNA catalyst at a temperature of 220 ^{o}C. The experimental error for the conversion is estimated to be +/- 5%.

3.5.3.2 Deactivation

The rate of deactivation was used to calculate a deactivation constant as described in section 2.5.2. The deactivation constant was calculated from the conversion over the range of 48-312 hours TOS and was found to be 0.0051 hr^{-1}. Figure 3-24 shows the graphs of ln[Xa/(1-Xa)] versus time on stream with the gradient of the slope equal to $-k_d$.

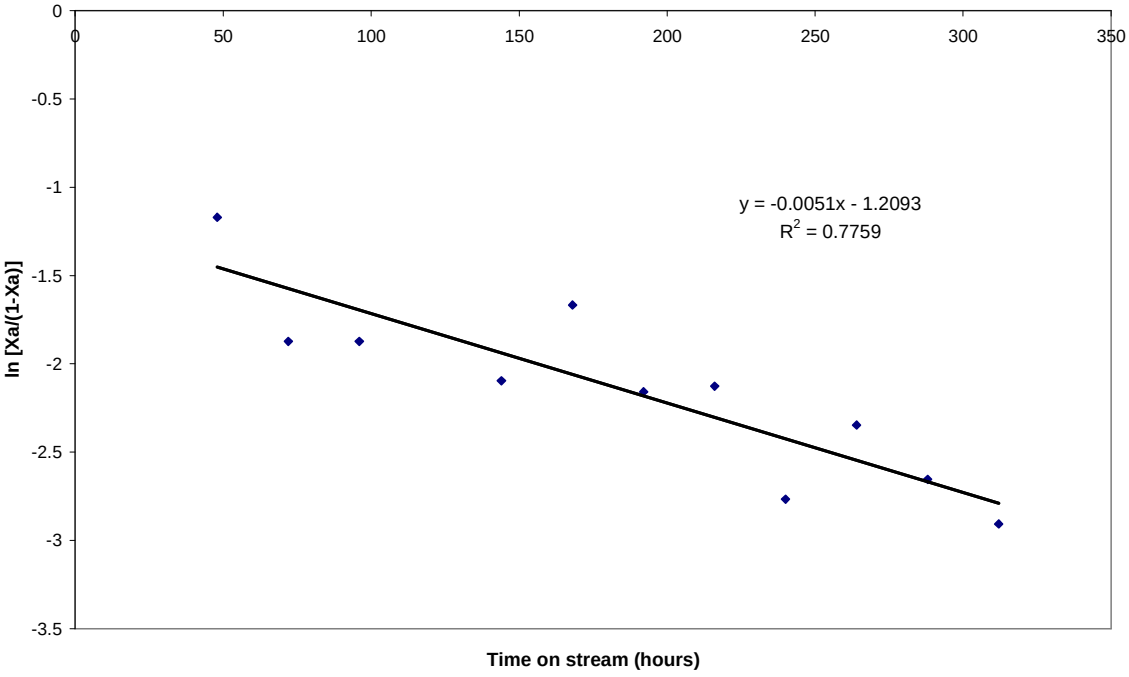

Figure 3-24: Graph of ln[Xa/(1-Xa)] versus time on stream for CoNA FT reaction at 220 ^{o}C.

3.5.3.3 Alpha Values

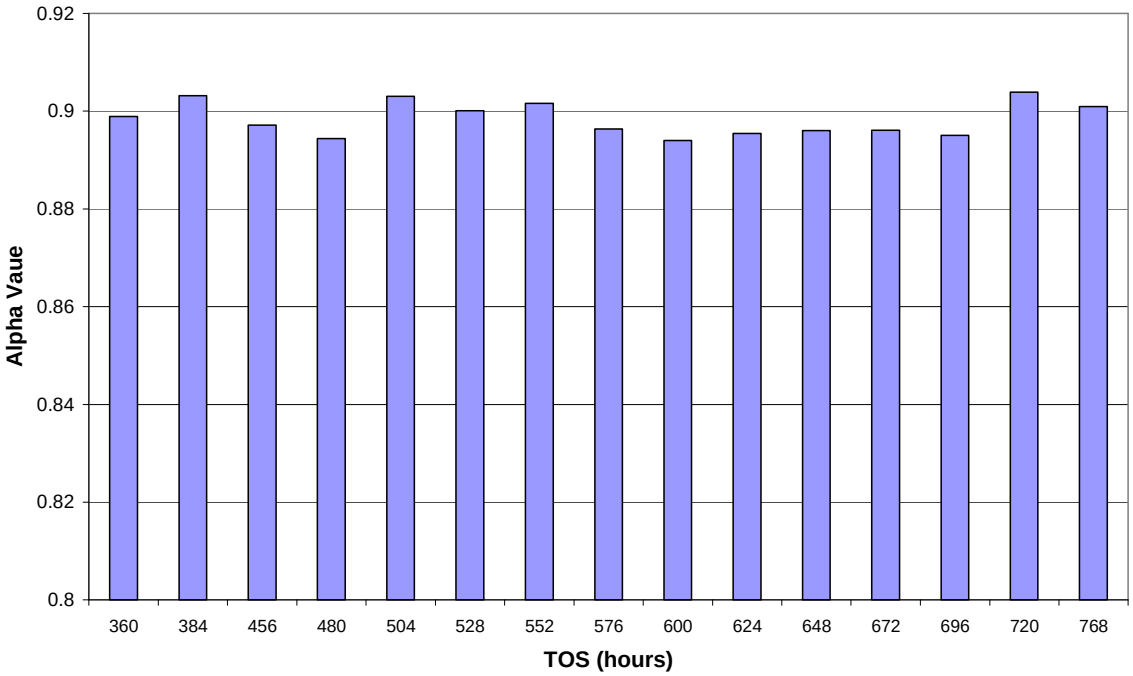

Figure 3-25: Alpha values versus time on stream for CoNA catalyst at reaction temperature of 220 ^{o}C

Alpha values at steady state as a function of time on stream for the CoNA catalyst are shown in figure 3-25. The alpha values remain constant with time on stream at around 0.89-0.9, with an average of 0.9 between 360-768 hours.

3.5.3.4 Liquid hydrocarbons and wax product distribution

The hydrocarbon product distributions for the wax and liquid hydrocarbons samples at 48, 168, 360 and 686 hours TOS are shown in figures 3-26 to 3-33. It can be observed that the distribution of the products in both the liquid hydrocarbons and the waxes moves towards heavier hydrocarbons with time on stream.

3.5.3.4.1 48 hours TOS

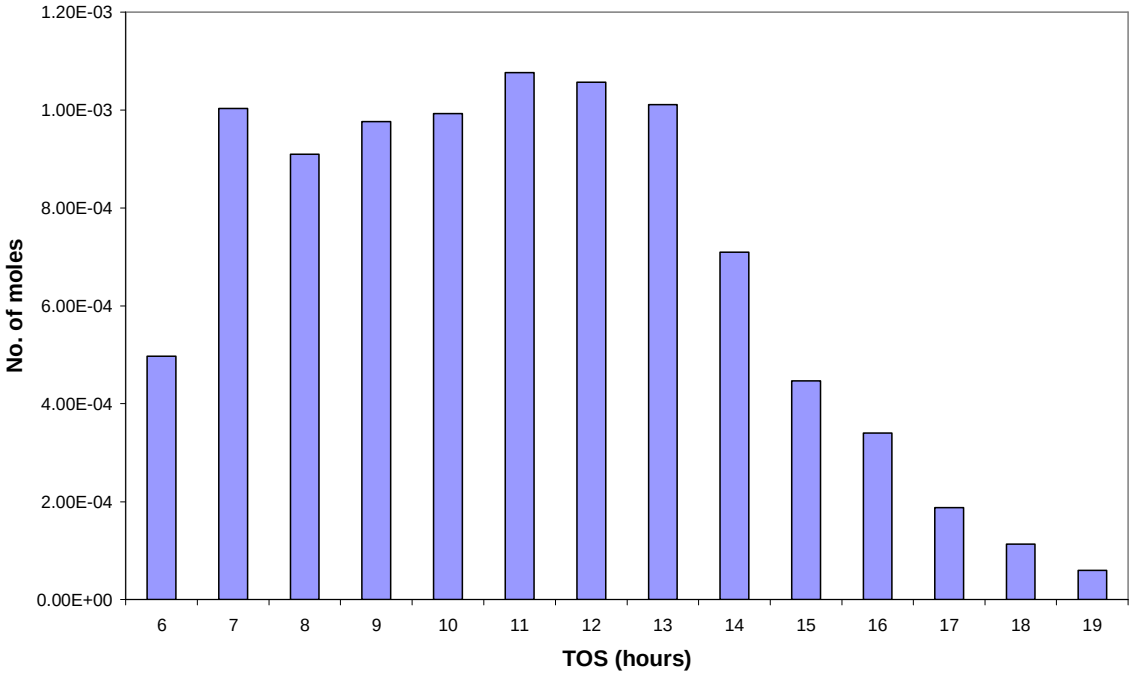

Figure 3-26: Hydrocarbon product distribution as a function of carbon number for CoNA liquid hydrocarbon sample at 48 hours TOS

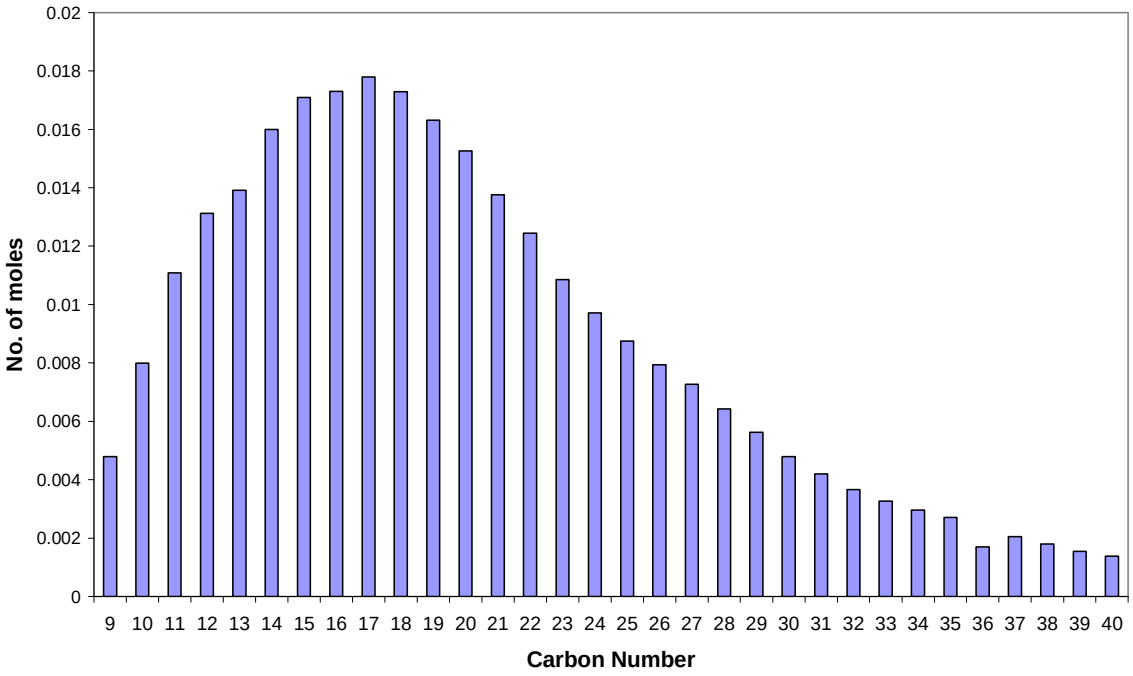

Figure 3-27: Hydrocarbon product distribution as a function of carbon number for CoNA wax sample at 48 hours TOS.

3.5.3.4.2 168 hours TOS

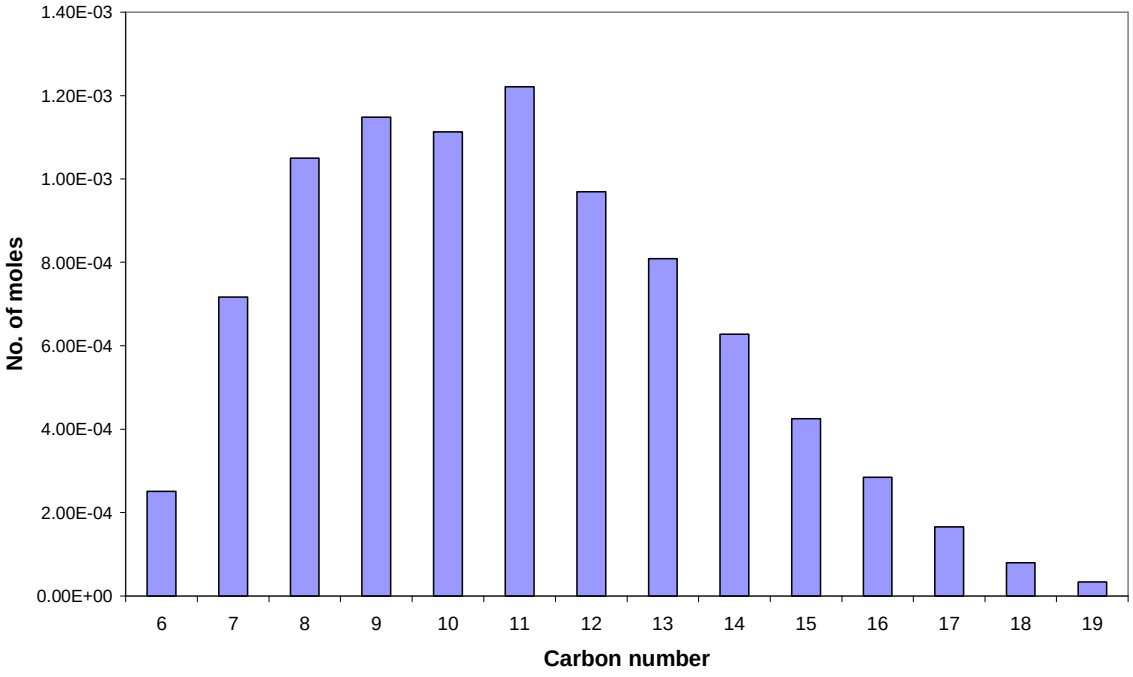

Figure 3-28: Hydrocarbon product distribution as a function of carbon number for CoNA liquid hydrocarbon sample at 168 hours TOS.

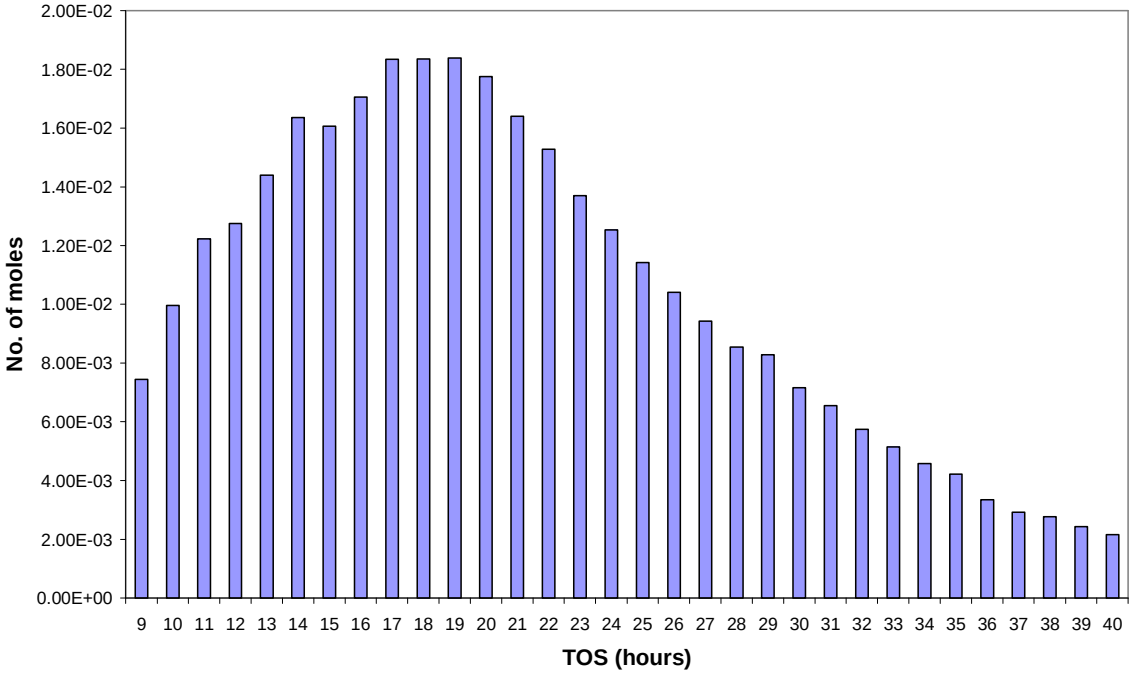

Figure 3-29: Hydrocarbon product distribution as a function of carbon number for CoNA wax sample at 168 hours TOS.

3.5.3.4.3 360 hours TOS

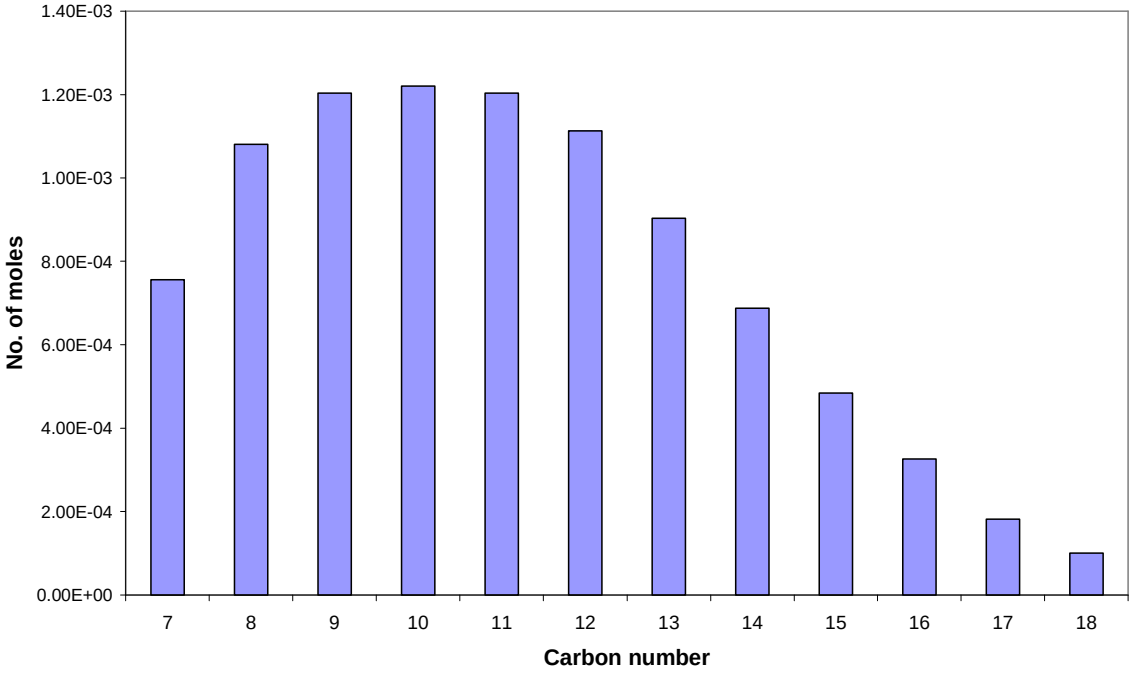

Figure 3-30: Hydrocarbon product distribution as a function of carbon number for CoNA liquid hydrocarbon sample at 360 hours TOS

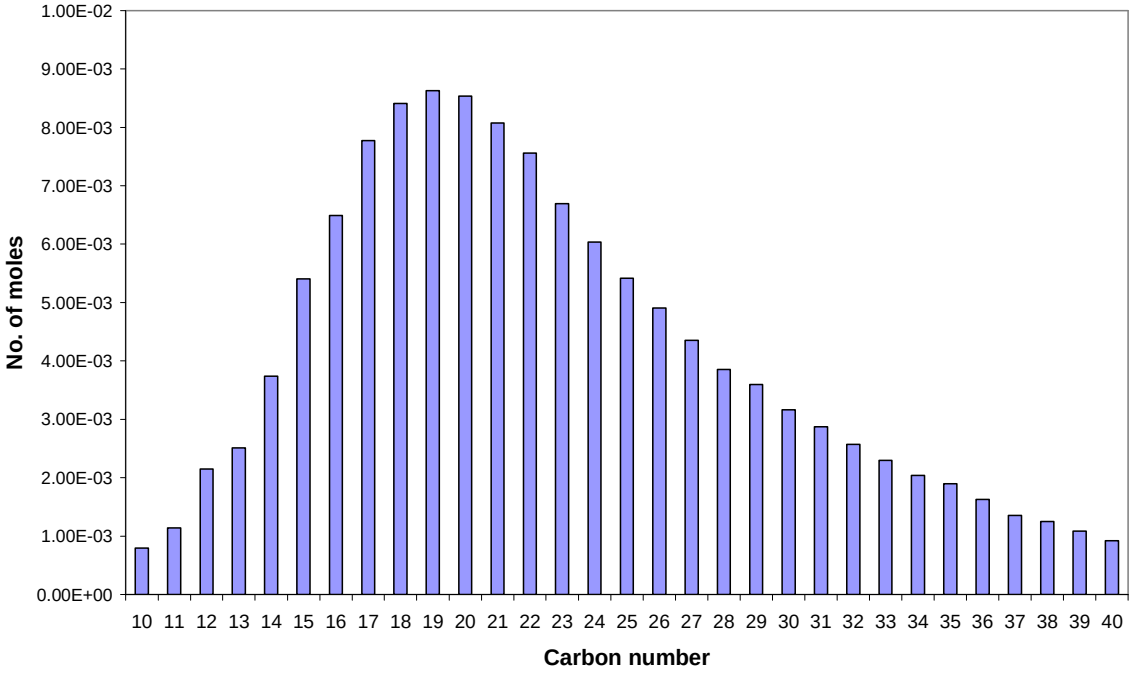

Figure 3-31: Hydrocarbon product distribution as a function of carbon number for CoNA wax sample at 360 hours TOS.

3.5.3.4.4 648 hours TOS

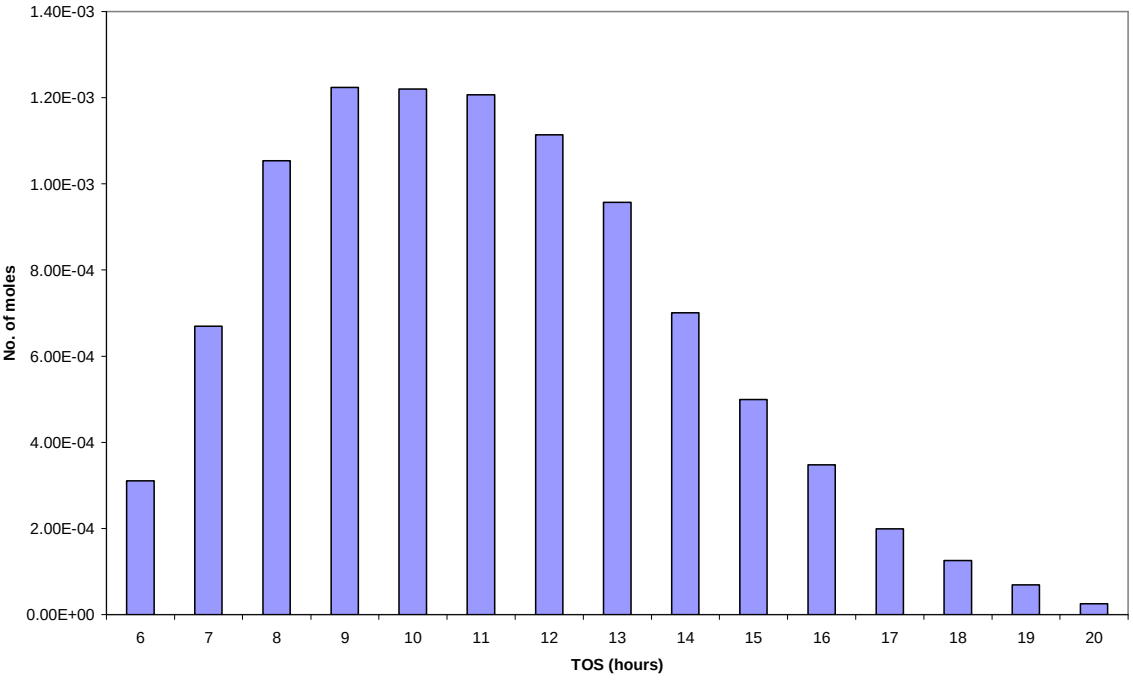

Figure 3-32: Hydrocarbon distribution as a function of carbon number for CoNA liquid hydrocarbon sample at 648 hours TOS

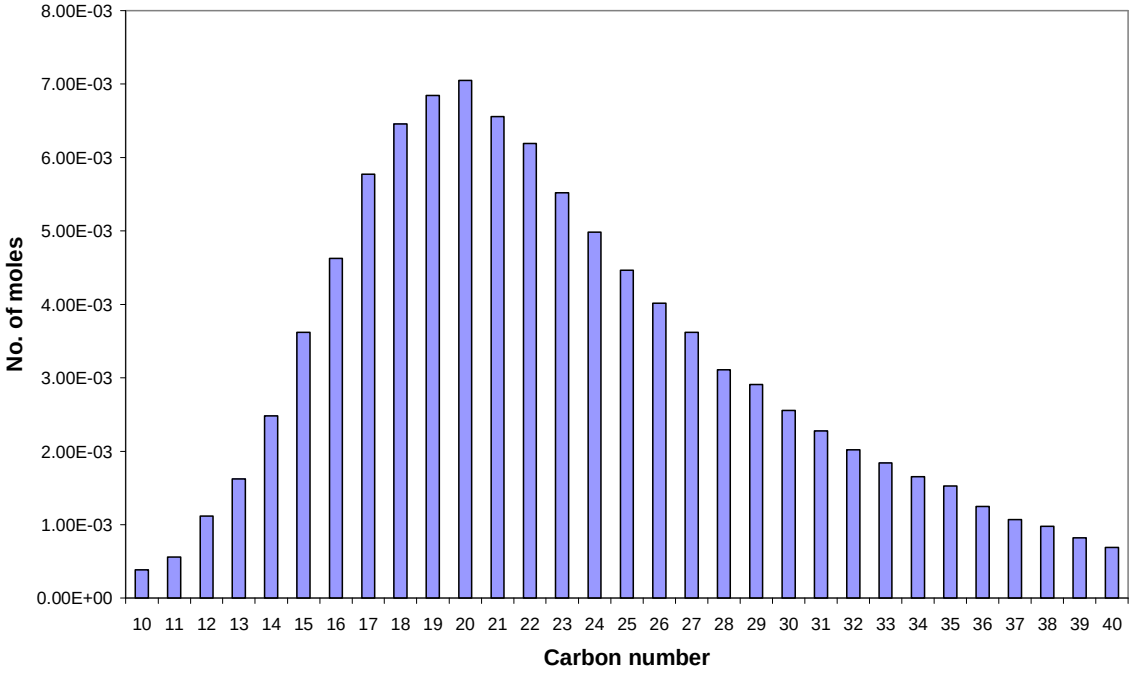

Figure 3-33: Hydrocarbon product distribution as a function of carbon number for CoNA wax sample at 648 hours TOS.

3.5.4 Post Reaction analysis

3.5.4.1 Thermogravimetric analysis-Differential Scanning Calorimetry and mass spectrometric analysis.

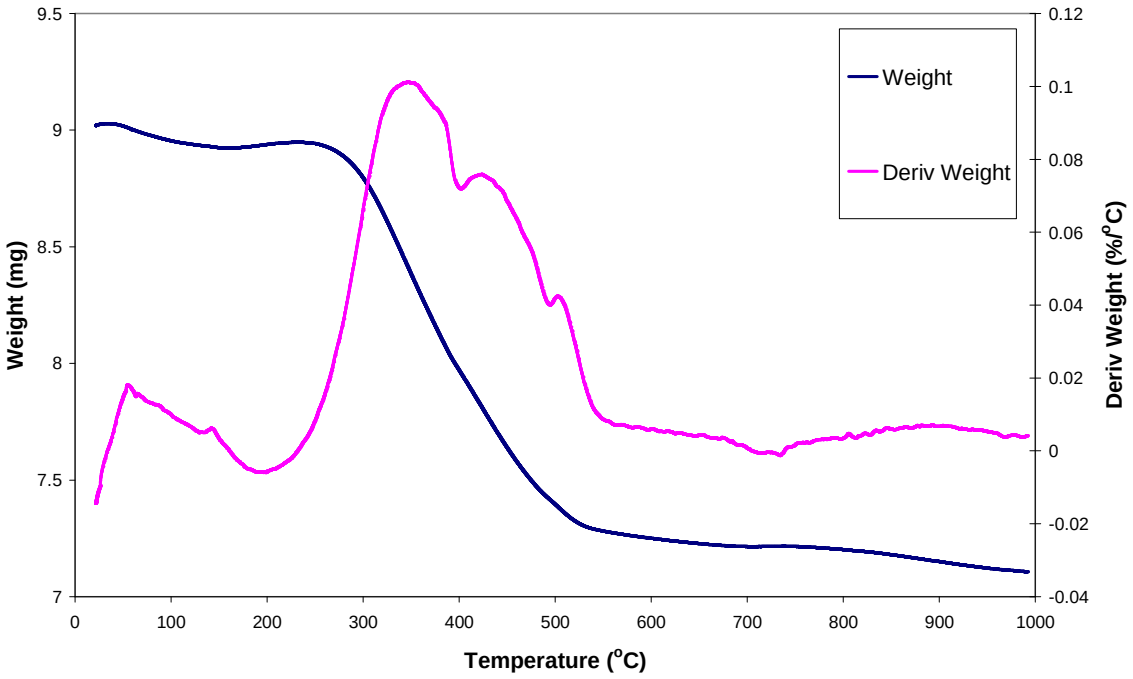

Figure 3-34: TGA weight and derivative profiles in oxygen for post FT reaction cobalt nitrate on alumina.

Figures 3-34 and 3-35 show the TGA-DSC profiles in oxygen obtained for the CoNA catalyst post Fischer-Tropsch reaction. There is an initial weight loss before 100 ^{o}C followed by a slight weight gain at around 200 ^{o}C. The main weight loss occurs from 240-570 ^{o}C and can be seen clearly in the derivative weight profile to be three overlapping events. From the heat flow data it can be seen that this main weight loss is exothermic.

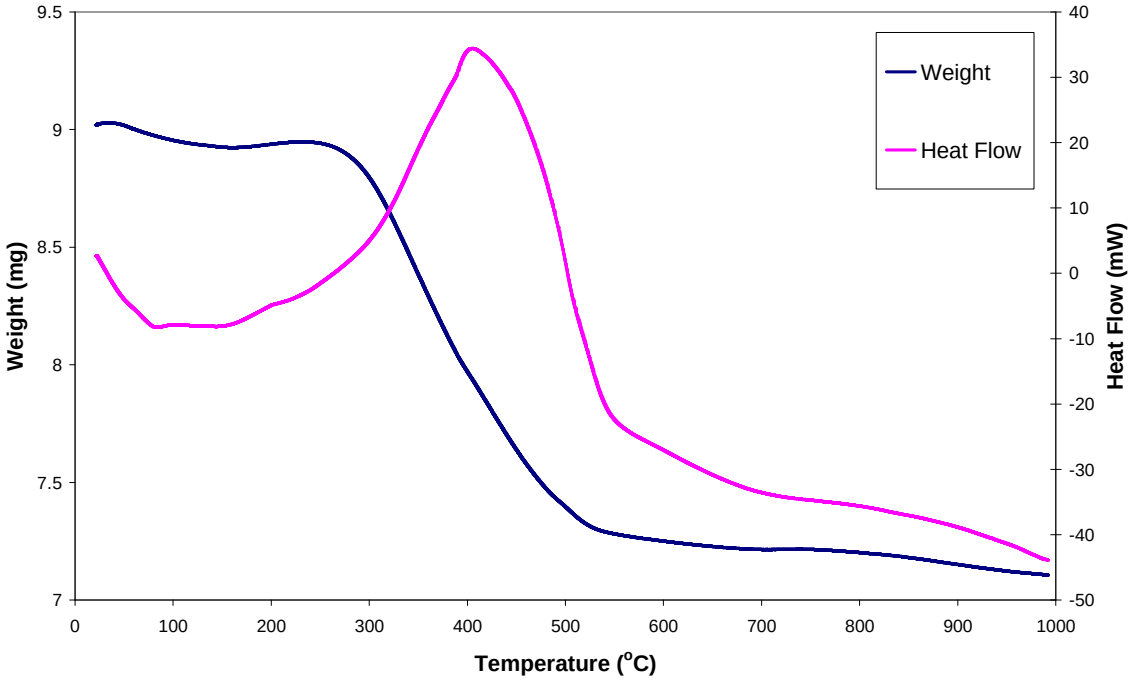

Figure 3-35: TGA-DSC weight and heat flow profiles in oxygen for post FT reaction cobalt nitrate on alumina.

The CoNA catalyst in oxygen post reaction was also followed through mass spectrometric analysis. Figure 3-36 shows gaseous products evolved as a function of temperature. The main weight loss corresponds to the evolution of water, carbon monoxide and carbon dioxide.

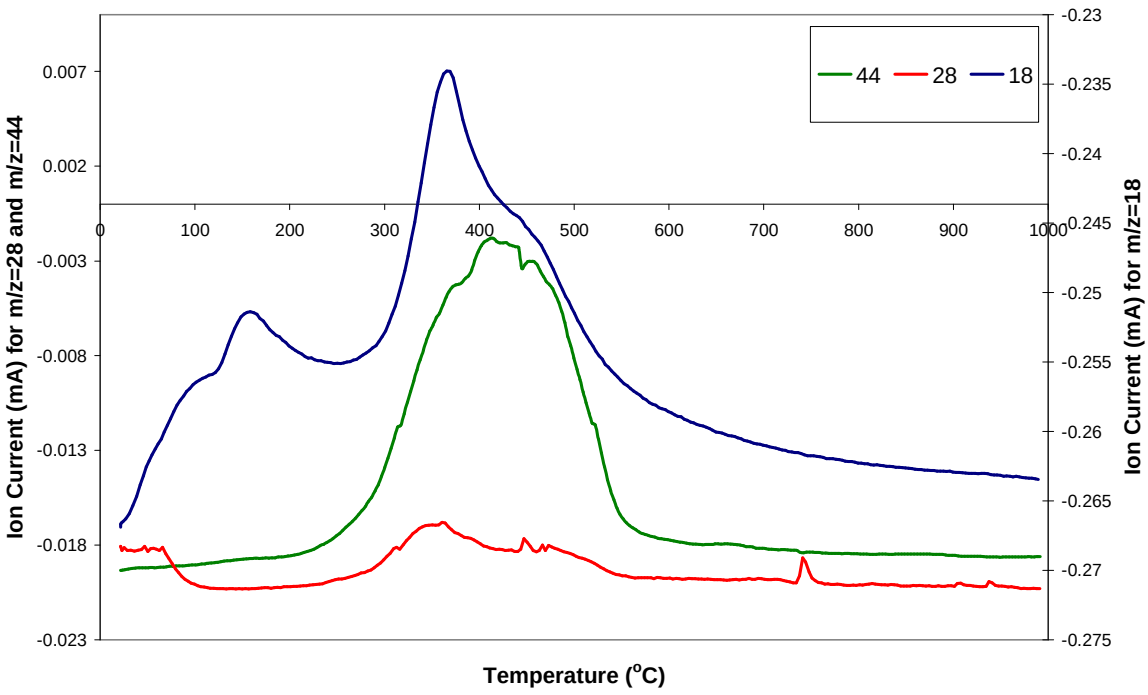

Figure 3-36: Mass spectrometric data of H_2O (m/z=18), CO (m/z=28) and CO_2 (m/z=44) in oxygen for post FT reaction cobalt nitrate on alumina.

3.5.4.1.1 X-Ray Diffraction

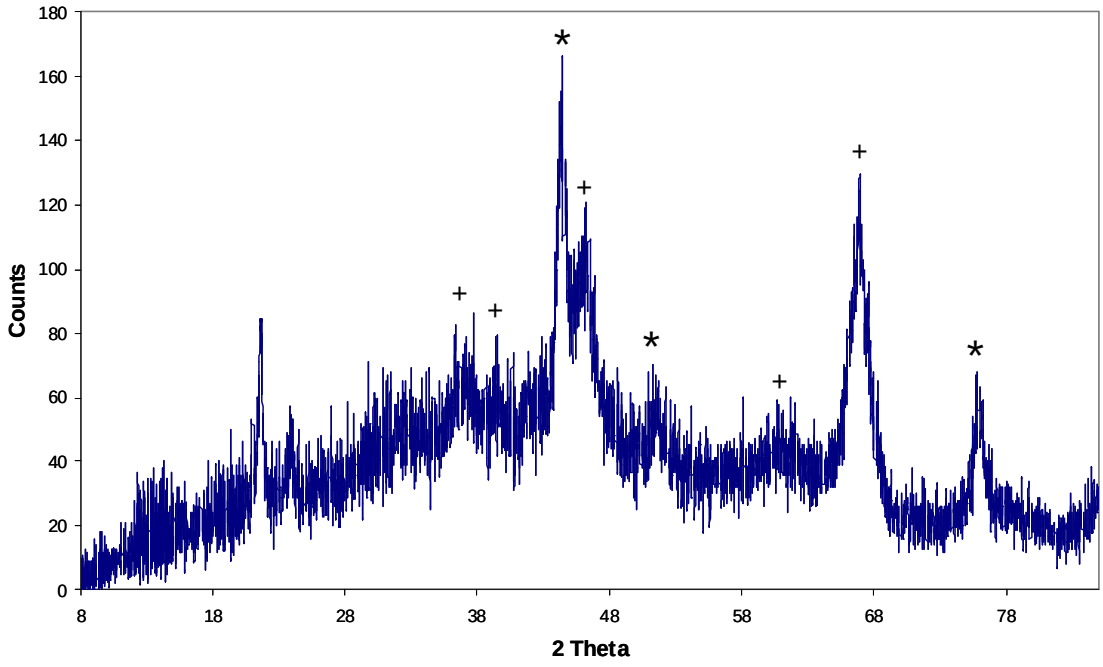

Figure 3-37: X-Ray diffraction pattern for cobalt nitrate on alumina catalyst post FT reaction. Phases denoted are (*) Co metal and (+) Al_2O_3. The experimental error for cobalt size calculated from X-ray diffraction is less than +/- 1 nm.

Figure 3-37 shows the X-ray diffraction pattern for the CoNA catalyst post Fischer Tropsch reaction. The presence of diffraction peaks centred at $2\theta = 44.3^{o}$, 51.5^{o} and 75.7^{o} is indicative of metallic cobalt. The remaining peaks are characteristic of the alumina support. The average cobalt metal particle size, calculated using the Scherrer equation, was found to be 12 nm.

3.6 Cobalt acetate on Alumina

Results have been taken from previous work and are shown in sections 3.6.1.1-3.6.1.2 and 3.6.2.1-3.6.2.3 [92]. This has been done in order to aid interpretation of the other results.

3.6.1 Oxygen

3.6.1.1 Thermogravimetric analysis-Differential scanning calorimetry

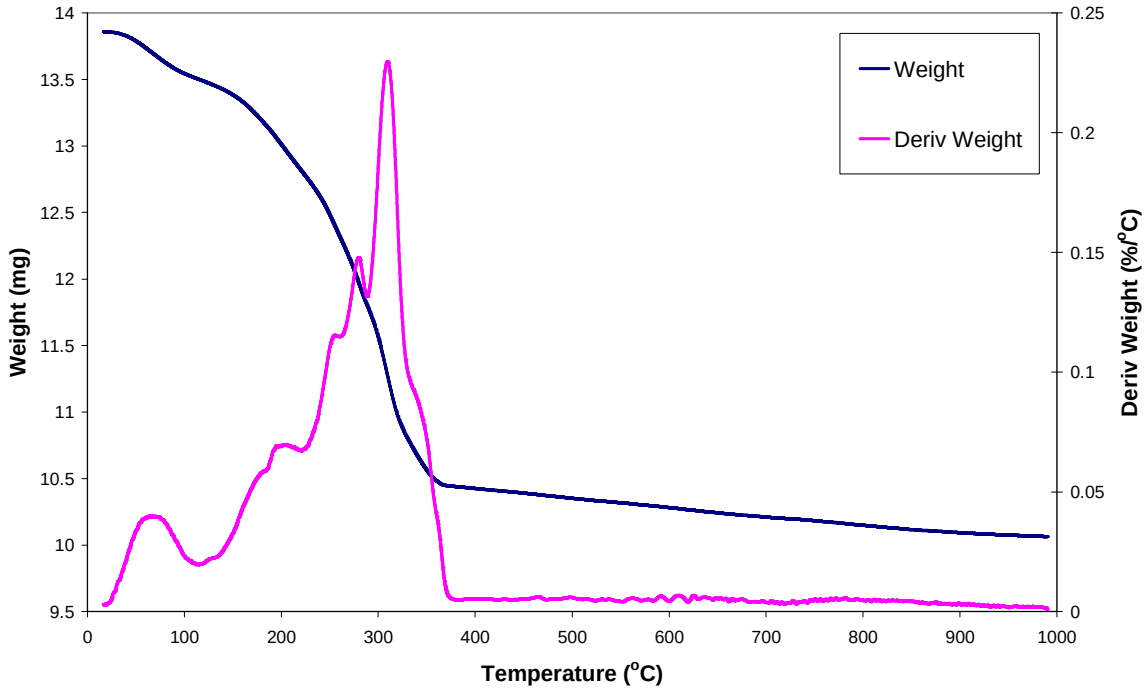

Figure 3-38: TGA weight and derivative weight profile in oxygen for cobalt acetate on alumina.

The TGA curves in figure 3-38 show significant weight loss upon heating to 400 ^{o}C. Above this temperature very little weight loss occurs. From the derivative weight profile it can be seen that the decomposition is complex, comprising of a peak before 100 ^{o}C followed by a broad main peak with several shoulders with a maximum at 310 ^{o}C. The DSC data shown in figure 3-39 indicates an endothermic event before 100 ^{o}C which can be attributed to desorption of water. Further to this endothermic loss of water, the DSC curve exhibits two exotherms at higher temperatures. The second of these is highly exothermic with a small shoulder suggesting two separate thermal events. The maximum for these exothermic events occur at 204 ^{o}C and 304 ^{o}C.

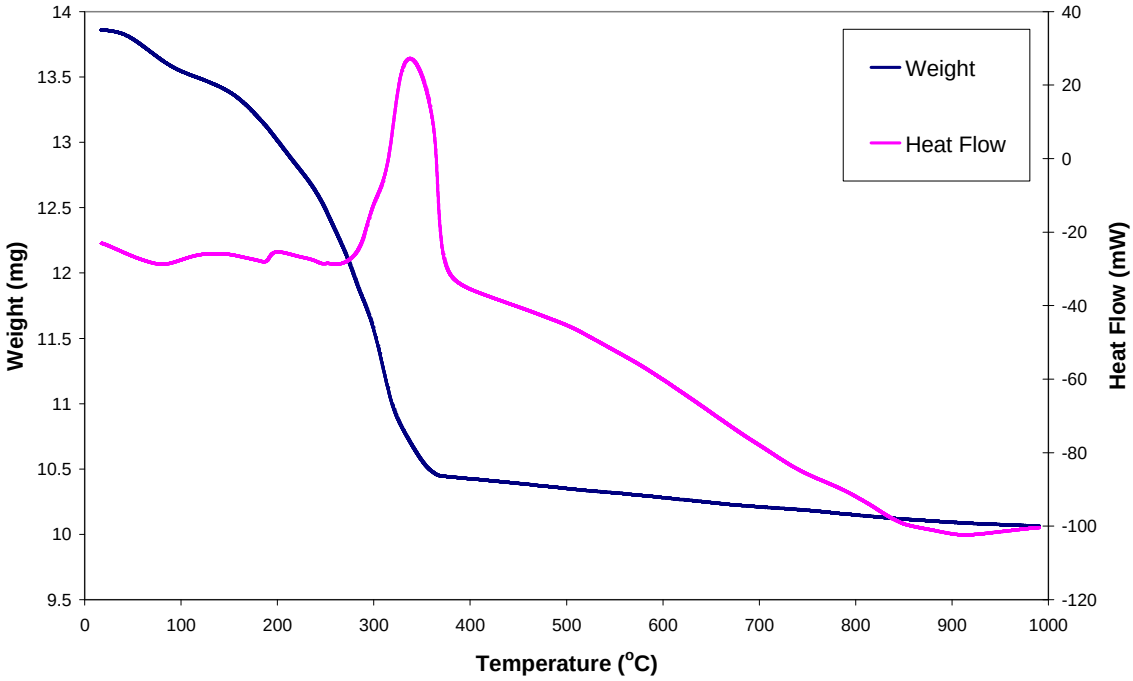

Figure 3-39: TGA-DSC weight and heat flow profiles in oxygen for cobalt acetate on alumina.

3.6.1.2 Mass spectrometric analysis

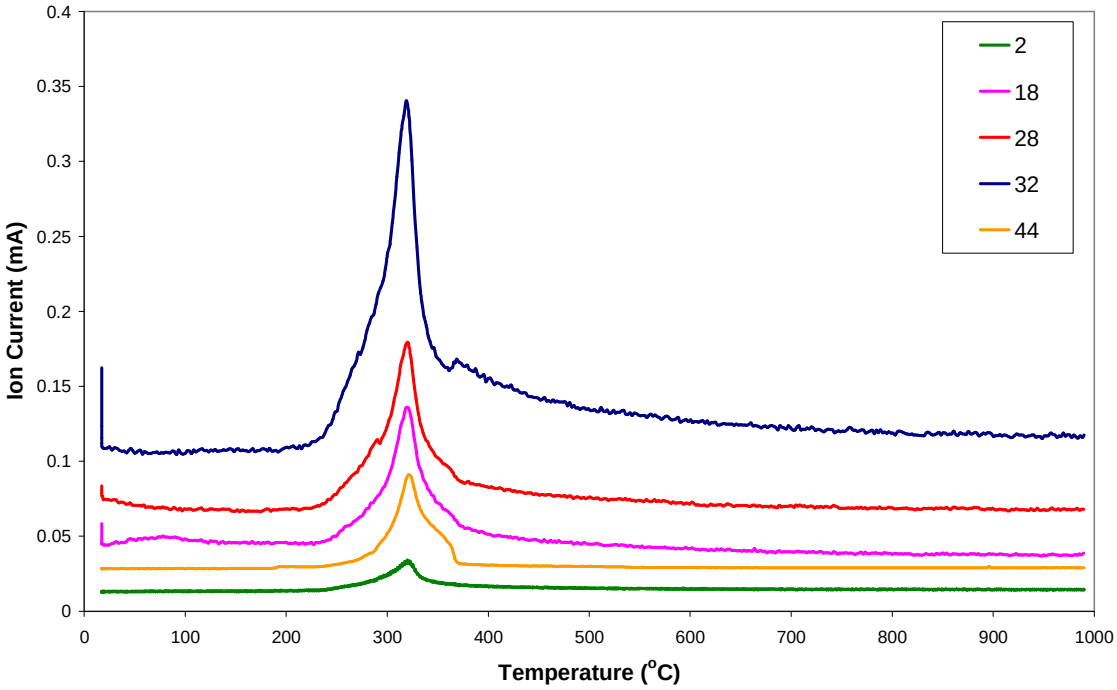

Figure 3-40: Mass spectrometric data of H_2 (m/z=2), H_2O (m/z=18), CO (m/z=28), O_2 (m/z=32) and CO_2 (m/z=44) in oxygen for cobalt acetate on alumina.

The products from the decomposition in oxygen of the cobalt acetate on alumina catalyst, reported by the mass spectrometric analysis, are shown above in figure 3-40. Apart from the evolution of water before 100 ^{o}C, all the products detected evolve around 320 ^{o}C. A shoulder is present on some of the evolved gas peaks indicating the possibility of more than one evolution. The mass spectrometric data for the decomposition of CoAA in oxygen shows the release of CO and CO_2, as well as hydrogen and water. The most interesting feature however is the evolution of oxygen, rather than its expected uptake.

3.6.1.3 Effect of heating rate

Figure 3-41 presents the TGA weight and derivative profiles for the CoAA catalyst ramped at 1 ^{o}C min^{-1} to 400 ^{o}C in 2% Oxygen-Argon. Several overlapping peaks are seen in the derivative weight profile, with the decomposition complete by 285 ^{o}C. Decreasing the ramp rate from 10 to 1 ^{o}C min^{-1} has shifted the decomposition derivative peak maxima 55 ^{o}C lower in temperature.

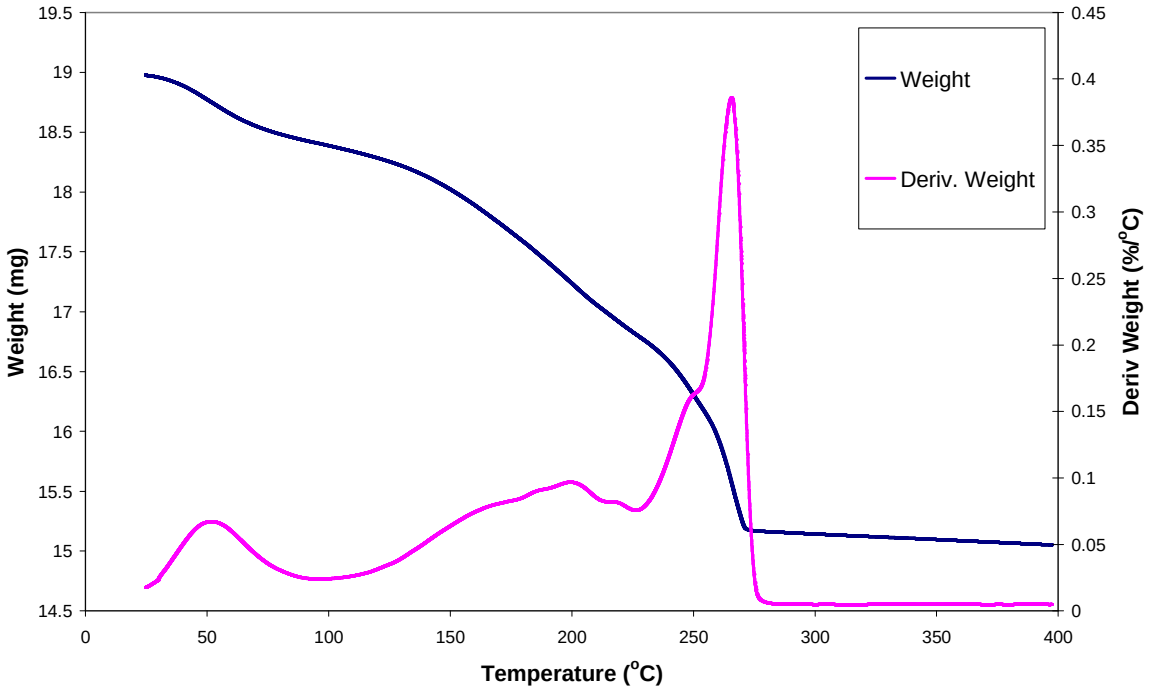

Figure 3-41: TGA weight and derivative weight profiles in oxygen at 1 ^{o}C min^{-1} for cobalt acetate on alumina.

From theses results a suitable temperature profile was determined for calcination for the cobalt acetate on alumina catalysts and is as follows:

- Ramp 1 ^{o}C min^{-1} to 300 ^{o}C and hold for 120 minutes in 2% Oxygen-Argon at 40 ml min^{-1}.

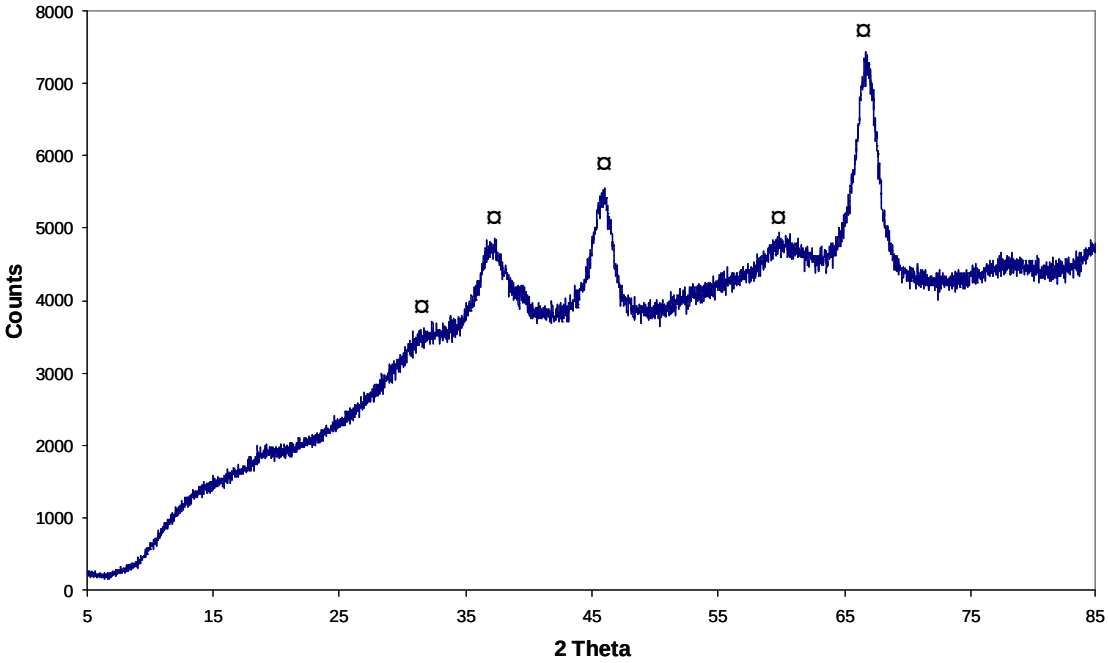

Figure 3-42: X-ray diffraction pattern for the calcined cobalt acetate on alumina. Phases denoted are (¤) Al_2O_3.

The XRD pattern of the CoAA catalyst, calcined as previously specified, is shown in figure 3-42. The catalyst exhibited diffraction peaks at 2θ of ca. 31.3^{o}, 37.0^{o}, 46.1^{o}, 60.2^{o} and 66.7^{o}, indicating the presence of Al_2O_3 support. No reflections corresponding to cobalt oxide were observed.

3.6.2 Hydrogen (after calcination in oxygen)

3.6.2.1 Thermogravimetric analysis-differential scanning calorimetry

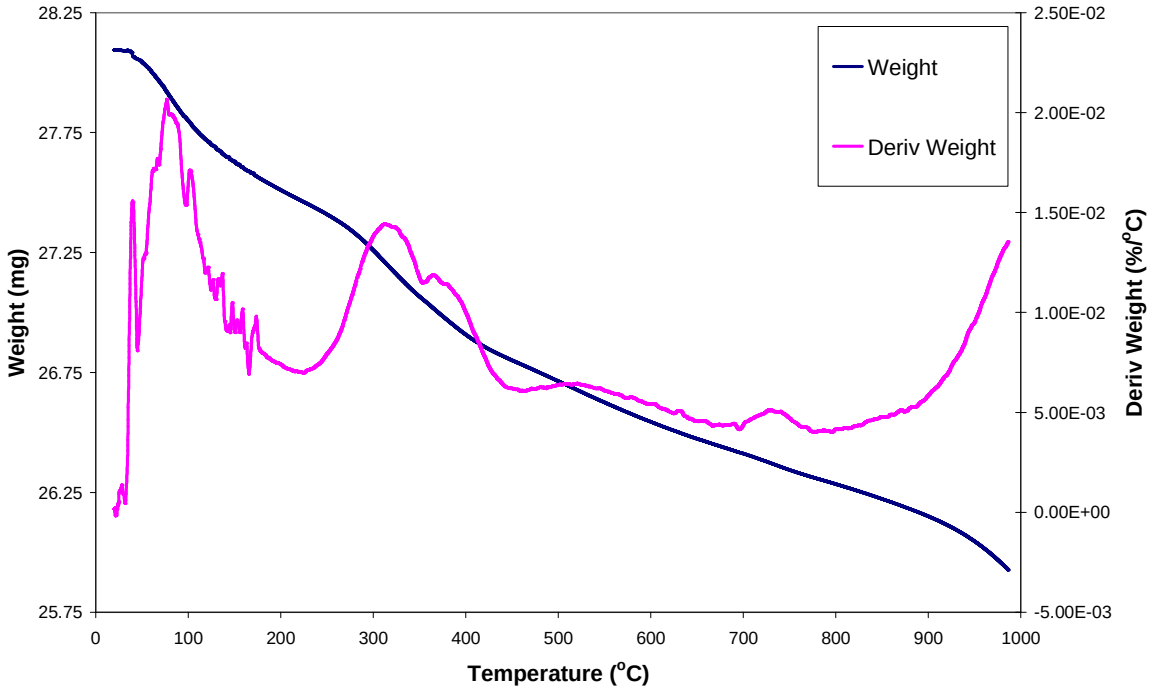

Figure 3-43: TGA weight and derivative weight profile in hydrogen (after calcination in oxygen) for cobalt acetate on alumina.

The weight loss, derivative weight and heat flow curves obtained from the TGA analysis in a hydrogen atmosphere for the calcined CoAA catalyst are depicted in figures 3-43 and 3-44. In the derivative weight curve for CoAA a peak can be observed at around 70 ^{o}C. A further weight loss, which from the derivative weight profile appears to occur as two separate events at 318 ^{o}C and 377 ^{o}C, can also be seen. Further peaks are seen at 510 ^{o}C and 735 ^{o}C with a continuous weight loss region observed above 800 ^{o}C.

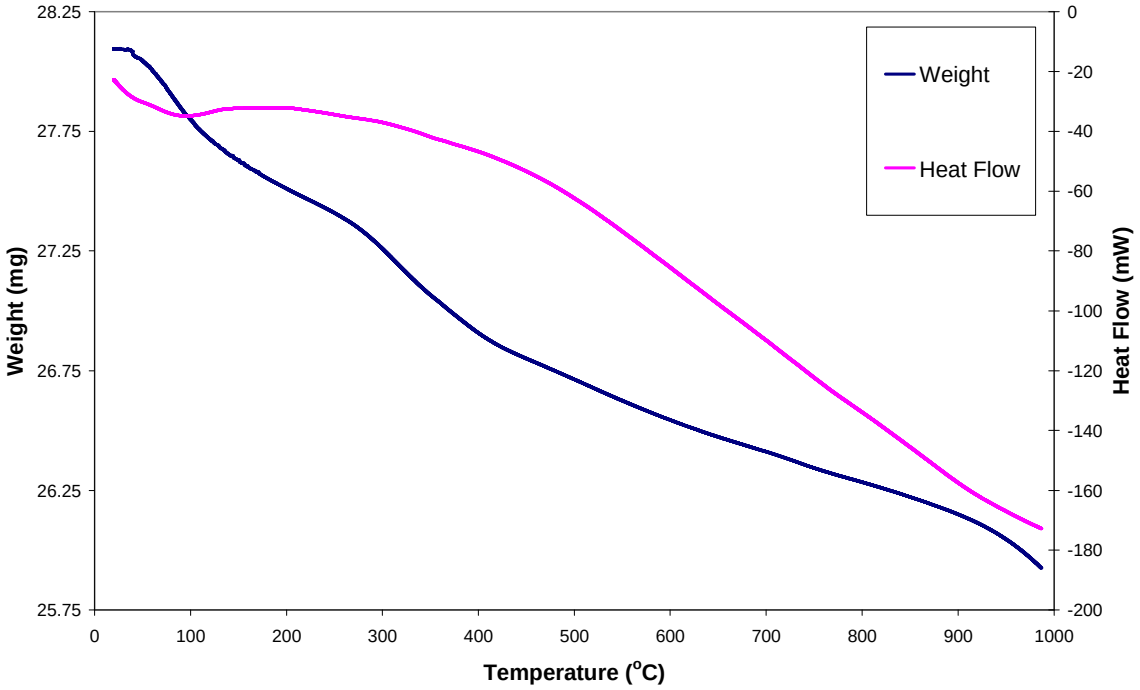

Figure 3-44: TGA-DSC weight and heat flow profiles in hydrogen (after calcination in oxygen) for cobalt acetate on alumina.

3.6.2.2 Mass spectrometric data

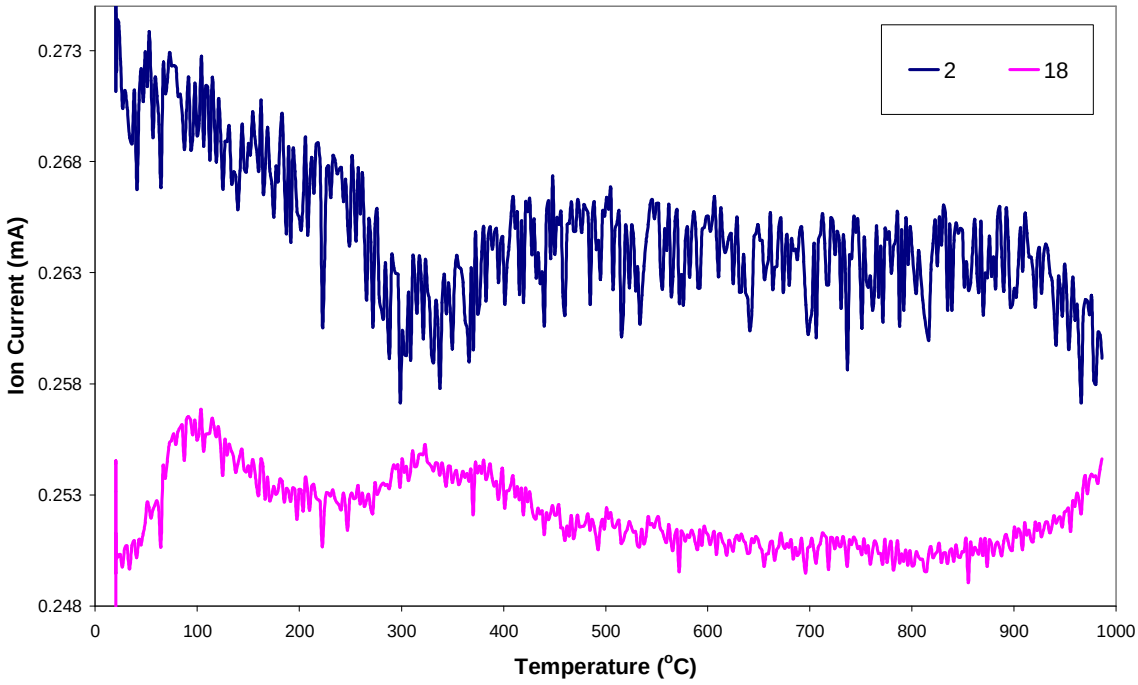

Figure 3-45: Mass spectrometric data of H_2 (m/z=2) and H_2O (m/z=18) in hydrogen (after calcination in oxygen) for cobalt acetate on alumina.

For the CoAA catalyst, evolution of water corresponding to the uptake of hydrogen can be observed on three separate occasions. These occur at 100 ^{o}C, two overlapping evolutions centred at 350 ^{o}C and as a continuous increase in hydrogen consumption above 850 ^{o}C.

3.6.2.3 Hot-stage X-Ray diffraction

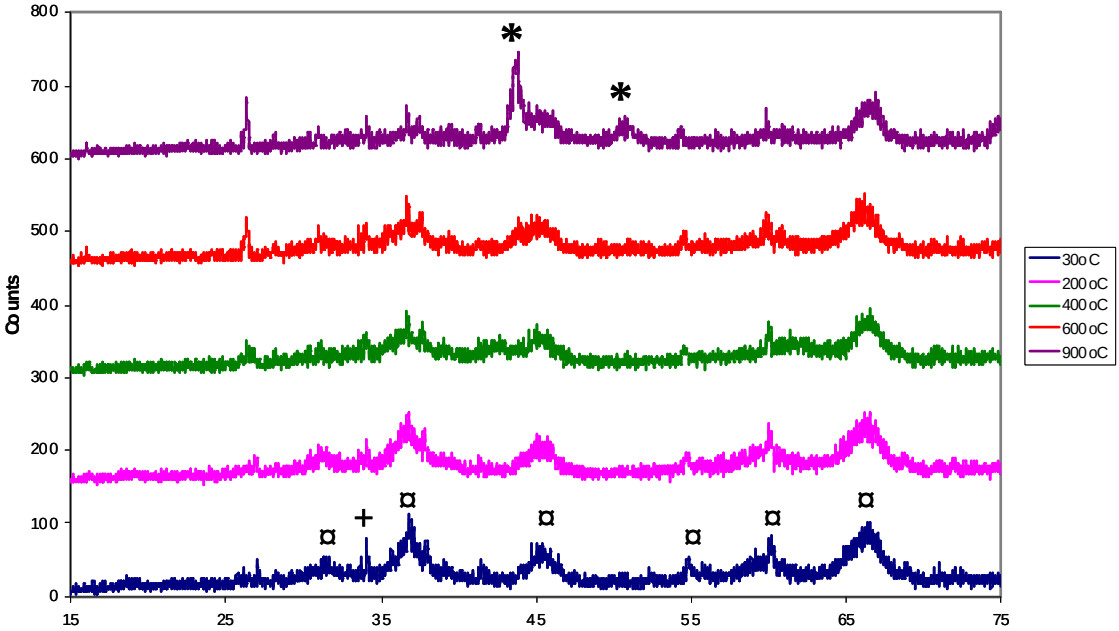

Figure 3-46: Hot-stage XRD patterns in hydrogen (after calcination in oxygen) for cobalt acetate on alumina. The phases denoted are (¤) Co_3O_4, (+) CoO and (*) metallic Co. The XRD patterns are offset for clarity. The experimental error for cobalt sizes calculated from X-ray diffraction is less than +/- 1 nm.

The hot-stage XRD patterns for calcined CoAA catalysts are presented in figure 3-46. At 30 ^{o}C the pattern clearly exhibits crystalline Co_3O_4, by 600 ^{o}C cobalt metal can be detected. From the broadening of lines, the crystallite size of cobalt metal can be estimated, and shows at 800 ^{o}C and 900 ^{o}C the particles were 12 nm and 13 nm, respectively.

3.6.2.4 Effect of heating rate

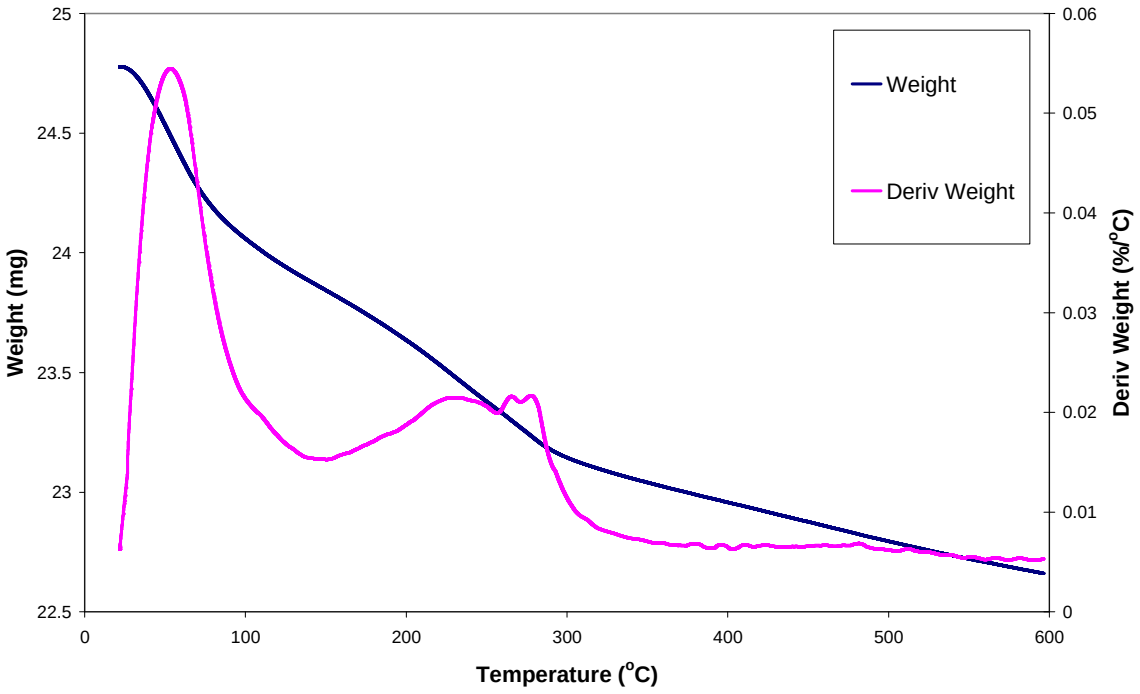

Figure 3-47: TGA weight and derivative weight profiles in hydrogen at 1 ^{o}C min^{-1} for calcined cobalt acetate on alumina.

The TGA weight and derivative weight profiles for calcined CoAA catalyst in 2% hydrogen-nitrogen atmosphere at 1 ^{o}C min^{-1} are shown in figure 3-47. It can be observed that the significant part of the weight loss occurs below 400 ^{o}C.

From the above TGA data and by taking into account that reducing in pure hydrogen is likely to decrease the temperature of reduction, the following *in-situ* reduction procedure was decided upon:

- Ramp 1 ^{o}C min^{-1} to 300 ^{o}C and hold for 10 hours in hydrogen.

3.6.2.5 Extent of reduction

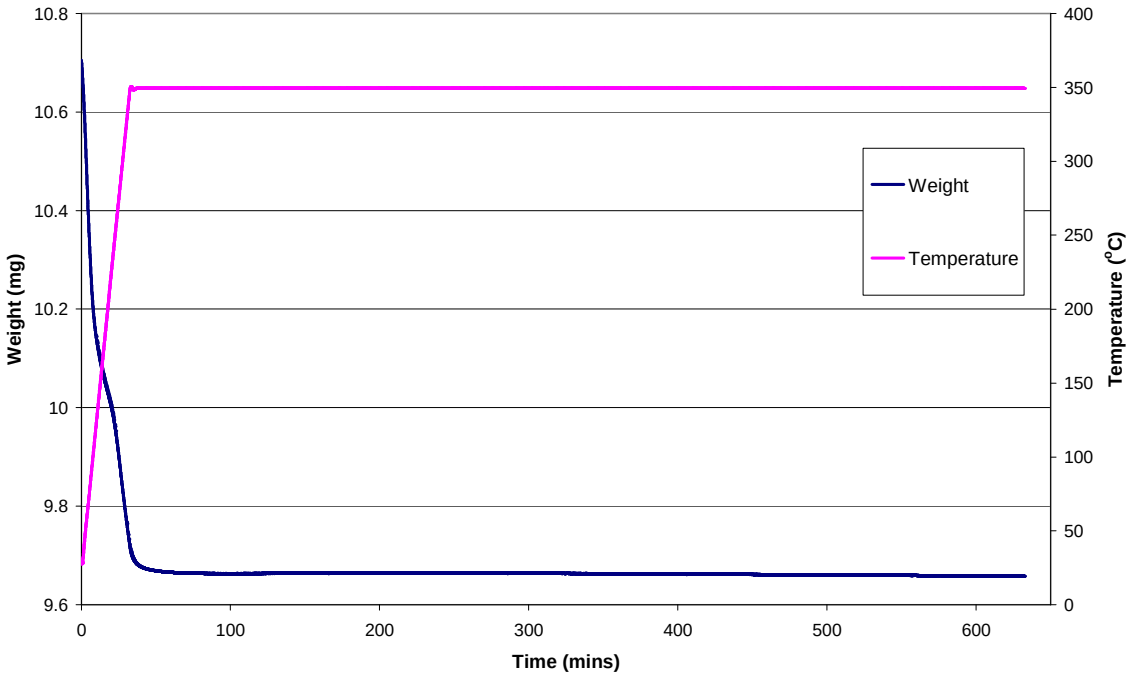

Figure 3-48: TGA weight profile as a function of time in hydrogen for calcined CoAA catalyst.

Figure 3-48 shows the TGA weight profile as a function of time following the reduction of the calcined CoAA catalyst. The catalyst was ramped at 10 ^{o}C min^{-1} to the desired reduction temperature of 350 ^{o}C and held for 10 hours. When TGA is used to estimate the degree of reduction, reduction of Co_3O_4 to metallic Co, requiring a calculated weight lost 26.6% is assumed. The weight loss from the TGA is 3.8% suggesting that the extent of reduction for CoAA catalyst is 15%.

3.6.2.6 CO chemisorption

The number of surface metal sites in the CoAA catalyst was evaluated by CO chemisorption as described in section 2.3.5. The amount of chemisorbed CO was found to be 17µmol/g_{cat}. Relative percentage cobalt dispersion and average crystallite size were determined from the chemisorption data. Assuming an adsorption stoichiometry of 1 CO molecule per surface cobalt atom, the dispersion was calculated to be 0.49%.

3.6.3 FT reaction

3.6.3.1 Conversion

Figure 3-49 shows the conversion as a function of time obtained for the CoAA catalyst at 220 ^{o}C and 240 ^{o}C. There is an initial increase in the conversion from 29 to 38% after 50 hours time on stream. The conversion then decreases and after 452 hours on stream reaches a nearly constant value of 11-12%. At 671 hours time on stream, increasing the temperature to 240 ^{o}C led to an increase in the conversion to 35%. Thereafter the conversion dropped to 29% at 764 hours.

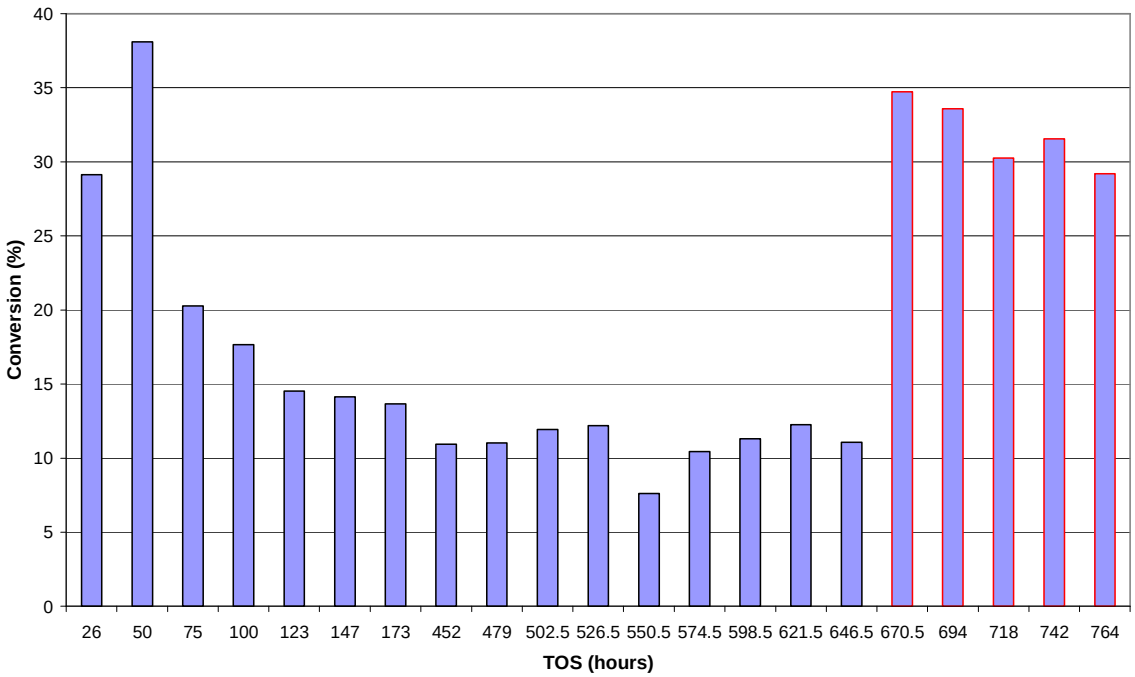

Figure 3-49: Conversion as a function of time-on-stream for the CoAA catalyst at a temperature of 220 ^{o}C and then 240 ^{o}C. The experimental error for the conversion is estimated to be +/- 5%.

3.6.3.2 Deactivation

From the conversion, deactivation constants were calculated as described in section 2.5.2. Figures 3-50 and 3-51 show the plot of ln(Xa/(1-Xa) versus TOS at 220 ^{o}C and 240 ^{o}C, respectively. The deactivation constants were calculated to be 0.1685 hr^{-1} at 220 ^{o}C and 0.0025 hr^{-1} at 240 ^{o}C.

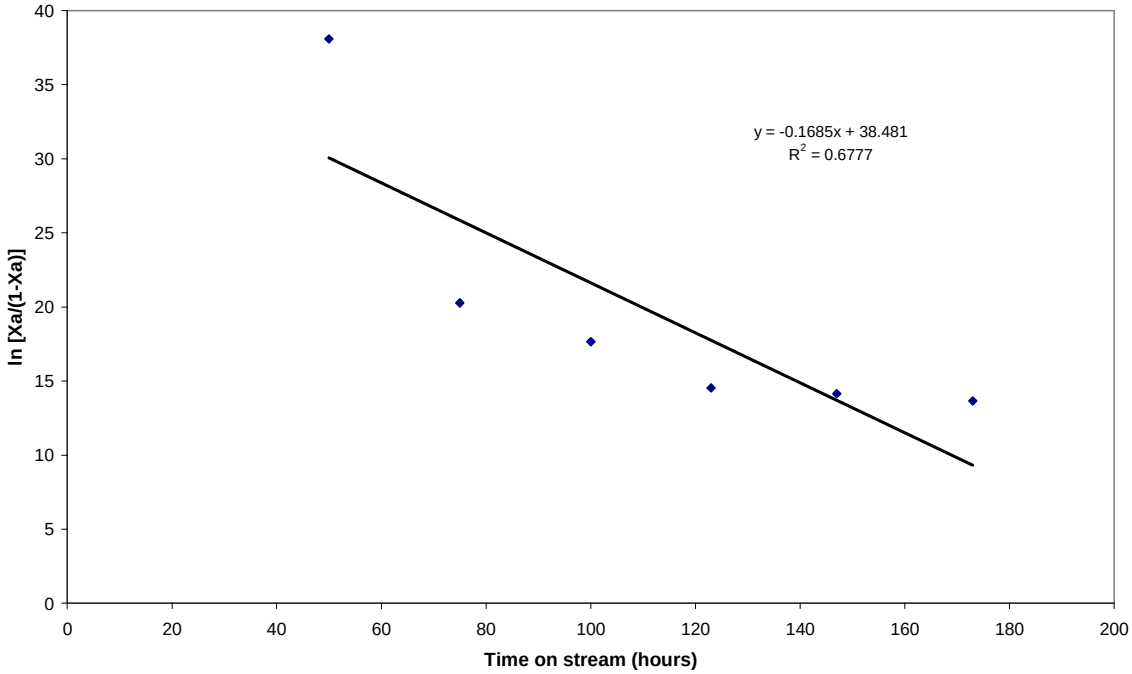

Figure 3-50: Graph of ln[Xa/(1-Xa)] vs. time on stream for FT reaction at 220 ^{o}C.

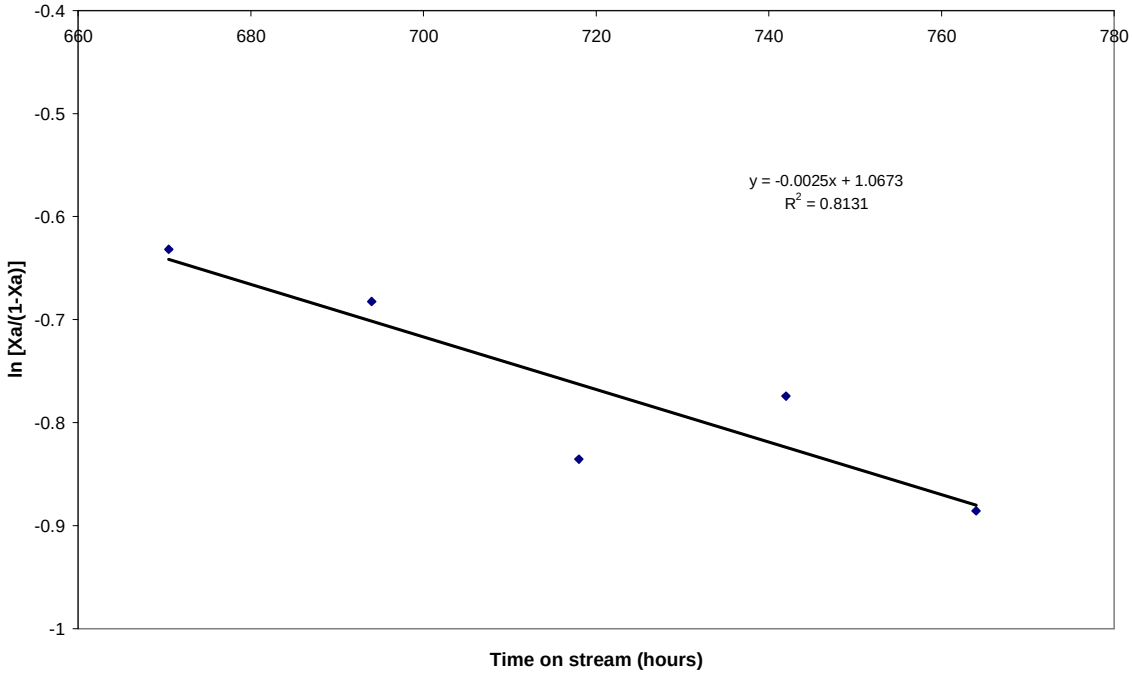

Figure 3-51: Graph of ln[Xa/(1-Xa)] vs. time on stream for FT reaction at 240 ^{o}C.

3.6.3.3 Alpha values

Figure 3-52 shows the alpha values as a function of time on stream for the CoAA catalyst at a reaction temperature of 220 ^{o}C and 240 ^{o}C, respectively. At steady state at 220 ^{o}C (26-647 hours TOS), the average alpha value was found to be 0.82. On increasing the temperature to 240 ^{o}C (671-742 hours TOS), a decrease in the alpha value to an average value of around 0.77 was observed.

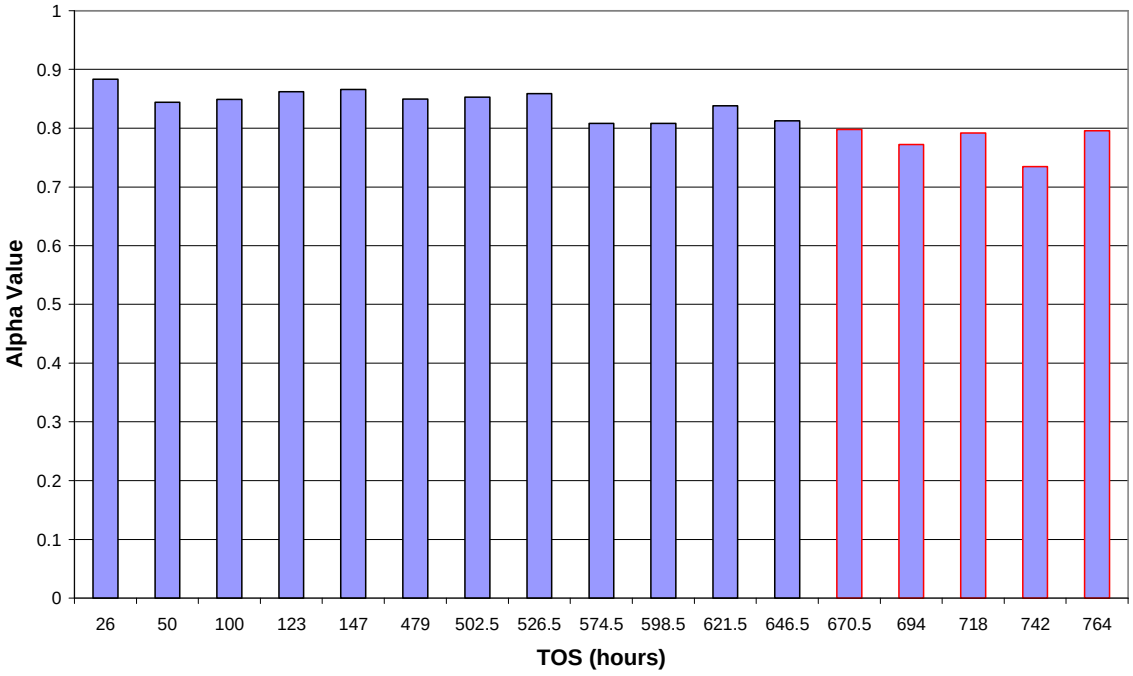

Figure 3-52: Alpha values versus time on stream for CoAA catalyst at reaction temperature of 220^{o}C and 240^{o}C.

3.6.3.4 Wax and liquid hydrocarbon product distribution

The hydrocarbon product distributions for the wax and liquid hydrocarbons samples at 75, 173, 622, 694 and 764 hours TOS are shown in figures 3-53 to 3-62.

3.6.3.4.1 75 hours TOS

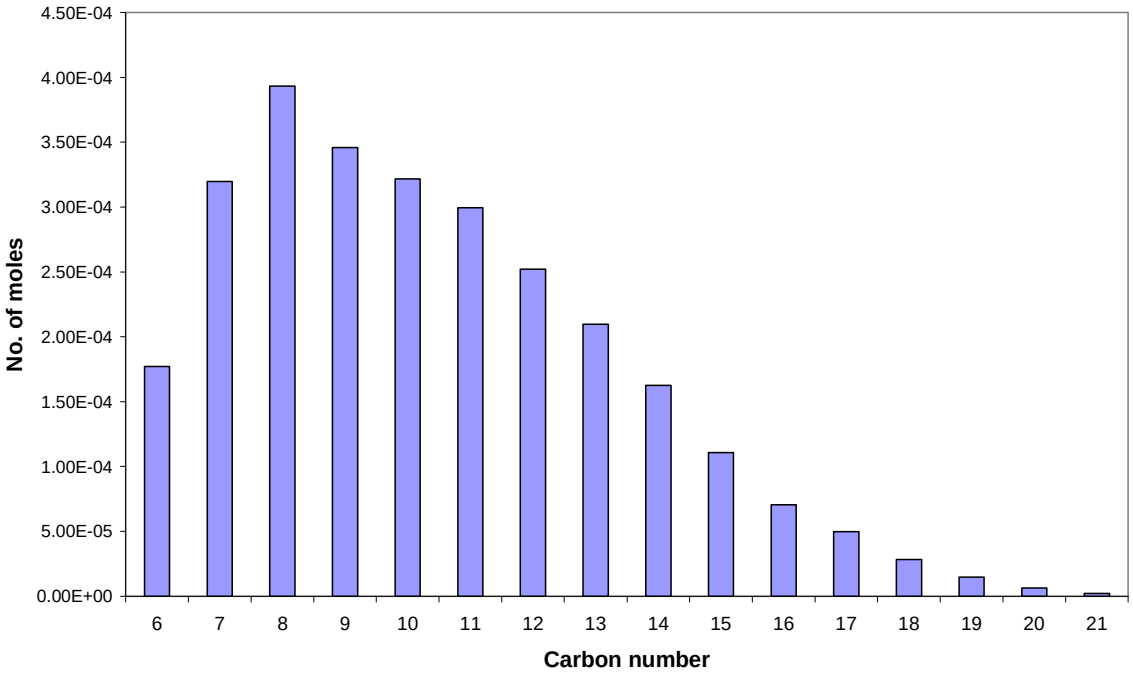

Figure 3-53: Hydrocarbon product distribution as a function of carbon number for CoAA liquid hydrocarbon sample at 75 hours TOS (T=220°C)

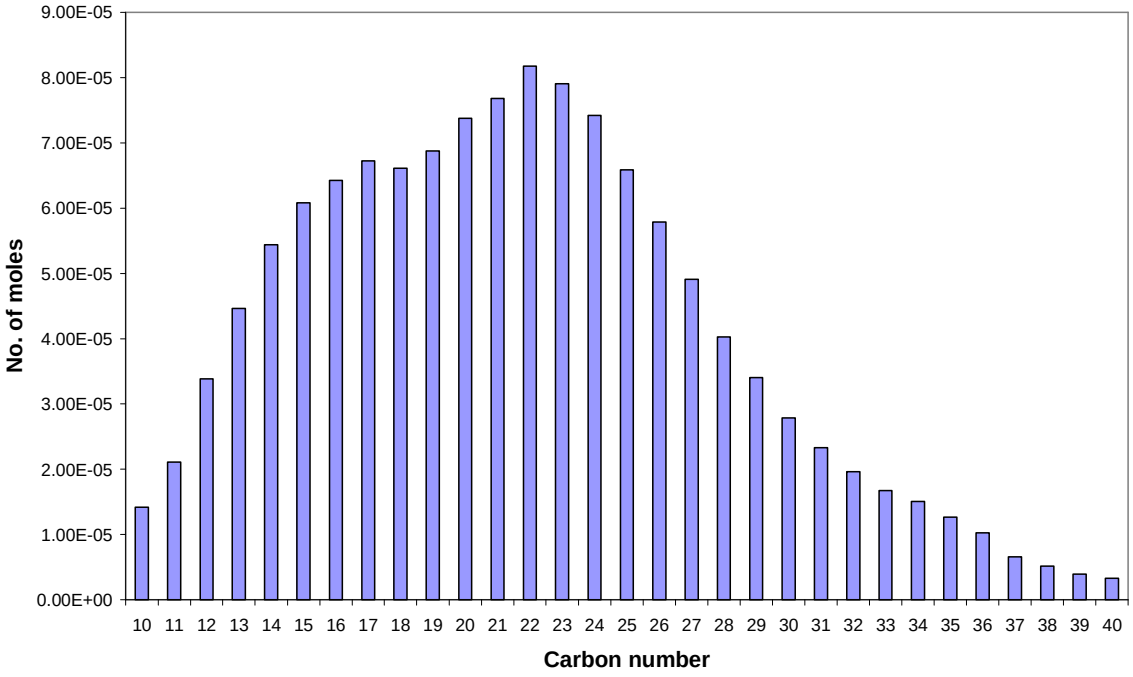

Figure 3-54: Hydrocarbon product distribution as a function of carbon number for CoAA wax sample at 75 hours TOS (T=220°C)

3.6.3.4.2 173 hours TOS

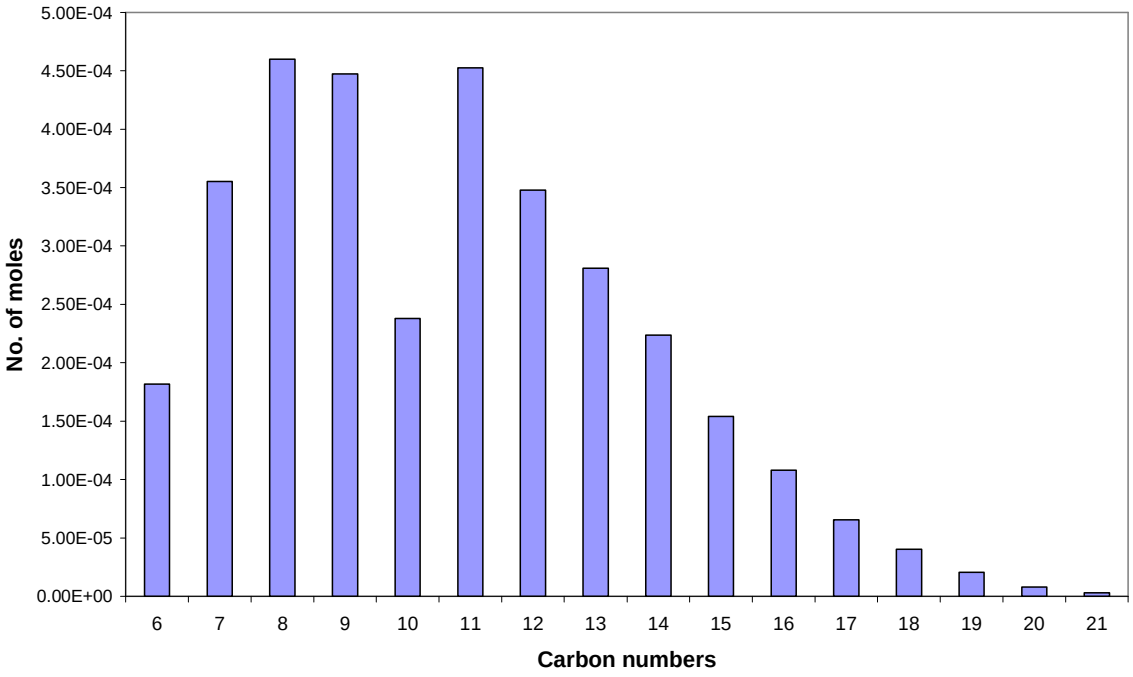

Figure 3-55: Hydrocarbon product distribution as a function of carbon number for CoAA liquid hydrocarbon sample at 173 hours TOS (T=220^{o}C)

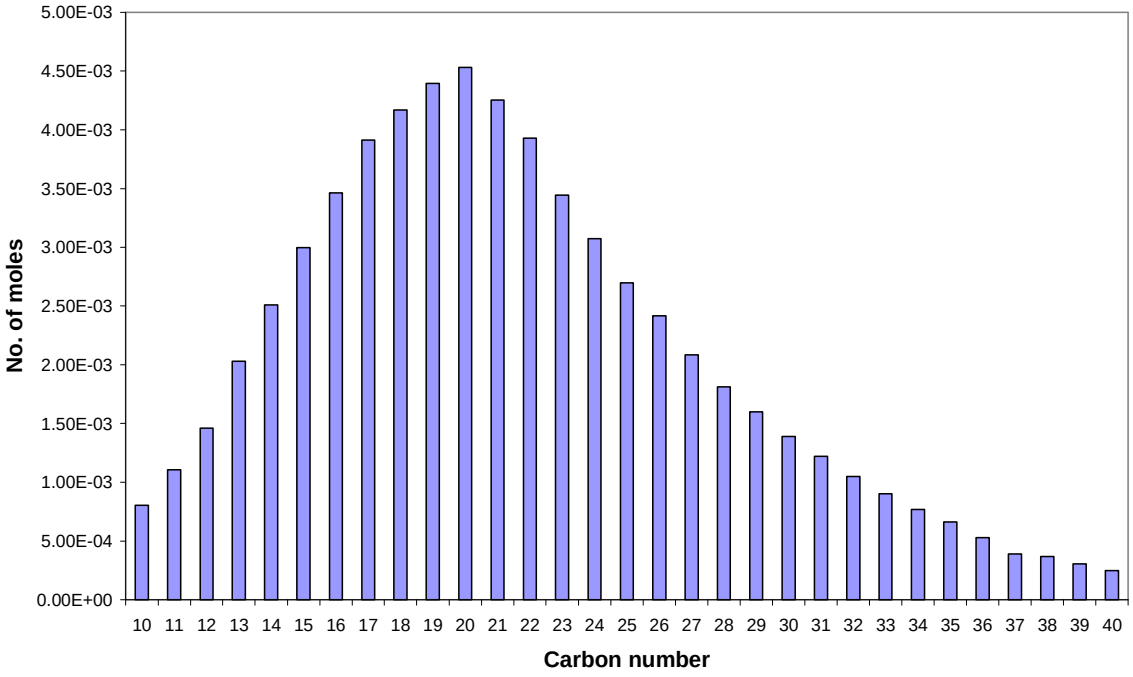

Figure 3-56: Hydrocarbon product distribution as a function of carbon number for CoAA wax sample at 173 hours TOS (T=220^{o}C)

3.6.3.4.3 622 hours

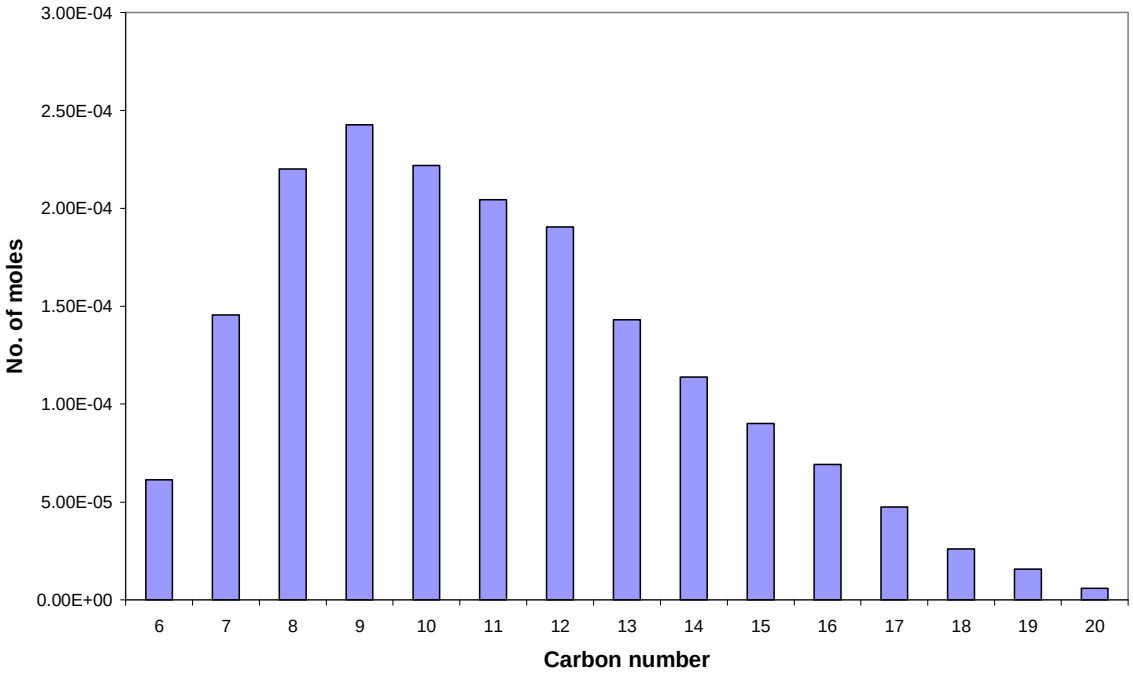

Figure 3-57: Hydrocarbon product distribution as a function of carbon number for CoAA liquid hydrocarbon sample at 622 hours TOS (T=220^{o}C)

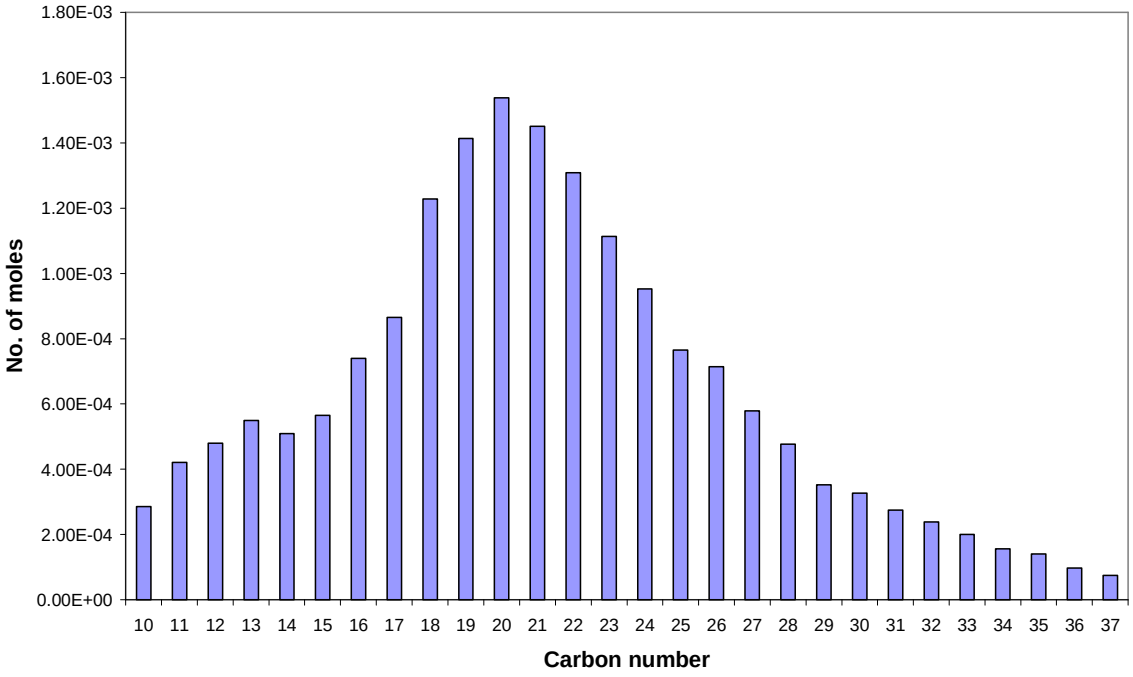

Figure 3-58: Hydrocarbon product distribution as a function of carbon number for CoAA wax sample at 622 hours TOS (T=220^{o}C)

3.6.3.4.4 694 hours TOS

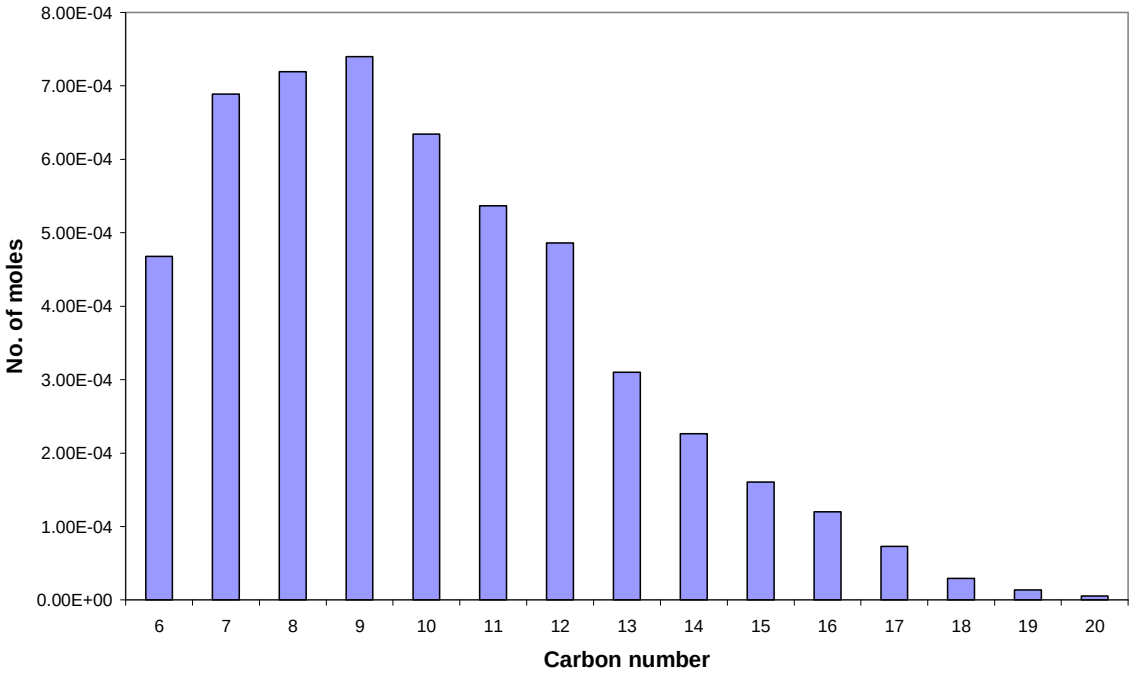

Figure 3-59: Hydrocarbon product distribution as a function of carbon number for CoAA liquid hydrocarbon sample at 694 hours TOS (T=240^{o}C)

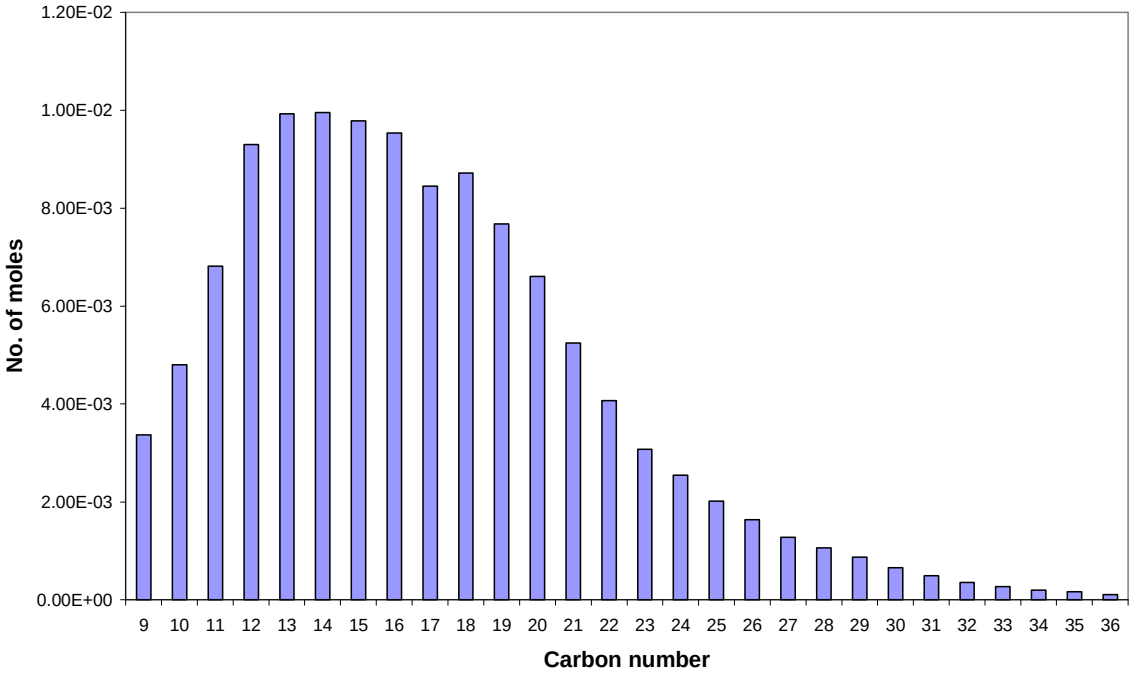

Figure 3-60: Hydrocarbon product distribution as a function of carbon number for CoAA wax sample at 694 hours TOS (T=240^{o}C)

3.6.3.4.5 764 hours TOS

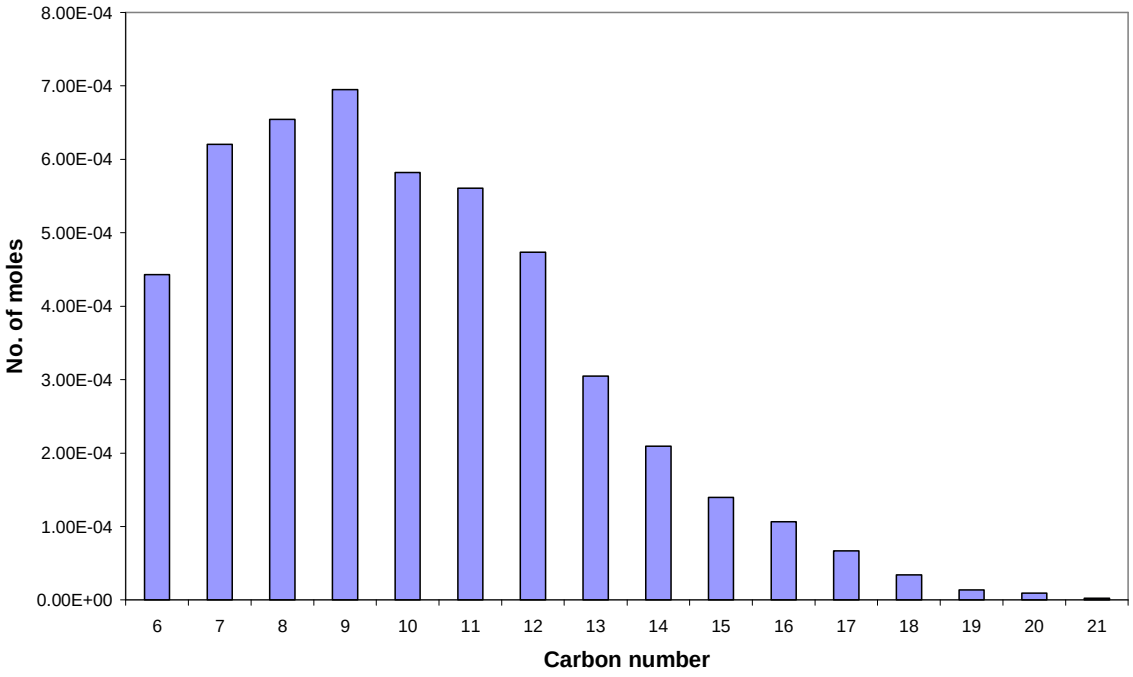

Figure 3-61: Hydrocarbon product distribution as a function of carbon number for CoAA liquid hydrocarbon sample at 764 hours TOS (T=240^{o}C)

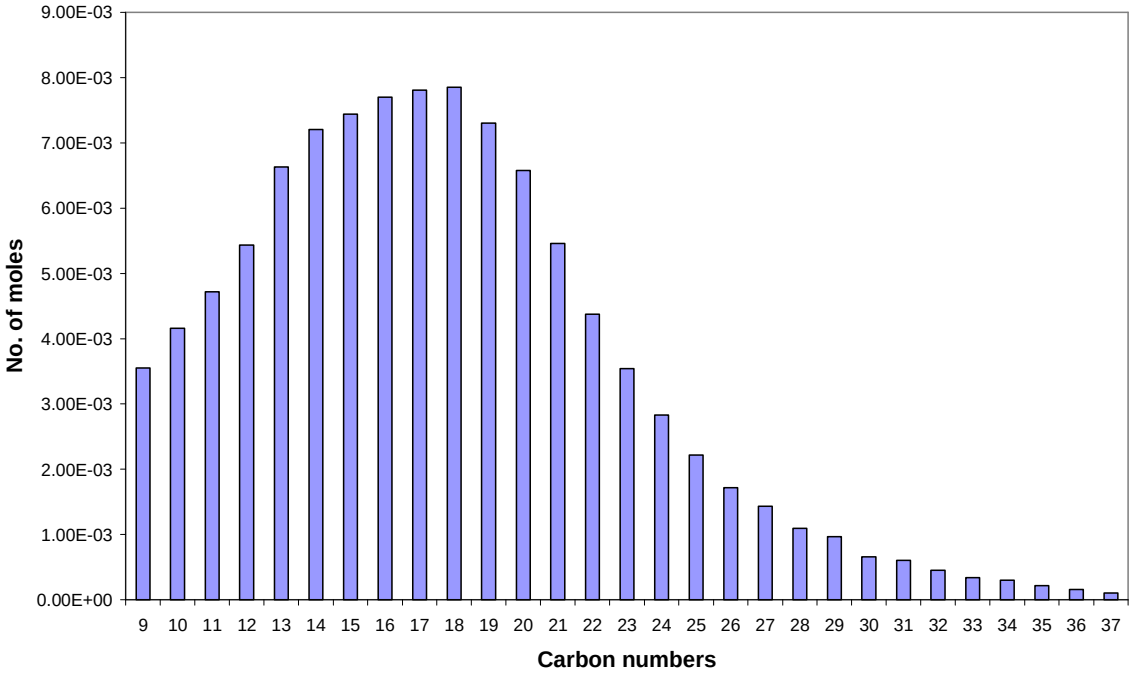

Figure 3-62: Hydrocarbon product distribution as a function of carbon number for CoAA wax sample at 764 hours TOS (T=240^{o}C)

3.6.4 Post FT Reaction analysis

3.6.4.1 Thermogravimetric analysis-Differential Scanning Calorimetry analysis

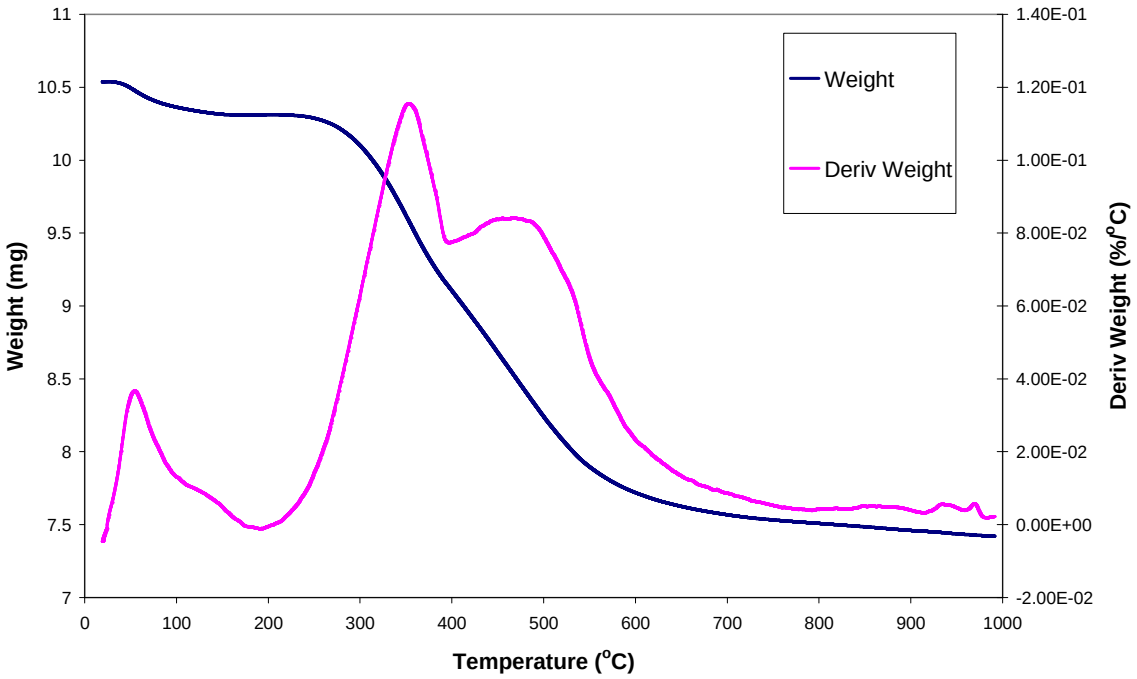

Figure 3-63: TGA weight and derivative weight profiles in oxygen for cobalt acetate on alumina post FT reaction.

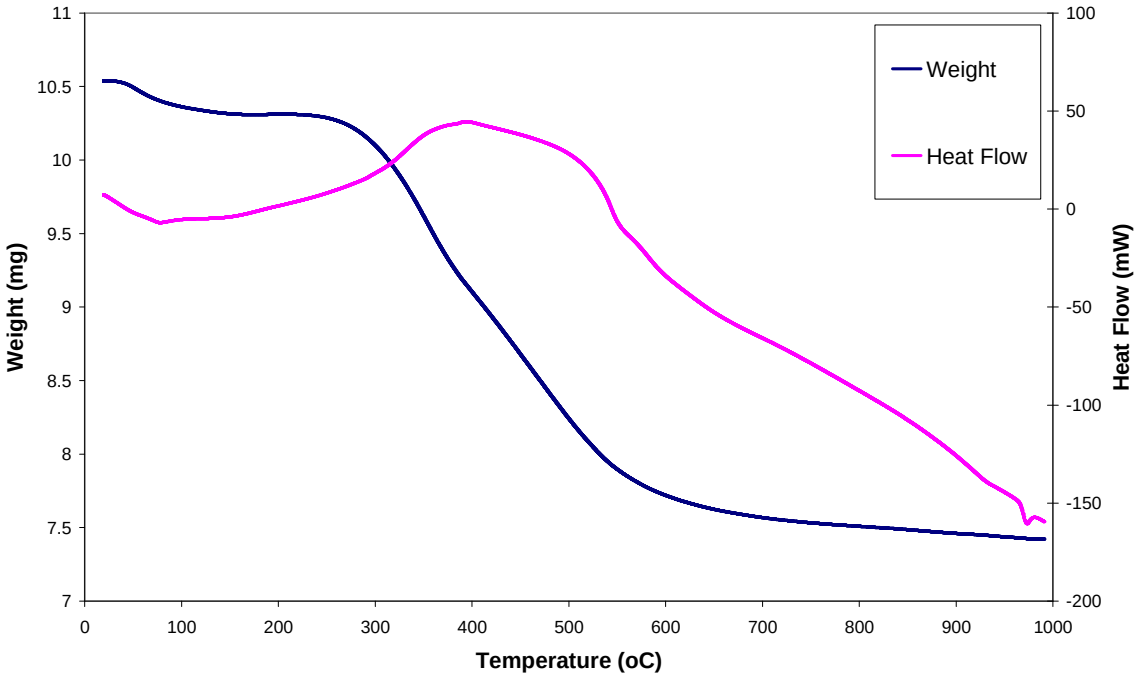

Figure 3-64: TGA-DSC weight and heat flow profiles in oxygen for cobalt acetate on alumina catalyst post FT reaction.

Results of the TGA-DSC analysis in oxygen of the CoAA catalyst post Fischer-Tropsch reaction are presented in figures 3-63 and 3-64. From the derivative weight profile it is clear that the main weight loss consists of two overlapping events with maxima at 355^{o}C and 470 ^{o}C. Smaller weight loss events are observed at 970 ^{o}C and below 200 ^{o}C.

From the heat flow data it is clear that the main part of the weight loss corresponds to a broad exotherm. The high temperature weight loss above 900^{o}C and the weight loss before 200^{o}C are seen to be endothermic.

3.6.4.1.1 Mass Spectrometric analysis

Figure 3-65 presents the mass spectrometric data in oxygen for the CoAA catalysts post FT reaction. It can be clearly seen that the initial weight loss before 200 ^{o}C is due to desorption of water. This is followed by the evolution of water, carbon dioxide and carbon monoxide which corresponds to the main weight loss seen in the TGA data. Beyond 650 ^{o}C only the evolution of water and carbon monoxide is observed. We also know from the mass spec data that the high temperature weight loss ~970 ^{o}C is accompanied by the evolution of oxygen (trace not shown).

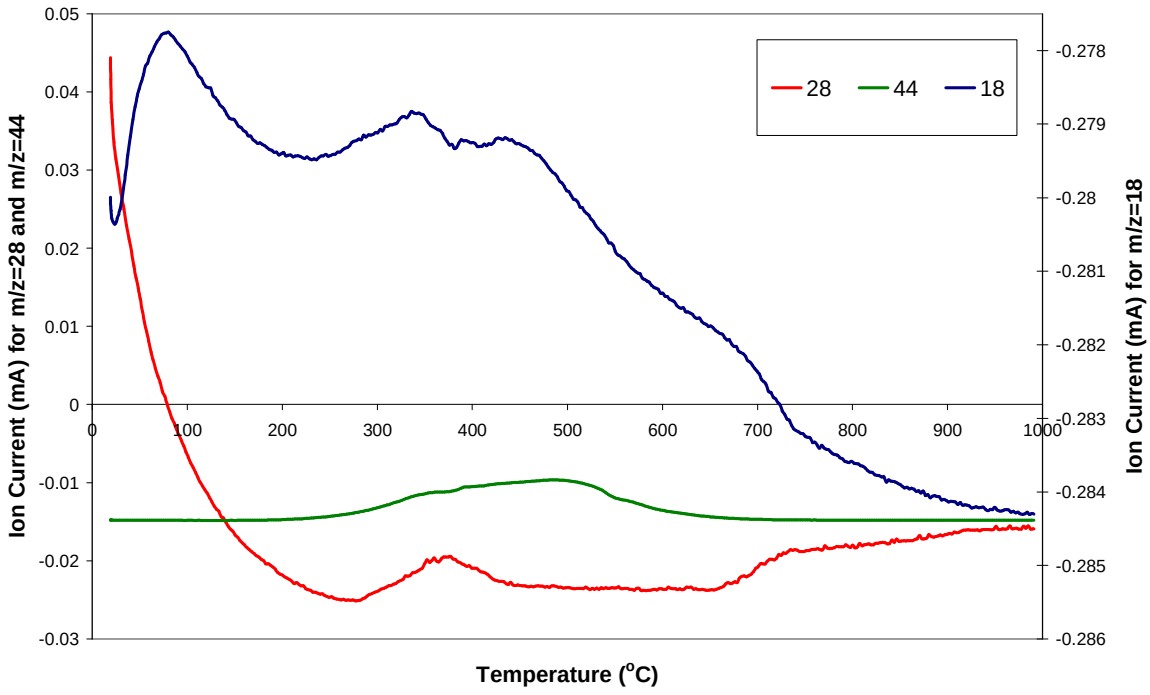

Figure 3-65: Mass spectrometric data of H_2O (m/z=18), CO (m/z=28) and CO_2 (m/z=44) in oxygen for cobalt acetate on alumina post FT reaction.

3.6.4.1.2 X-Ray Diffraction

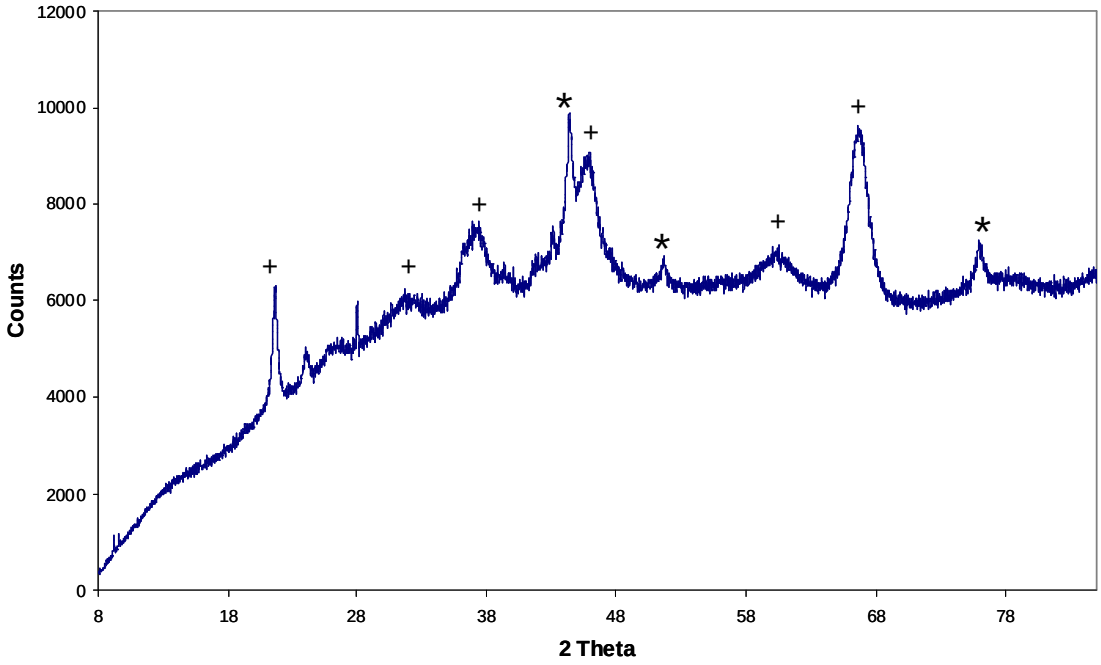

Figure 3-66: X-Ray diffraction pattern for cobalt acetate on alumina catalyst post FT reaction. The experimental error for cobalt particle size calculated from X-ray diffraction is less than +/- 1 nm.

The X-ray diffraction pattern of the CoAA catalyst post FT reaction is presented in figure 3-66. The pattern reveals the presence of metallic cobalt crystalline phase. The diameter of the cobalt crystallite was calculated from the width of the diffraction peak at $2\theta = 44.3^{o}$ and found to be 12 nm.

3.7 Cobalt nitrate on Zinc Oxide BP

This section relates to the characterisation of the cobalt nitrate on zinc oxide catalyst received from BP in the uncalcined form. The treatments in both argon and oxygen examined the calcination process of the catalyst. A calcination procedure was determined and the treatment in hydrogen examines the reduction of this calcined catalyst.

3.7.1 Argon treatment

3.7.1.1 Thermogravimetric Analysis-Differential Scanning Calorimetry analysis

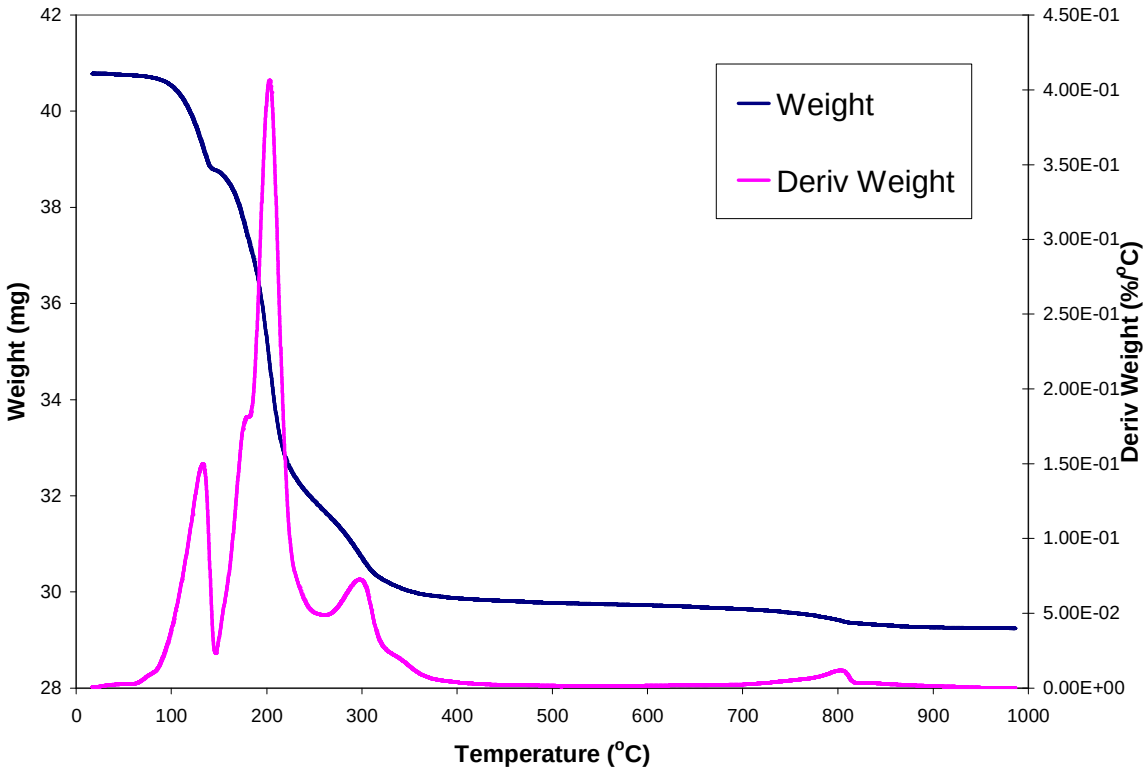

Figure 3-67: TGA weight and derivative profiles in argon for cobalt nitrate on zinc oxide.

The weight and derivative weight profiles in figure 3-67 show the decomposition of the cobalt nitrate on zinc oxide catalyst in argon. It is evident from these curves that the main part of the decomposition occurs as several overlapping events before 500 ^{o}C. A further, smaller weight loss event is observed at around 807 ^{o}C. From the heat flow data shown in figure 3-68 it is clear that all the weight loss

events are endothermic. The catalyst showed a weight loss of around 27% by 500 ^{o}C and around 28.3% by 1000 ^{o}C.

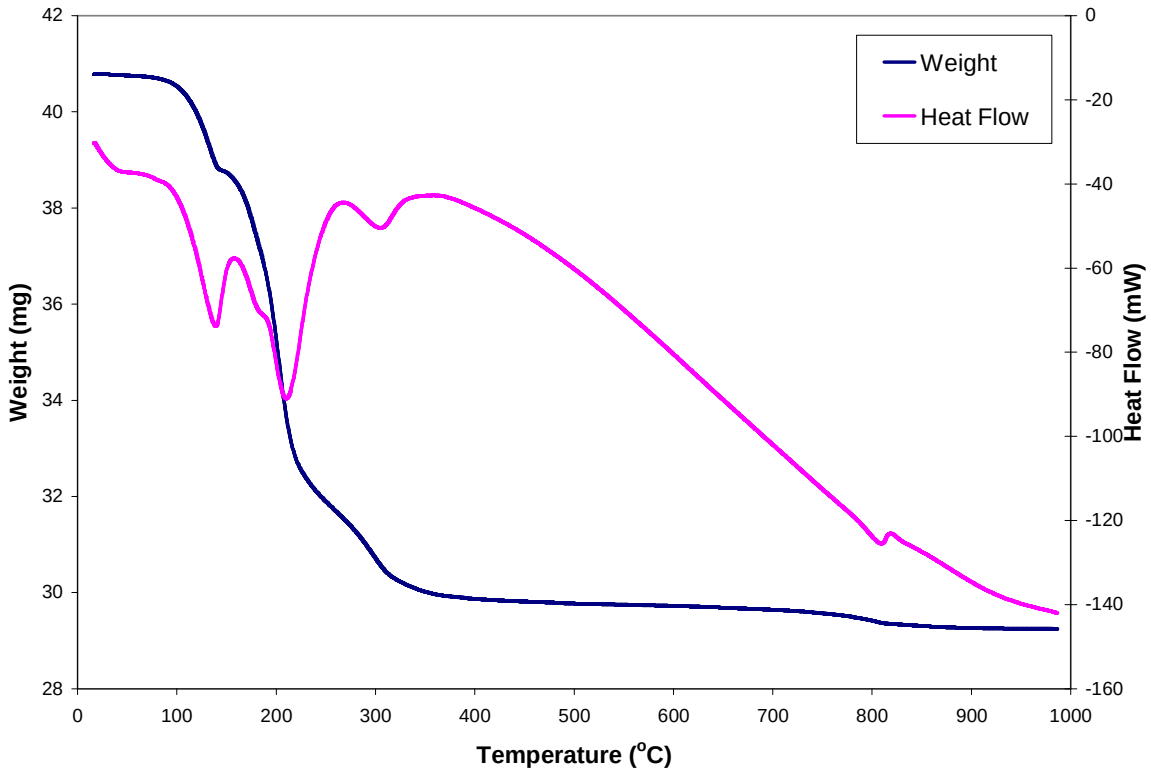

Figure 3-68: TGA-DSC weight and heat flow profiles in argon for cobalt nitrate on zinc oxide.

3.7.1.2 Mass spectrometric analysis

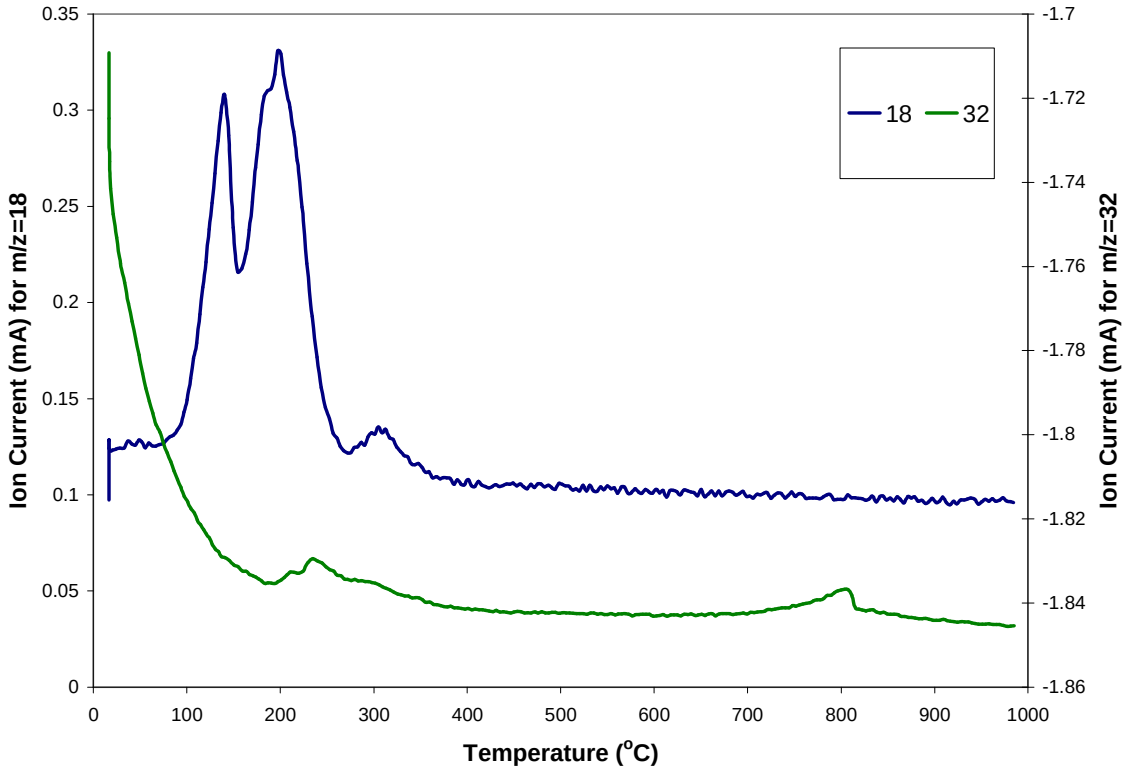

Figure 3-69: Mass spectrometric data of H_2O (m/z=18) and O_2 (m/z=18) in argon for cobalt nitrate on zinc oxide.

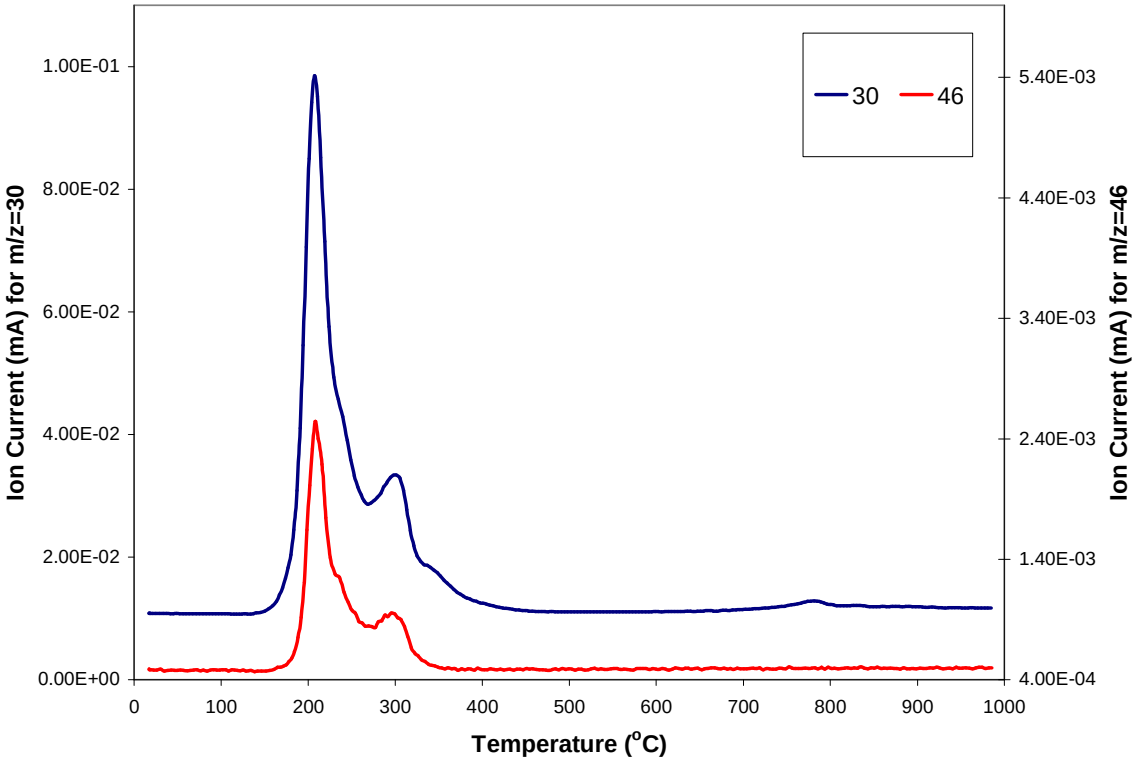

Figure 3-70: Mass spectrometric data of NO (m/z=30) and NO_2 (m/z=46) in argon for cobalt nitrate on zinc oxide.

Figures 3-69 and 3-70 show the mass spectrometric data collected simultaneously with the TGA-DSC data. When heated in argon the CoNZ catalyst decomposed via the evolution of water, oxygen, nitrogen monoxide, nitrogen dioxide and N_2O (not shown). Decomposition of the nitrate precursor appears to occur as two distinct events, at 208 ^oC and 300 ^oC. However, an evolution of N_2O (177 ^oC) and a shoulder of NO (~350 ^oC) suggest that there may be further components to the decomposition. From the mass spectrometric data of evolved O_2 (m/z=32), a small peak is observed at 807 ^oC, which corresponds to the high temperature event on the TGA-DSC profiles.

3.7.1.3 Hot-stage X-Ray Diffraction

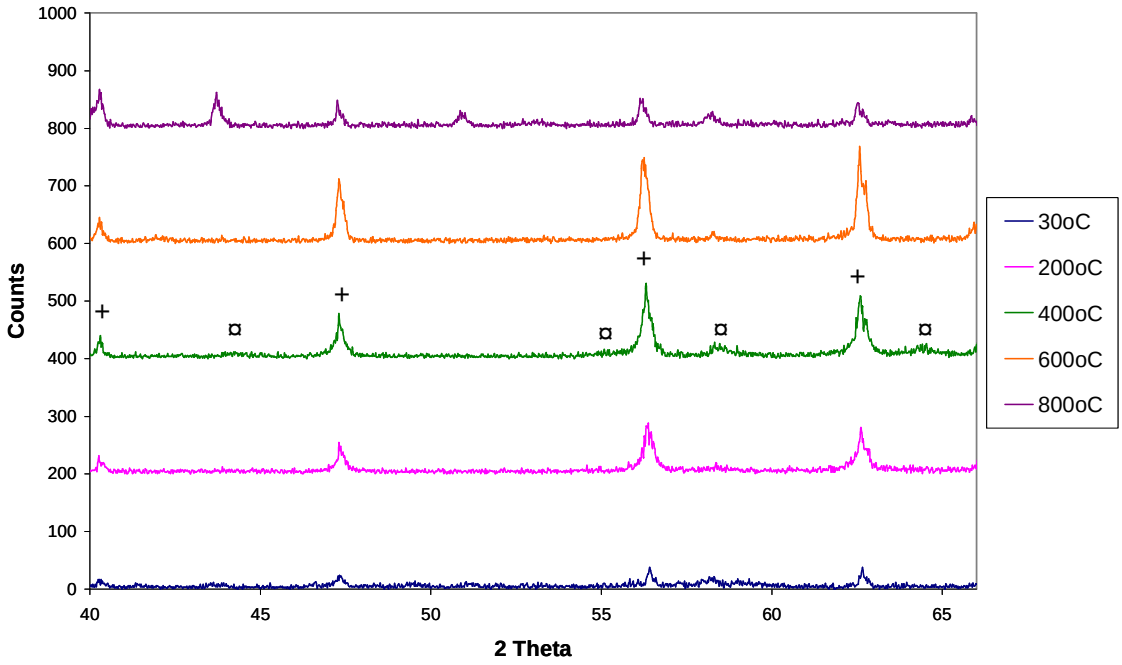

Figure 3-71: Hot-stage XRD pattern in argon for cobalt nitrate on zinc oxide. The phases denoted are (¤) Co_3O_4 and (+) ZnO. The XRD patterns are offset for clarity. The experimental error for Co_3O_4 crystallite size calculated from X-ray diffraction is less than +/- 1 nm.

Figure 3-71 shows the hot stage X-ray diffraction patterns for the CoNZ catalyst in argon. The XRD pattern at room temperature shows cobalt nitrate and zinc oxide as the only crystalline components. Upon heating to 200 ^oC the XRD patterns show reflections corresponding to the Co_3O_4 phase. The intensity of the reflections belonging to the Co_3O_4 phases was found to increase up to 400 ^oC; by 500 ^oC the intensity of these reflections had decreased and at 700 ^oC, the presence of metallic cobalt is observed.

The average size of Co_3O_4 crystals for this catalyst was calculated using the Scherrer method for the diffraction line situated at 58.4°. At 400 °C the Co_3O_4 crystallite size was found to be around 20 nm. Below 400 °C, particle size could not be determined by XRD.

3.7.2 Oxygen treatment

3.7.2.1 Thermogravimetric Analysis-Differential Scanning Calorimetry

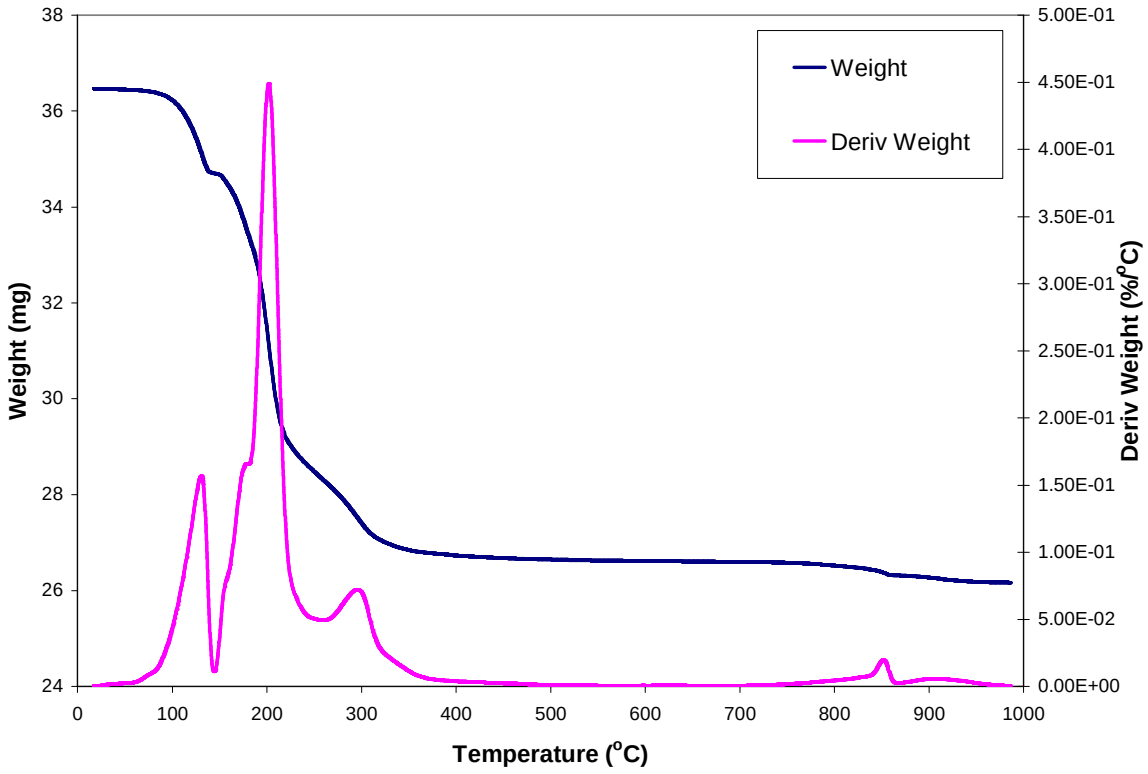

Figure 3-72: TGA weight and derivative weight profiles in oxygen for cobalt nitrate on zinc oxide.

Figure 3-72 and 3-73 present the TGA-DSC data for the CoNZ catalyst in oxygen. It can be seen that weight loss occurs over two main regions. The initial and more significant weight loss is complete by around 500 °C with a further weight loss of around 1.3% occurring at 855 °C. All weight losses exhibited for the CoNZ catalyst were endothermic. The total weight loss was around 28.2% for this sample.

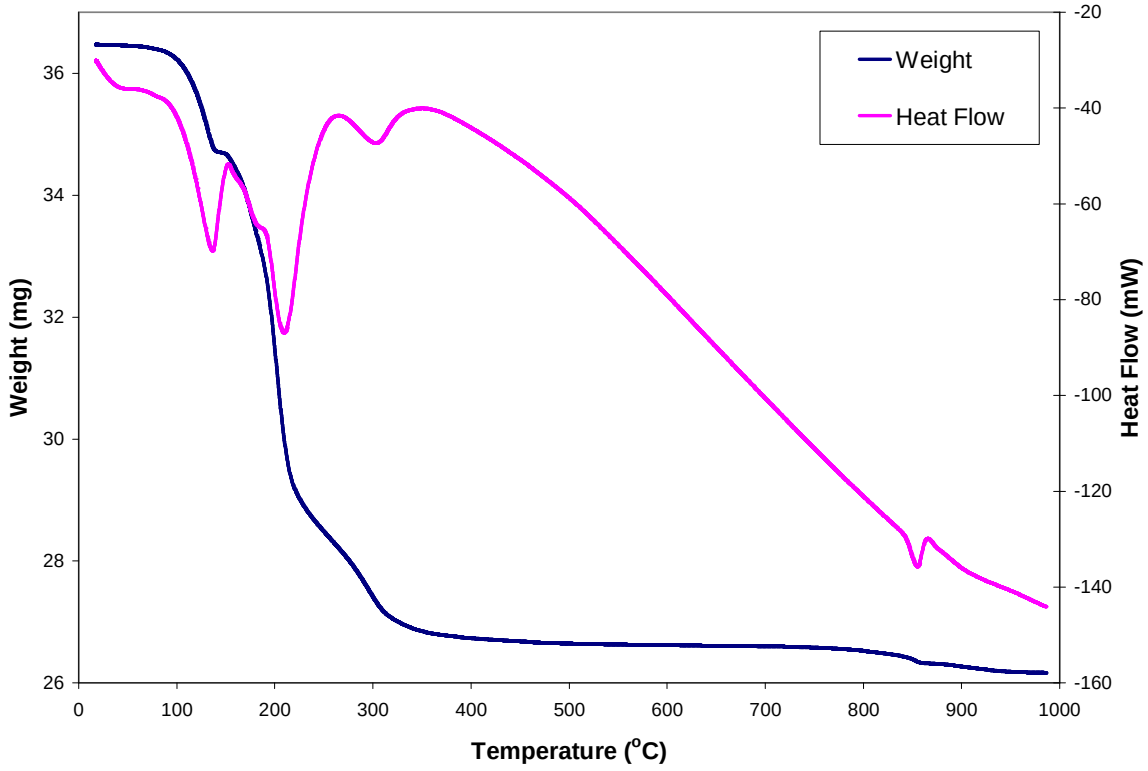

Figure 3-73: TGA-DSC weight and heat flow profiles in oxygen for cobalt nitrate on zinc oxide.

3.7.2.2 Mass spectrometric analysis

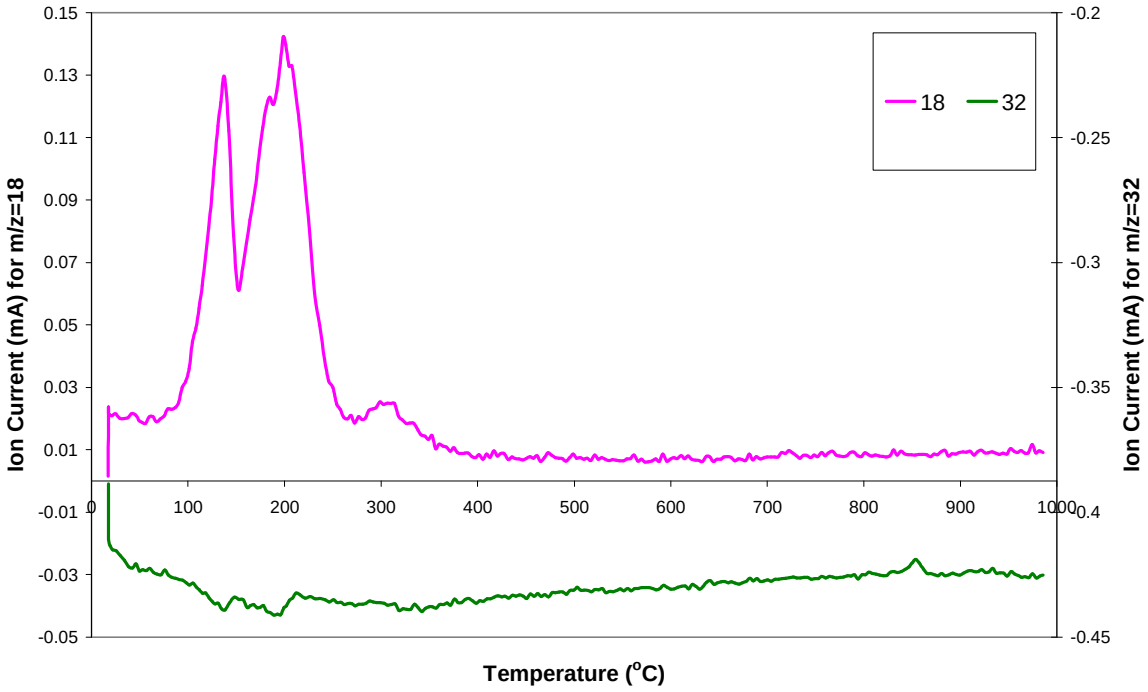

Figure 3-74: Mass spectrometric data of H_2O (m/z=18) and O_2 (m/z=32) in oxygen for cobalt nitrate on zinc oxide.

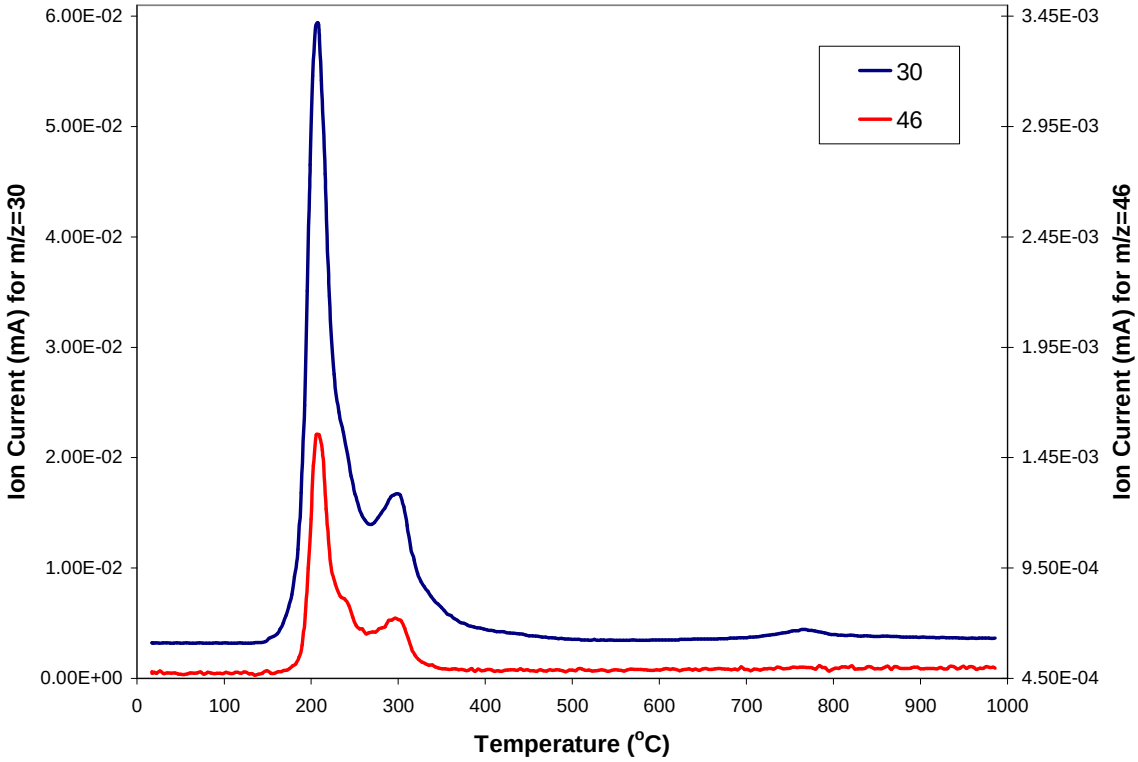

Figure 3-75: Mass spectrometric data of NO (m/z=30) and NO_2 (m/z=46) in oxygen for cobalt nitrate on zinc oxide.

Mass spectrometry data showed that the decomposition in oxygen corresponded to the uptake of oxygen and evolution of water, nitrogen monoxide, nitrogen dioxide and N_2O. Above 500 °C, the evolution of oxygen and nitrogen monoxide was detected.

3.7.2.3 Hot-stage X-Ray diffraction

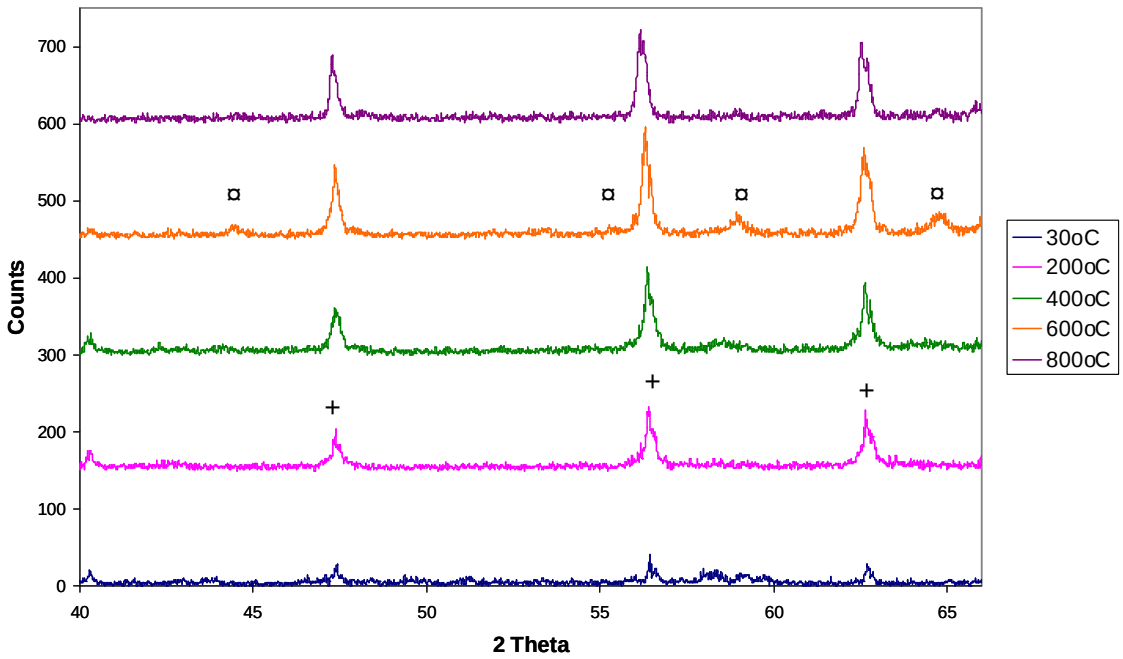

Figure 3-76: Hot-stage XRD patterns in oxygen for cobalt nitrate on zinc oxide. Phases denoted are (¤) Co_3O_4 and (+) ZnO. The XRD patterns are offset for clarity.

The hot-stage XRD patterns for the CoNZ catalyst in oxygen are shown in figure 3-76. Co_3O_4 is first observed at 200 ^oC and becomes more intense to around 700 ^oC. Crystallite size of Co_3O_4 at different temperatures was measured as described previously and the results presented in table 3-4. There is a variation of the particle size of the Co_3O_4 for this sample, ranging from 11 nm to 25 nm.

Table 3-4: Co_3O_4 crystallite size as determined by hot-stage XRD in oxygen of cobalt nitrate on zinc oxide. The experimental error for Co_3O_4 crystallite sizes calculated from X-ray diffraction is less than +/- 1 nm.

Temperature (^oC)	Co_3O_4 Crystallite size (nm)
300	21
400	16
500	11
600	25
700	25

3.7.2.4 Effect of heating rate

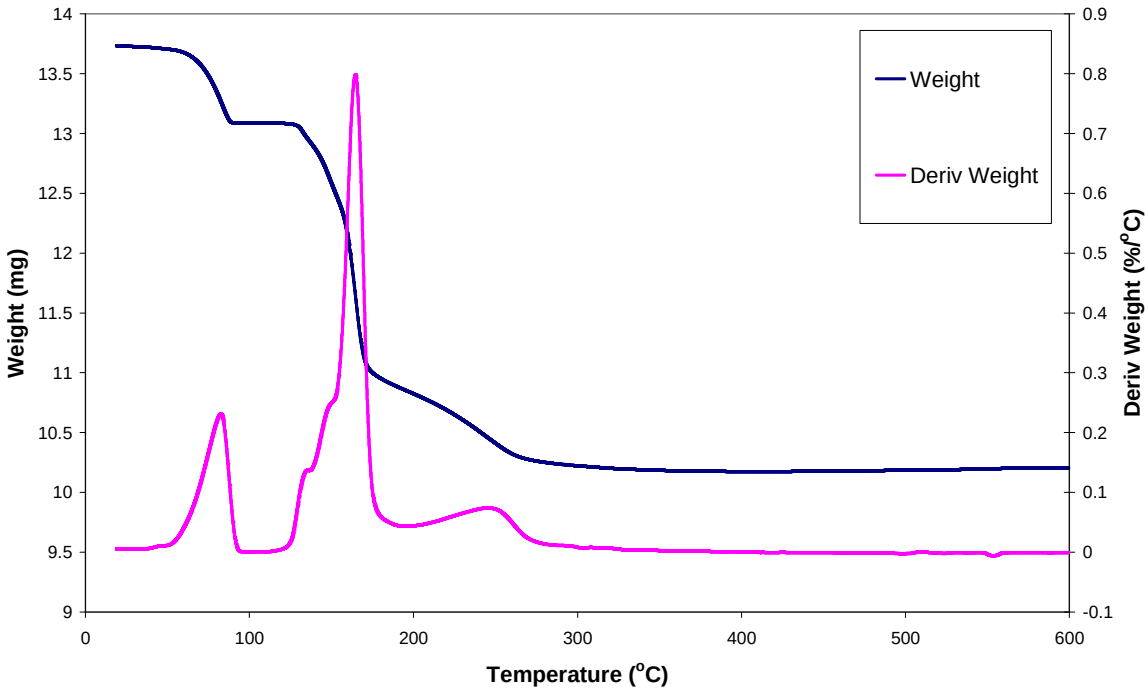

Figure 3-77: TGA weight and derivative weight profiles in oxygen for the cobalt nitrate on zinc oxide at a heating rate of 1 $^oC\ min^{-1}$.

The TGA weight and derivative weight profiles for CoNZ catalyst at 1 ^{o}C min^{-1} in oxygen is shown in figure 3-77. It can be observed that decreasing the heating rate has caused the decomposition to be complete at a much lower temperature.

From this data a suitable temperature for temperature for calcination was determined and is as follows:

- 1 ^{o}C min^{-1} to 300 ^{o}C and hold for 120 minutes in 2% Oxygen-Argon at 40 ml min^{-1}

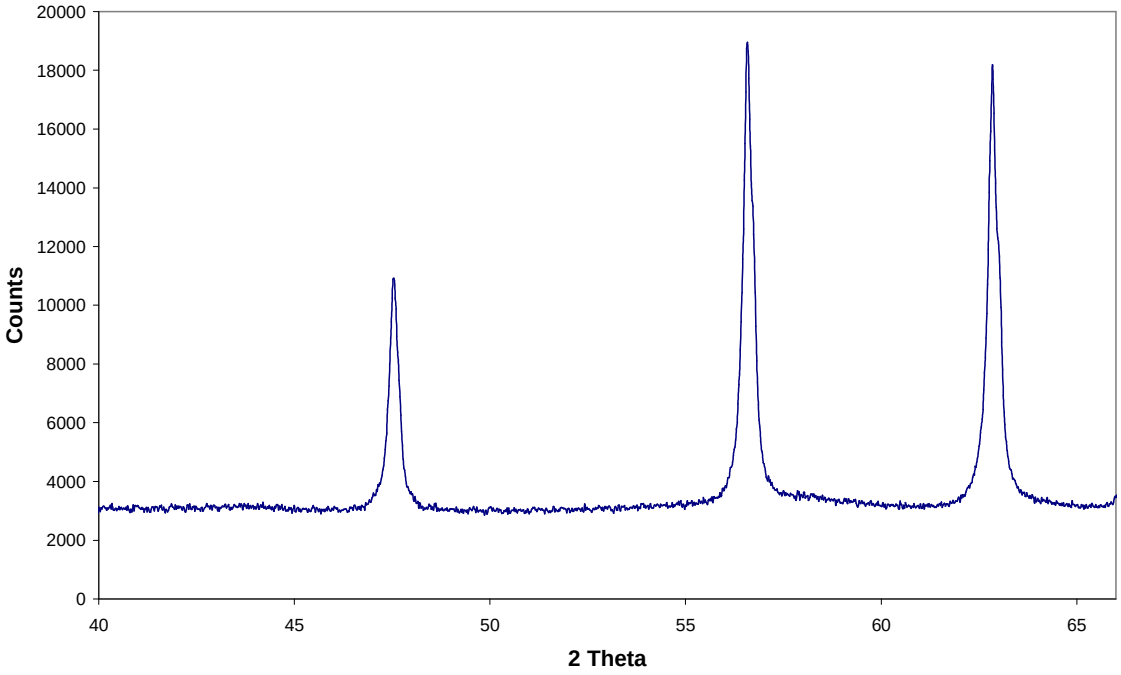

Figure 3-78: X-ray diffraction pattern for calcined CoNZn catalyst

XRD pattern of the calcined CoNZ catalyst is shown in figure 3-78. No discernable peaks for any cobalt oxide phase could be identified. This suggests that either no crystalline cobalt oxide was present or the cobalt oxide is highly dispersed and is below the limits of XRD detection. Characteristic peaks at 47.5^{o}, 56.6^{o} and 62.8^{o} ascribed to the ZnO support can be observed.

3.7.2.5 High Resolution Transmission Electron Microscopy (HRTEM)

TEM images of the calcined CoNZ catalyst are shown in figure 3-79. A low magnification, bright field image of the CoNZ catalyst is shown in Figure 3-79a.

Since the atomic masses of Co and Zn do not differ considerably from one another it is not possible to distinguish which areas belong to the Co component and which belong to the support material. Contrast in the bright field images appear to be due to uneven sample thickness. Therefore to make a distinction between cobalt oxide and zinc oxide it was necessary to use examination of lattice spacing at higher magnification. In figure 3-79b the dark regions can be seen to contain lattice fringe spacing measuring 4.6 Å. The area highlighted in figure 3-79c can be seen as a much higher resolution image in figure 3-79d which allowed again for the identification of lattice spacing corresponding to Co_3O_4. The shapes of the particles were relatively similar, with most in the range 20-35 nm (length in the elongated direction).

Figure 3-79:,TEM micrographs of the calcinced cobalt nitrate on zinc oxide catalyst. (a) Low magnification and (b-e) higher magnification images.

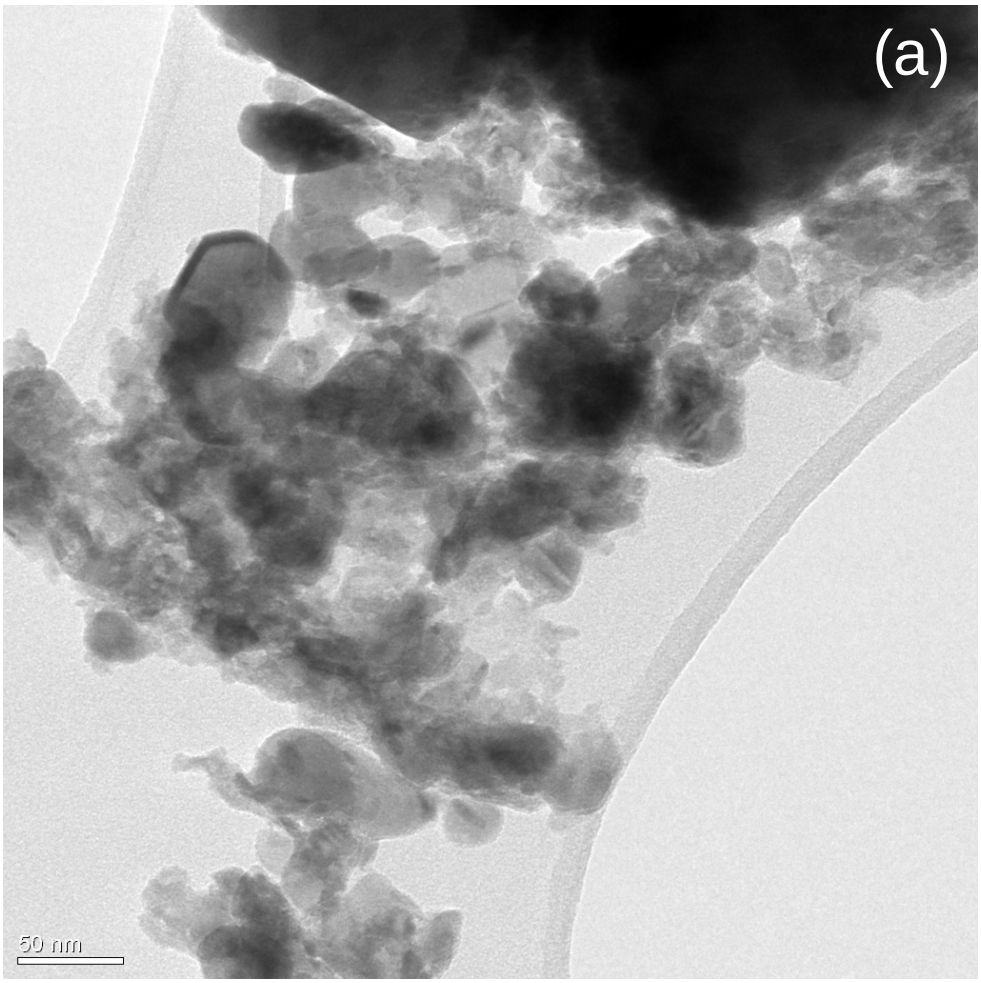

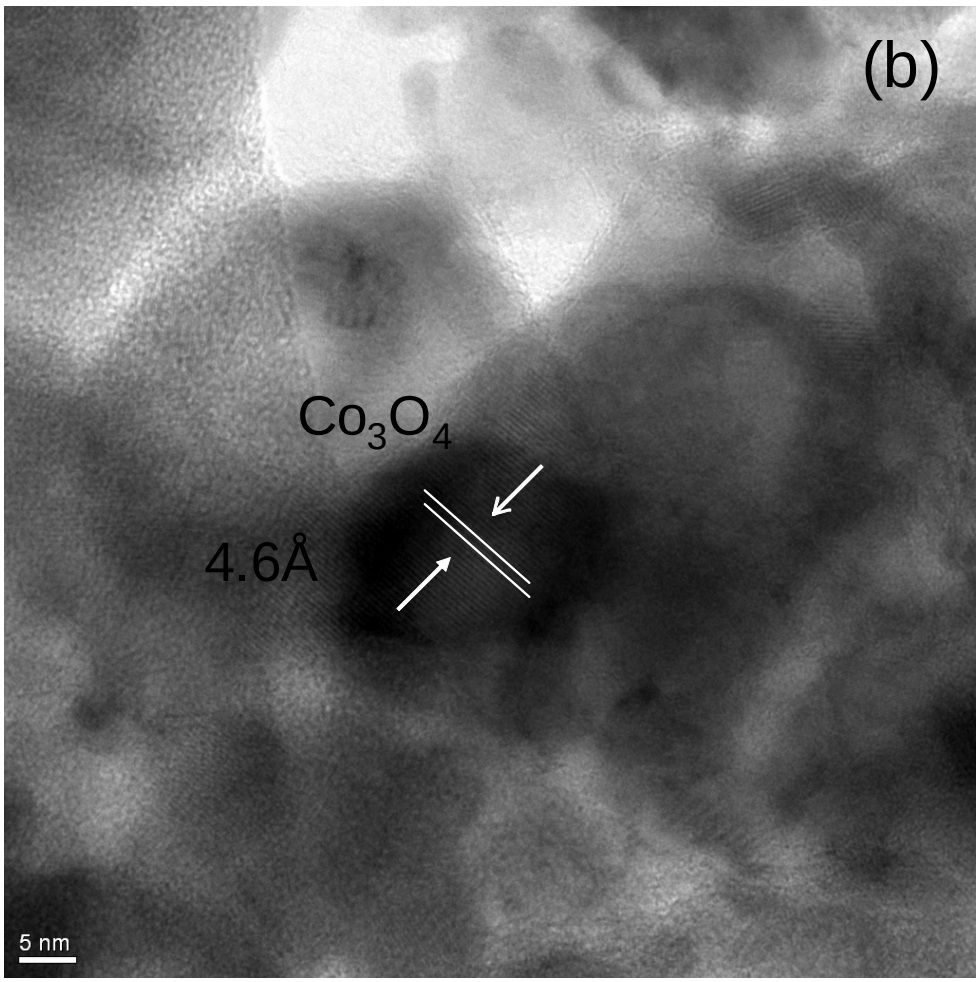
(b)
Co_3O_4
4.6Å
5 nm

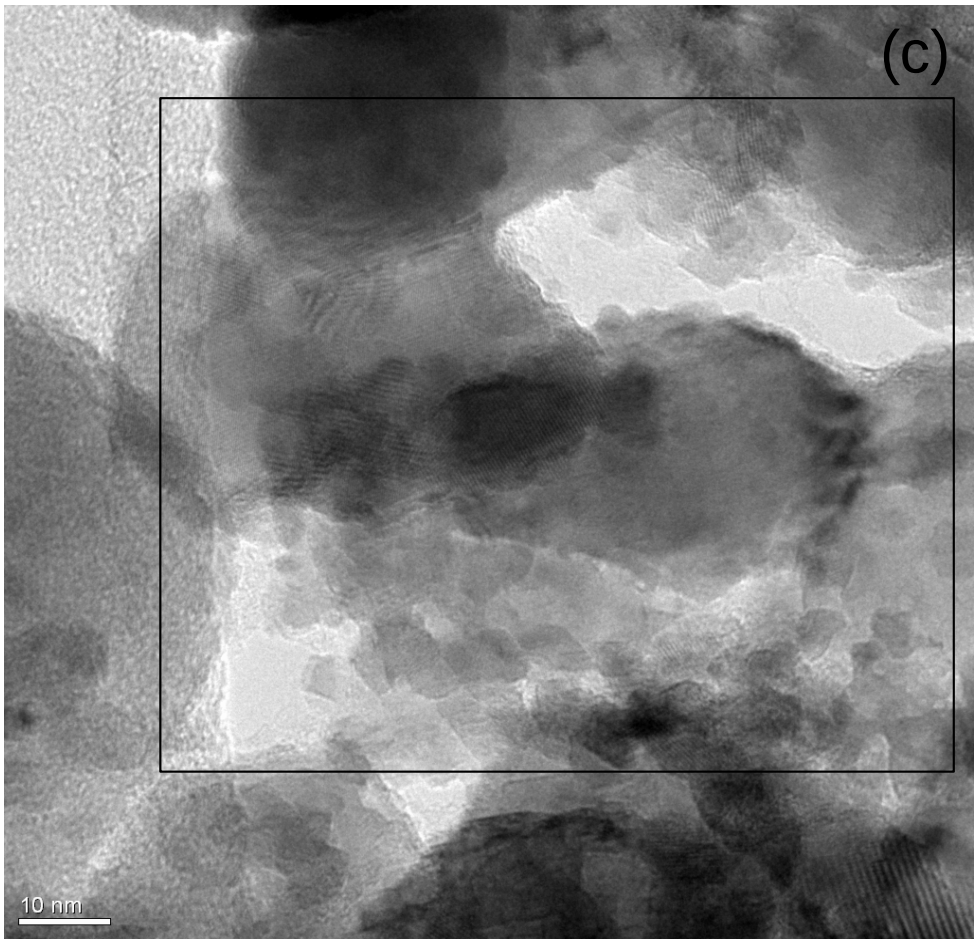
(c)
10 nm

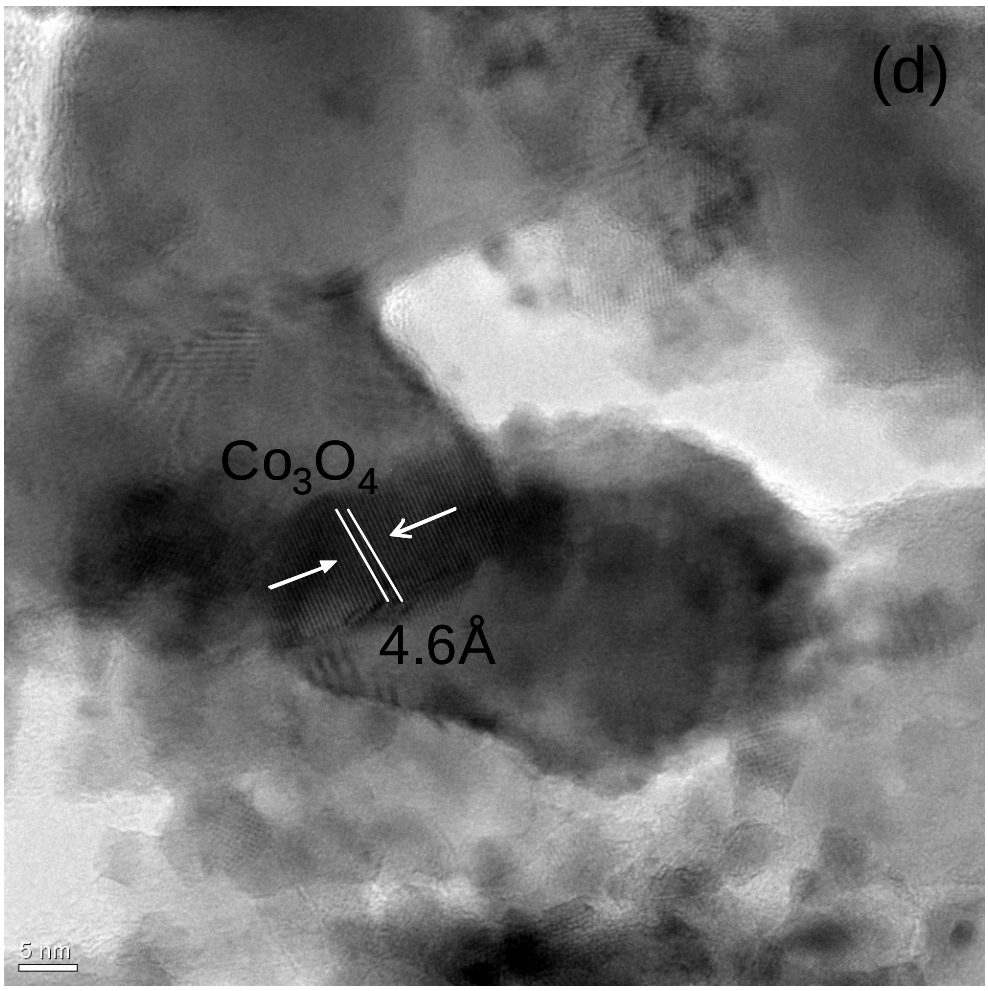
(d)
Co_3O_4
4.6Å
5 nm

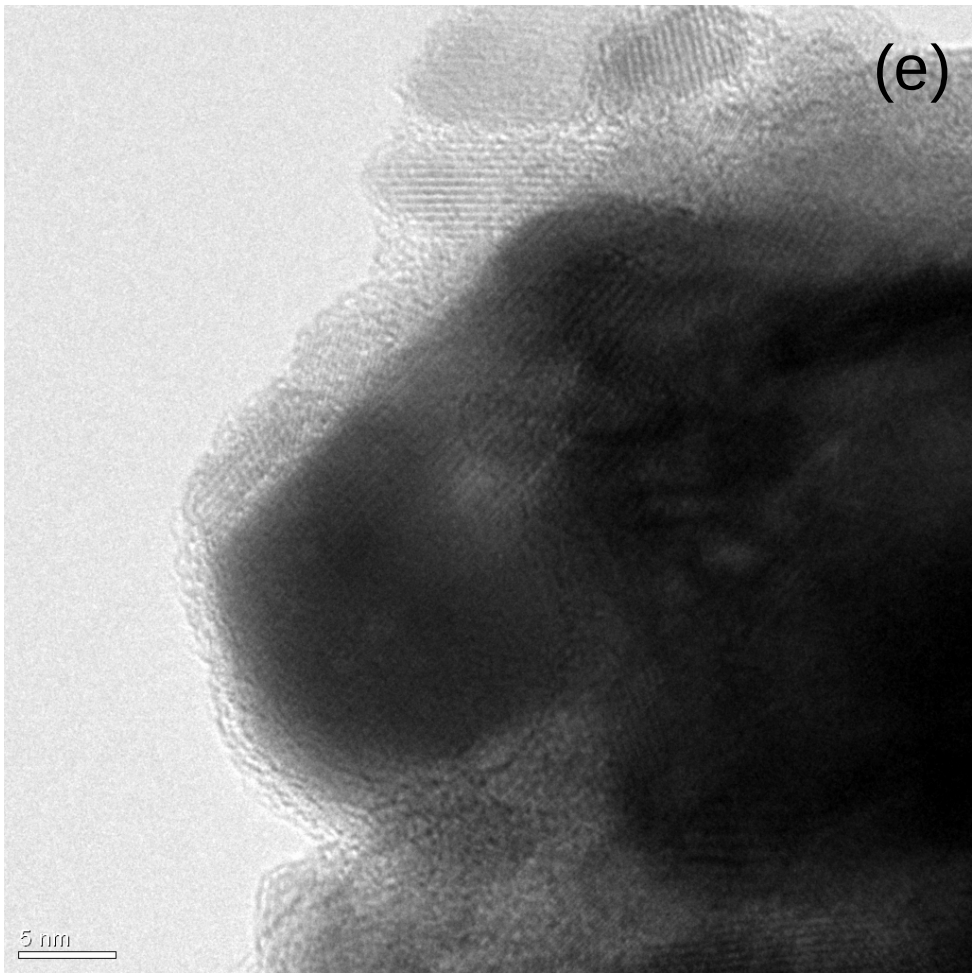
(e)
5 nm

3.7.3 Hydrogen treatment (following calcination in oxygen)

3.7.3.1 Thermogravimetric analysis-Differential Scanning Calorimetry

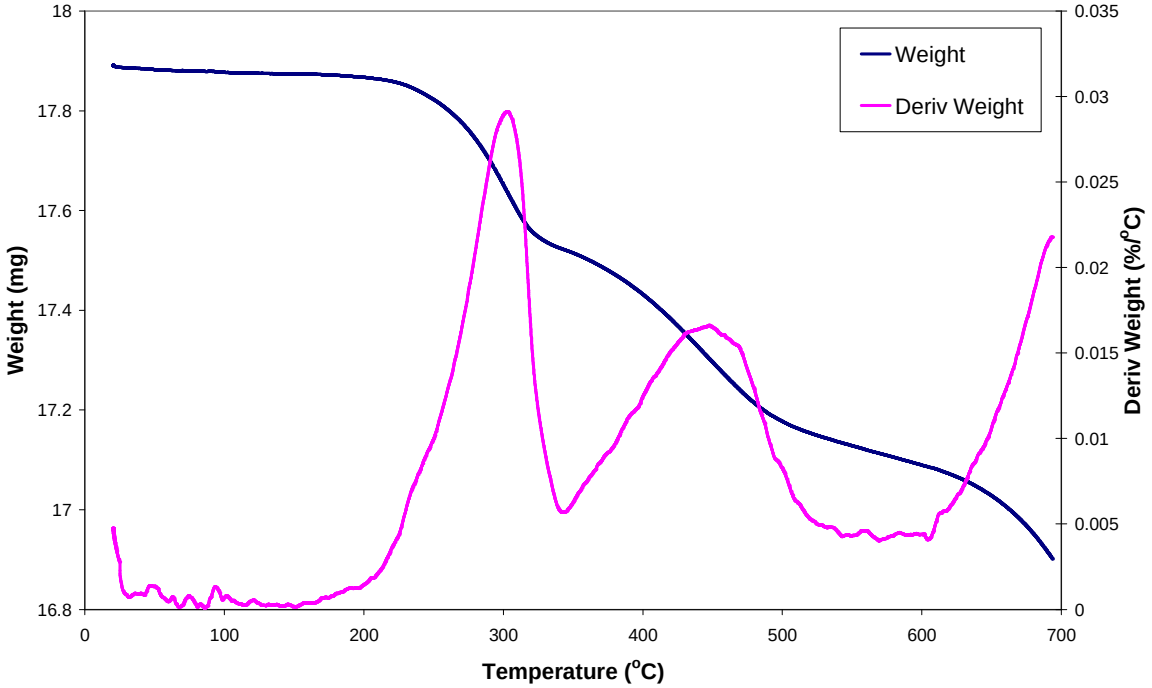

Figure 3-80: TGA weight and derivatie weight profiles in hydrogen (after calcination in oxygen) for cobalt nitrate on zinc oxide.

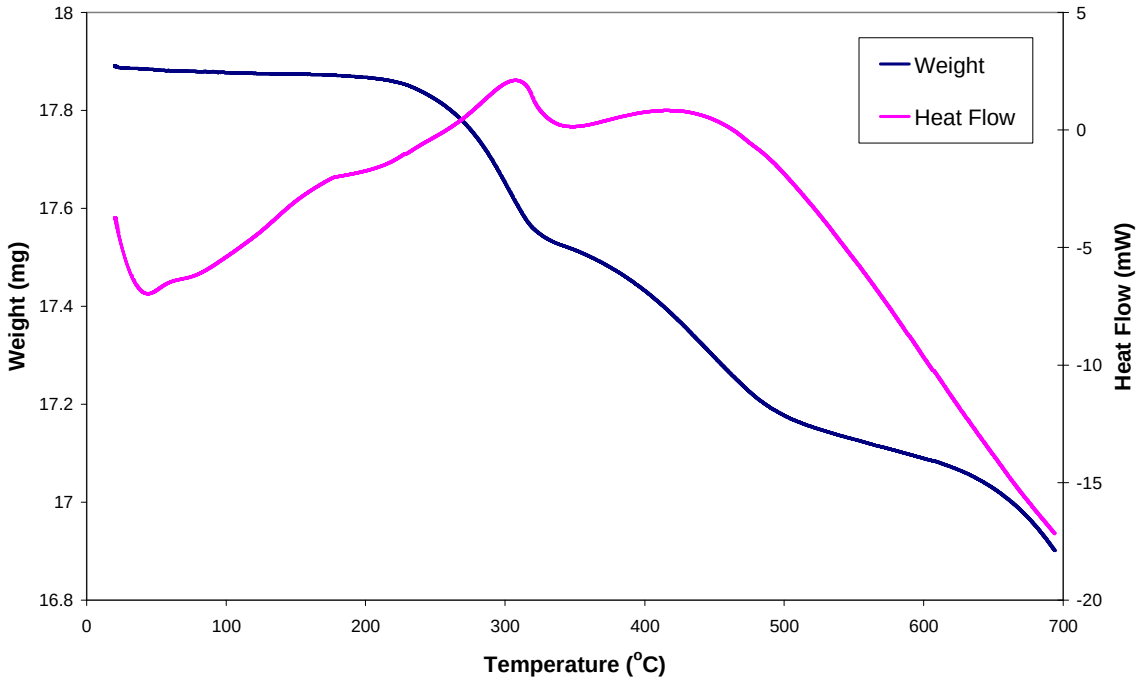

Figure 3-81: TGA-DSC weight and heat flow profiles in hydrogen (after calcination in oxygen) for cobalt nitrate on zinc oxide.

Figures 3-80 and 3-81 present the TGA-DSC data for the calcined CoNZ catalyst in hydrogen. Two main weight losses are apparent with maxima at 305 ^{o}C and 450 ^{o}C and are most probably due to the reduction of the supported cobalt oxide species. The observed weight losses were 1.9 % and 2.3 % for the first and second reduction events, respectively.

3.7.3.2 Hot-stage X-ray Diffraction (XRD)

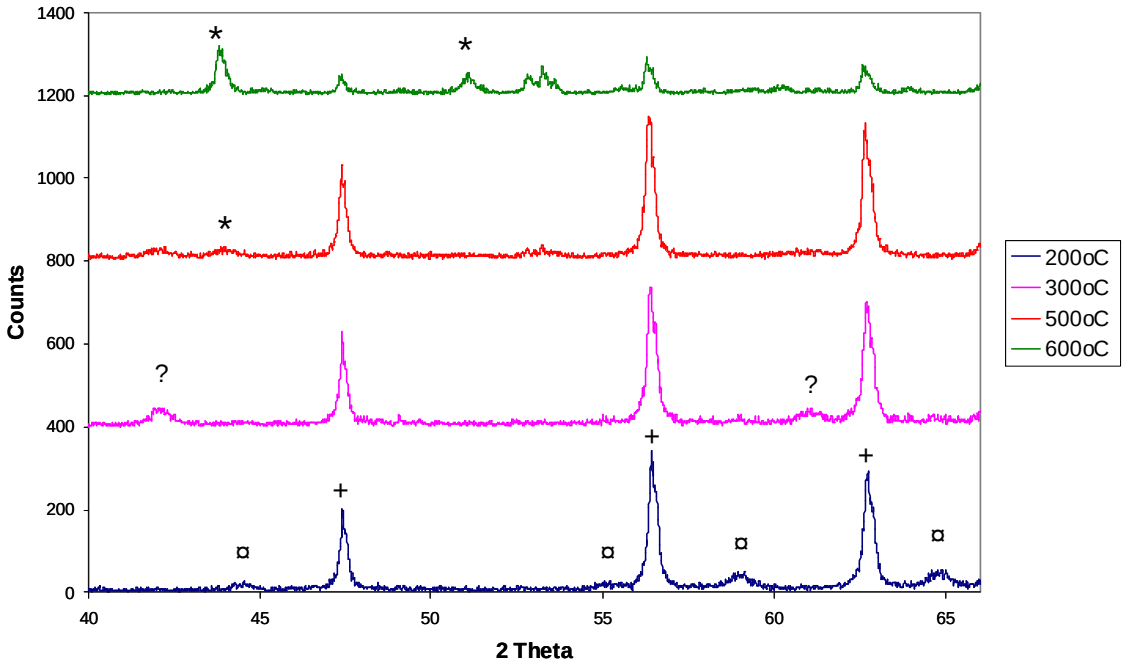

Figure 3-82: Hot-stage XRD in hydrogen (after calcination in oxygen) for cobalt nitrate on zinc oxide BP. The phases denoted are (¤) Co_3O_4, (Δ) CoO, (*) metallic Co and (+) ZnO.

The *in-situ* hot-stage XRD patterns in figure 3-82 show the reduction of Co_3O_4 to metallic cobalt. Between 30 ^{o}C and 200 ^{o}C the location of the peaks, confirm that Co_3O_4 was the only crystalline phase of cobalt present. Peaks at 42.0^{o} and 61.0^{o} confirm the presence of CoO from 300 ^{o}C to 500 ^{o}C, with metallic cobalt appearing at 400-600 ^{o}C. It should be noted that the hot-stage XRD results are consistent with the mass spectrometric data showing the reduction of Co_3O_4 to CoO and its subsequent reduction at higher temperatures to metallic cobalt. At 500 ^{o}C, the XRD reflections relating to the cobalt metal were so broad that accurate estimation of size was not possible.

3.7.3.3 Effect of heating rate

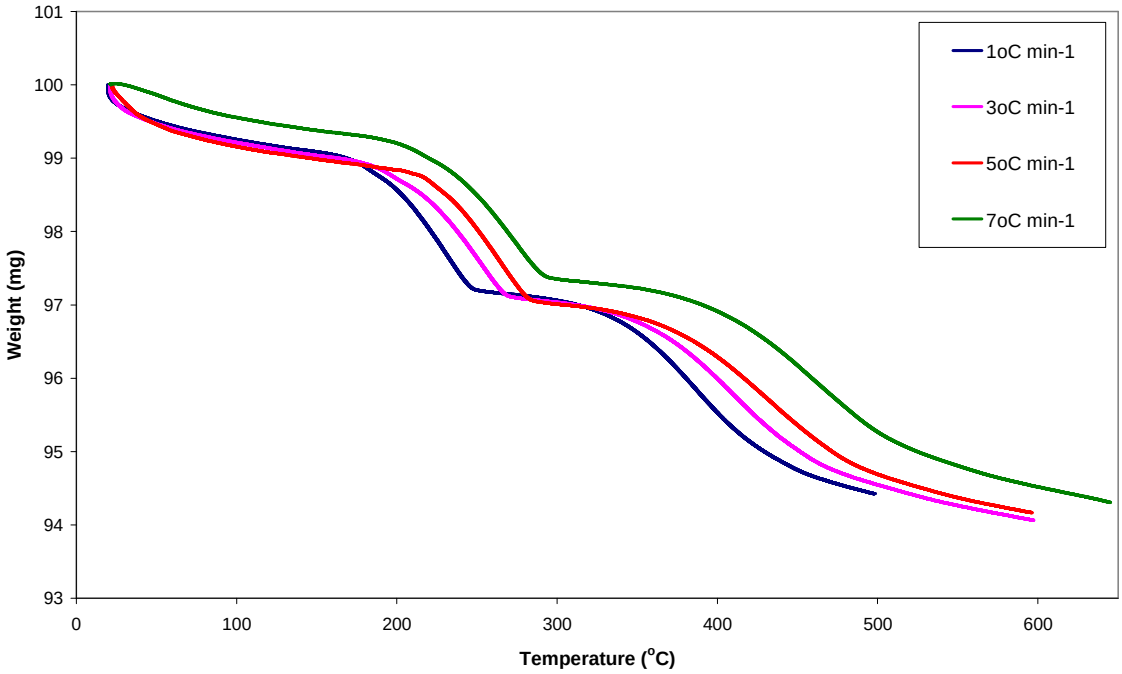

Figure 3-83: TGA weight profiles in hydrogen for calcined cobalt nitrate in zinc oxide BP at different heating rates.

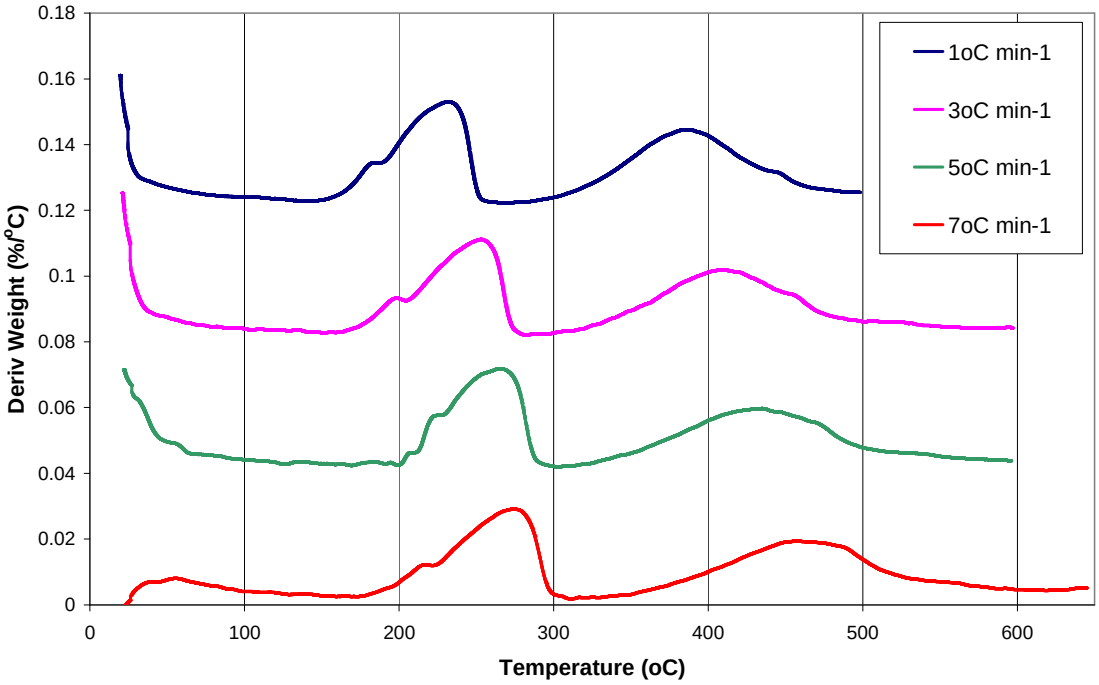

Figure 3-84: TGA derivative weight profiles in hydrogen for the calcined cobalt nitrate on zinc oxide BP at different heating rates.

Figures 3-83 and 3-84 present a series of TGA weight and derivative weight profiles for calcined CoNZ catalyst in hydrogen, obtained at various heating rates

of 1, 3, 5 and 7 ^{o}C min^{-1}. With increasing heating rate it can be observed that the derivative weight maxima for both the first and second reduction events increased.

3.7.3.4 CO chemisorption

CO-pulse chemisorption experiments were carried out on the calcined CoNZ catalyst as described in section 2.3.5. The amount of adsorbed CO was 28 µmol/g_{cat}. Assuming a stoichiometry of between CO and surface cobalt is 1:1, the value of metal dispersion calculated from the chemisorbed CO is 1.7 %.

3.7.4 FT reaction

3.7.4.1 Conversion

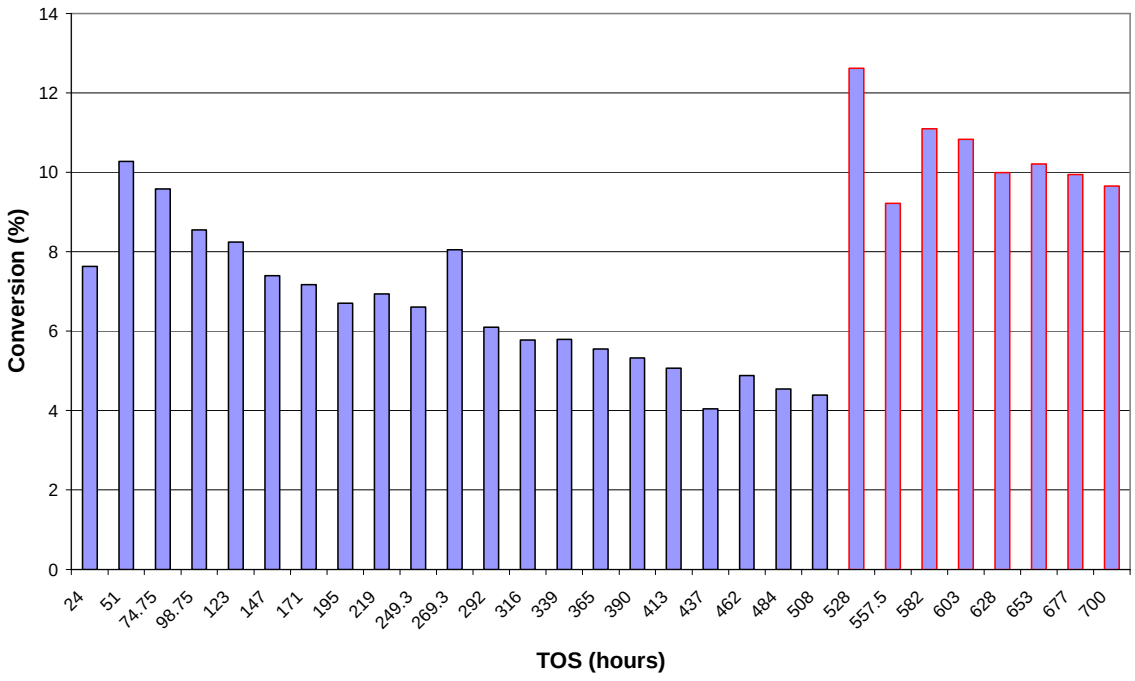

Figure 3-85: CO conversion as a function of time-on-stream for calcined CoNZ catalyst at a temperature of 220 ^{o}C and 240 ^{o}C. The experimental error for the conversion is estimated to be +/- 5%.

Figure 3-85 presents the CO conversion against time-on-stream for the CoNZ catalyst. The reaction temperature was increased after 508 hours TOS from 220 ^{o}C to 240 ^{o}C. Overall, at 220 ^{o}C, the conversion decreased from ~10 % CO conversion at 51 hours TOS to 4-5 % CO conversion over a run time of 437 hours. Upon raising the reaction temperature to 240 ^{o}C, the conversion increased to ~13

% before decreasing gradually to 10 % after 120 hours at the elevated temperature (628 hours total).

3.7.4.2 Deactivation

Using the equation shown in section 2.5.2, deactivation constants were calculated at 220 ^{o}C and 240 ^{o}C. The deactivation was calculated in the range 51-413 hour TOS and 528-700 hours TOS for 220 ^{o}C and 240 ^{o}C, respectively. The calculated values for the calcined CoNZ catalyst were 0.0019 hr^{-1} at 220 ^{o}C and 0.0017 hr^{-1} at 240 ^{o}C.

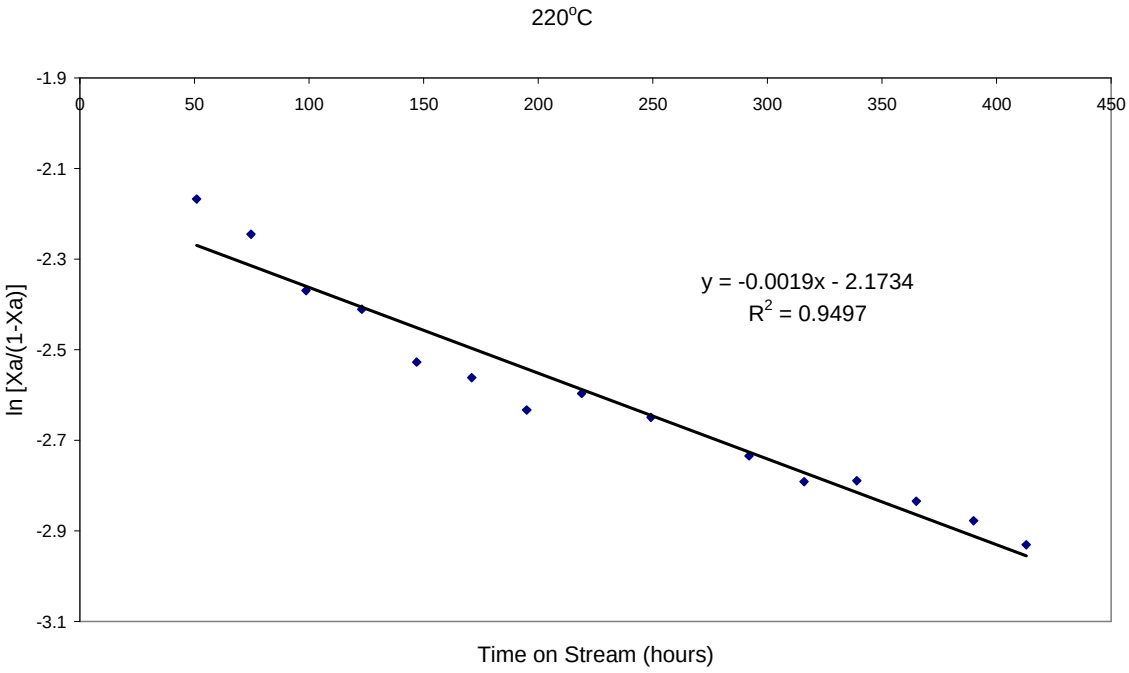

Figure 3-86: Graph of ln[Xa/(1-Xa)] versus time on stream for CoNZ FT reaction at 220 ^{o}C.

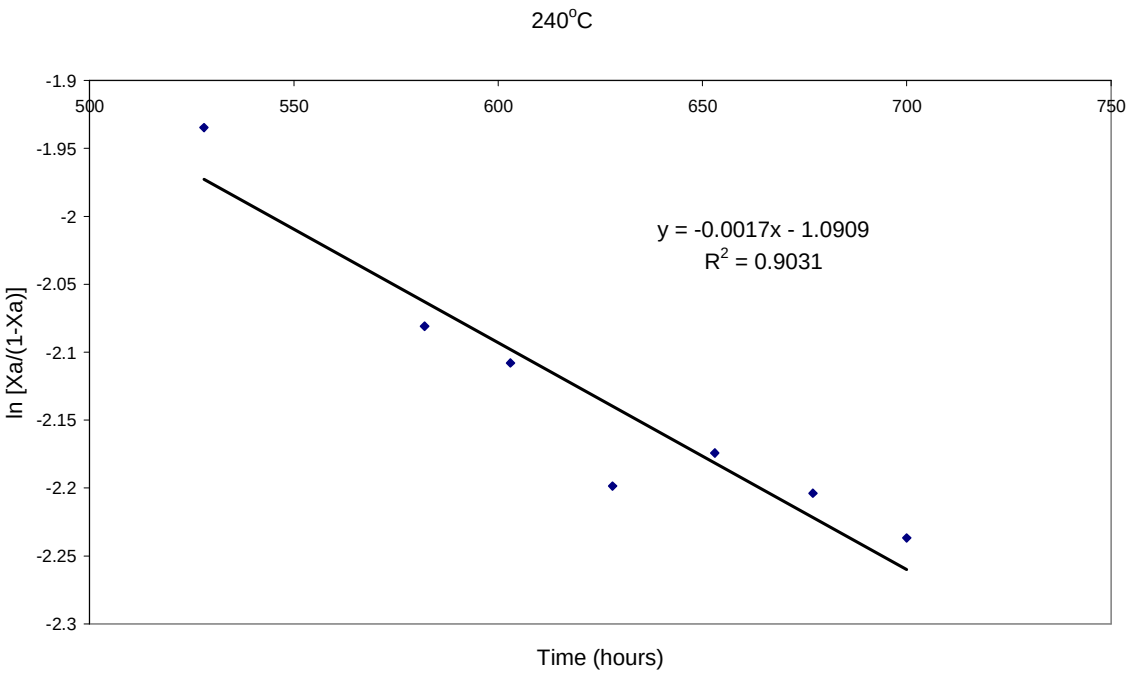

Figure 3-87: Graph of ln[Xa/(1-Xa)] versus time on stream for CoNZ FT reaction at 240 °C.

3.7.4.3 Alpha Values

The alpha values obtained for the calcined CoNZ catalyst as a function of TOS at 220 °C and 240 °C are shown in figures 3-88 and 3-89, respectively. At 220 °C, it can be observed that the alpha value increased with time on stream and reached an average value of 0.92 at around 365 hours TOS. On increasing the temperature to 240 °C the alpha value decreases to an average of 0.87.

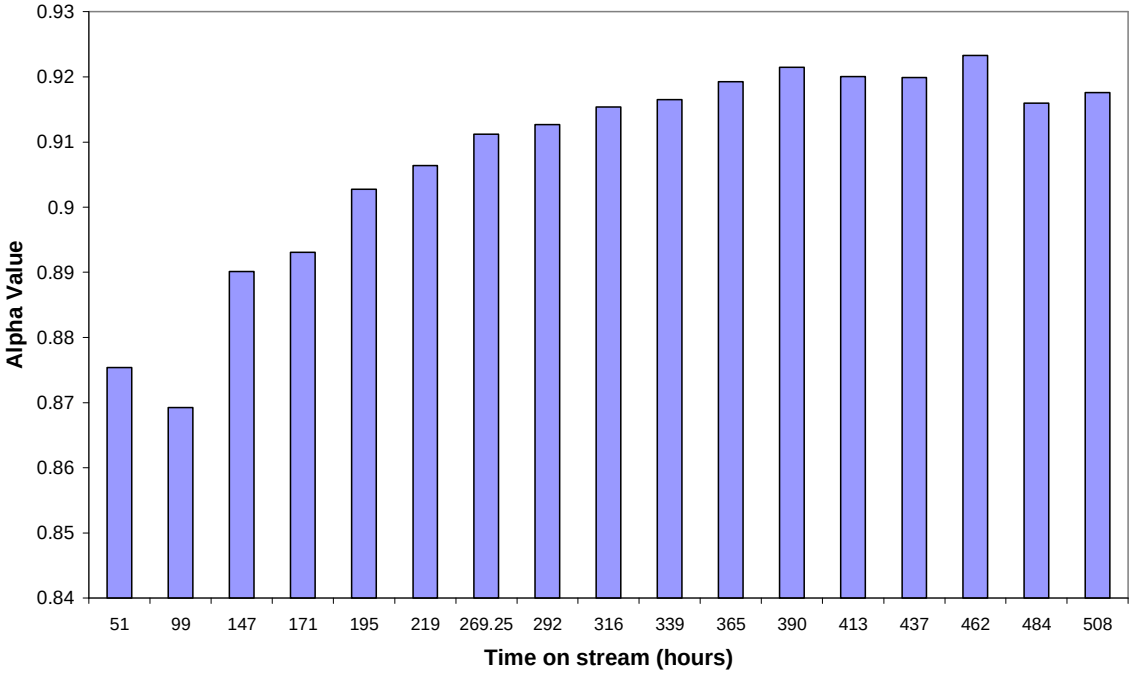

Figure 3-88: Alpha values versus time on stream for CoNZ catalyst at reaction temperature of 220 ^{o}C

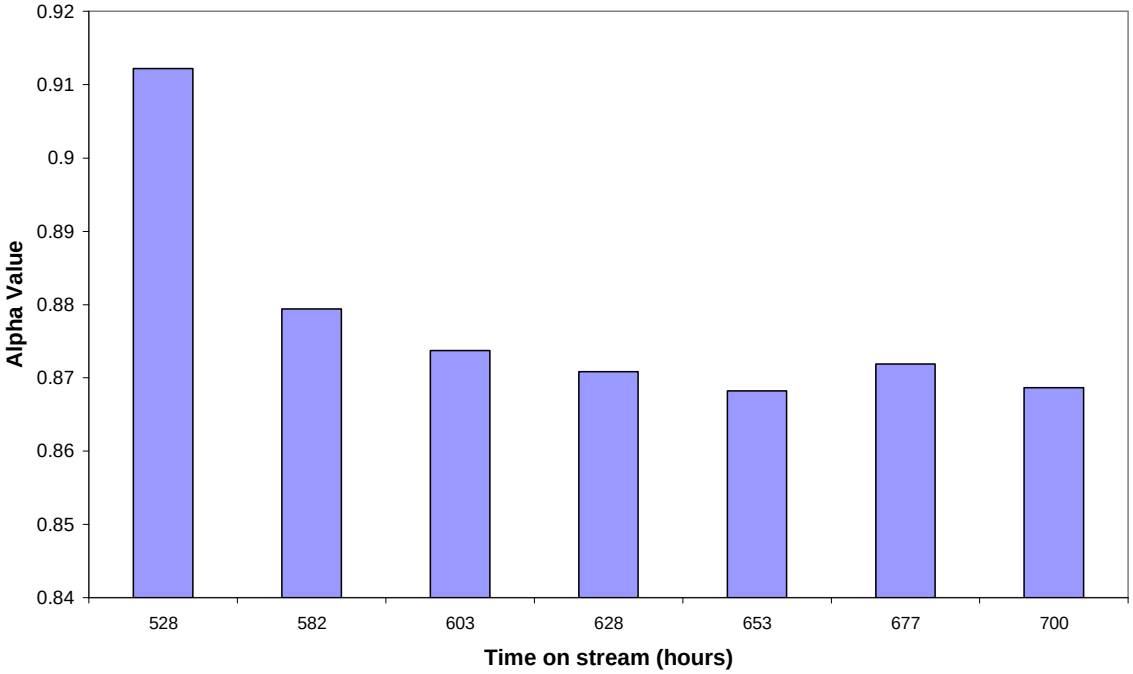

Figure 3-89: Alpha values versus time on stream for CoNZ catalyst at reaction temperature of 240 ^{o}C.

3.7.4.4 Organic liquid and wax selectivity

The hydrocarbon product distributions for the wax and liquid hydrocarbons samples at 51, 219, 462, 528 and 700 hours TOS are shown in figures 3-90 to 3-98.

3.7.4.4.1 51 hours TOS

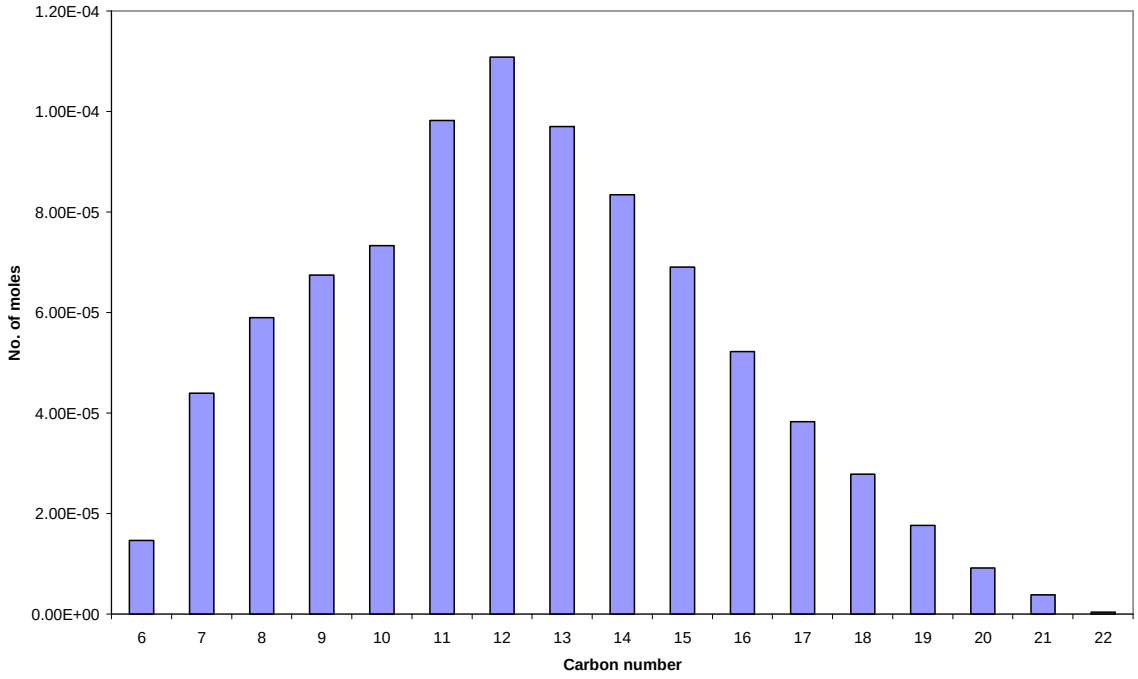

Figure 3-90: Hydrocarbon product distribution as a function of carbon number for CoNZ liquid hydrocarbon sample at 51 hours TOS (T=220 ^{o}C).

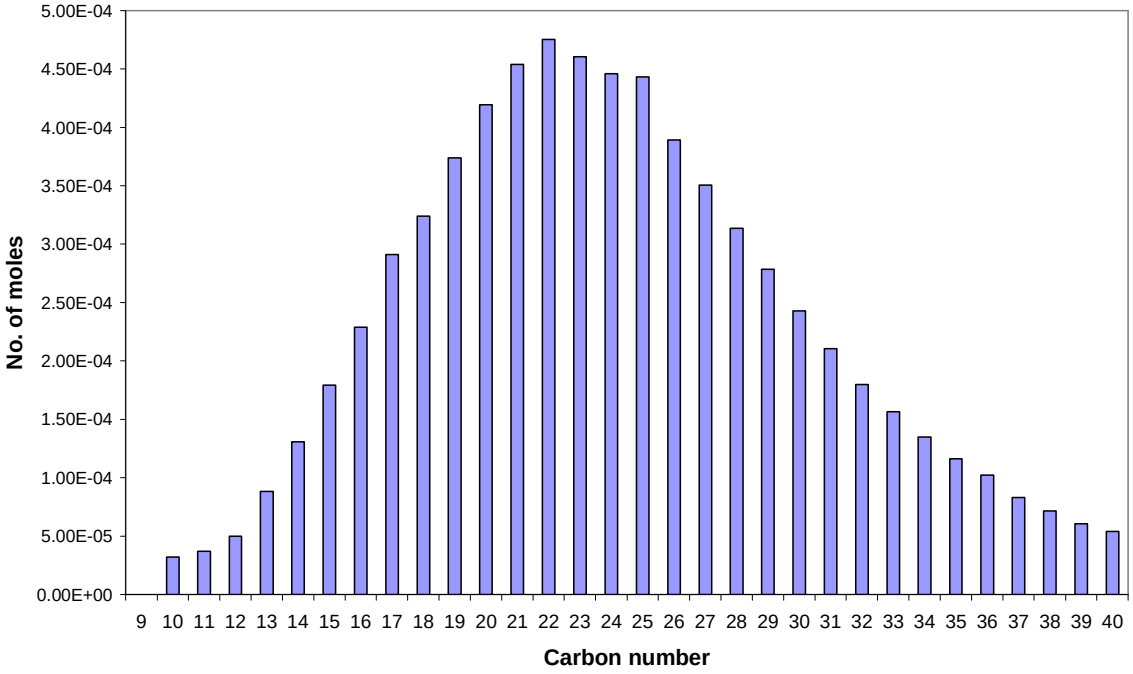

Figure 3-91: Hydrocarbon product distribution as a function of carbon number for CoNZ wax sample at 51 hours TOS (T=220 ^{o}C).

3.7.4.4.2 219 hours TOS

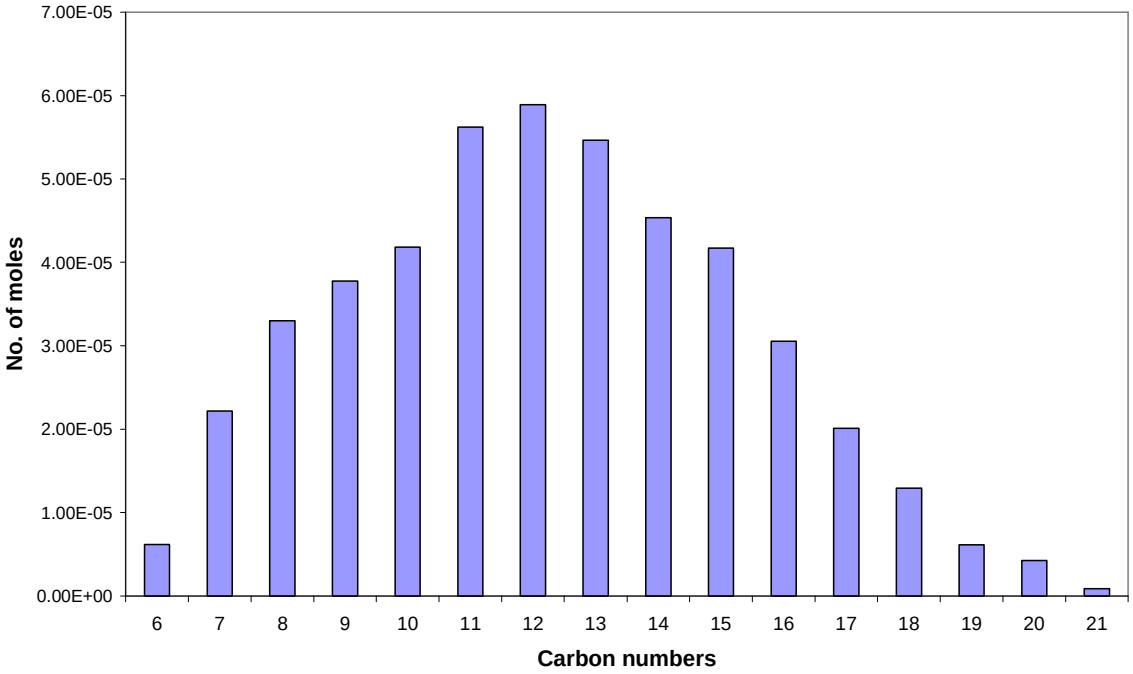

Figure 3-92: Hydrocarbon product distribution as a function of carbon number for CoNZ liquid hydrocarbon sample at 219 hours TOS (T=220 ^{o}C).

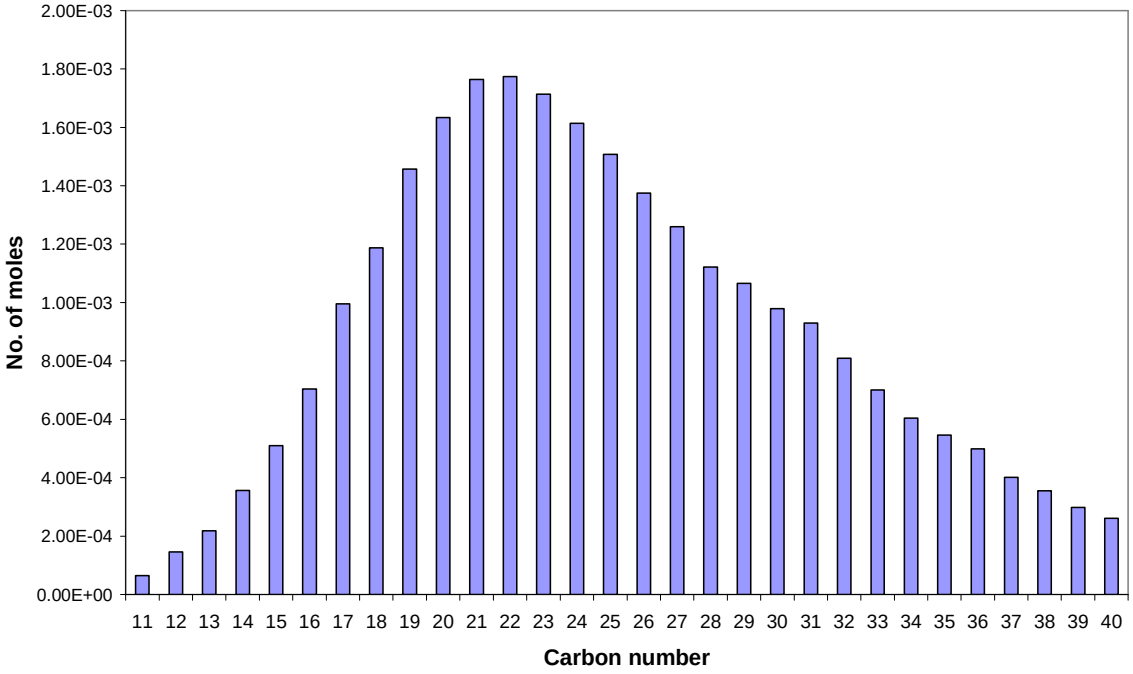

Figure 3-93: Hydrocarbon product distribution as a function of carbon number for CoNZ wax sample at 219 hours TOS (T=220 ^{o}C).

3.7.4.4.3 462 hours TOS

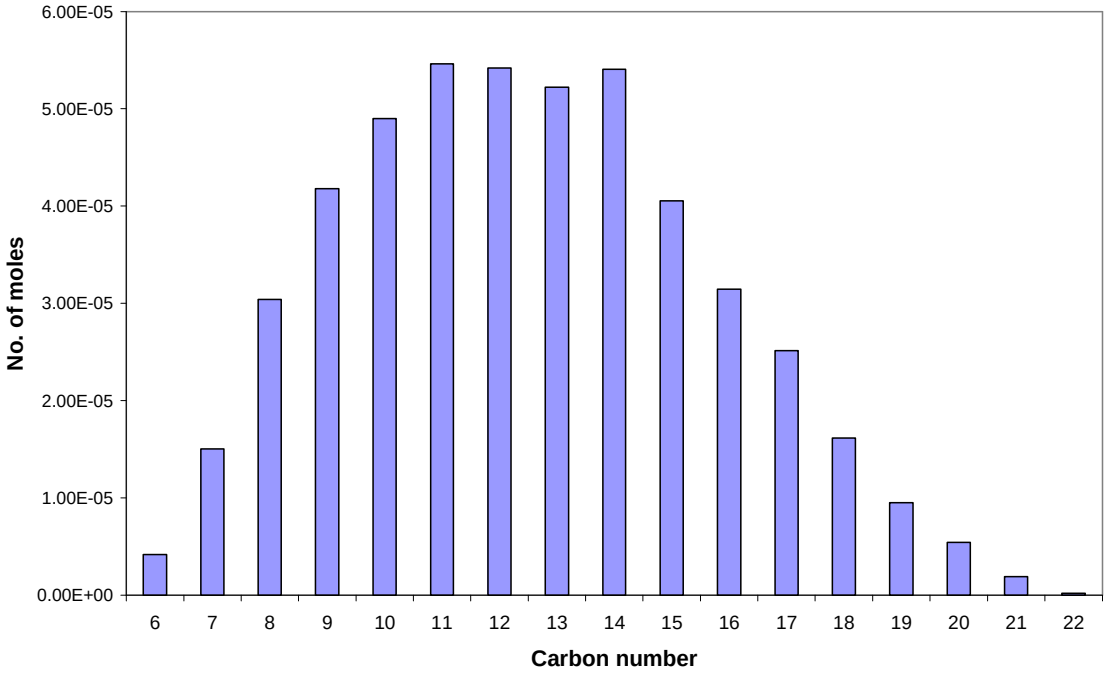

Figure 3-94: Hydrocarbon product distribution as a function of carbon number for CoNZ liquid hydrocarbon sample at 462 hours TOS (T=220 ^{o}C).

3.7.4.4.4 528 hour TOS

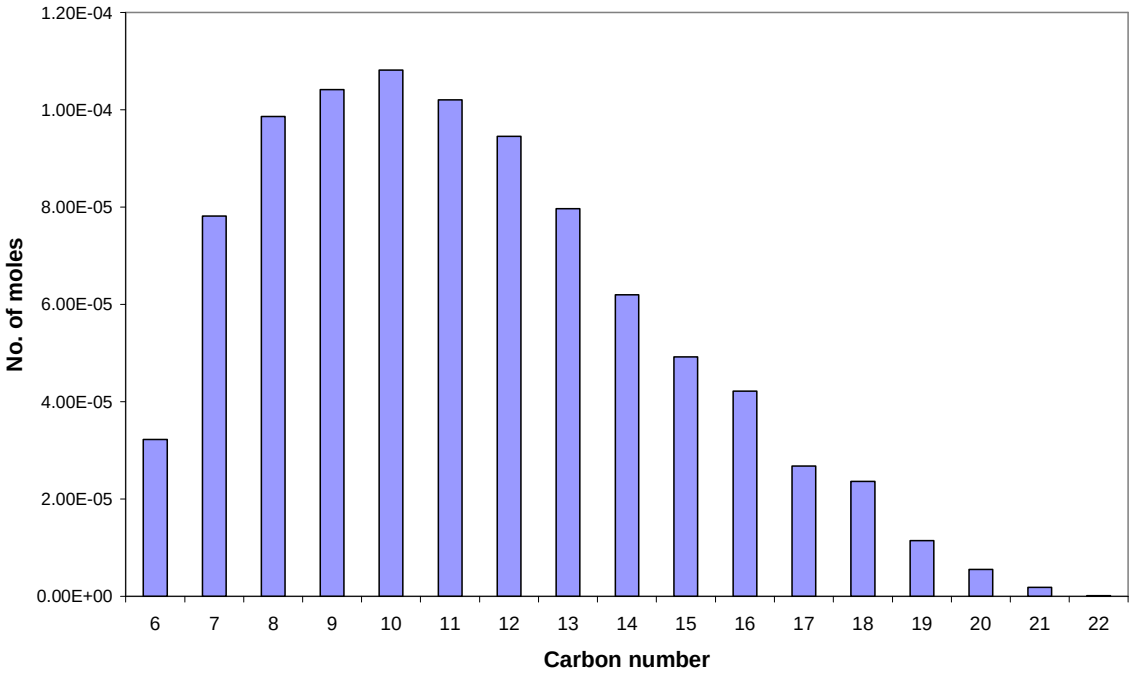

Figure 3-95: Hydrocarbon product distribution as a function of carbon number for CoNZ liquid hydrocarbon sample at 528 hours TOS (T=240 ^{o}C).

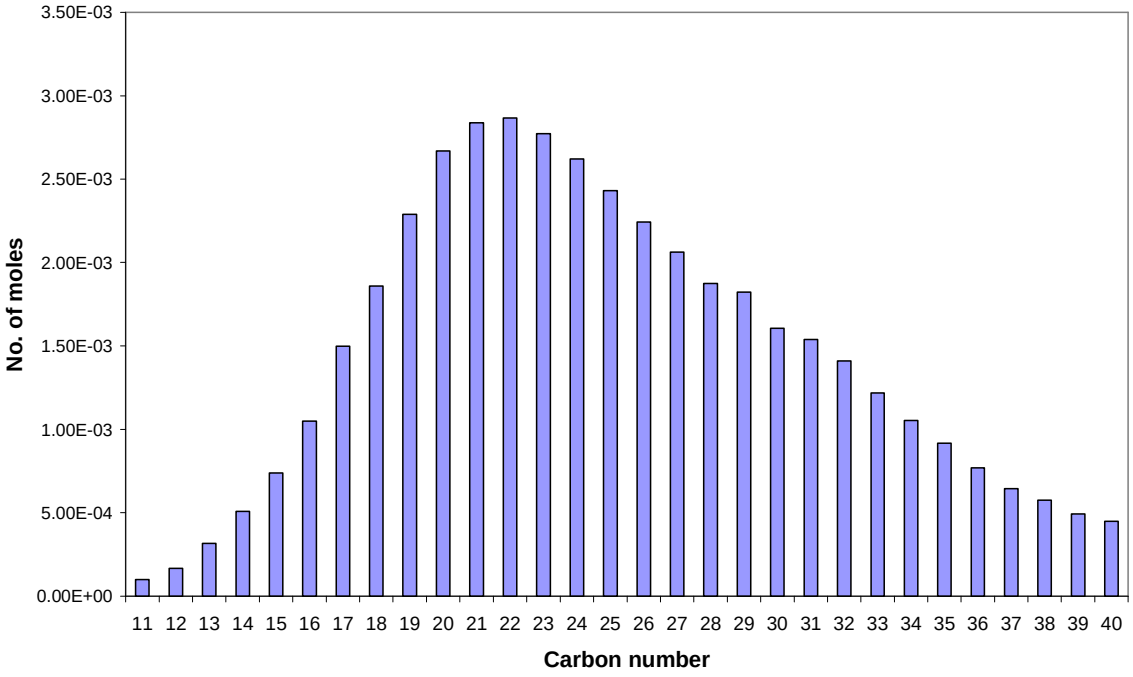

Figure 3-96: Hydrocarbon product distribution as a function of carbon number for CoNZ wax sample at 528 hours TOS (T=240 ^{o}C).

3.7.4.4.5 700 hours TOS

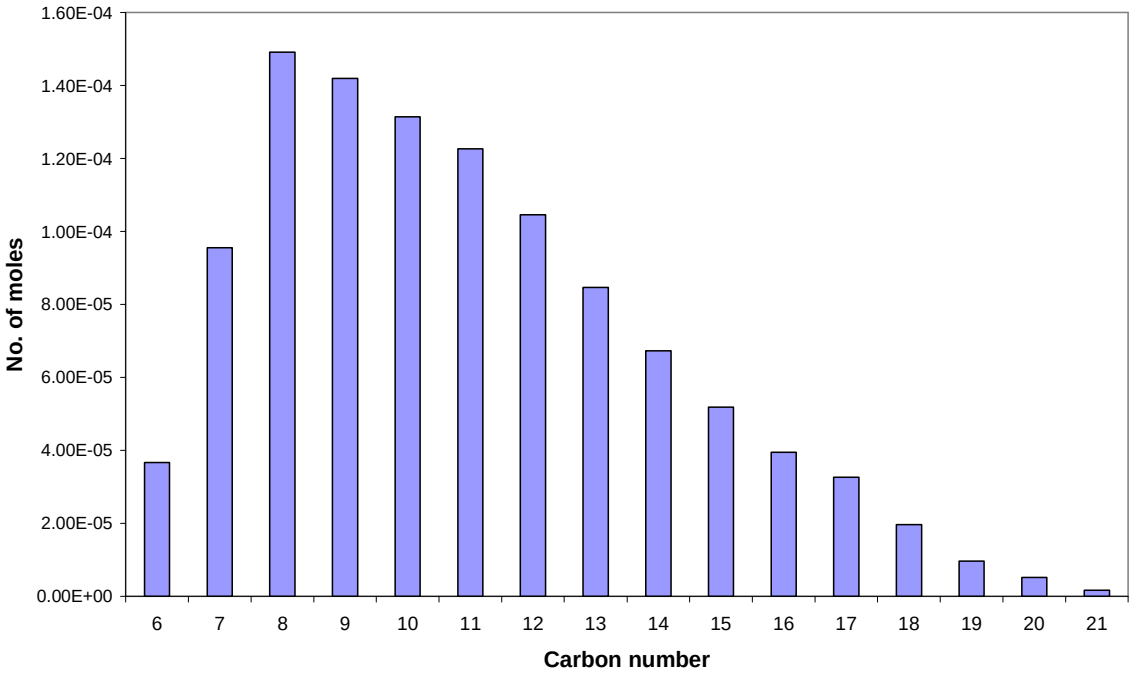

Figure 3-97: Hydrocarbon product distribution as a function of carbon number for CoNZ liquid hydrocarbon sample at 700 hours TOS (T=240 ^{o}C).

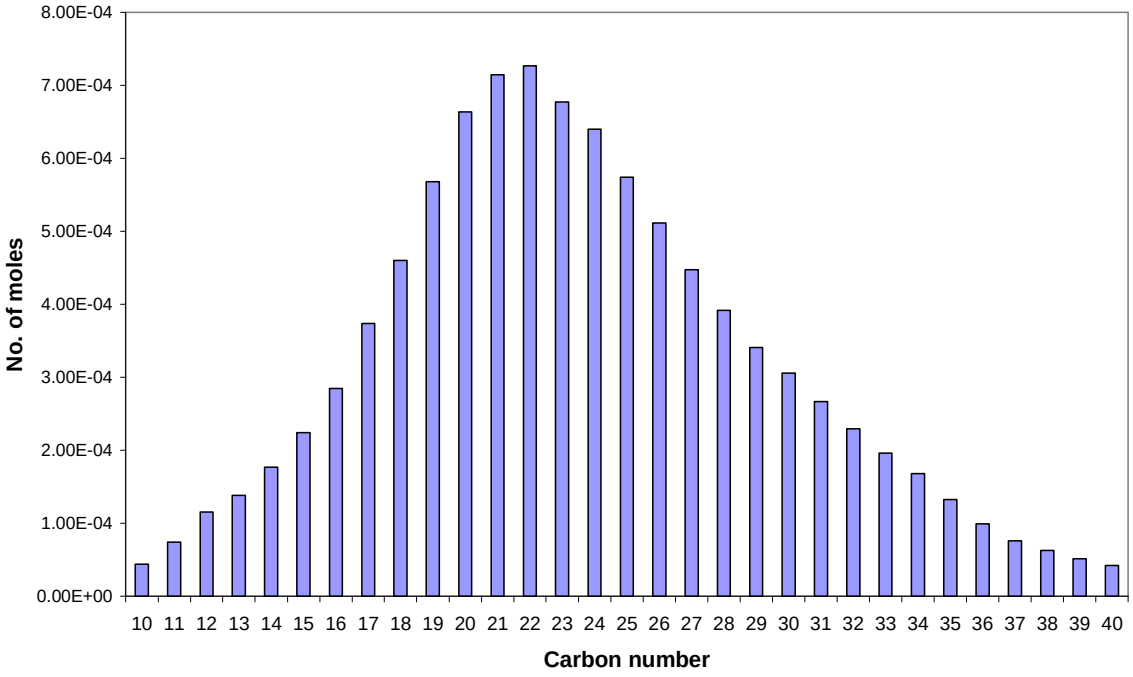

Figure 3-98: Hydrocarbon product distribution as a function of carbon number for CoNZ wax sample at 700 hours TOS (T=240 ^{o}C).

3.7.5 FT post reaction analysis

3.7.5.1 Thermogravimetric analysis-Differential scanning calorimetry

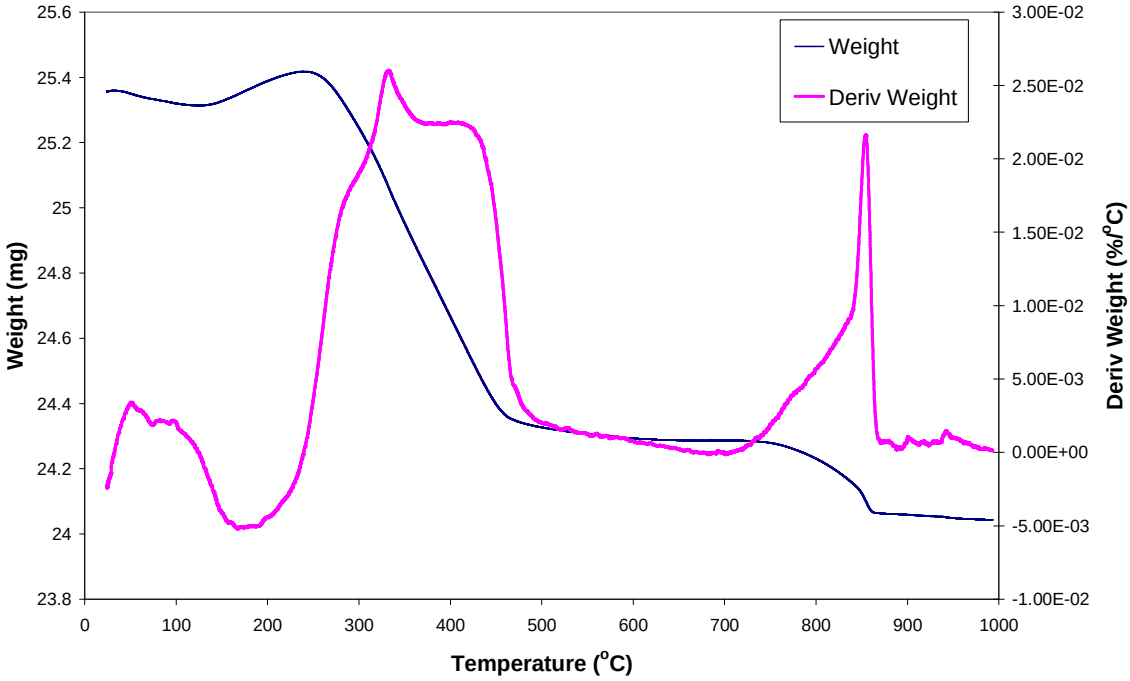

Figure 3-99: TGA weight and derivative weight profiles in oxygen for cobalt nitrate on zinc oxide catalyst post FT reaction.

From the profiles in figure 3-99 it can be seen that there is an initial weight loss before 150 ^{o}C. Between 135-245 ^{o}C, the weight and derivative weight profiles suggest a gain in weight, which is thought to be associated with the re-oxidation of the catalyst. However, the main part of the weight loss occurs between 250-470 ^{o}C and contributes ~80 % of the total weight lost. There is also a further high temperature weight loss at 855 ^{o}C. The initial and final weight losses, before 150 ^{o}C and at 855 ^{o}C, respectively, can be seen from the heat flow data in figure 3-100 to be endothermic. The region of weight gain seen on the TGA data appears to be relatively featureless in the heat flow profile, however, in contrast to this it can be seen that the main weight loss is highly exothermic.

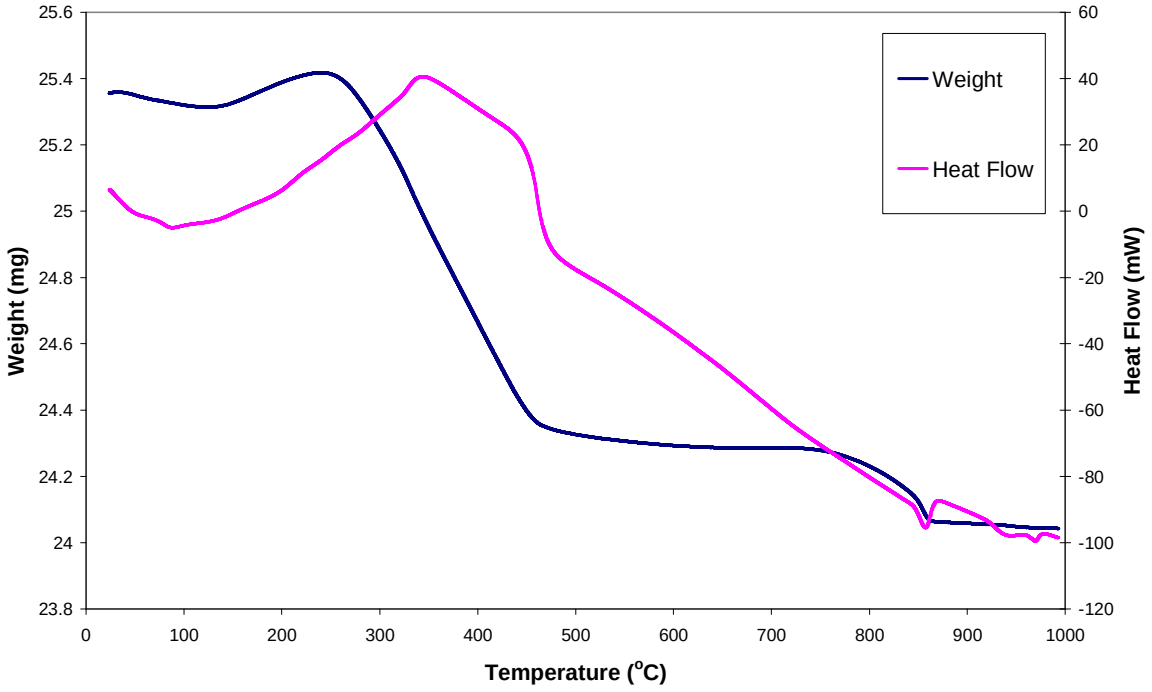

Figure 3-100: TGA-DSC weight and heat flow profiles in oxygen for cobalt nitrate on zinc oxide post FT reaction.

3.7.5.1.1 Mass spectrometric analysis

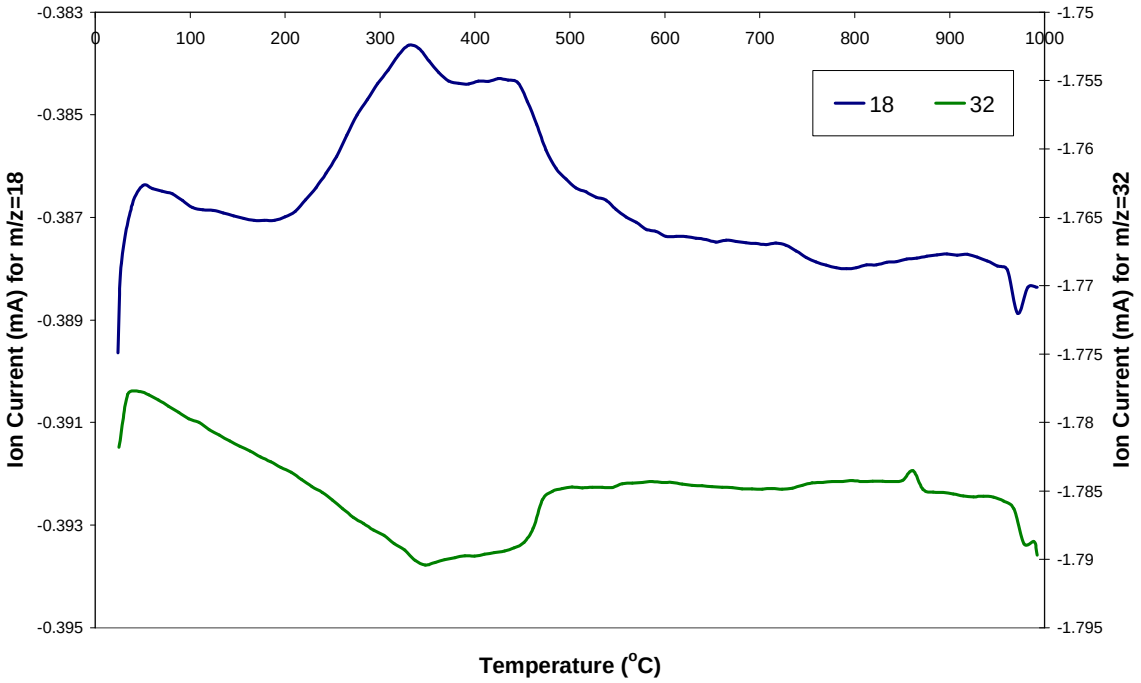

Figure 3-101: Mass spectrometric data of H_2O (m/z=18) and O_2 (m/z=32) for CoNZ catalyst post FT reaction in oxygen.

The mass spectrometric data obtained for the calcined CoNZ catalyst post FT reaction is presented in figures 3-101 and 3-102. When heated in oxygen, the sample evolved gases with prominent peaks corresponding to water, carbon monoxide and carbon dioxide. The high temperature weight loss at 855 ^{o}C is seen to involve the evolution of oxygen.

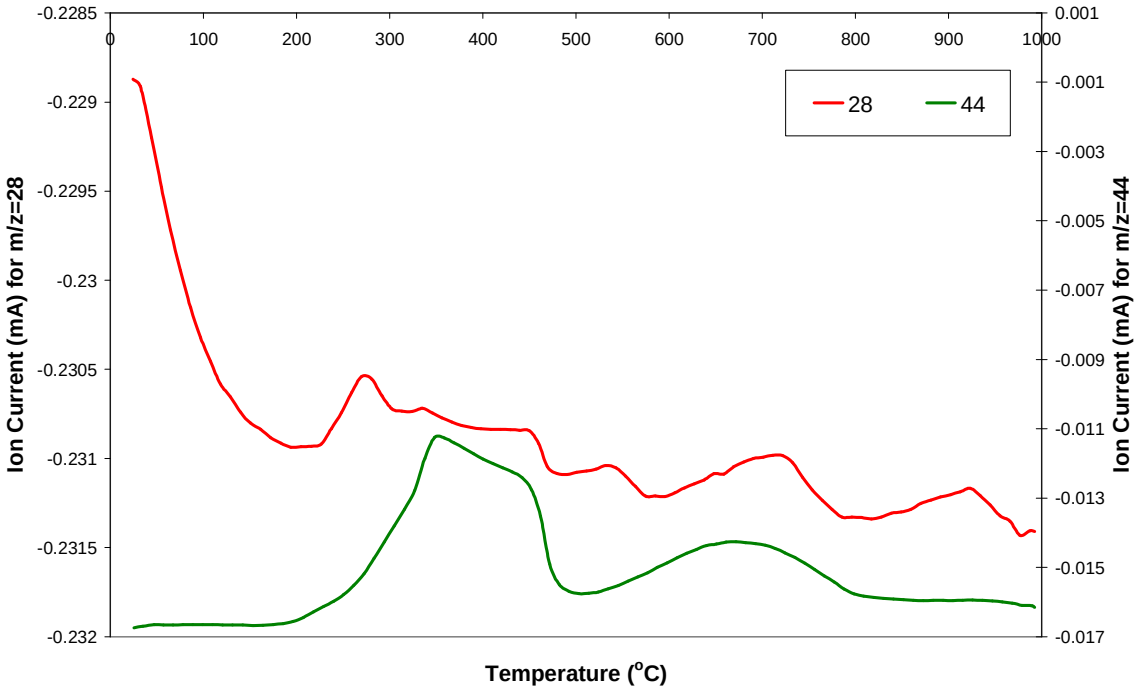

Figure 3-102: Mass spectrometric data of CO (m/z=28) and CO_2 (m/z=44) in oxygen for calcined CoNZ catalyst post FT reaction.

3.7.5.1.2 X-Ray Diffraction

The X-ray diffraction pattern of the CoNZ catalyst post reaction is presented in figure 3-103. The pattern showed reflections characteristic of metallic cobalt as well as peaks corresponding to the ZnO support. The mean cobalt crystallite size calculated using the Scherrer equation was found to be around 9 nm.

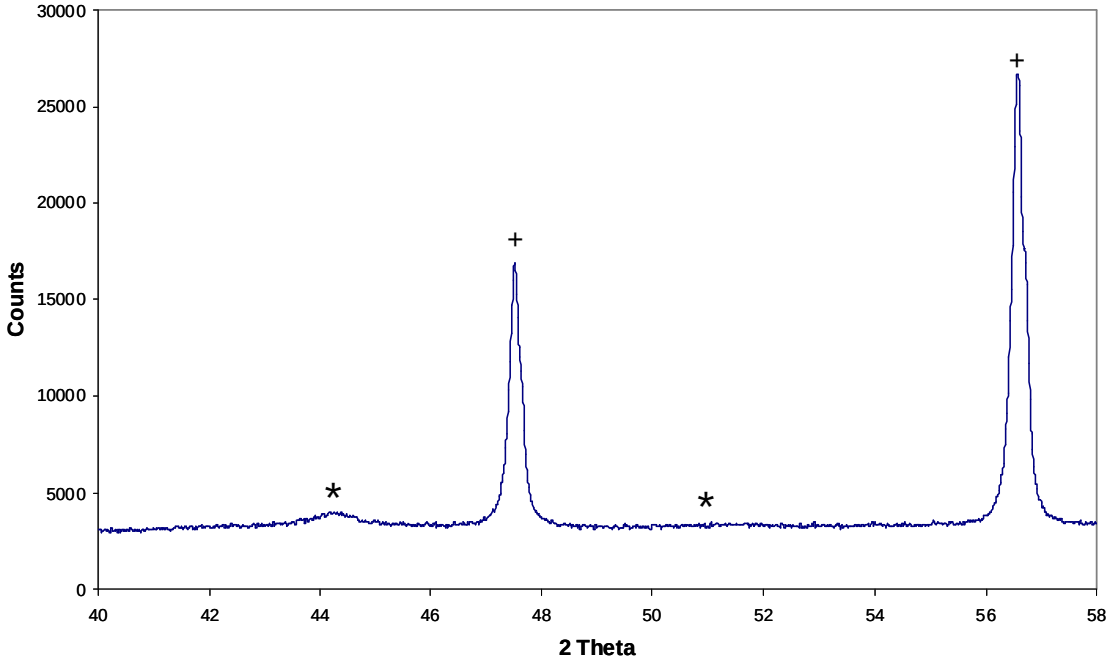

Figure 3-103: X-Ray diffraction pattern for cobalt on zinc oxide (CoNZ) catalyst post FT reaction. The phases denoted are (*) metallic Co and (+) ZnO. The experimental error for cobalt crystallite size calculated from X-ray diffraction is less than +/- 1 nm.

3.8 Cobalt nitrate on Zinc Oxide BP - Supplied calcined

This section relates to the cobalt nitrate on zinc oxide catalysts supplied from BP in the calcined form. No information was supplied with regards to calcination procedure.

3.8.1 Catalyst as supplied

3.8.1.1 X-Ray Diffraction

The X-ray diffraction pattern for the BP calcined cobalt on zinc oxide catalyst is shown in figure 3-104. The pattern is constituted by XRD peaks which can be attributed to Co_3O_4 phase and the ZnO support. The mean diameter of cobalt oxide crystallites were calculated from the XRD pattern by use of the Scherrer equation and found to be 14 nm.

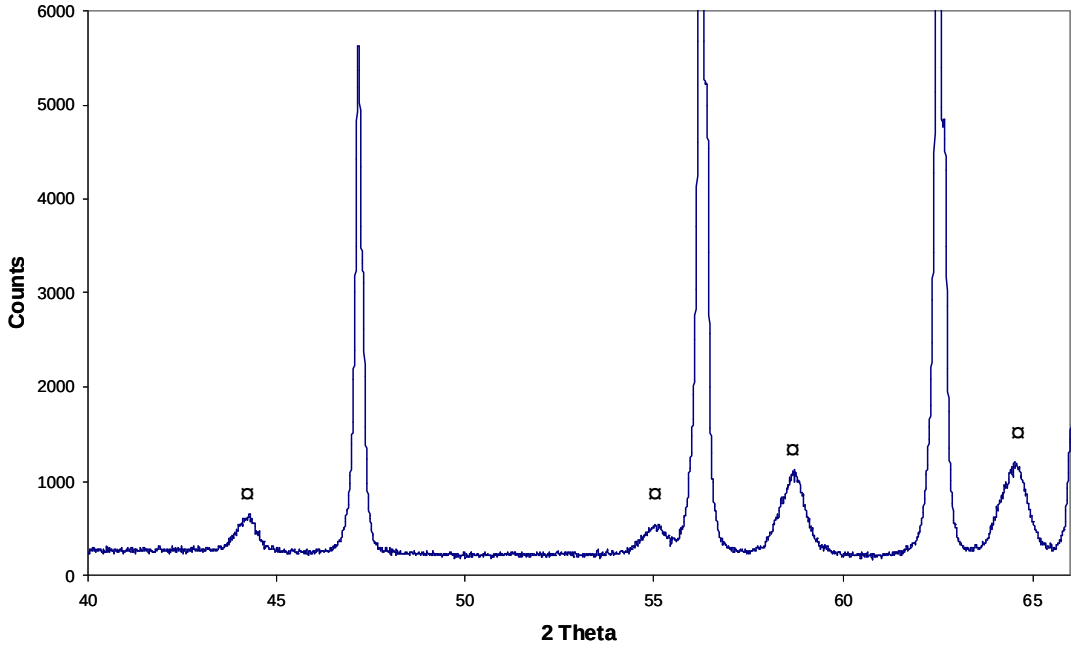

Figure 3-104: X-Ray diffraction pattern of CoNZ BP calcined catalyst. Phases denoted are (¤) Co_3O_4. The experimental error for Co_3O_4 crystallite size calculated from X-ray diffraction is less than +/- 1 nm.

3.8.2 High Resolution Transmission Electron Microscopy

Cobalt nitrate on zinc oxide, calcined at BP, was studied by transmission electron microscopy. Micrographs of the calcined catalyst are shown in figure 3-105. Figure 3-105a shows the TEM image of the catalyst at low magnification. Analysis of the TEM images (figure 1-305 a-c and d) show that the cobalt oxide particles are dispersed on the zinc oxide as slightly elliptical particles 17-25 nm in size. The

high magnification image (figure 3-105 d) shows a lattice spacing of 0.46 nm, indicating the possible presence of Co_3O_4. Figure 3-105(e) shows lattice fringe spacing corresponding to ZnO support.

Figure 3-105: TEM micorgraphs of the cobalt nitrate on zinc oxide calcined at BP (CoNZC). (a-c) Low magnification images and (d-f) higher magnification images.

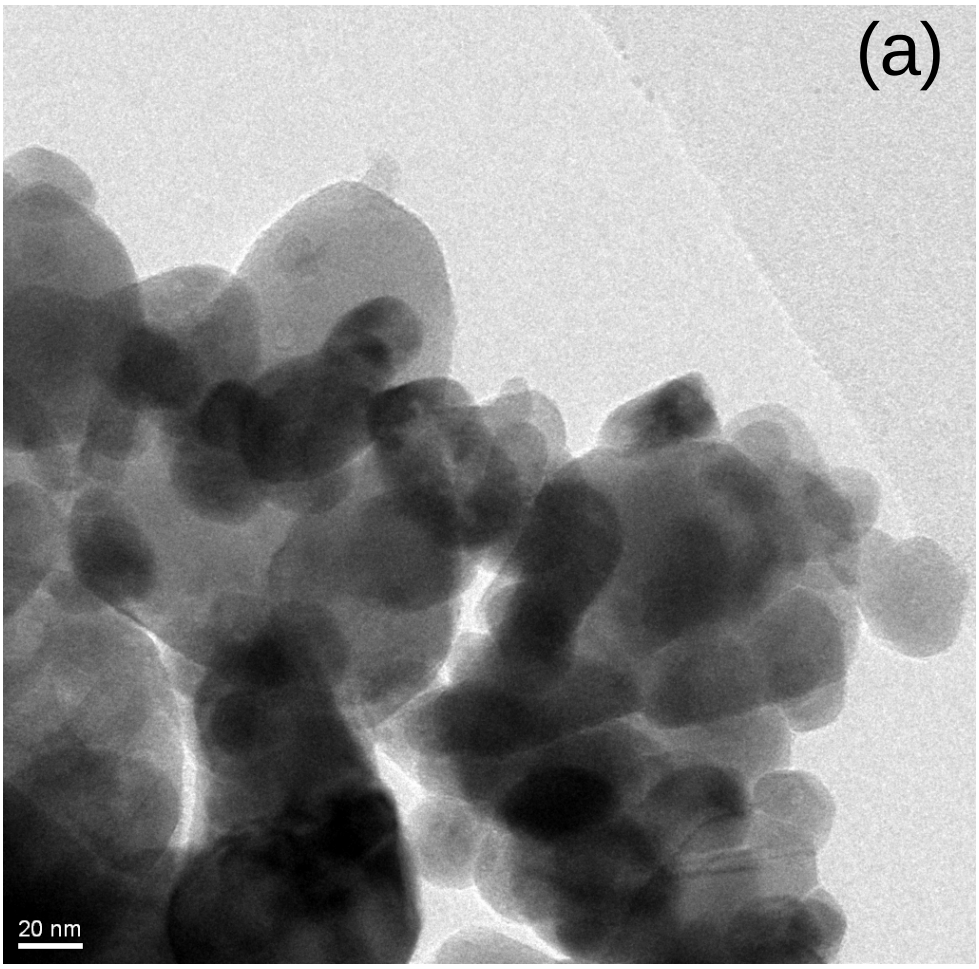

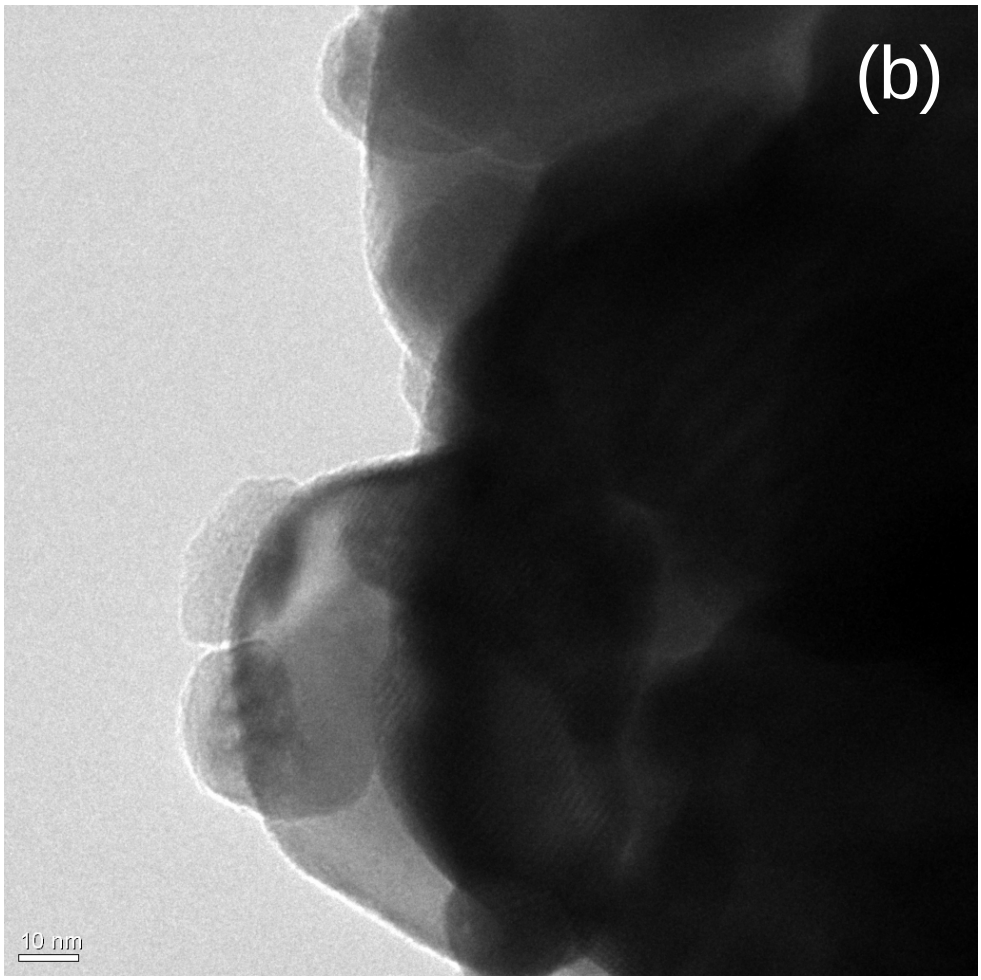
(b)
10 nm

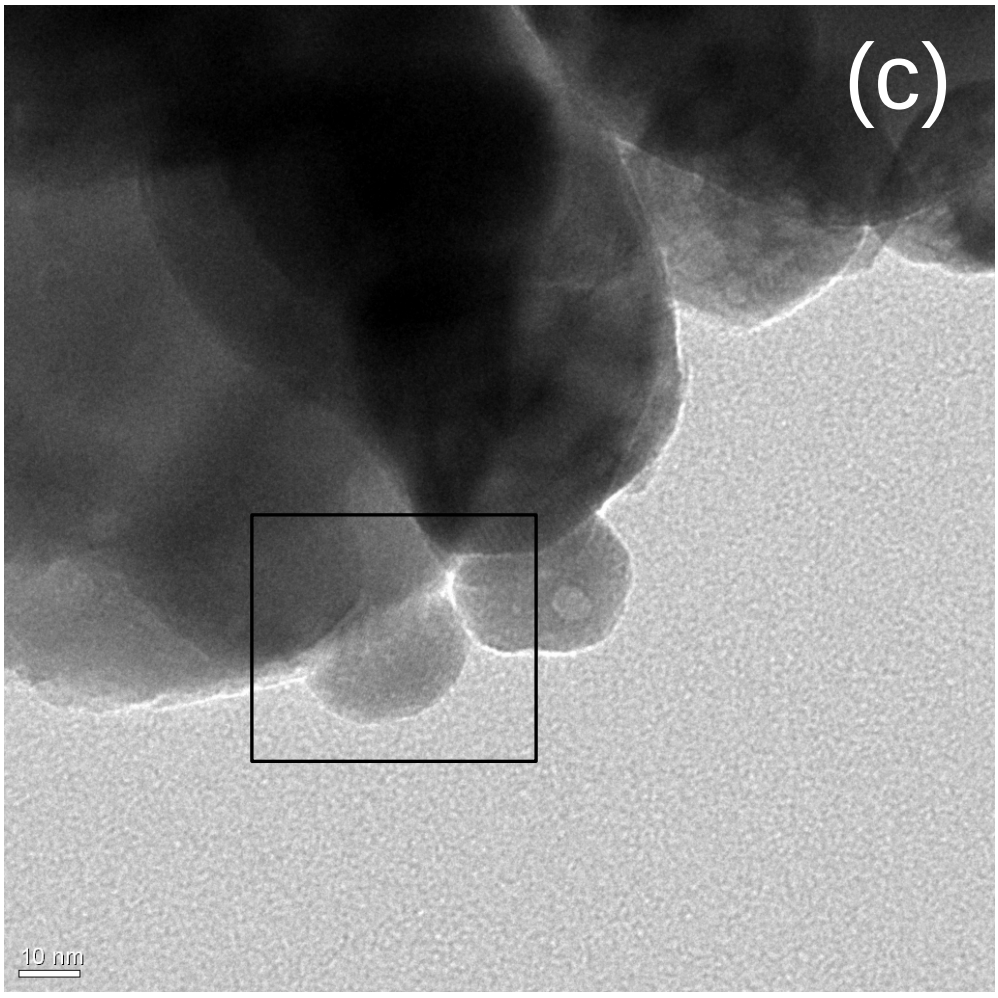
(c)
10 nm

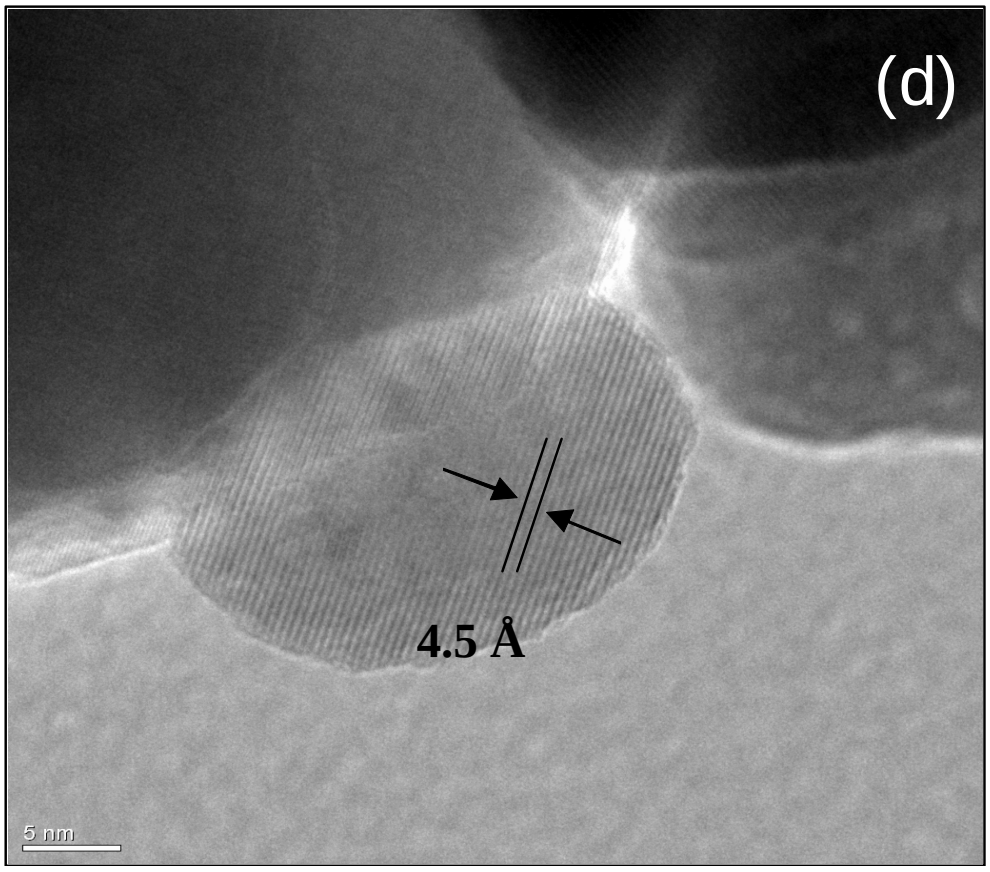
(d)
4.5 Å
5 nm

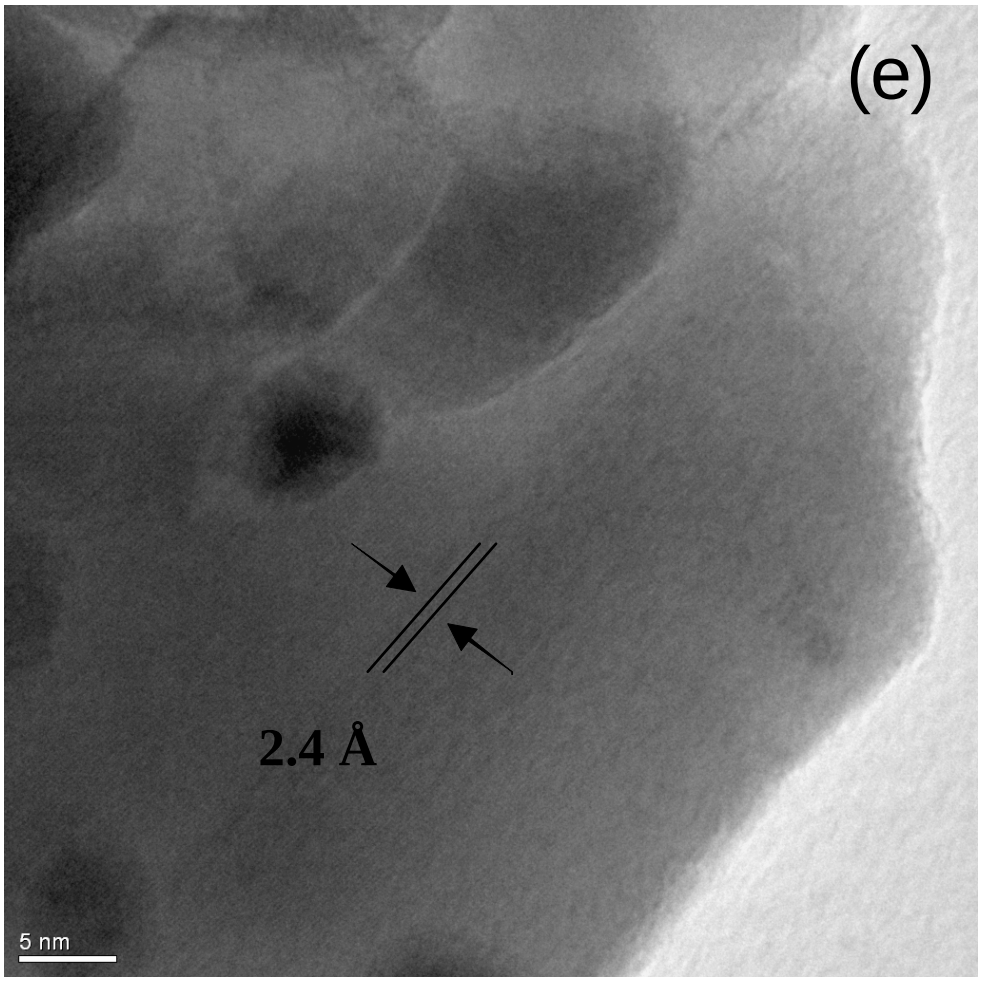
(e)
2.4 Å
5 nm

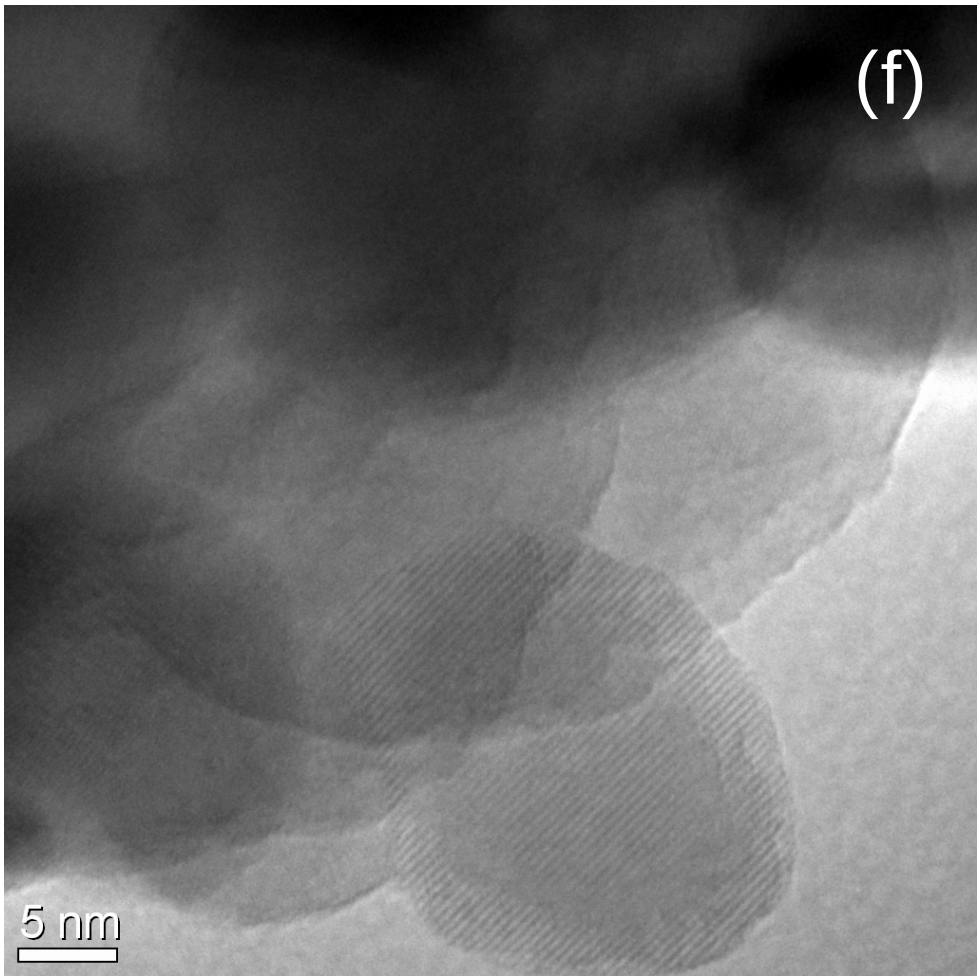

3.8.3 Hydrogen Treatment

3.8.3.1 Thermogravimetric analysis-Differential Scanning Calorimetry

The TGA-DSC data for the CoNZ BP calcined catalyst in hydrogen is shown in figures 3-106 and 3-107. The derivative weight profile possesses two distinct peaks with temperature maxima at 360 ^{o}C and 560 ^{o}C. The weight loss was 0.91 mg and 1.258 mg respectively and can be ascribed to the reduction of cobalt oxide particles in a two-step process. It can be seen from the heat flow profile in figure 3-107 that both of the weight loss events were relatively featureless although the weight loss centred at 360 ^{o}C appears to be slightly exothermic.

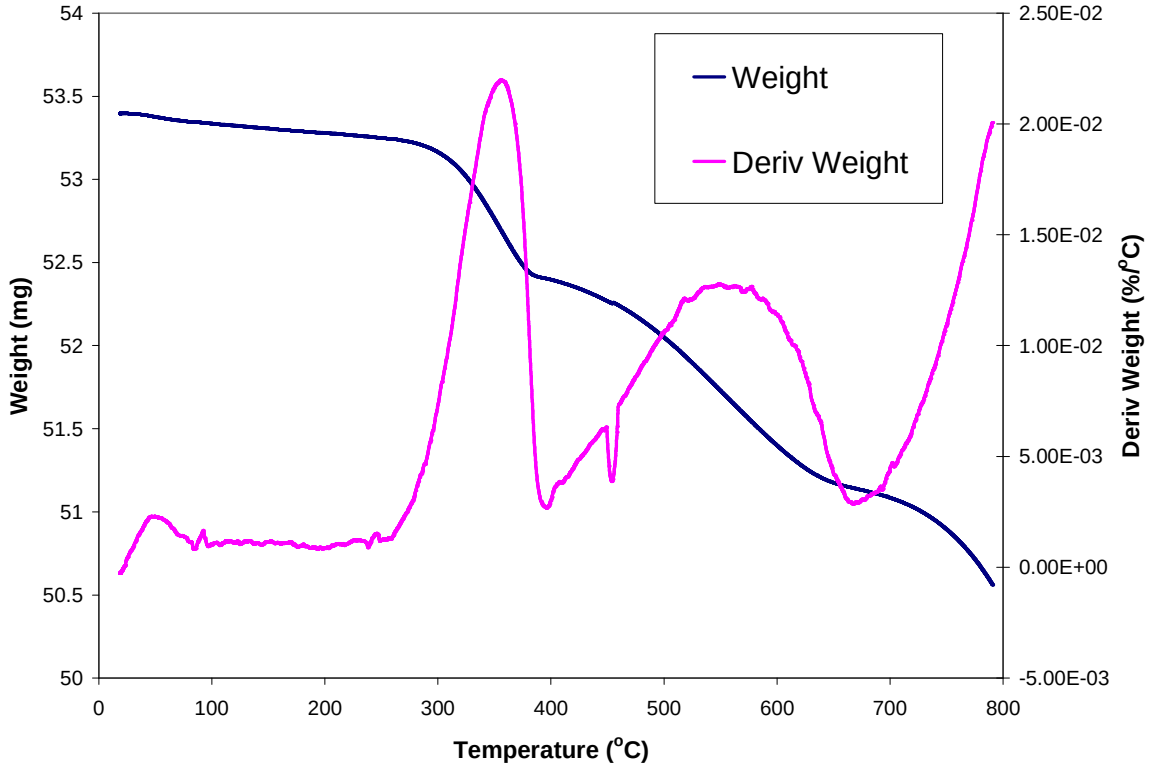

Figure 3-106: TGA weight and derivative profiles in hydrogen for cobalt nitrate on zinc oxide calcined at BP.

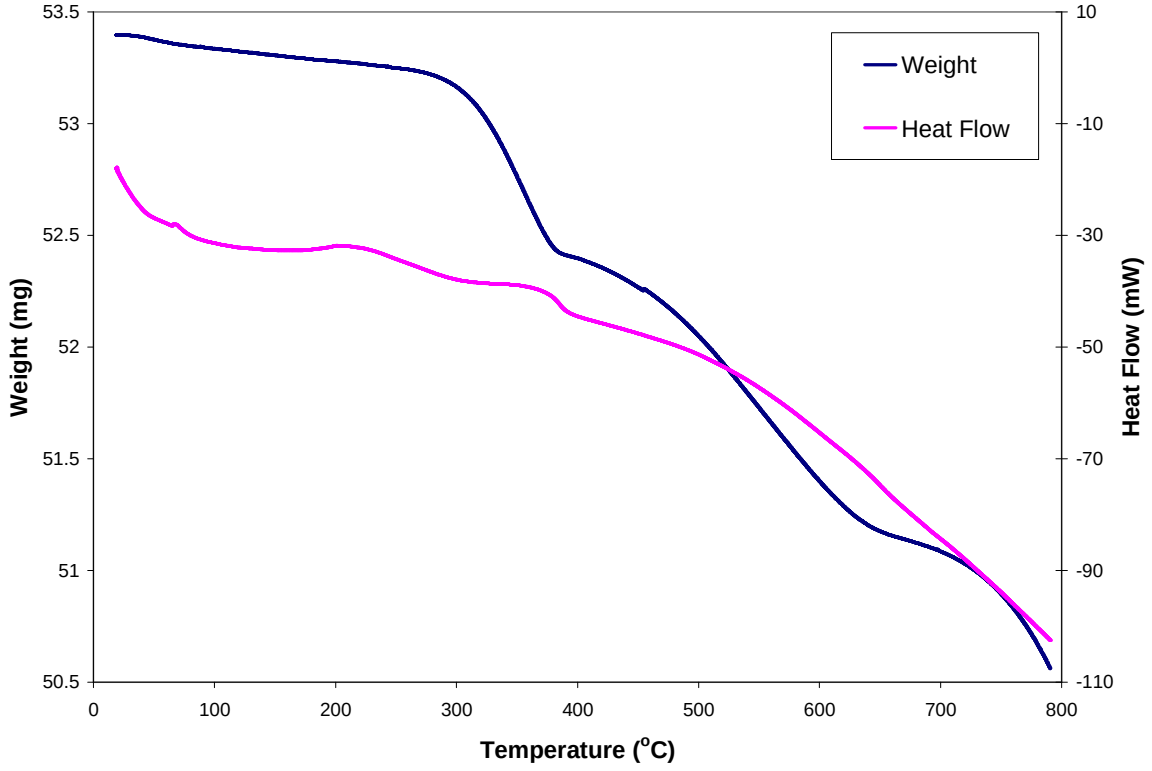

Figure 3-107: TGA-DSC weight and heat flow profiles in hydrogen for cobalt nitrate on zinc oxide calcined at BP.

3.8.3.2 Hot-stage X-Ray diffraction (XRD)

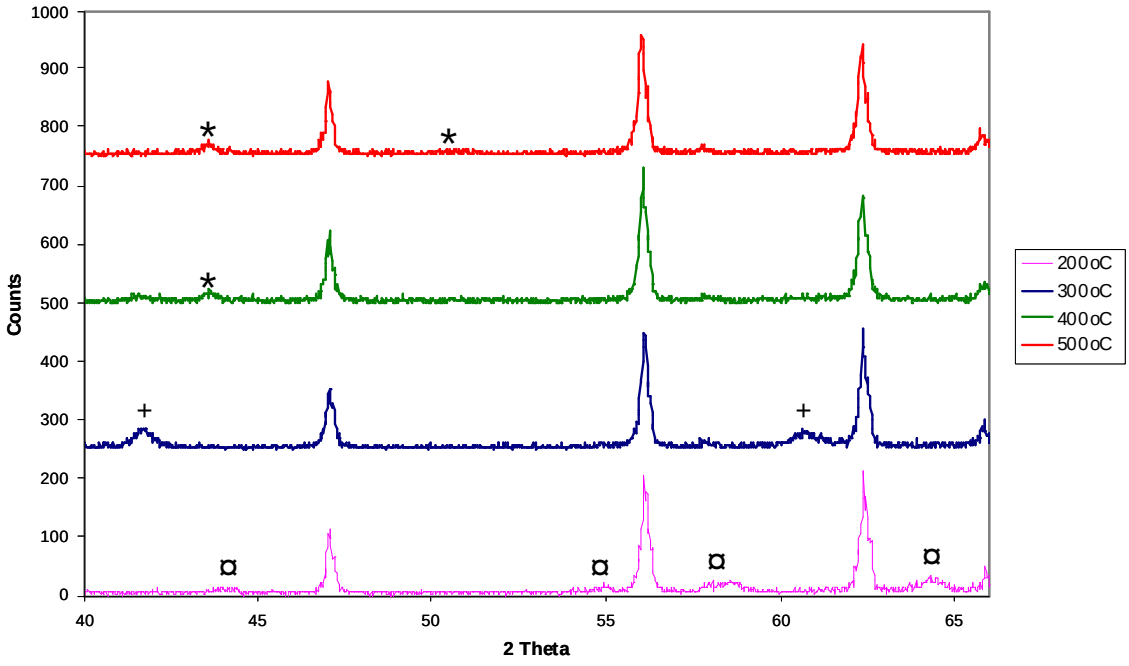

Figure 3-108: Hot-stage XRD patterns of cobalt nitrate on zinc oxide BP calcined in hydrogen. Phases denoted are (¤) Co_3O_4, (+) CoO and (*) metallic Co. The XRD patterns have been offset for clarity. The experimental error for cobalt crystallite sizes calculated from X-ray diffraction is less than +/- 1 nm.

The hot-stage X-Ray diffraction analysis in hydrogen was carried out as described in section 2.3.3 and is shown in figure 3-108. At room temperature, the XRD pattern shows reflections characteristic of the Co_3O_4 spinel. On heating in hydrogen to 300^{o}C, the X-Ray diffraction pattern contained peaks relating to CoO and ZnO phases. From 400 ^{o}C onwards reflections revealing the presence of metallic cobalt are present. The average size of cobalt crystallites determined from the XRD patterns at 400^{o}C and 500^{o}C was 14 nm and 15 nm, respectively.

3.8.3.3 Effect of heating rate

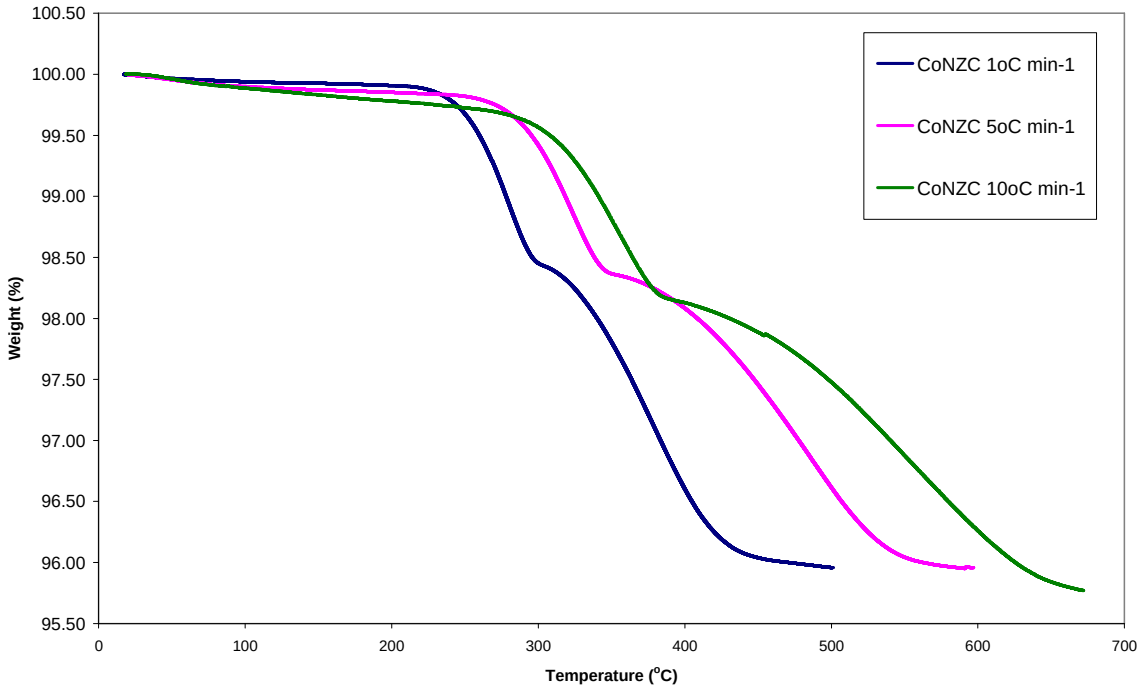

Figure 3-109: TGA weight profiles in hydrogen for cobalt nitrate on zinc oxide calcined at BP at different heating rates

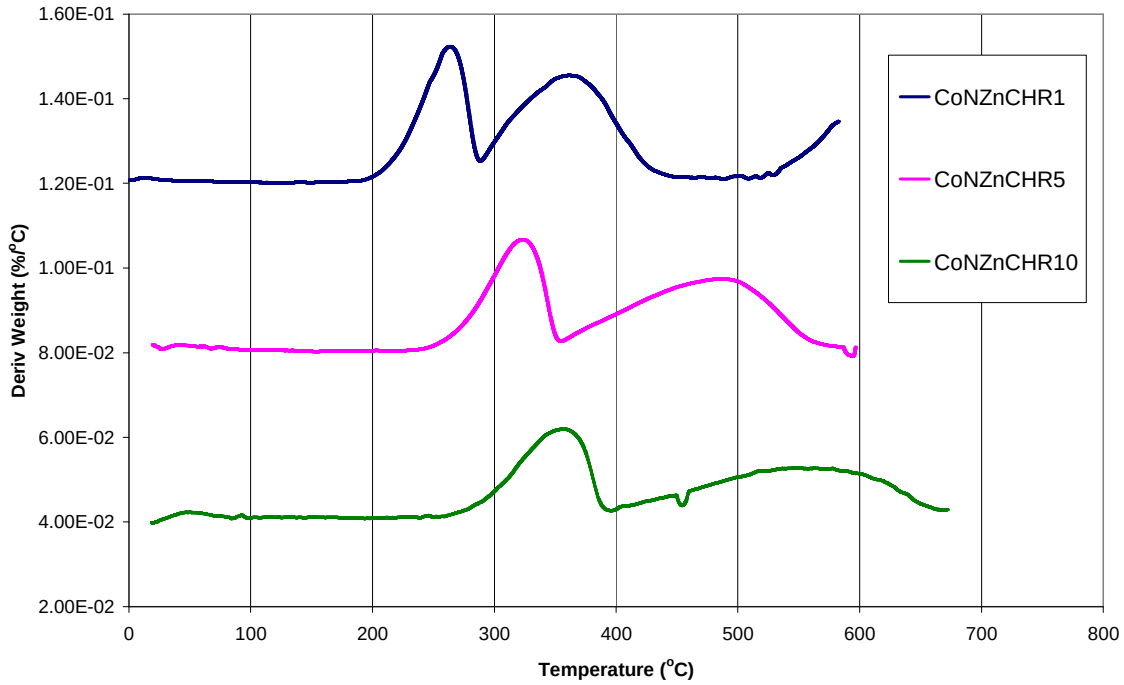

Figure 3-110: TGA derivative weight profiles in hydrogen for cobalt nitrate on zinc oxide calcined at BP at different heating rates.

Figures 3-109 and 3-110 contain a series of TGA weight and derivative weight profiles for the BP calcined CoNZ catalyst in hydrogen obtained at different temperature ramp rates of 1, 5 and 10 ^{o}C min^{-1}. As the heating rate was increased from 1 ^{o}C min^{-1} to 10 ^{o}C min^{-1} the derivative weight peak maxima moved to higher temperatures. This results in a change in peak maximum temperature from 267 to 360 ^{o}C for the 1st reduction peak and 364 to 560 ^{o}C for the 2nd reduction peak. From the TGA profiles shown in figure 3-109 it can be seen that the total percentage weight loss is the same for each heating rate.

3.8.3.4 Effect of hydrogen concentration

The effect of different hydrogen concentrations on the reduction of the catalysts was investigated using TGA. Analysis of the BP precalcined cobalt nitrate on zinc oxide catalyst was carried out as described in section 2.3.2. From figures 3-111 and 3-112 it can be seen clearly that derivative weight profiles are affected by the concentration of hydrogen used. In particular, the temperatures which correspond to the maxima of the reduction profiles and the shape of the profiles themselves. At 10 ^{o}C min^{-1}, on going from 5% hydrogen to 75% hydrogen the maximum temperatures of the 1st and 2nd reduction peaks have been reduced by ~55 and ~150 ^{o}C, respectively. Similar results were found at heating rates of 1 ^{o}C min^{-1} and 5 ^{o}C min^{-1}, with results shown in table 3-5. For all heating rates, increasing the concentration of reducing gas from 5% to 75% hydrogen reduced the maximum temperature of both reduction peaks. This effect became more marked with increased heating rate. For all of the heating rates the decrease in temperature of the 2nd reduction peak is around three times greater than that of the 1st reduction peak. However although the concentration of hydrogen gas used affected the temperature at which reduction was complete, it can be seen clearly from figure 3-111 that it had no effect on the total weight loss.

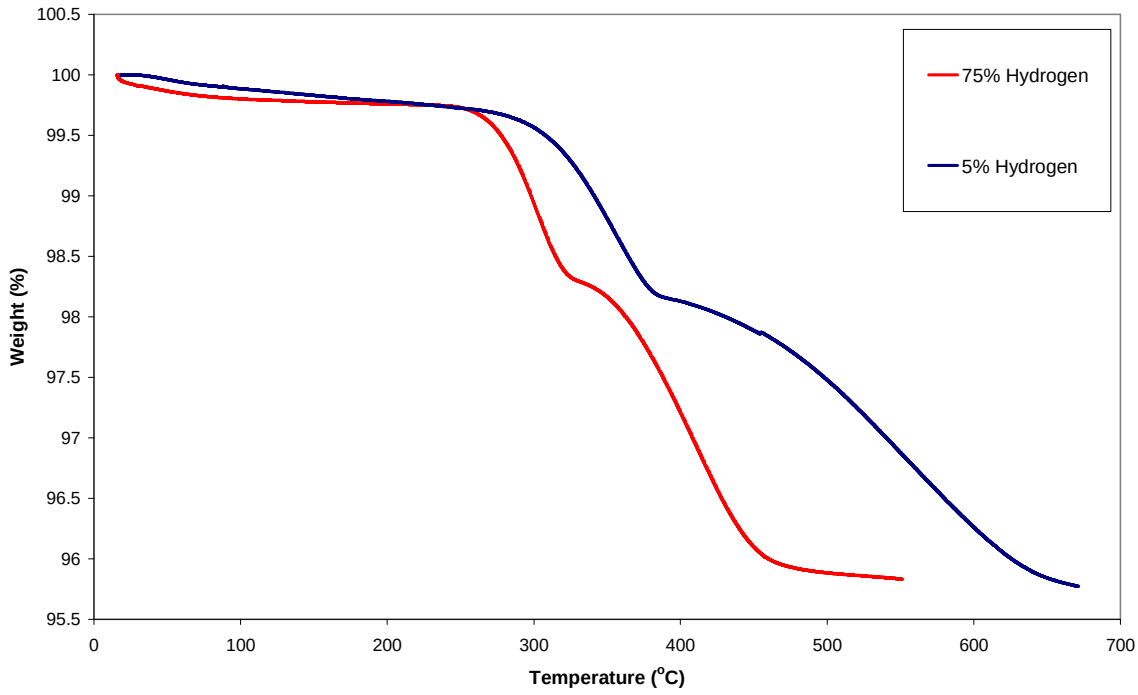

Figure 3-111: TGA percentage weight profile in varying concentrations of hydrogen for cobalt nitrate on zinc oxide calcined at BP. Ramp rate of 10°C min^{-1}.

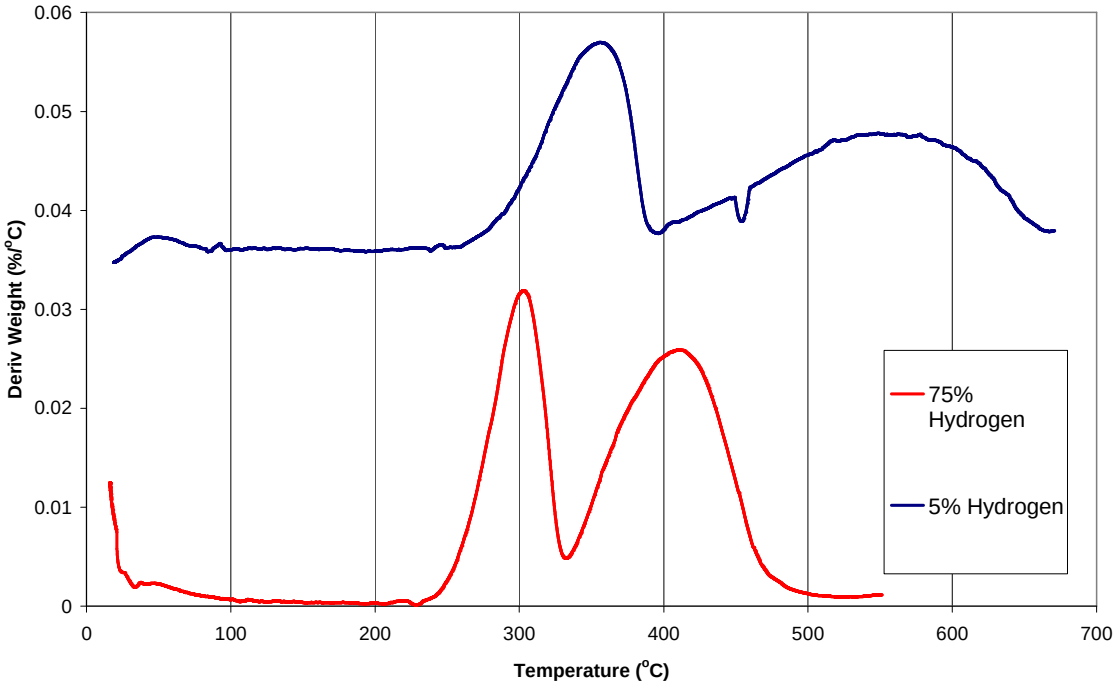

Figure 3-112: TGA derivative weight profile in varying concentrations of hydrogen for cobalt nitrate on zinc oxide calcined at BP. Ramp rate of 10°C min^{-1}.

Table 3-5: Change in DTA peak temperature maxima for BP precalcined cobalt on zinc oxide catalysts in different concentrations of reducing gas at several different heating rates.

Heating rate (^{o}C min^{-1})	Concentration of hydrogen gas (%)	T_{max} 1st redn peak	T_{max} 2nd redn peak
1	5	266	365
	75	252	329
5	5	326	490
	75	290	387
10	5	359	562
	75	303	413

3.8.3.5 CO chemisorption

CO chemisorption was carried out on the reduced cobalt on Zinc Oxide BP calcined catalyst and CO adsorbed measured as described in section 2.3.3. The amount adsorbed was found to be 78 µmoles g^{-1}. Using equation in section 2.3.2 this gave a dispersion of 0.46 %.

3.8.4 FT Reaction

3.8.4.1 Conversion

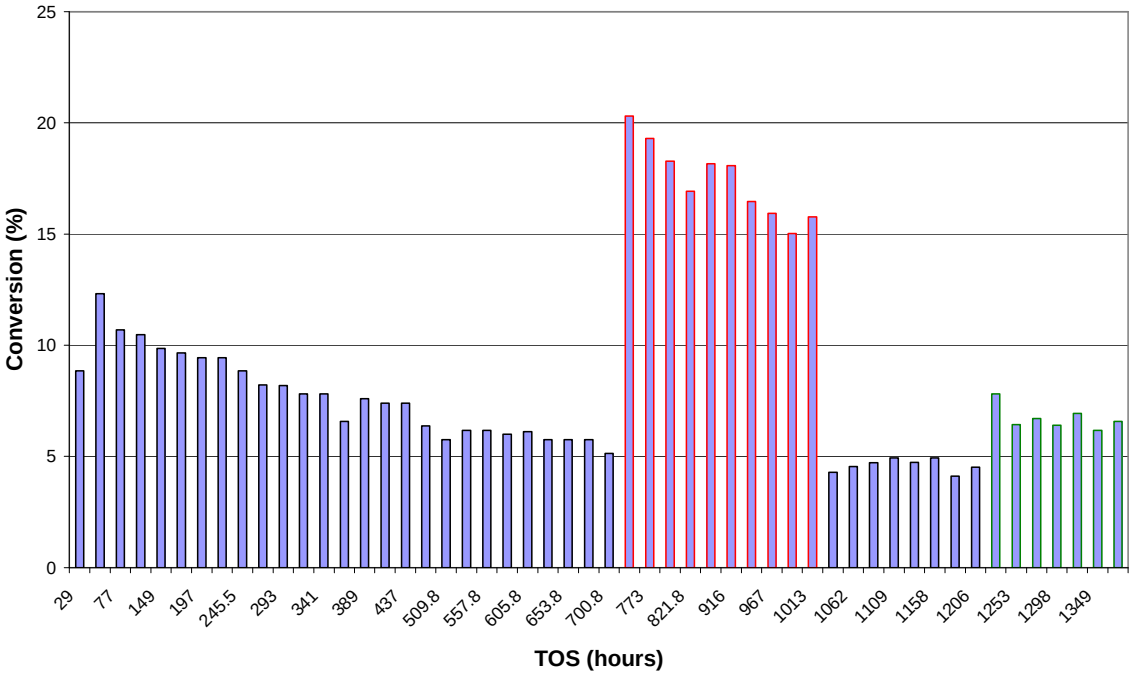

Figure 3-113: Conversion as a function of time-on-stream for the CoNZC catalyst at a temperature of 220 ^{o}C, 240 ^{o}C and 230 ^{o}C. The experimental error for the conversion is estimated to be +/- 5%.

The CO conversion data for the BP calcined cobalt on zinc oxide catalyst is presented in figure 3-113. The conversion increased to 12% after 77 hours on stream and decreased gradually to around 6% after 485 hours. Once the system reached steady state the temperature was increased from 220 ^{o}C to 240 ^{o}C whereupon the conversion increased from 5% to 21%, before dropping to approximately 16% after 240 hours on stream at 240 ^{o}C (967 hours total). Upon returning the temperature to 220 ^{o}C, the conversion decreased to around 5%, suggesting the effect of increasing the temperature was transient, having no permanent effect on the catalyst. The temperature was then increased after 1206 hours on stream to 230 ^{o}C, resulting in a small increase in the conversion from 5% to 8%. Steady state was reached comparatively quickly at around 6-7% conversion.

3.8.4.2 Deactivation

From the conversion data, deactivation constants were calculated at each of the temperatures. Figures 3-114 to 3-116 show the graphs of ln[Xa/(1-Xa)] versus time on stream for each temperature of the FT reaction, with the gradient of each slope equal to $-k_d$. From the gradients of these slopes, the rate constants for deactivation were calculated and are shown in table 3.5. For 220 ^{o}C, the deactivation constant was calculated from 53 to 486 hours TOS. The deactivation constant for 240 ^{o}C was calculated from the range 726-967 hours TOS with that of 230 ^{o}C being measured in the range 1230-1373 hours TOS.

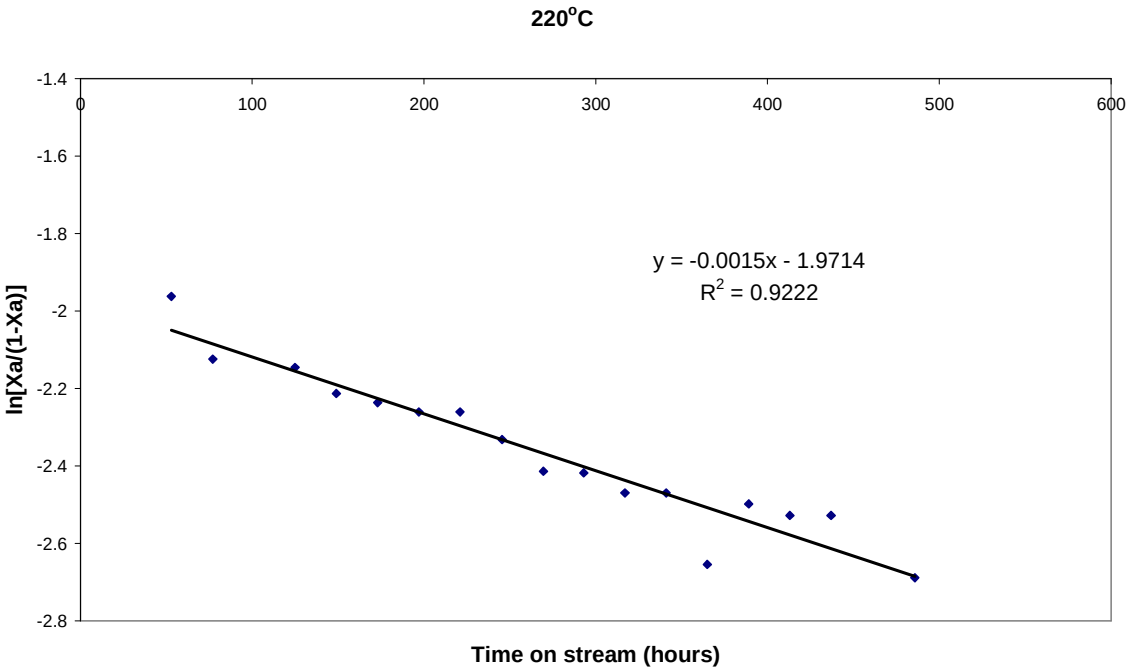

Figure 3-114: Graph of ln[Xa/(1-Xa)] vs. time on stream for FT reaction at 220 ^{o}C.

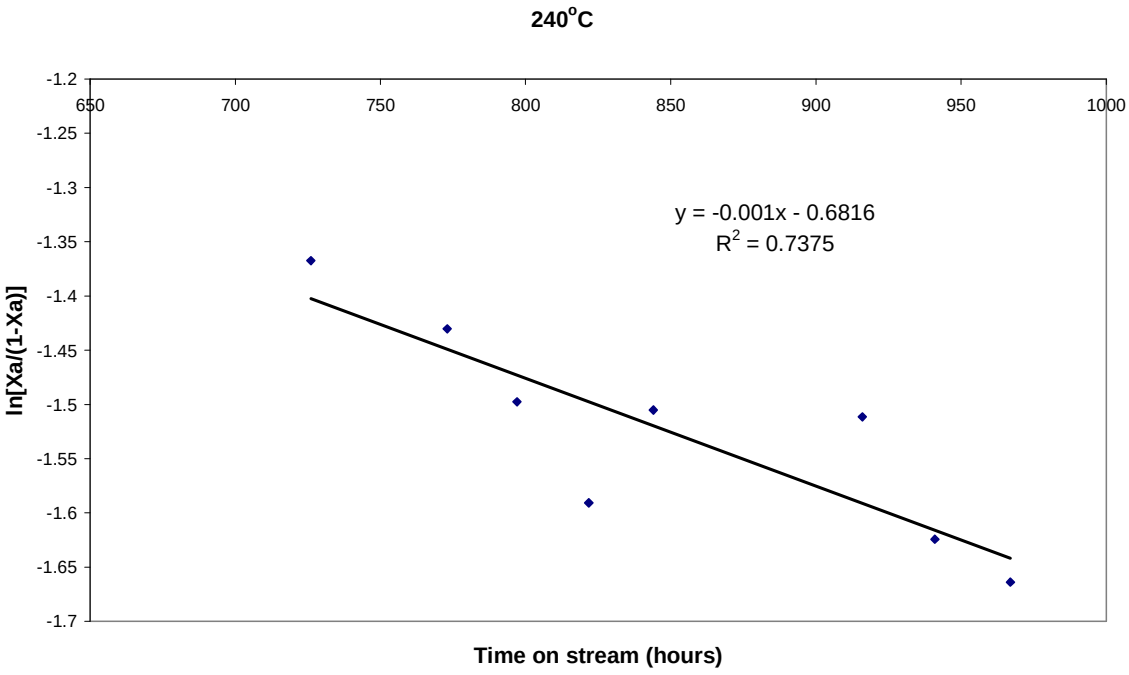

Figure 3-115: Graph of ln[Xa/(1-Xa)] vs. time on stream for FT reaction at 240 °C.

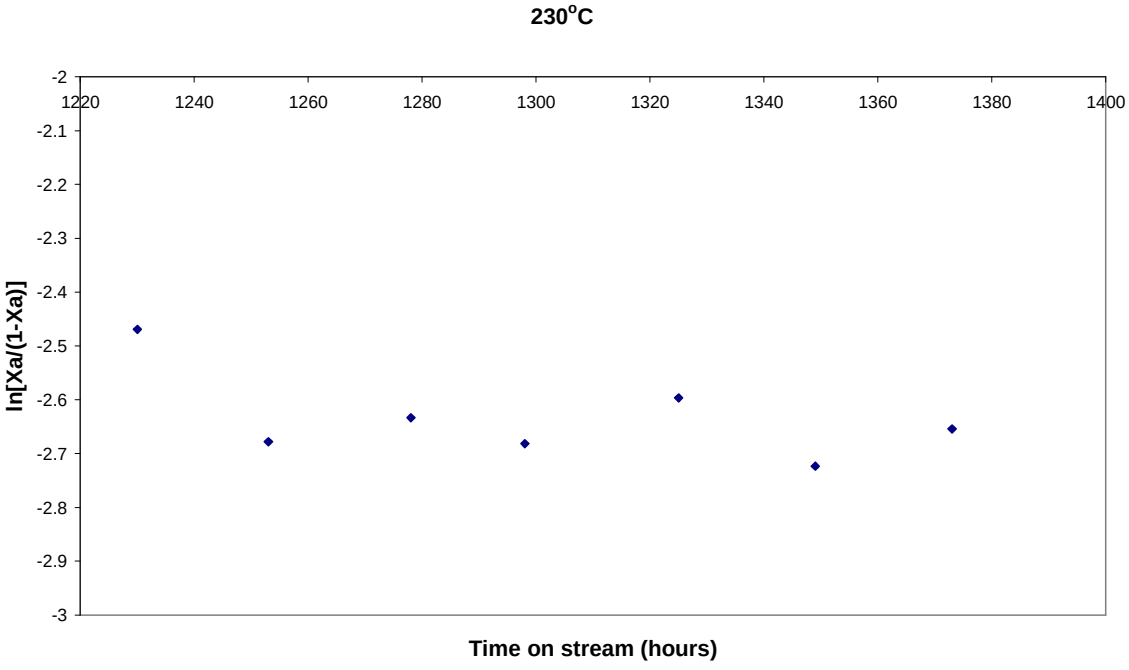

Figure 3-116: Graph of ln[Xa/(1-Xa)] vs. time on stream for FT reaction at 230 °C.

Table 3-6: Deactivation constants as calculated from the conversion for the CoNZC catalyst

Temperature (^{o}C)	Deactivation Constant (hr^{-1})
220	0.0015
240	0.001
230	-

It can be seen from the table (3-6) that the rate of deactivation was similar at 220 ^{o}C and 240 ^{o}C for the CoNZC catalyst. The deactivation constant could not be calculated at 230 ^{o}C. As seen from the figure 3-113, the reaction has almost reached steady state and any attempt to generate a deactivation constant would be heavily dependent upon the first point (8% at 1230 hours TOS).

3.8.4.3 Alpha values

Figures 3-117 to 3-120 show the plots of alpha values versus time on stream at reaction temperature of 220 ^{o}C, 240 ^{o}C, 220 ^{o}C and 230 ^{o}C. From these graphs it is clear that the reaction temperature had an influence on the selectivity of Fischer Tropsch products. Figure 3-117 shows that at a reaction temperature of 220 ^{o}C the alpha value increased steadily with TOS reaching steady state after 581 hours giving an average alpha value of 0.9. Increasing the reaction temperature to 240 ^{o}C caused a decrease in alpha values which, once steady state has been reached, gave an average value of 0.85. Returning the reaction temperature to 220 ^{o}C caused an steady increase of alpha values with time on stream, eventually reaching the same value as before (0.9). On increasing the temperature to 230 ^{o}C the alpha value decreased reaching an average value of 0.88 at steady state.

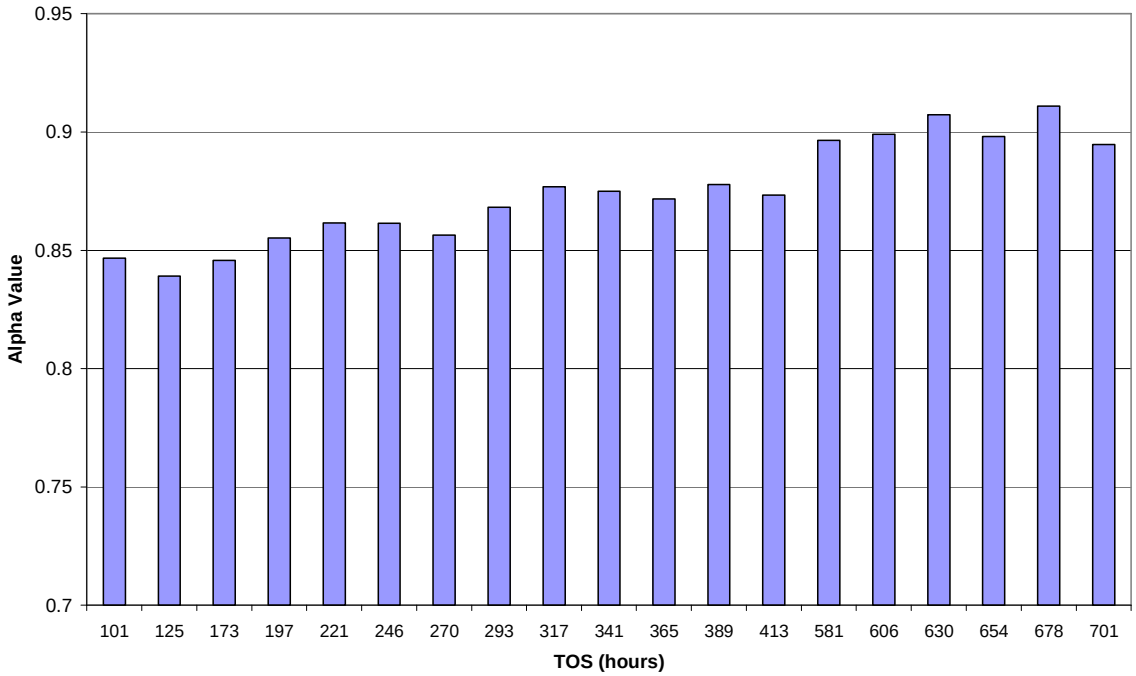

Figure 3-117: Alpha values versus time on stream for CoNZC catalyst at reaction temperature of 220 ^{o}C

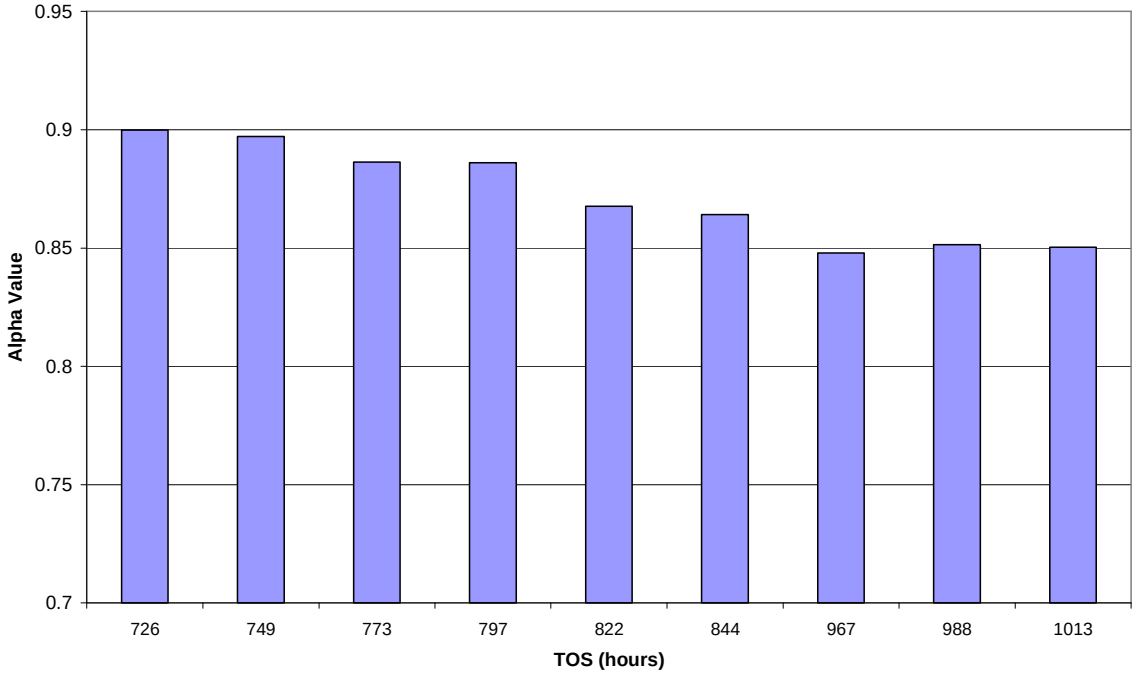

Figure 3-118: Alpha values versus time on stream for CoNZC catalyst at reaction temperature of 240 ^{o}C

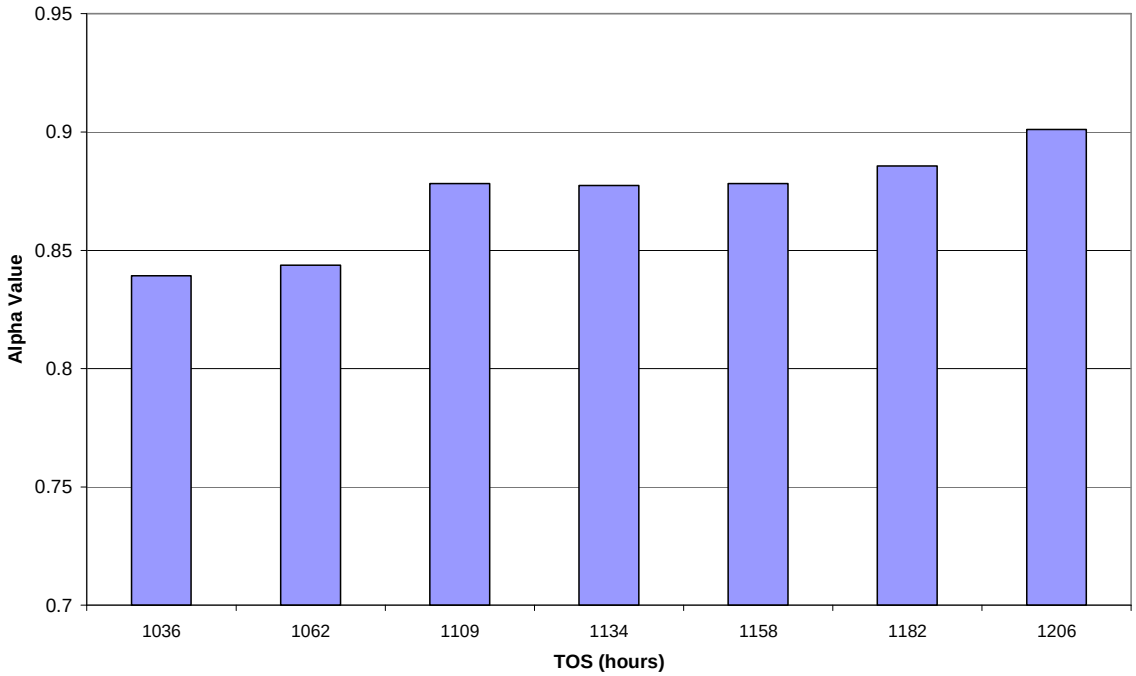

Figure 3-119: Alpha values versus time on stream for CoNZC catalyst at reaction temperature of 220 ^{o}C

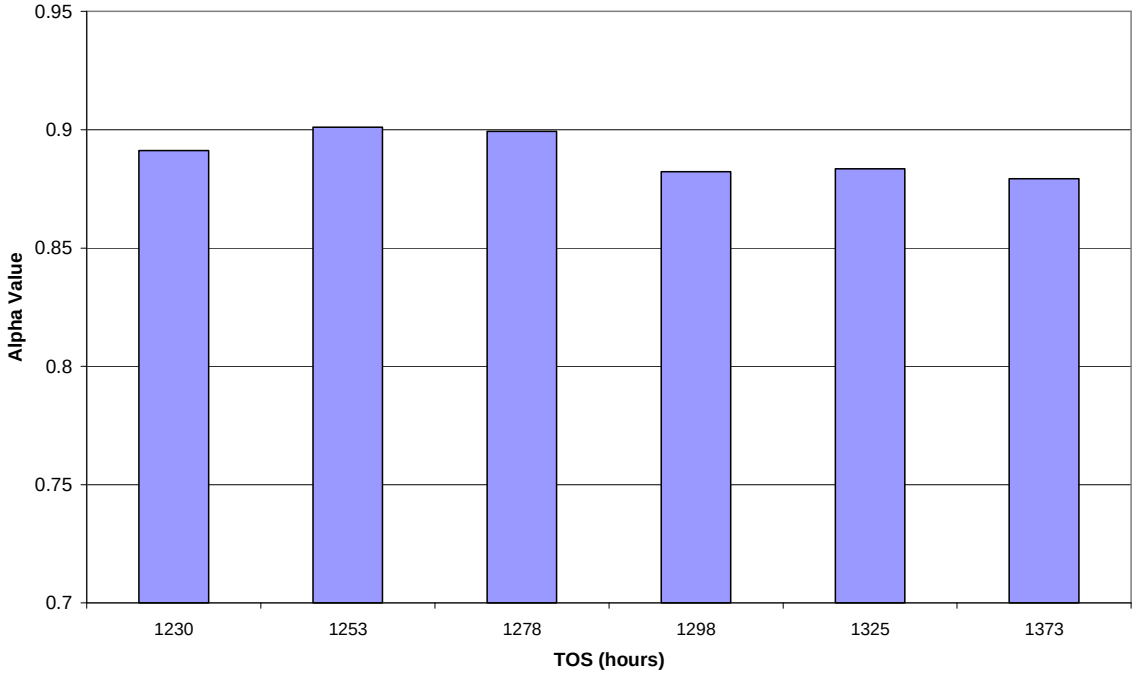

Figure 3-120: Alpha values Alpha values versus time on stream for CoNZC catalyst at reaction temperature of 230 ^{o}C

3.8.4.4 Product distribution of liquid hydrocarbons and waxes

Figure 3-121 to 3-141 show the selectivity of both the liquid hydrocarbons and wax products at various times on stream. At 53 hours TOS, only liquid hydrocarbons are being detected no wax products were observed. At 220 ^{o}C, it can be seen that the product distribution moves towards production of heavier hydrocarbons in both the liquid hydrocarbons and waxes with time on stream. On increasing the reaction temperature to 240 ^{o}C, the hydrocarbon selectivity shifted towards lower molecular weight products. A similar although less pronounced effect is seen when increasing the temperature to 230 ^{o}C.

3.8.4.4.1 53 hours TOS

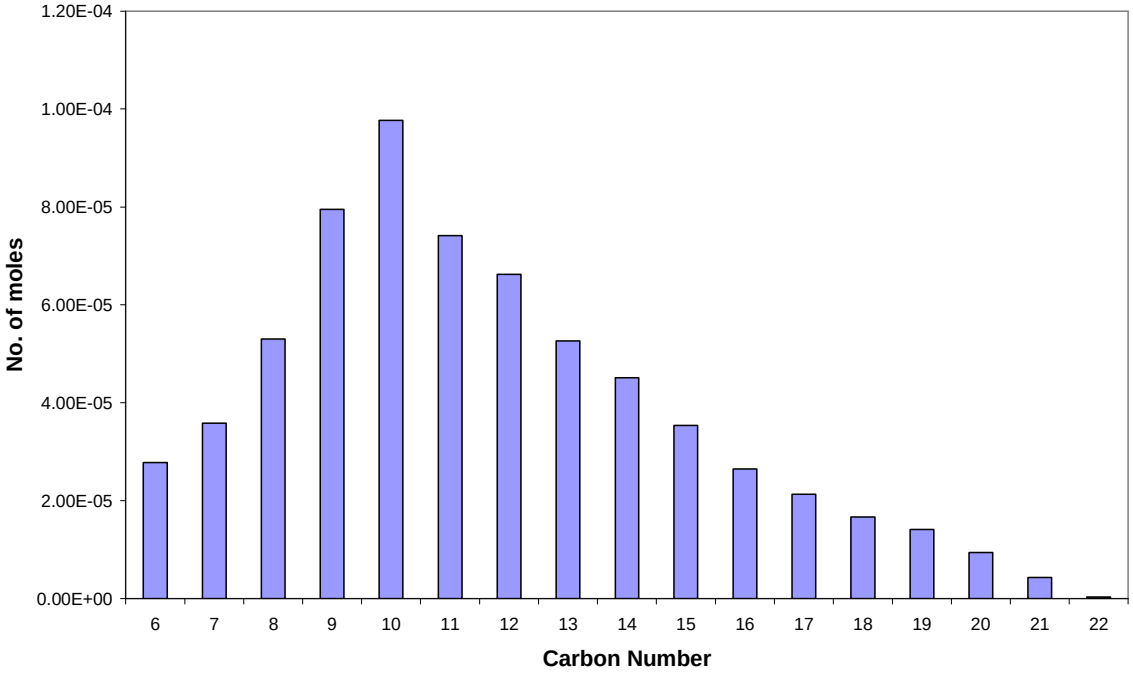

Figure 3-121: Hydrocarbon product distribution as a function of carbon number for CoNZC catalyst liquid hydrocarbon sample at 53 hours TOS (T=220 ^{o}C)

3.8.4.4.2 101 hours TOS

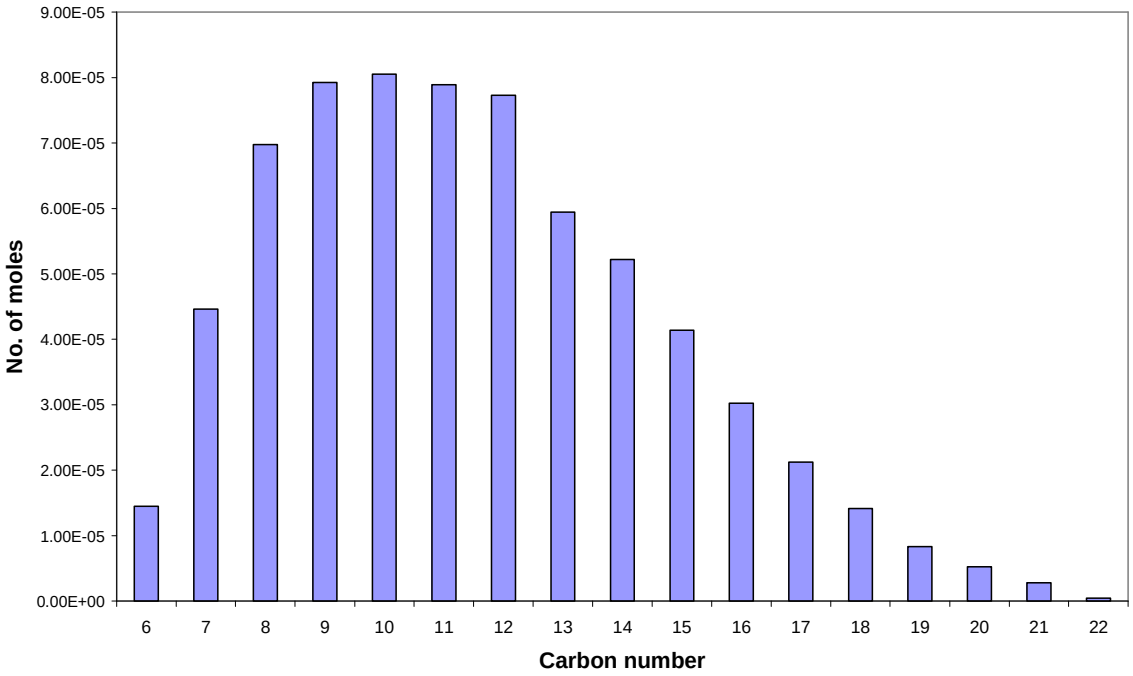

Figure 3-122: Hydrocarbon product distribution as a function of carbon number for CoNZC catalyst liquid hydrocarbon sample at 101 hours TOS (T=220 ^{o}C)

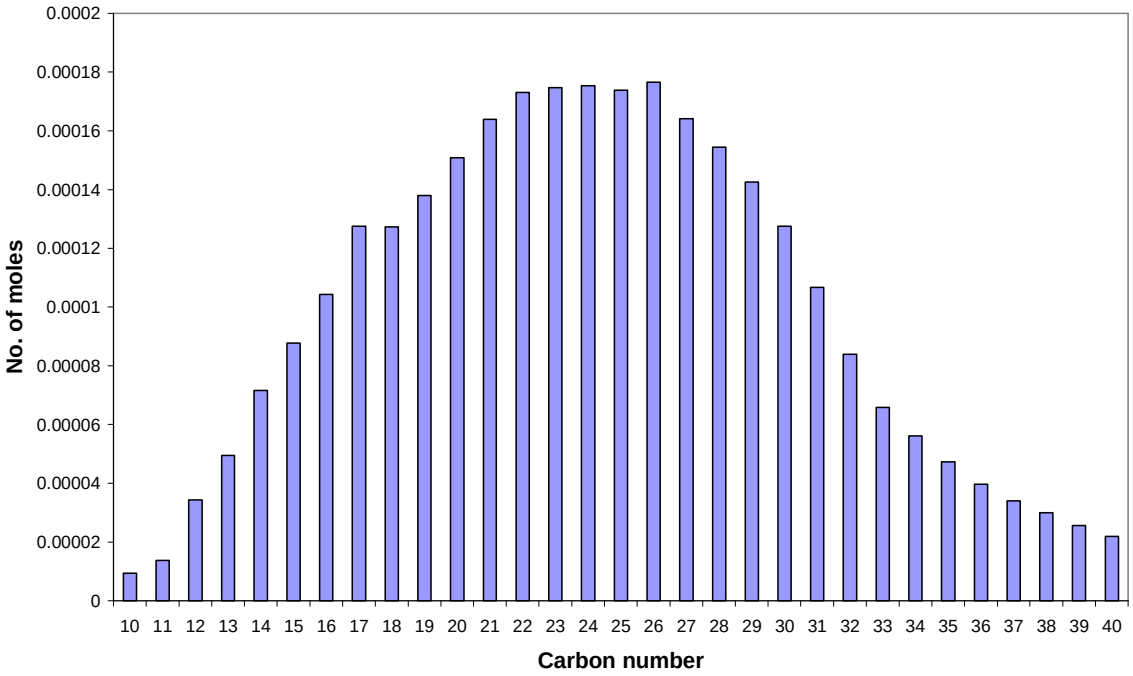

Figure 3-123: Hydrocarbon product distribution as a function of carbon number for CoNZC catalyst wax sample at 101 hours TOS (T=220 ^{o}C)

3.8.4.4.3 341 hour TOS

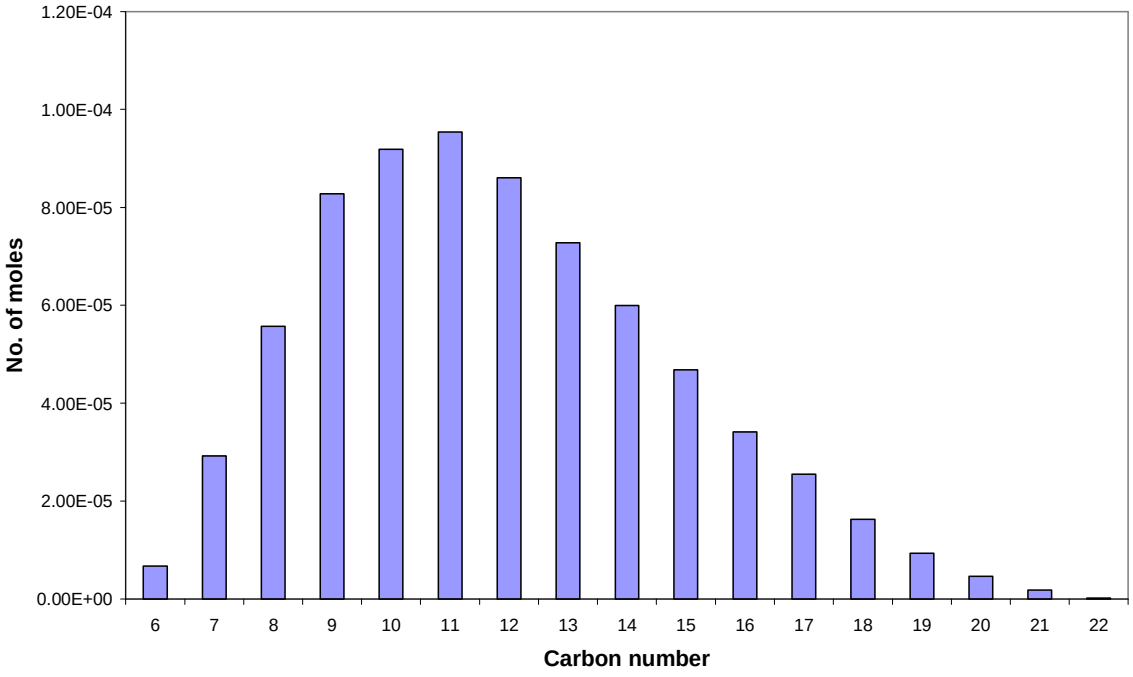

Figure 3-124: Hydrocarbon product distribution as a function of carbon number for CoNZC catalyst liquid hydrocarbon sample at 341 hours TOS (T=220 ^{o}C)

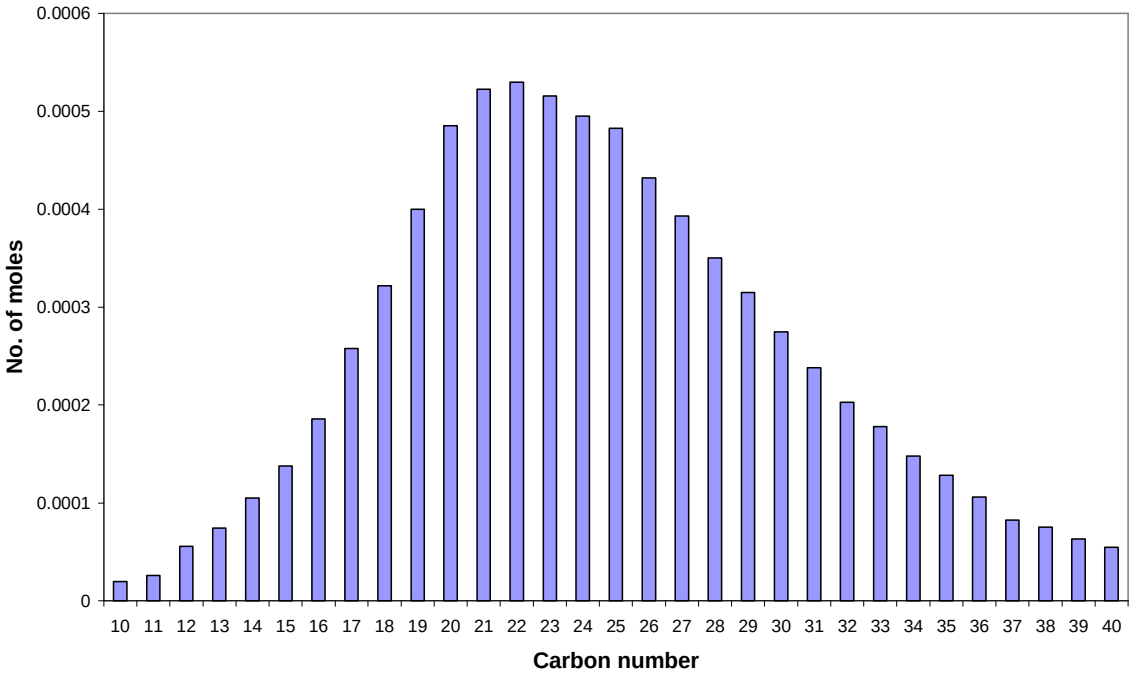

Figure 3-125: Hydrocarbon product distribution as a function of carbon number for CoNZC catalyst wax sample at 341 hours TOS (T=220 ^{o}C)

3.8.4.4.4 678 hour TOS

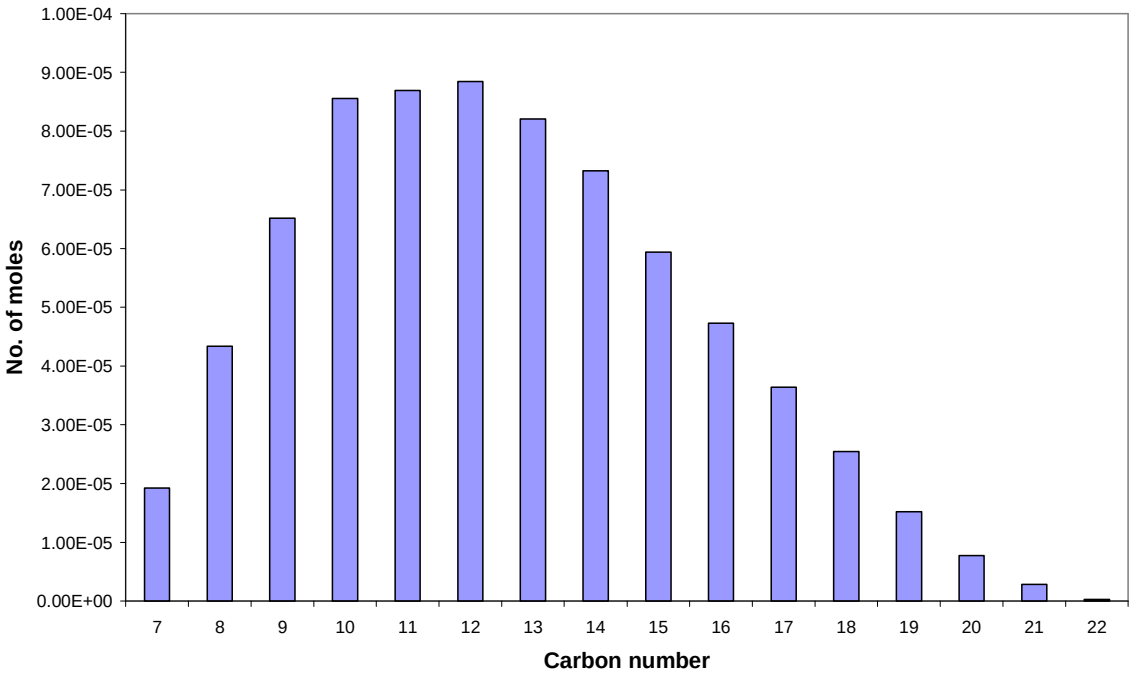

Figure 3-126: Hydrocarbon product distribution as a function of carbon number for CoNZC catalyst liquid hydrocarbon sample at 678 hours TOS (T=220 ^{o}C)

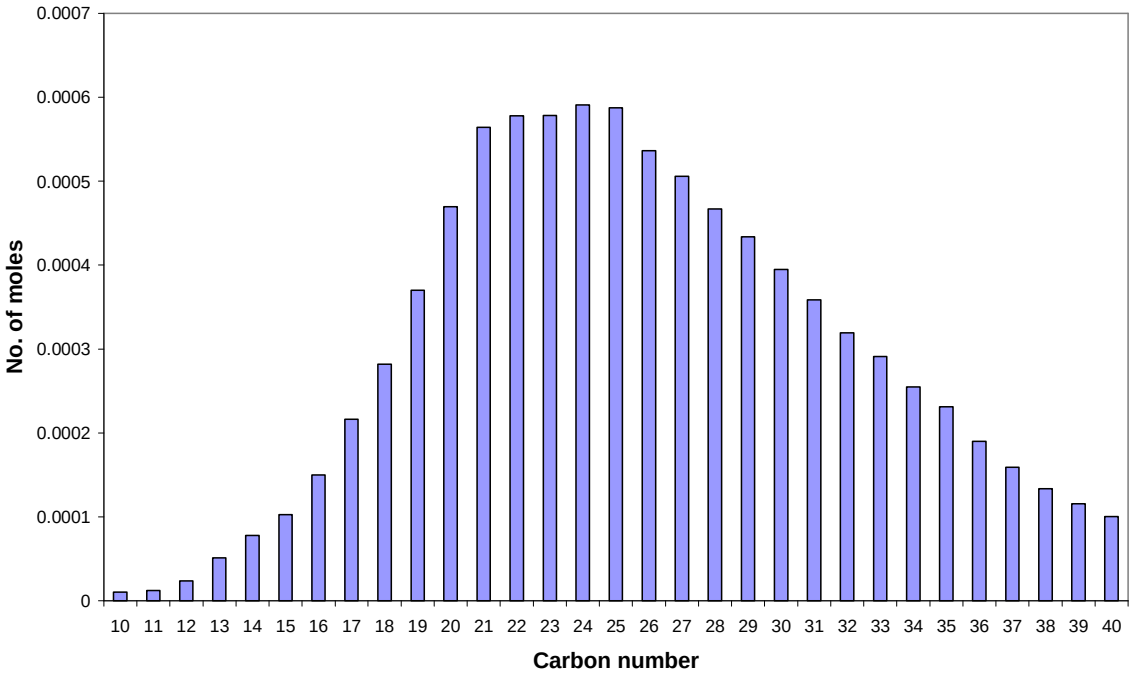

Figure 3-127: Hydrocarbon product distribution as a function of carbon number for CoNZC catalyst wax sample at 678 hours TOS (T=220 ^{o}C)

3.8.4.4.5 726 hours TOS

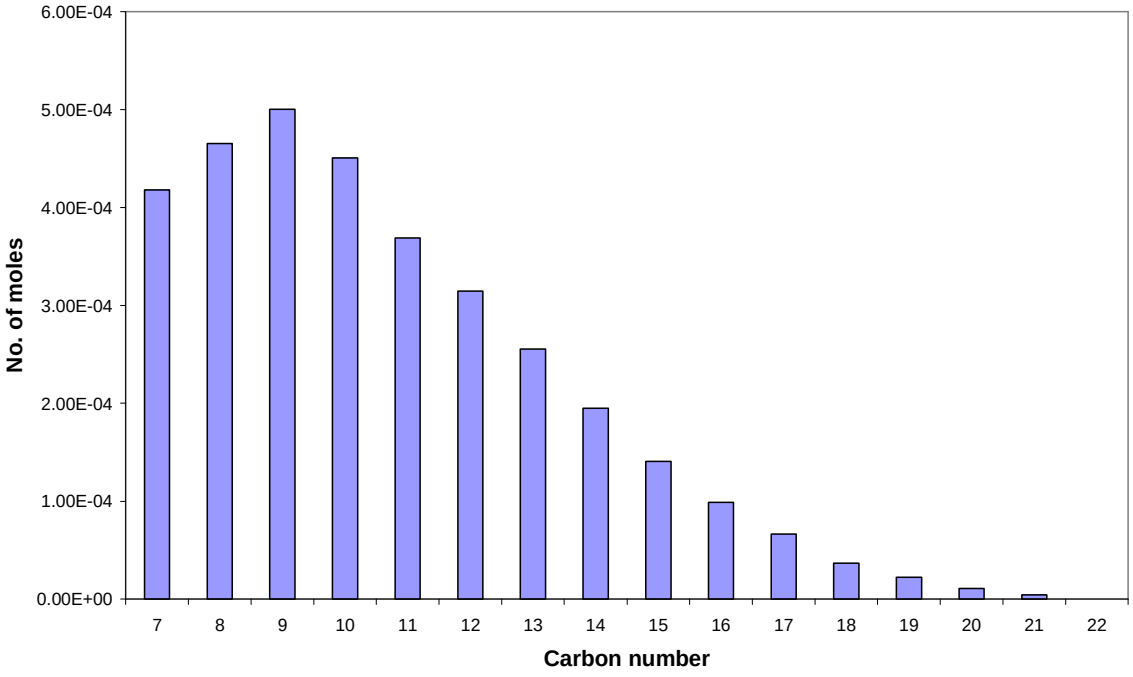

Figure 3-128: Hydrocarbon product distribution as a function of carbon number for CoNZC catalyst liquid hydrocarbon sample at 726 hours TOS (T=240 ^{o}C)

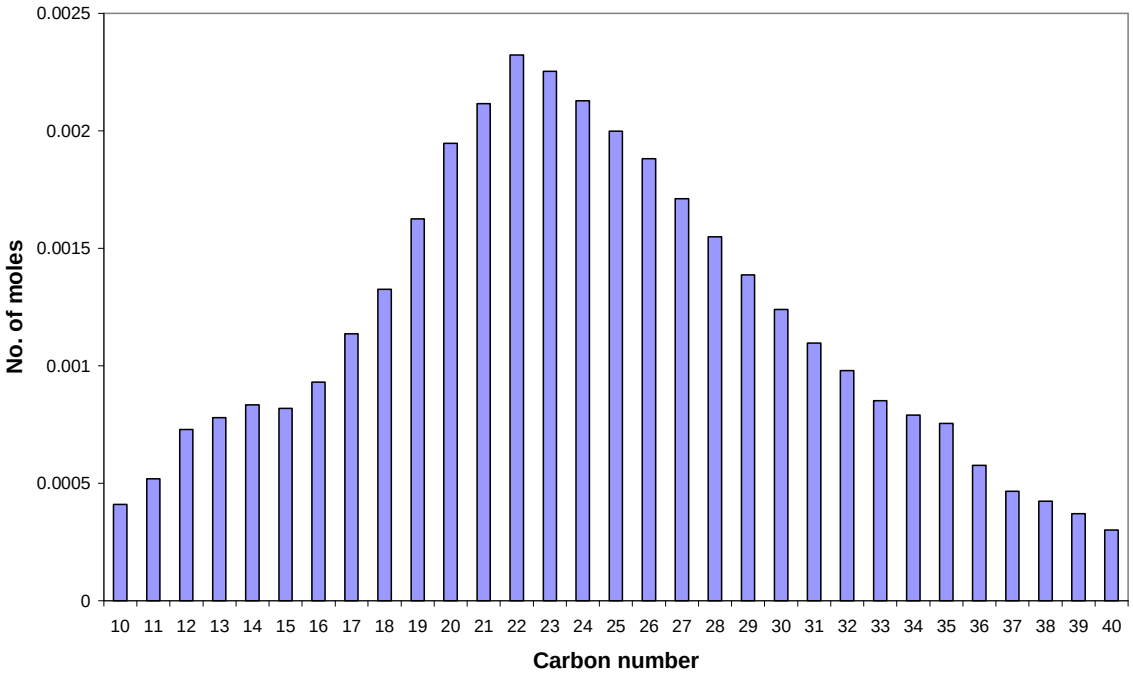

Figure 3-129: Hydrocarbon product distribution as a function of carbon number for CoNZC catalyst wax sample at 726 hours TOS (T=240 ^{o}C)

3.8.4.4.6 916 hours TOS

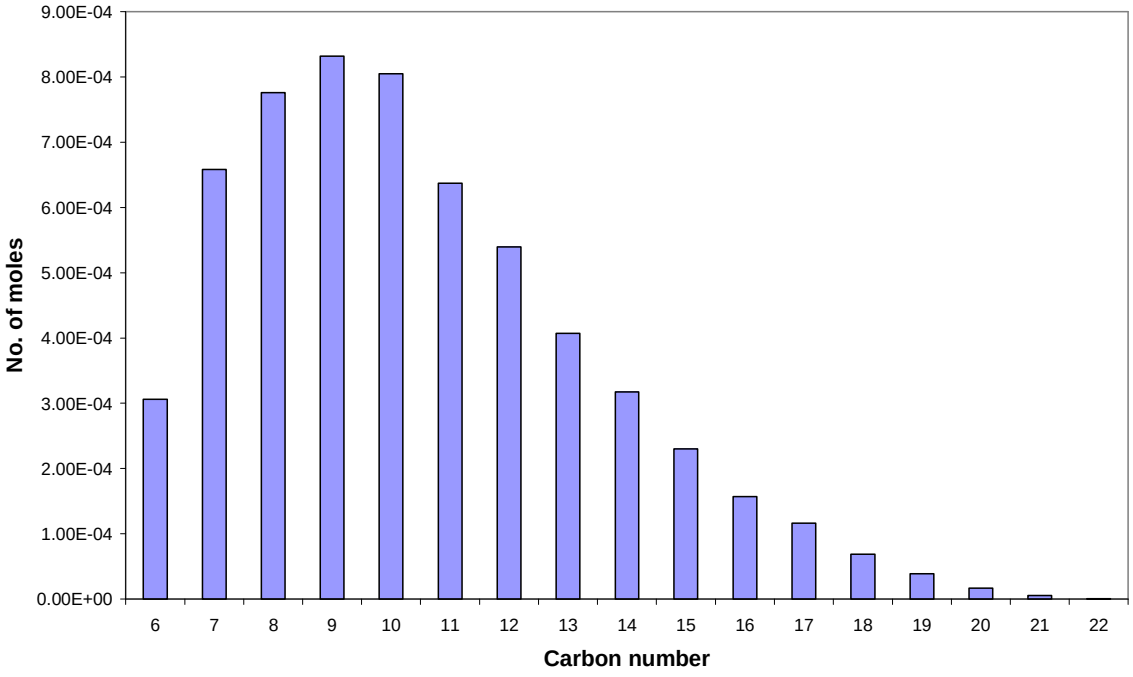

Figure 3-130: Hydrocarbon product distribution as a function of carbon number for CoNZC catalyst liquid hydrocarbon sample at 916 hours TOS (T=240 ^{o}C)

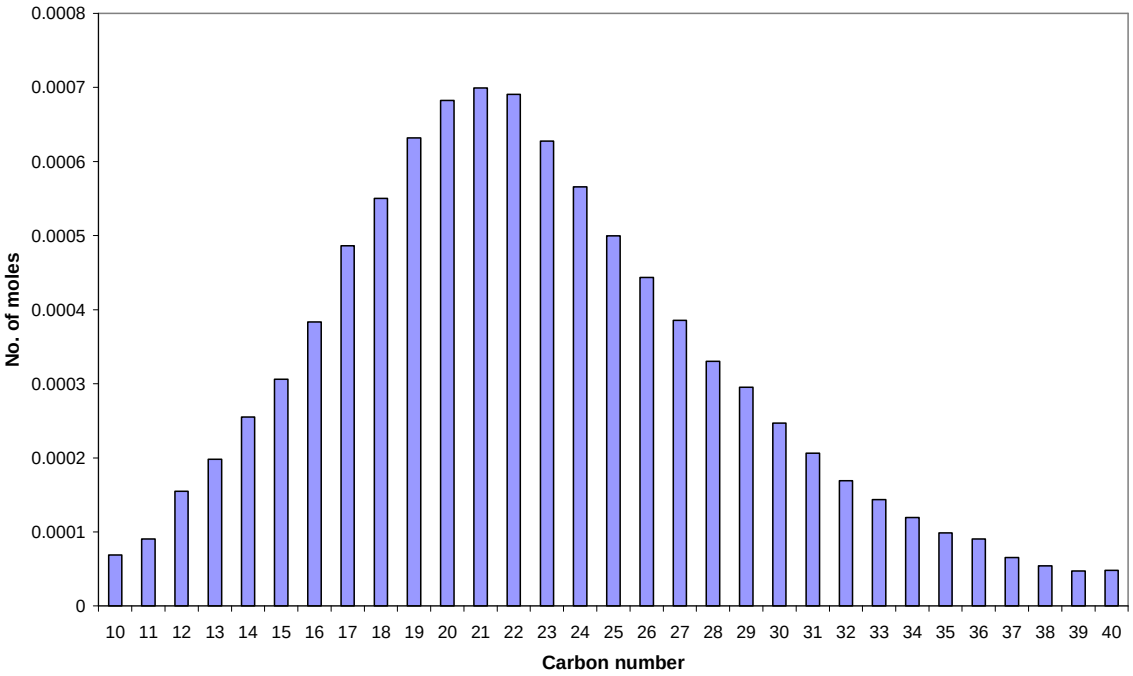

Figure 3-131: Hydrocarbon product distribution as a function of carbon number for CoNZC catalyst wax sample at 916 hours TOS (T=240 ^{o}C)

3.8.4.4.7 1013 hours TOS

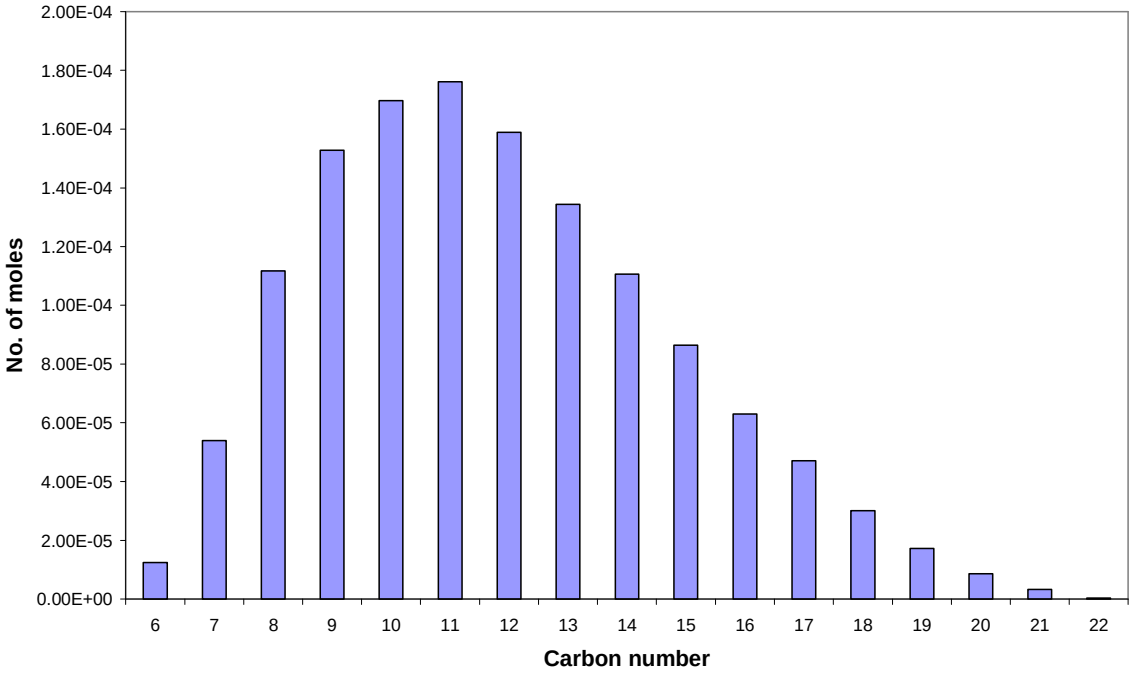

Figure 3-132: Hydrocarbon product distribution as a function of carbon number for CoNZC catalyst liquid hydrocarbon sample at 1013 hours TOS (T=240 ^{o}C)

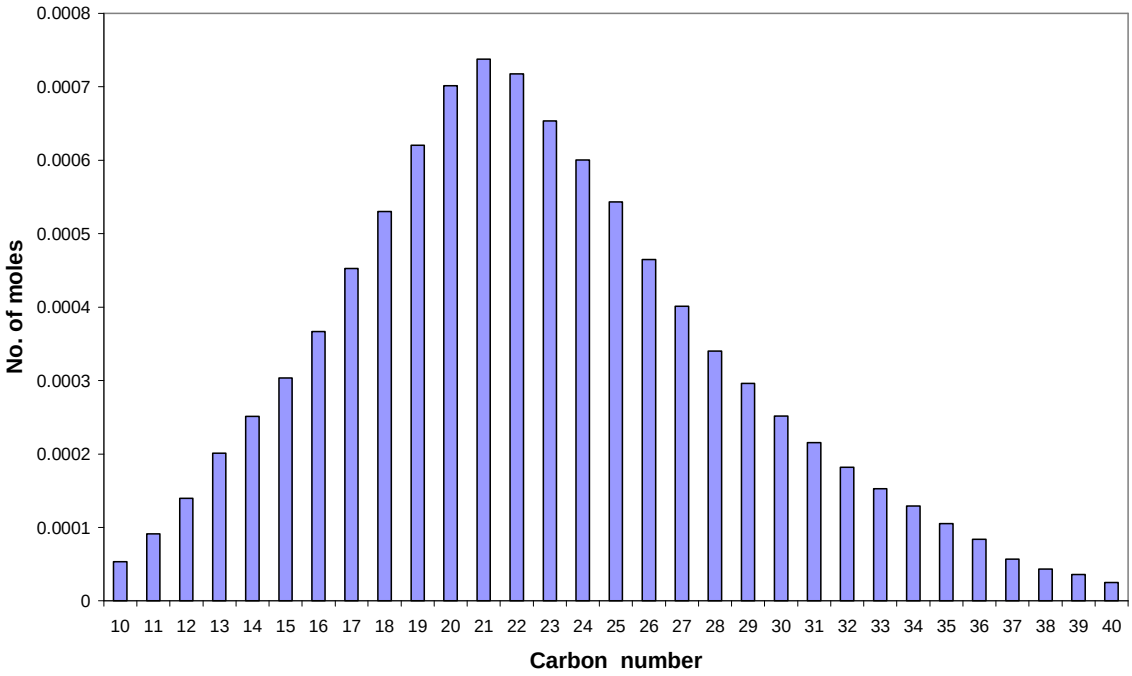

Figure 3-133: Hydrocarbon product distribution as a function of carbon number for CoNZC catalyst wax sample 1013 hours TOS (T=240 ^{o}C)

3.8.4.4.8 1062 hour TOS

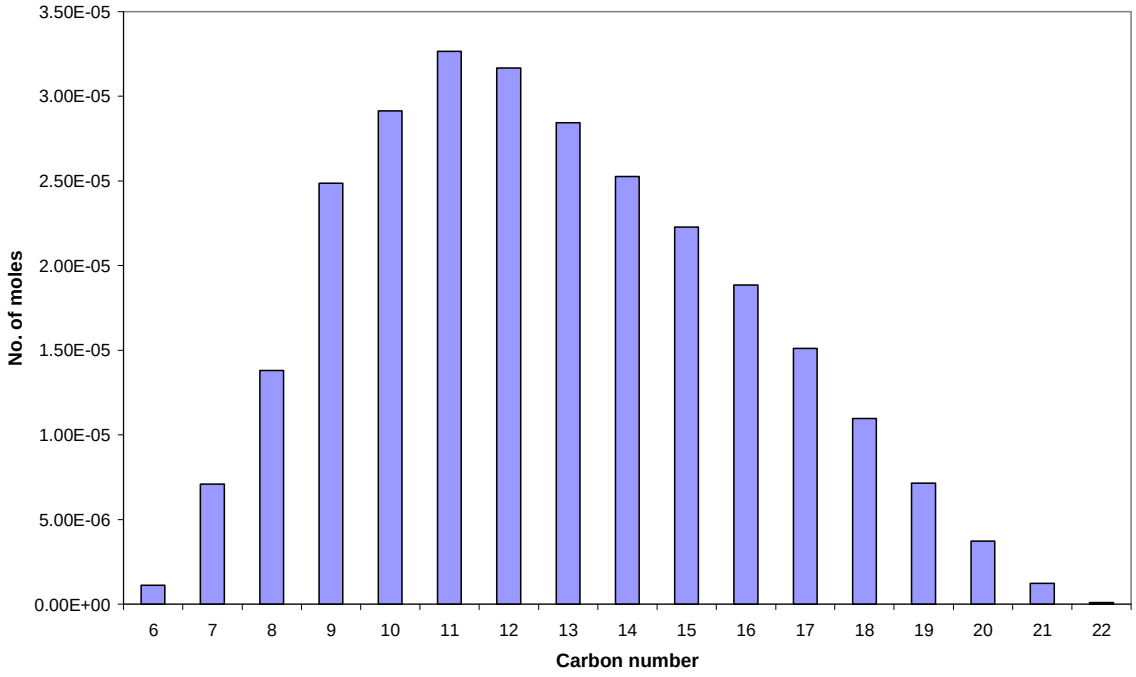

Figure 3-134: Hydrocarbon product distribution as a function of carbon number for CoNZC catalyst liquid hydrocarbon sample at 1062 hours TOS (T=220 ^{o}C)

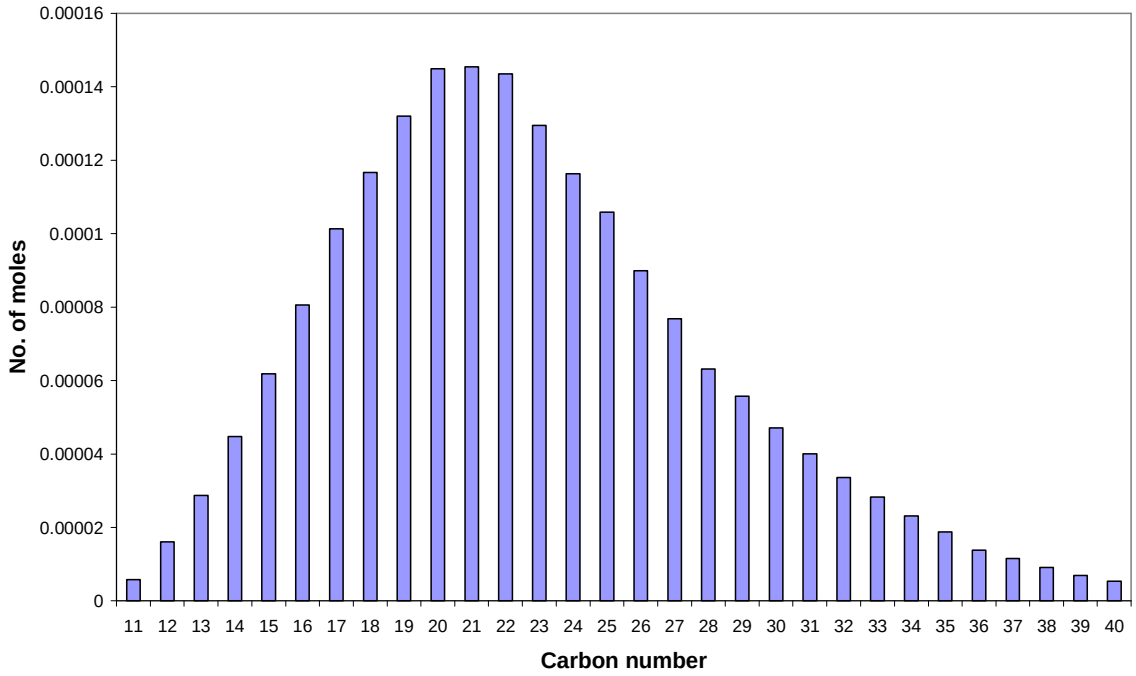

Figure 3-135: Hydrocarbon product distribution as a function of carbon number for CoNZC catalyst wax sample at 1062 hours TOS (T=220 ^{o}C)

3.8.4.4.9 1182 hour TOS

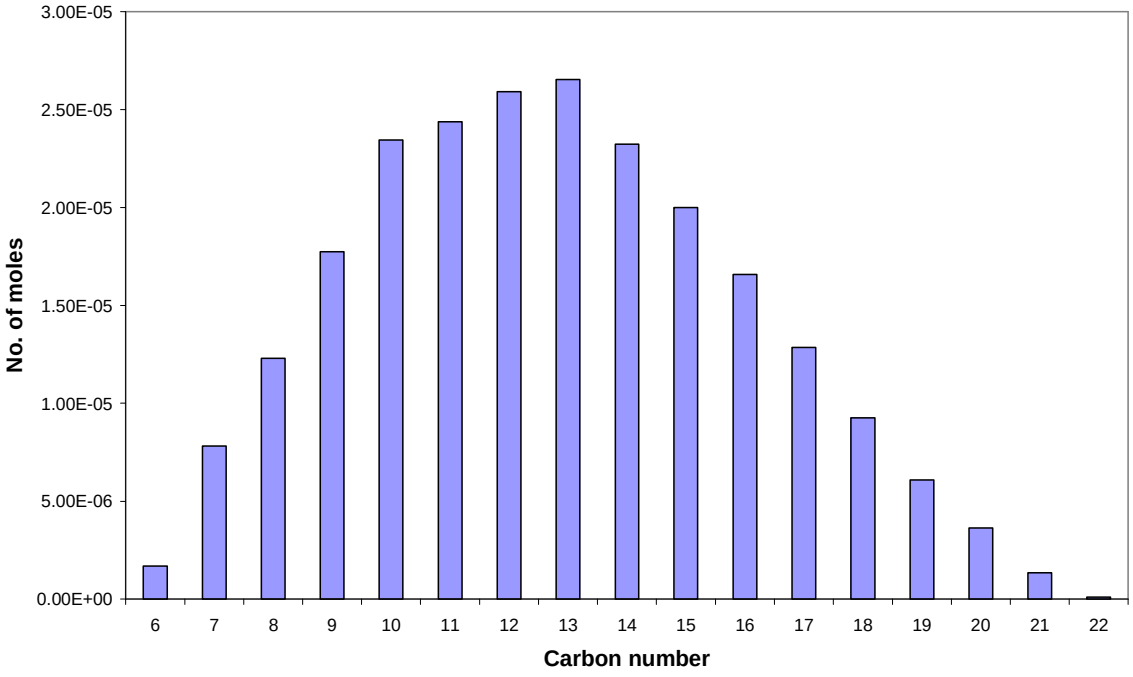

Figure 3-136: Hydrocarbon product distribution as a function of carbon number for CoNZC catalyst liquid hydrocarbon sample at 1182 hours TOS (T=220 ^{o}C)

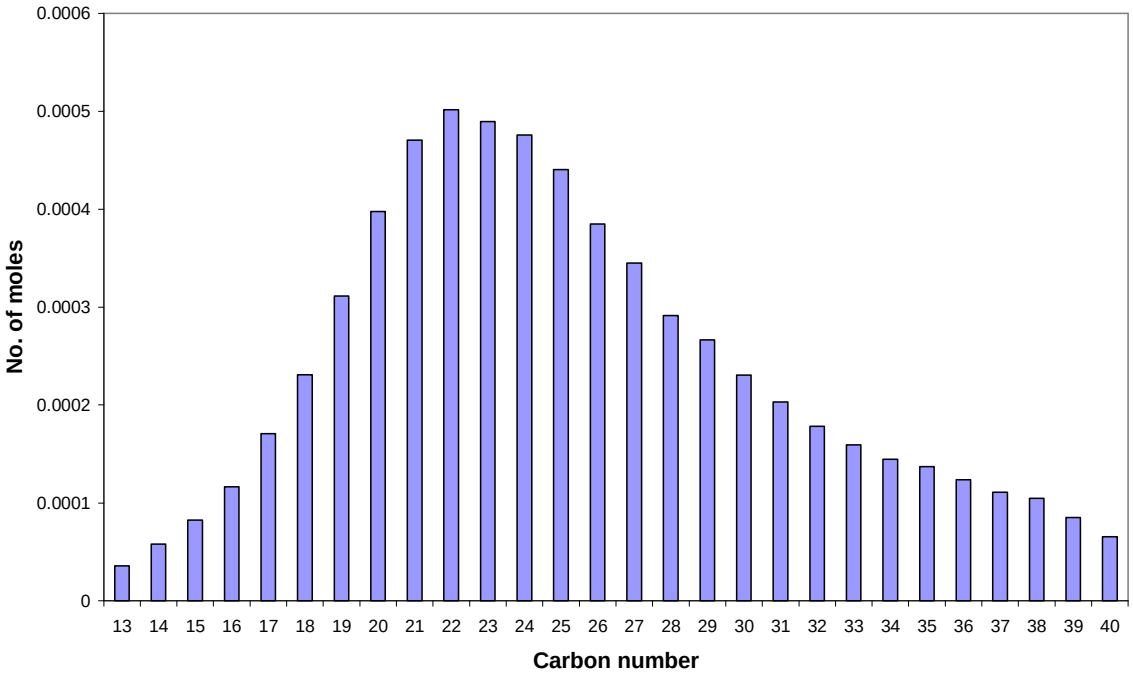

Figure 3-137: Hydrocarbon product distribution as a function of carbon number for CoNZC catalyst wax sample at 1182 hours TOS (T=220 ^{o}C)

3.8.4.4.10 1278 hours TOS

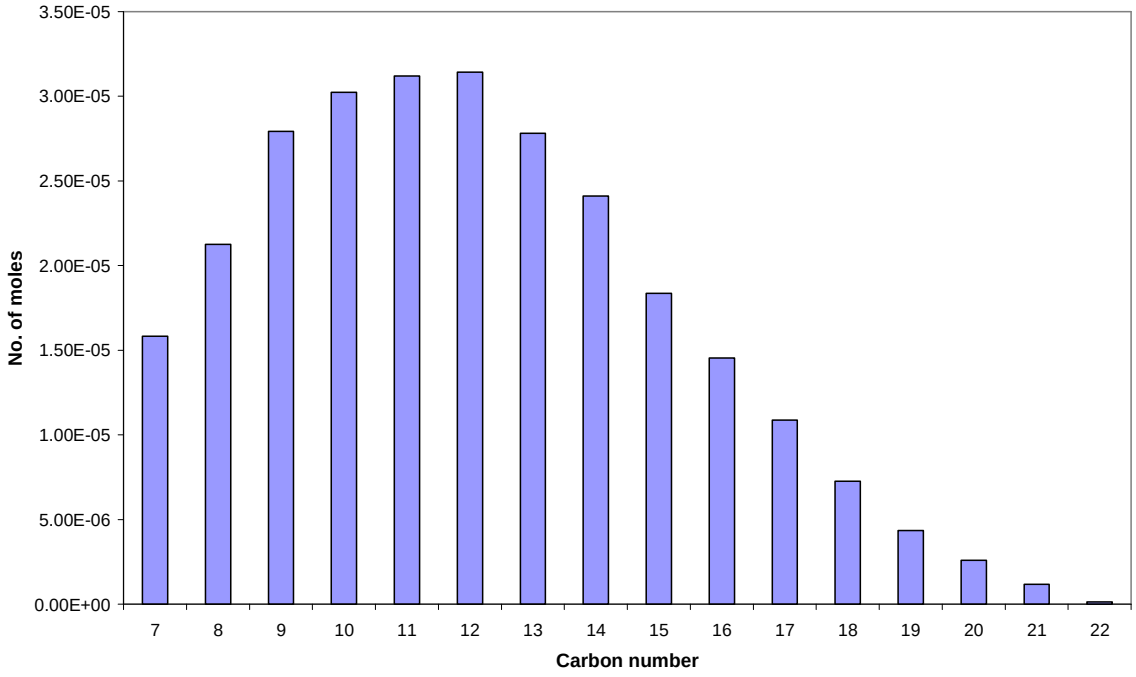

Figure 3-138: Hydrocarbon product distribution as a function of carbon number for CoNZC catalyst liquid hydrocarbon sample at 1278 hours TOS (T=230 ^{o}C)

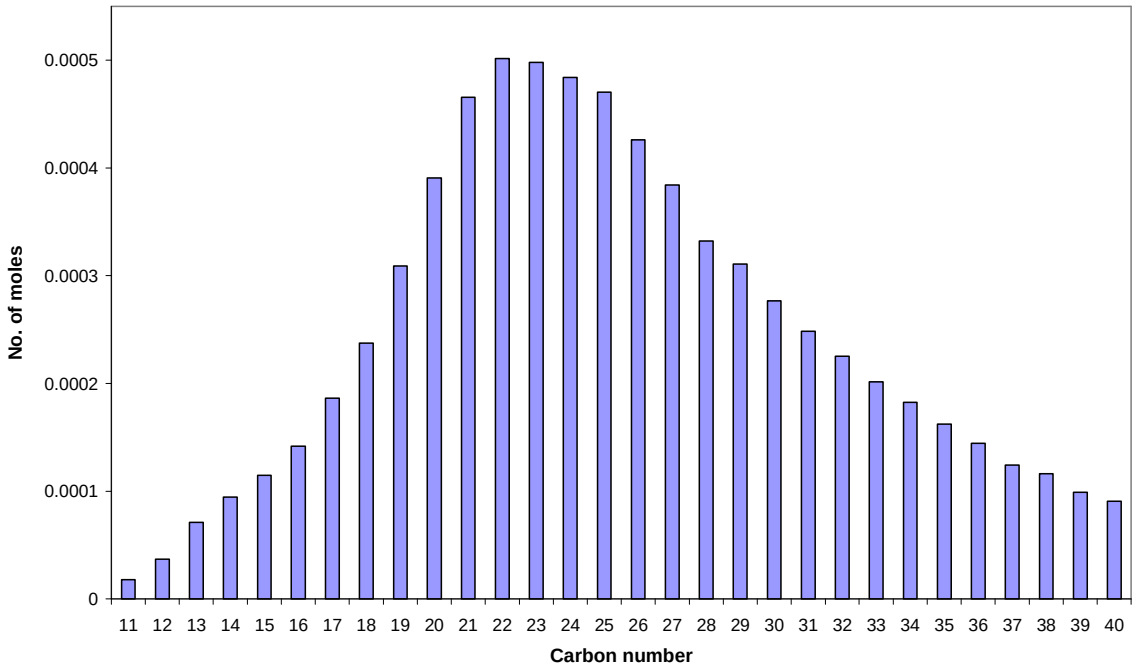

Figure 3-139: Hydrocarbon product distribution as a function of carbon number for CoNZC catalyst wax sample at 1278 hours TOS (T=230 ^{o}C)

3.8.4.4.11 1373 hours TOS

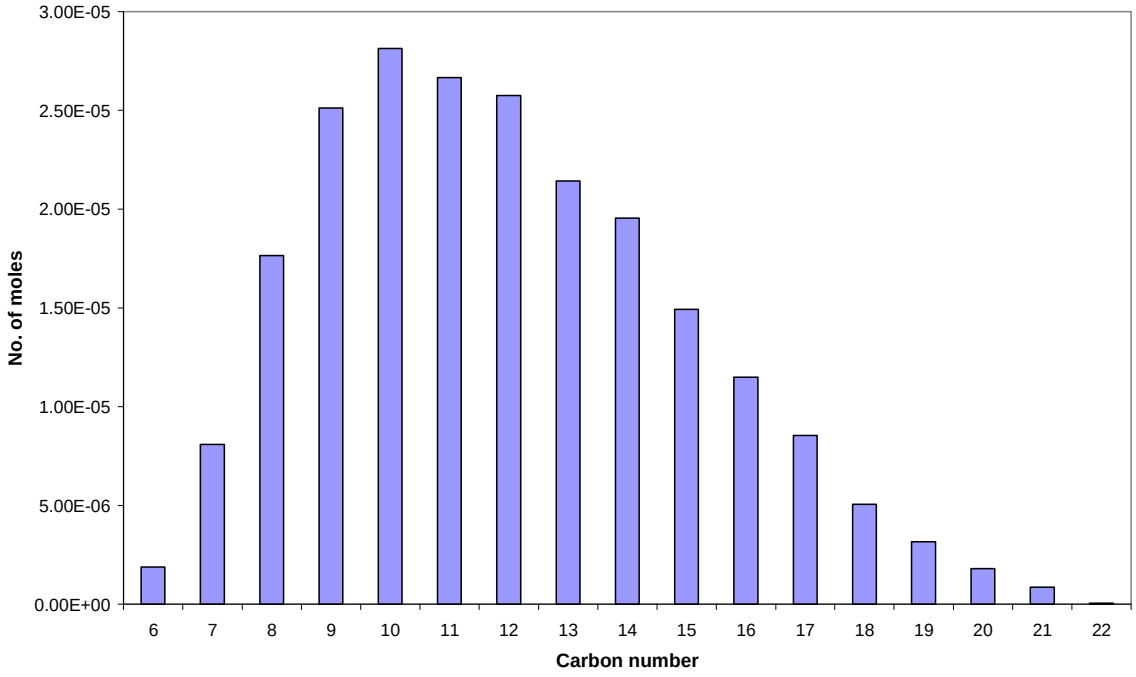

Figure 3-140: Hydrocarbon product distribution as a function of carbon number for CoNZC catalyst liquid hydrocarbon sample at 1373 hours TOS (T=230 ^{o}C)

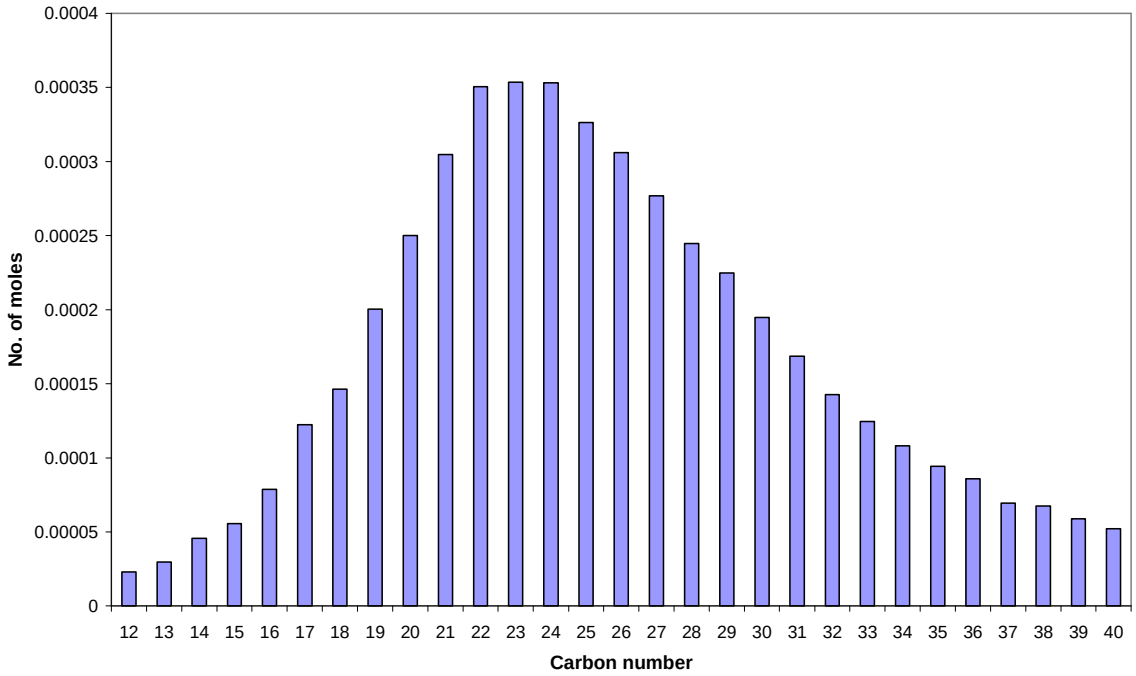

Figure 3-141: Hydrocarbon product distribution as a function of carbon number for CoNZC catalyst wax sample at 1373 hours TOS (T=230 ^{o}C)

3.8.5 Post FT reaction analysis

3.8.5.1 Thermogravimetric analysis-Differential Scanning calorimetry analysis

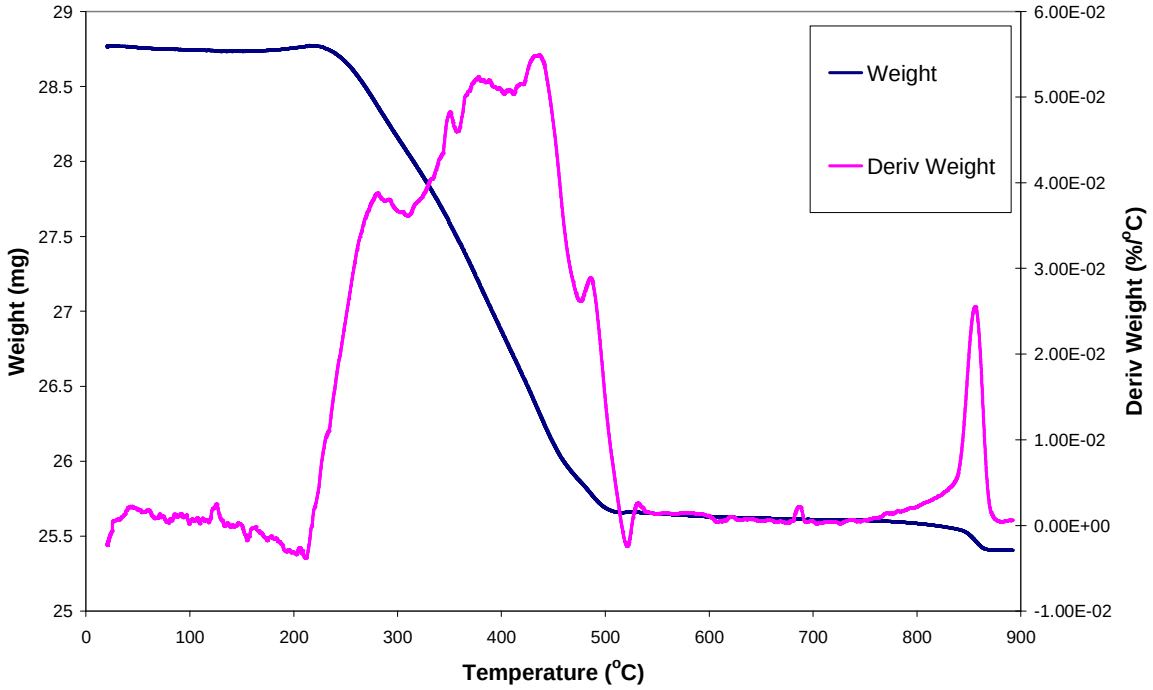

Figure 3-142: TGA weight and derivative weight profiles in oxygen for cobalt nitrate on zinc oxide catalyst (BP calcined) post FT reaction.

The TGA weight loss and derivative weight profile are presented in figure 3-142. From the weight loss curves it can be seen that the majority of weight loss occurs up to ~515 ^{o}C. This weight loss can be observed as a series of overlapping peaks in the derivative weight profile. There is a further high temperature weight loss at around 860 ^{o}C as well as a slight weight gain from 145-225 ^{o}C. From figure 3-143, the weight loss events before 515 ^{o}C can be seen to be exothermic. However, the smaller weight loss observed at higher temperature appears to be endothermic.

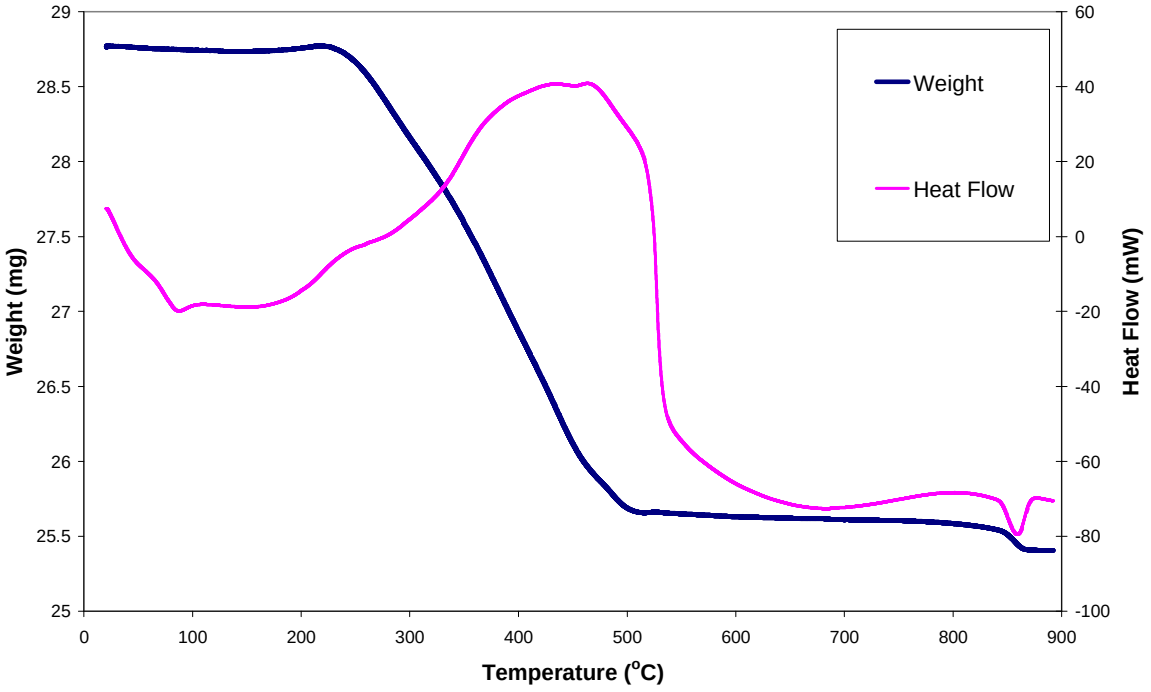

Figure 3-143: TGA-DSC weight and heat flow profiles in oxygen for cobalt nitrate on zinc oxide catalyst (BP calcined) post FT reaction.

3.8.5.1.1 Mass spectrometric analysis

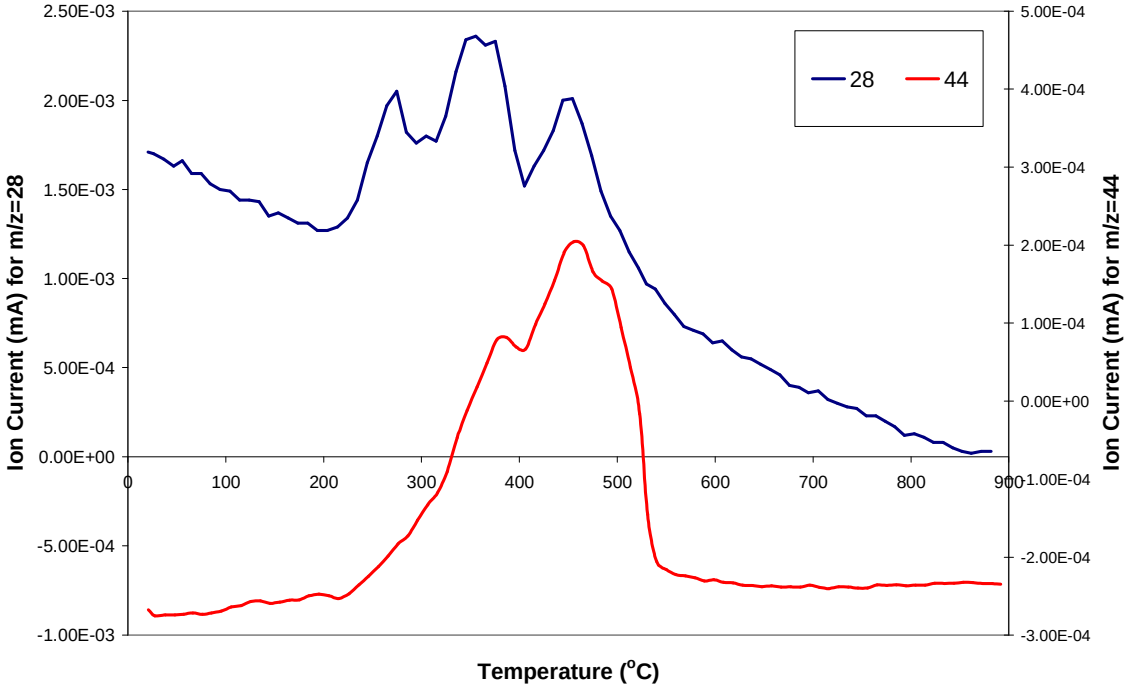

Figure 3-144: Mass spectrometric data of CO (m/z-28) and CO_2 (m/z=44) in oxygen for cobalt on zinc oxide catalyst (BP calcined) post FT reaction.

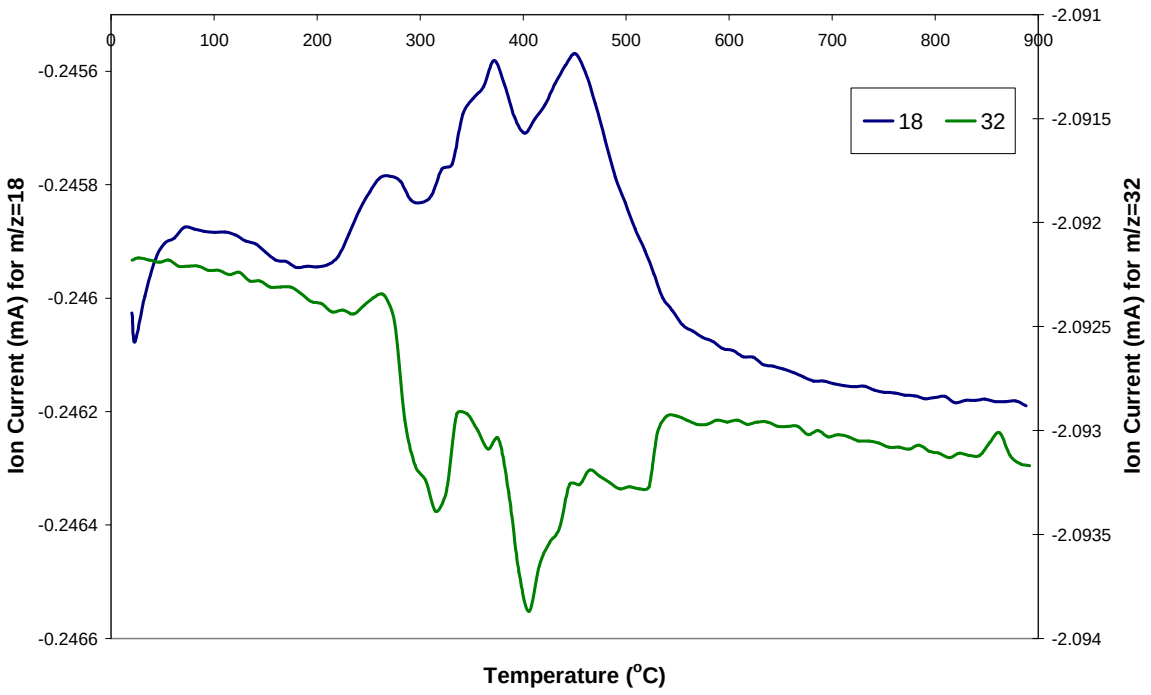

Figure 3-145: Mass spectrometric data of H_2O (m/z=18) and O_2 (m/z=32) in oxygen for cobalt on zinc oxide catalyst (BP calcined) post FT reaction.

Figures 3-144 and 3-144 show the evolution of products from heating the BP calcined cobalt on zinc oxide catalyst in oxygen post FT reaction. The first peak in the derivative weight profile, at about 280 ^{o}C can be seen to correspond to the evolution of water, carbon monoxide and oxygen. As the temperature increases we see the uptake of oxygen and the evolution of water, carbon dioxide and carbon monoxide between 310-515 ^{o}C. The high temperature weight loss is accompanied by the evolution of oxygen.

3.8.5.1.2 X-Ray Diffraction

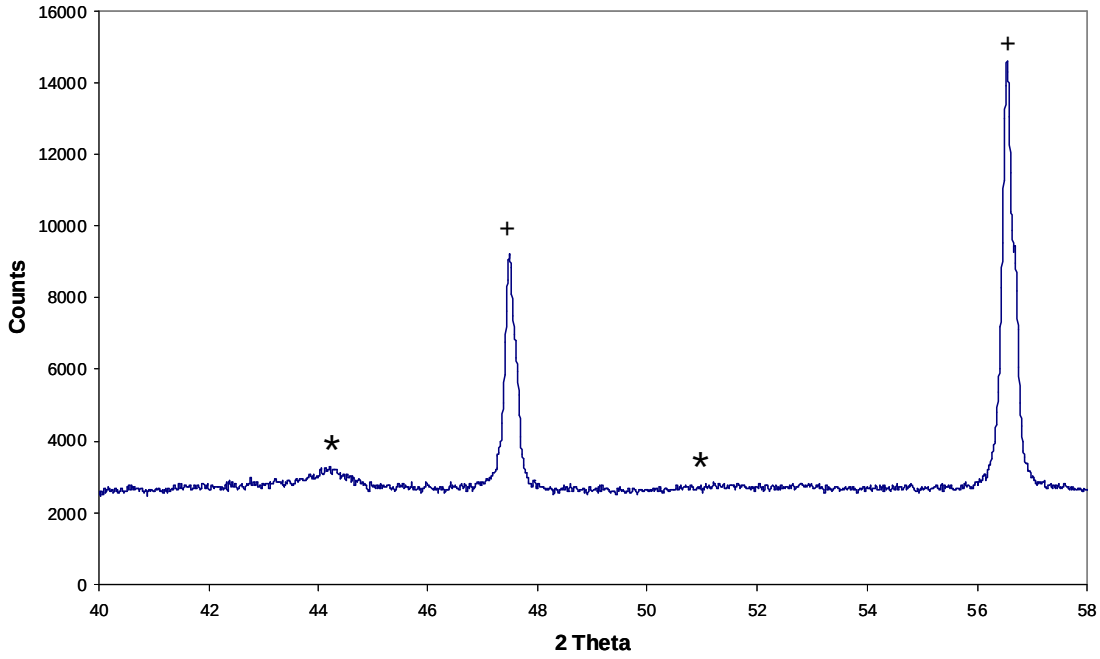

Figure 3-146: X-Ray diffraction pattern for cobalt on zinc oxide (BP calcined) catalyst post FT reaction. The experimental error for cobalt crystallite size calculated from X-ray diffraction is less than +/- 1 nm.

The X-Ray diffraction pattern of CoNZ BP calcined catalyst post reaction is shown in figure 3-146. The location of the peaks confirmed the presence of metallic cobalt. Using the Scherrer equation the average particle size of cobalt was found to be 10 nm. With the exception of cobalt the only other peaks detected were those of the zinc oxide support.

3.9 Cobalt nitrate on Zinc Oxide BP - Not Calcined

This section relates to the cobalt nitrate on zinc oxide catalyst supplied by BP in the uncalcined form. The catalyst was used as received with no calcination prior to characterisation and testing.

3.9.1 Hydrogen treatment

3.9.1.1 Thermogrametric analysis-Differential Scanning Calorimetry analysis

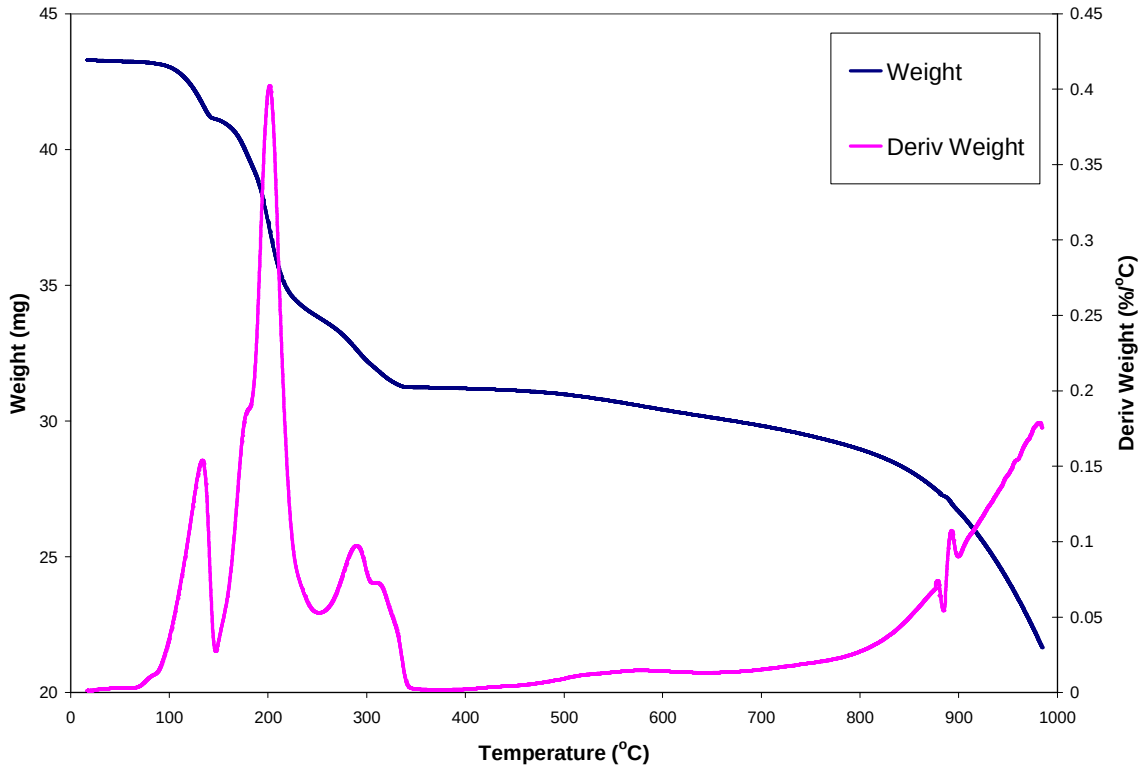

Figure 3-147: TGA weight and derivative weight profiles for cobalt nitrate on zinc oxide in hydrogen.

The derivative weight curve in figure 3-147 comprises of several overlapping peaks, which are probably due to the decomposition of the nitrate precursor and the reduction of the supported cobalt oxide species. There are several overlapping weight losses before 360 ^{o}C with a maximum at 202 ^{o}C. There is also an additional broader weight loss centred at 585 ^{o}C. However, the complexity of the derivative weight profiles makes it difficult to draw any conclusions in regard to the attribution of the peaks. It can be seen from the DSC data in figure 3-148 that the decomposition in hydrogen involves both endothermic and exothermic events.

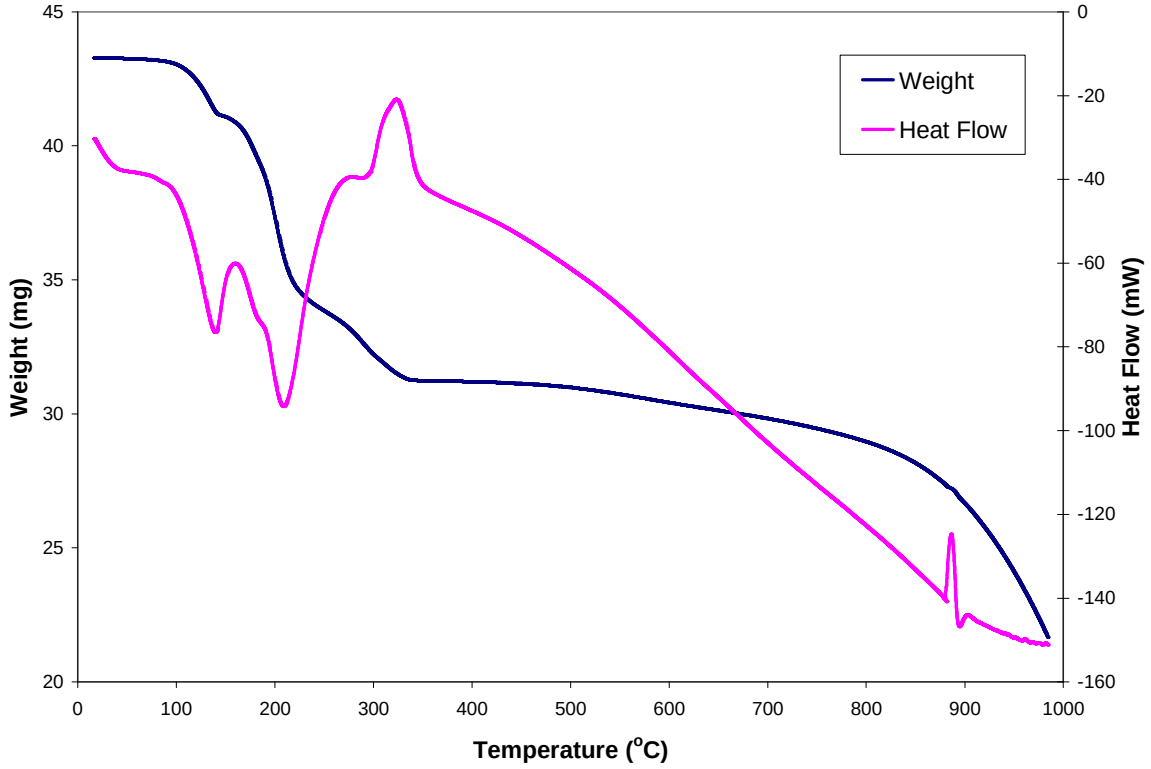

Figure 3-148: TGA-DSC weight and heat flow profiles for cobalt nitrate on zinc oxide in hydrogen.

3.9.1.2 Mass spectrometric analysis

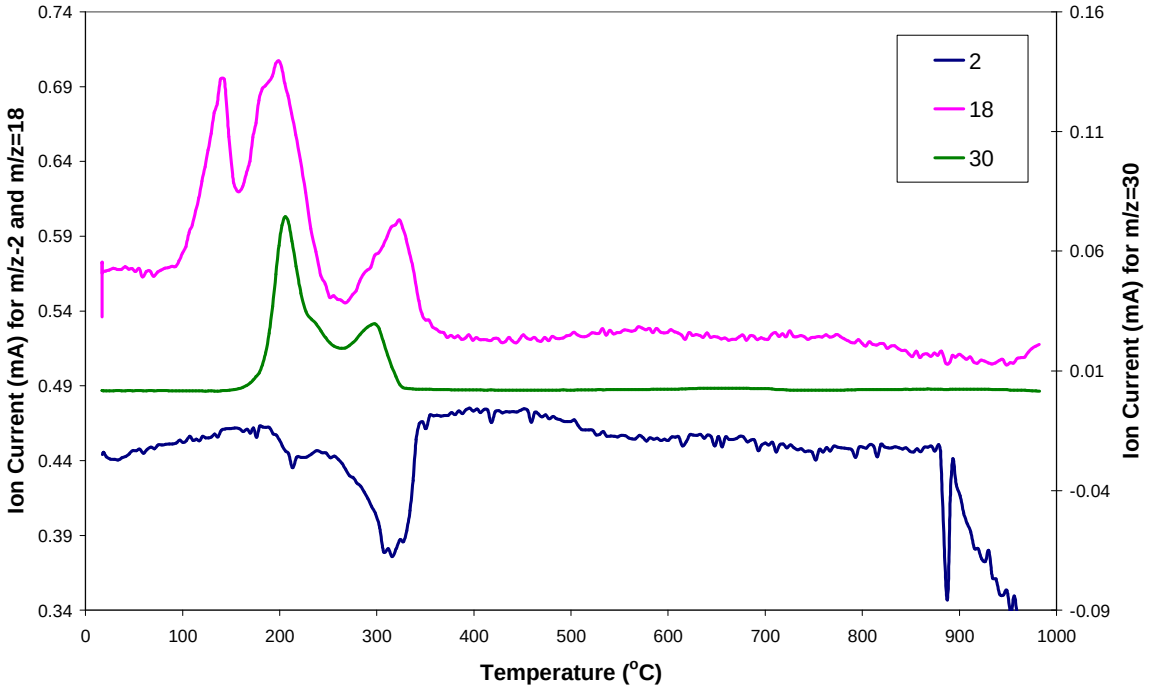

Figure 3-149: Mass spectrometric data of H_2 (m/z=2), water (m/z=18) and NO (m/z=30) for cobalt on zinc oxide in hydrogen.

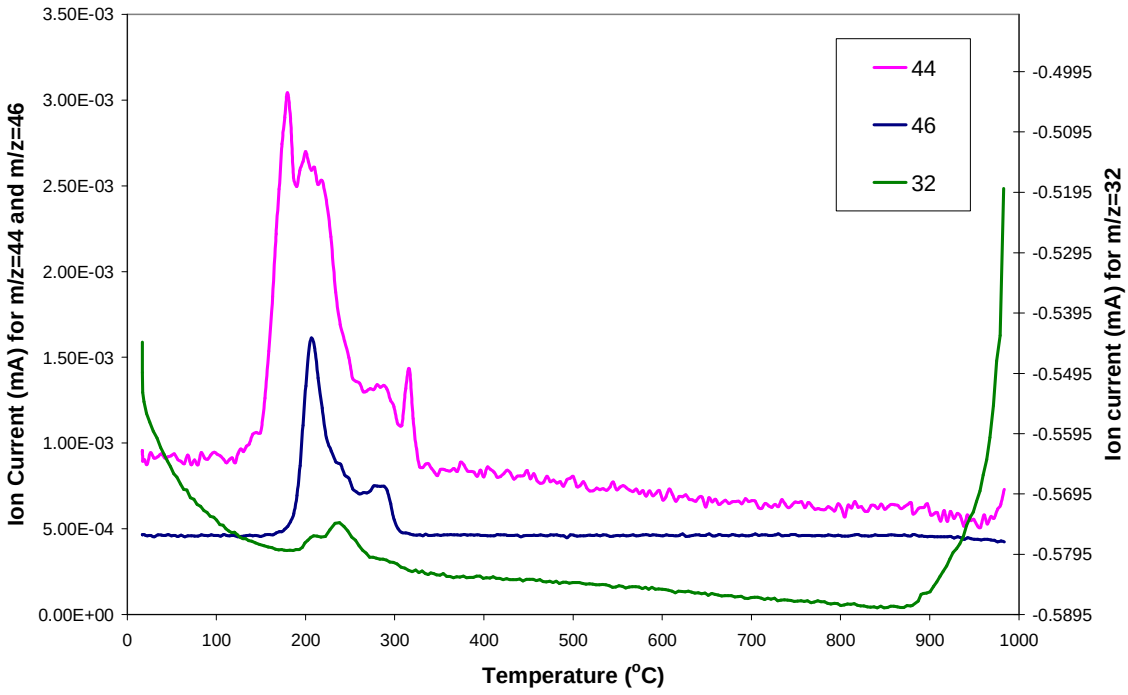

Figure 3-150: Mass spectrometric data of N_2O (m/z=44), NO_2 (m/z=46) and O_2 (m/z=32) for cobalt on zinc oxide catalyst in hydrogen.

The mass spectrometric data for CoNZ catalysts heated in hydrogen is presented in figure 3-149 and 3-150. The complex nature of the mass spectrometric profiles offers limited insight into the extent of reduction from the hydrogen consumption data. It appears that the nitrate precursor decomposes in hydrogen as two separate events via the evolution of NO, NO_2 and N_2O between 150-300 ^oC. A large hydrogen uptake peak with several shoulders can be seen around 190-380 ^oC. This corresponds to the evolution of water. The maximum of the hydrogen uptake peak, at 325 ^oC, corresponds to the exothermic peak on the heat flow profile. A further, much broader, region of hydrogen uptake coupled with the evolution of water can be seen from 450 ^oC onwards.

3.9.1.3 Hot-stage X-Ray Diffraction (XRD)

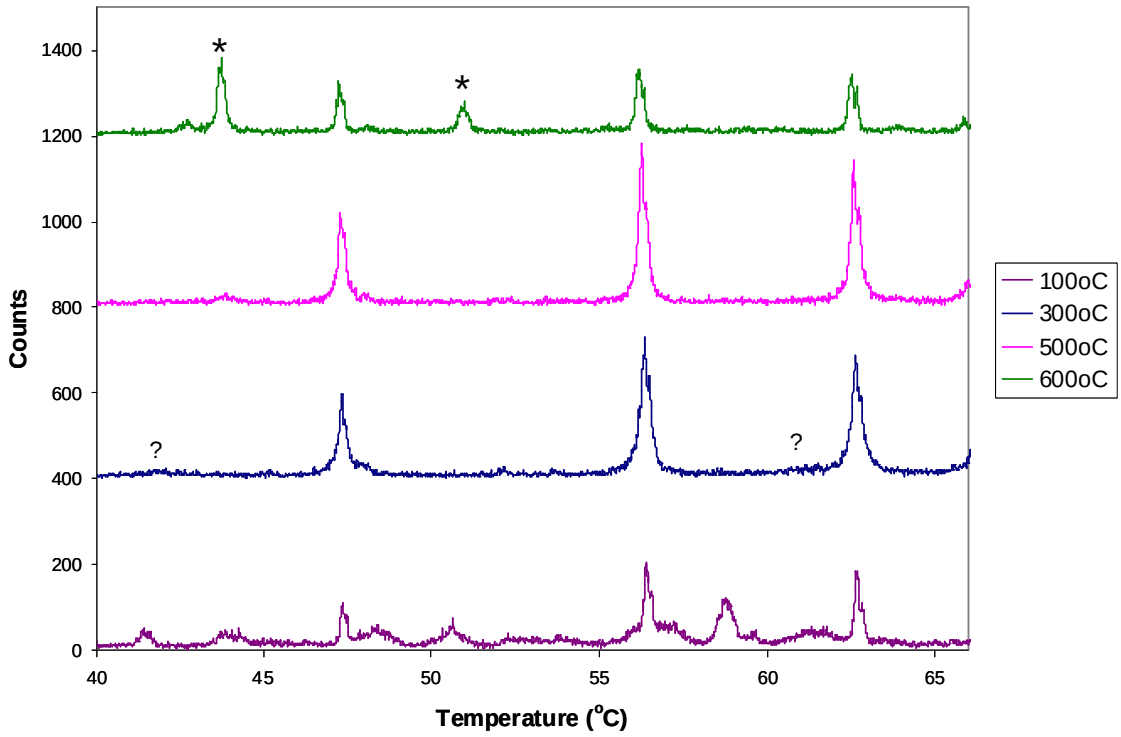

Figure 3-151: Hot-stage XRD patterns of cobalt nitrate on zinc oxide (no calcination) in hydrogen. The phases denoted are (Δ) CoO and (*) metallic Co. The experimental error for cobalt crystallite sizes calculated from X-ray diffraction is less than +/- 1 nm.

Results in figure 3-151 show the in-situ reduction of the CoNZ catalyst. From the pattern at room temperature it can be seen that the phases present are cobalt nitrate and zinc oxide. On heating to 300-400 ^{o}C peaks corresponding to CoO are present, although these are very broad and are difficult to differentiate from the background noise. Peaks at 43.8^{o} and 51.1^{o} indicating the presence of metallic cobalt are seen from 500-700 ^{o}C. Again using line broadening analysis, the crystallite size of the cobalt metal was calculated and found to be 21 nm and 32 nm at 600 ^{o}C and 700 ^{o}C, respectively.

3.9.2 FT Reaction

3.9.2.1 Conversion

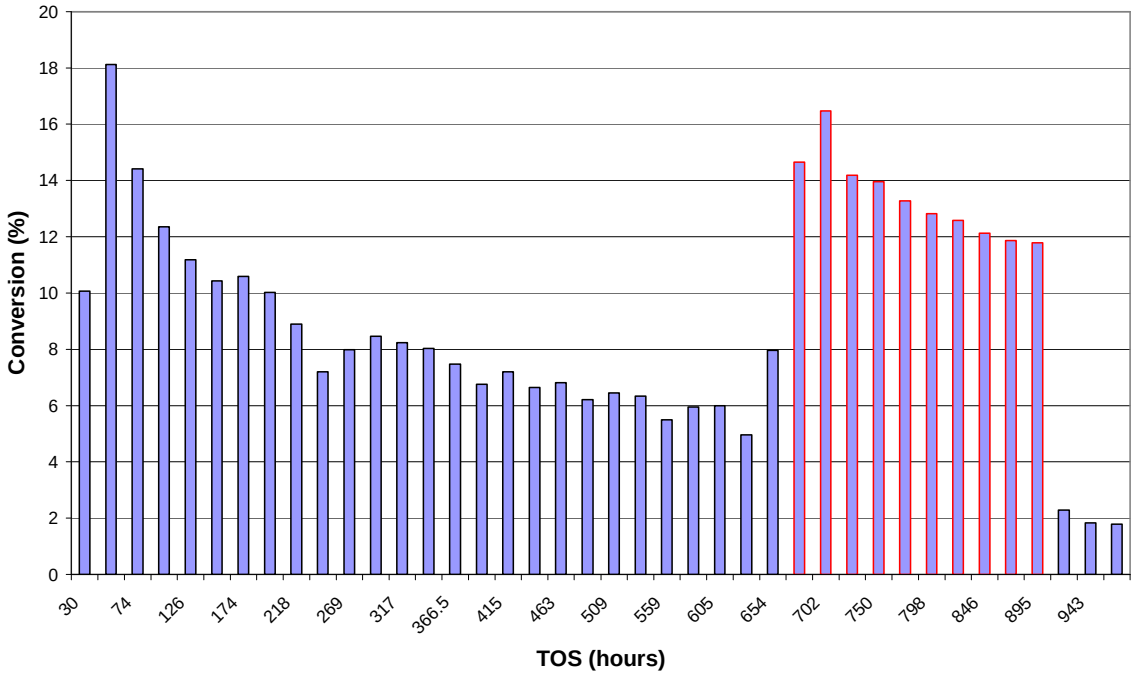

Figure 3-152: Conversion as a function of time-on-stream for the CoNZ (not calcined) catalyst at a temperature of 220 ^{o}C and 240 ^{o}C. The experimental error for the conversion is estimated to be +/- 5%.

The CO conversion for the uncalcined CoNZ catalyst is presented in figure 3-152. The graph shows the CO conversion increased to 18% after 50 hours. A significant reduction in conversion can then be observed, falling to ~6% by 486 hours on stream. On increasing the temperature from 220 ^{o}C to 240 ^{o}C, the activity increased, reaching a maximum conversion of 16% after 48 hours at 240 ^{o}C. The conversion then decreased to around 12% after 192 hours. Upon returning the temperature to 220 ^{o}C, the conversion dropped to ~2%.

3.9.2.2 Deactivation

Using the equation shown in section 2.5.2, deactivation constants were calculated at 220 ^{o}C and 240 ^{o}C to be 0.0018 and are shown in figure 3-153 and 3-154, respectively. This suggests that the rate of deactivation is similar at both temperatures.

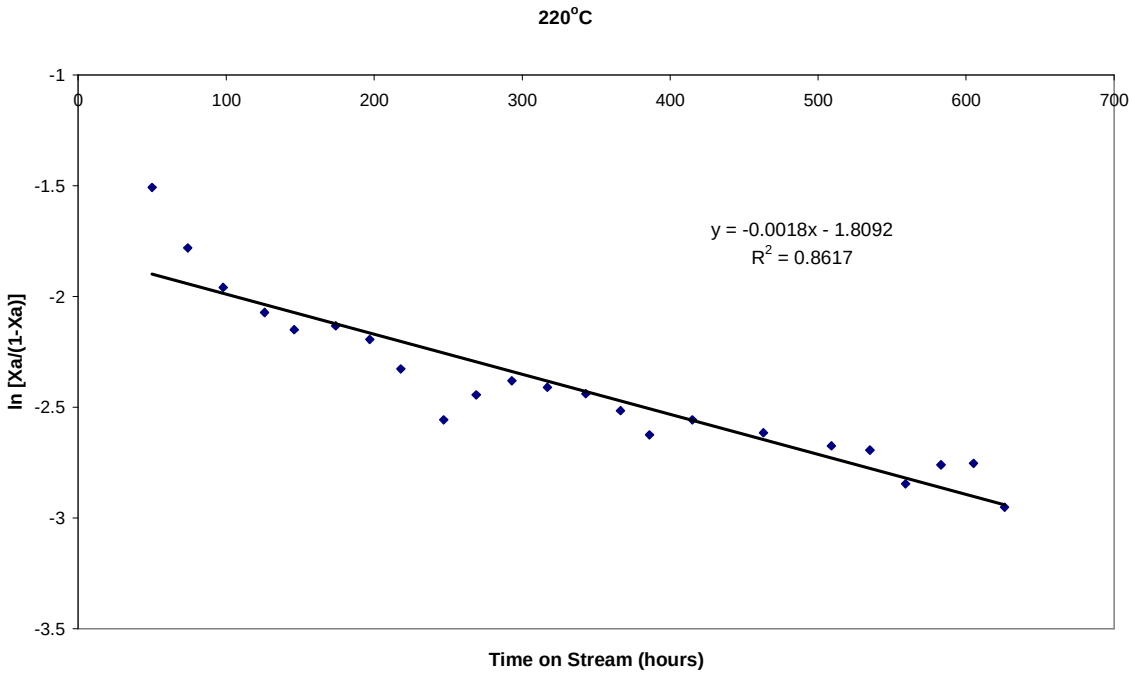

Figure 3-153: Graph of ln[Xa/(1-Xa)] versus time on stream for uncalcined CoNZ catalyst reaction at 220 °C.

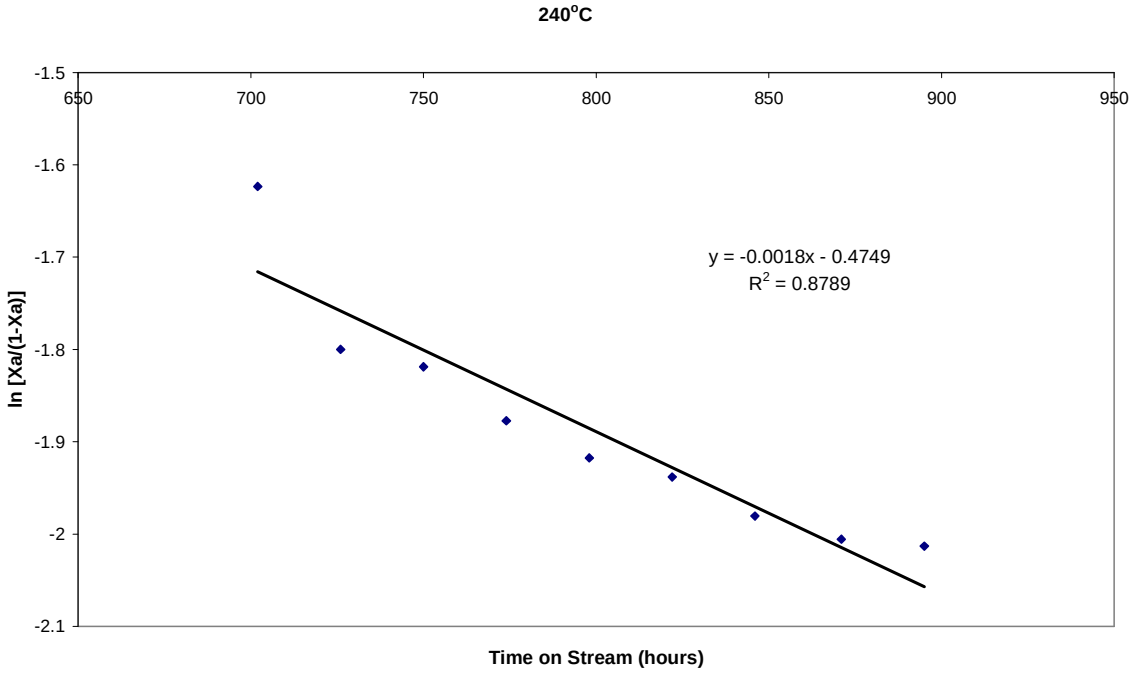

Figure 3-154: Graph of ln[Xa/(1-Xa)] versus time on stream for uncalcined CoNZ catalyst reaction at 240 °C.

3.9.2.3 Alpha values

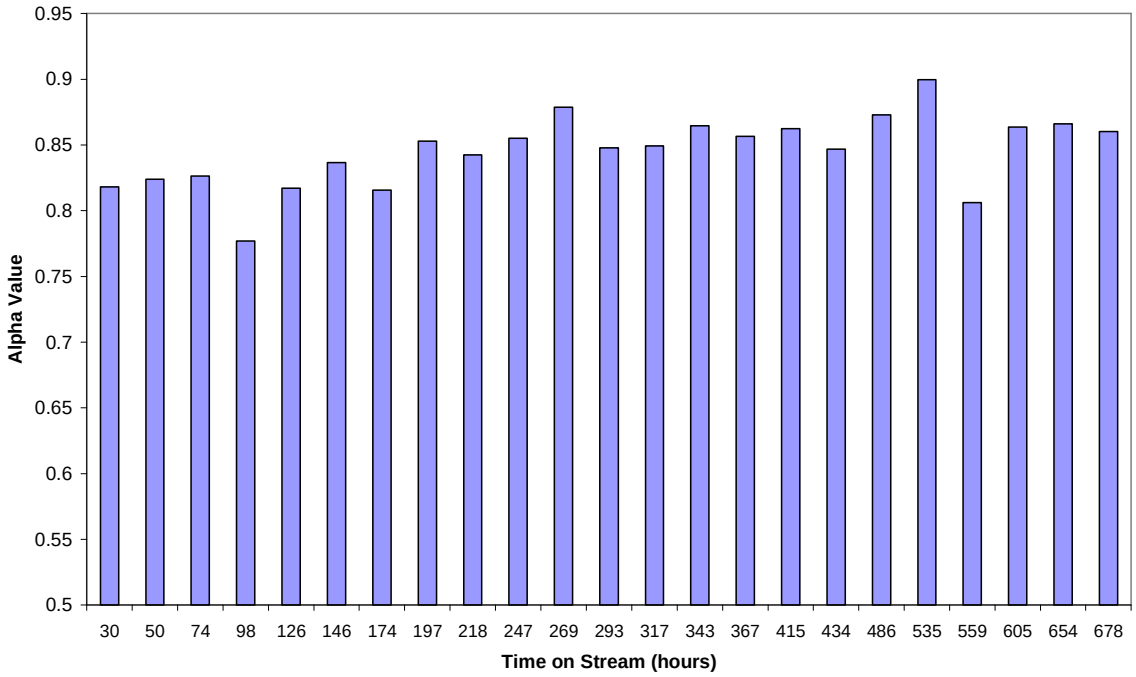

Figure 3-155: Alpha values versus time on stream for uncalcined cobalt on zinc oxide catalyst at reaction temperature of 220 ^{o}C

Alpha values as a function of time on stream for the uncalcined CoNZ catalyst at 220 ^{o}C are shown in figure 3-155. It can be seen that the chain growth probability increases with time on stream and reaches an average alpha value of 0.86 after 678 hour TOS at 220 ^{o}C.

3.9.2.4 Organic liquid and wax distribution

Figures 3-156 to 3-164 present the hydrocarbon product distribution for both the organic liquid and wax components at various times on stream. At 220 ^{o}C (74, 317 and 605 hour TOS) the product distribution moves towards production of longer chain hydrocarbons with time on stream. This can be observed in both the organic liquid and waxes. When the reaction temperature is increased to 240 ^{o}C, the selectivity can be seen to shift towards production of lower molecular weight hydrocarbons. At this temperature, there is no wax analysis due to the insufficient amount of wax produced.

3.9.2.4.1 74 hours TOS

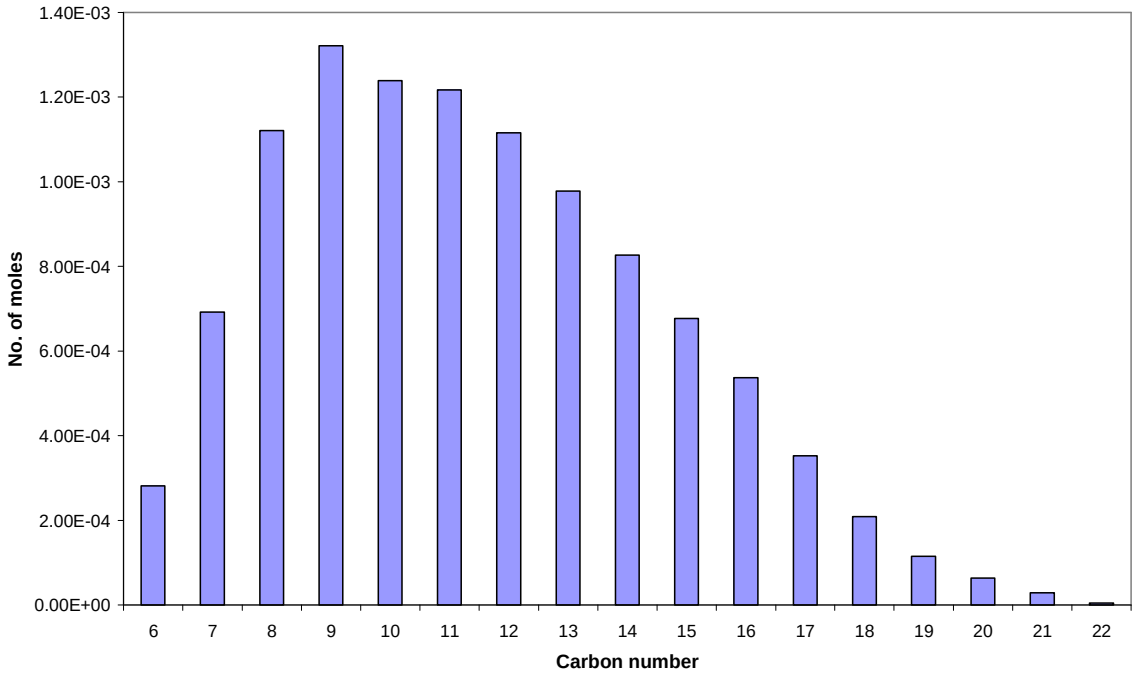

Figure 3-156: Hydrocarbon product distribution as a function of carbon number for uncalcined CoNZ catalyst liquid hydrocarbon sample at 74 hours TOS (T=220 °C)

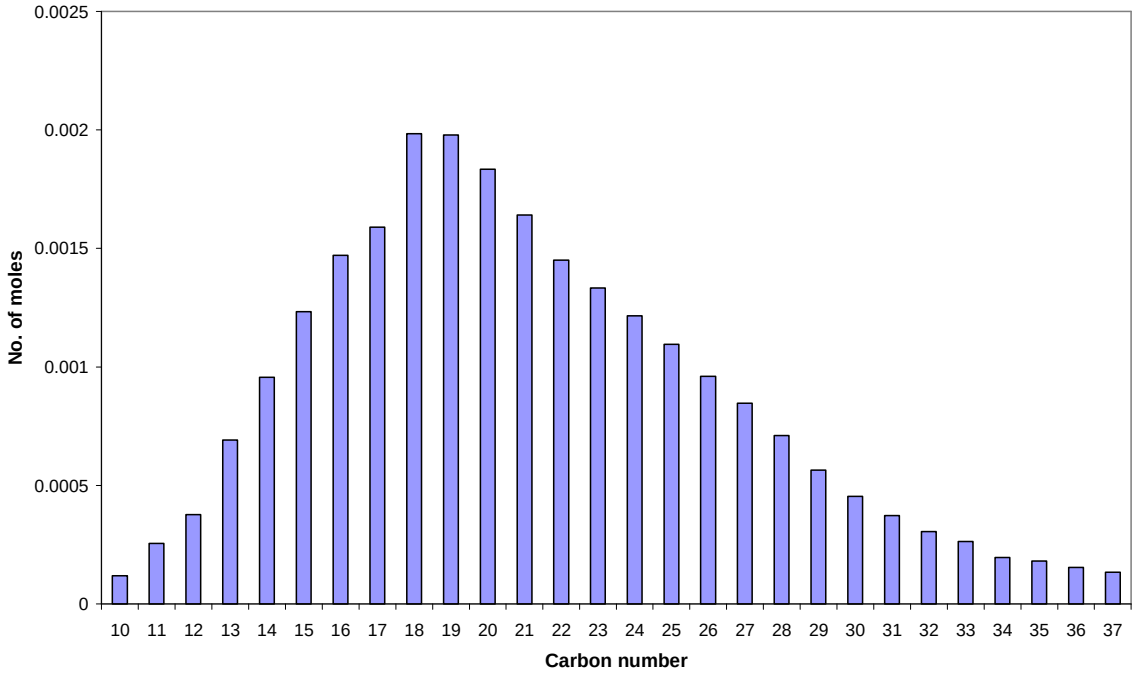

Figure 3-157: Hydrocarbon product distribution as a function of carbon number for uncalcined CoNZ catalyst wax sample at 74 hours TOS (T=220 °C)

3.9.2.4.2 317 hours TOS

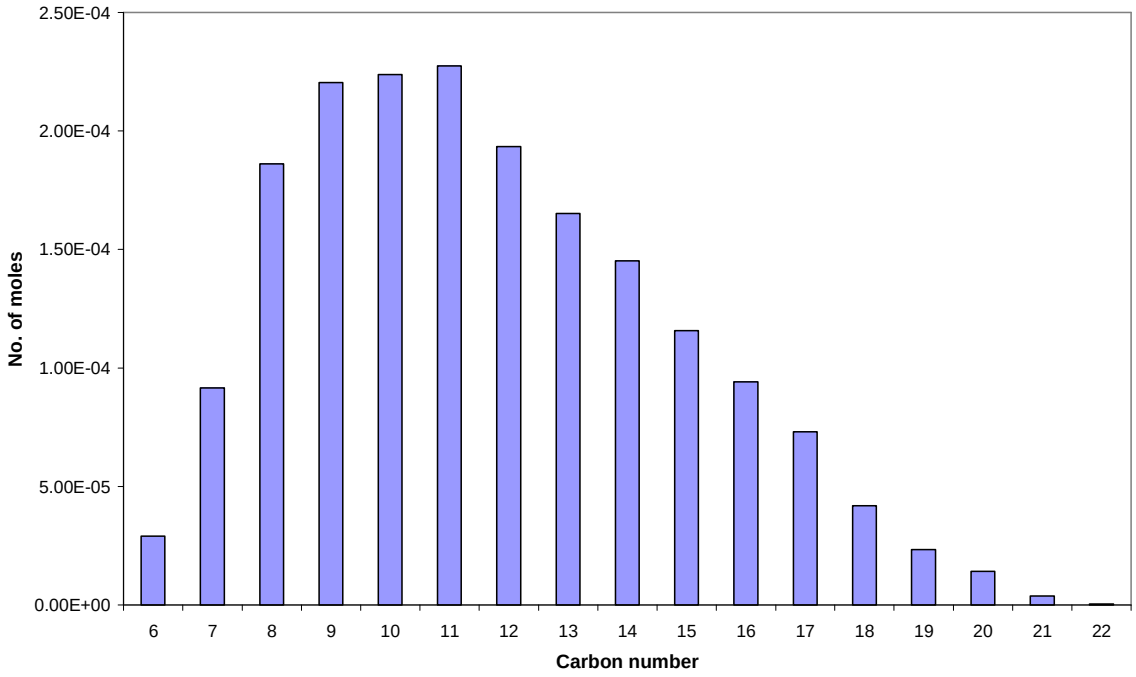

Figure 3-158: Hydrocarbon product distribution as a function of carbon number for uncalcined CoNZ catalyst liquid hydrocarbon sample at 317 hours TOS (T=220 ^{o}C)

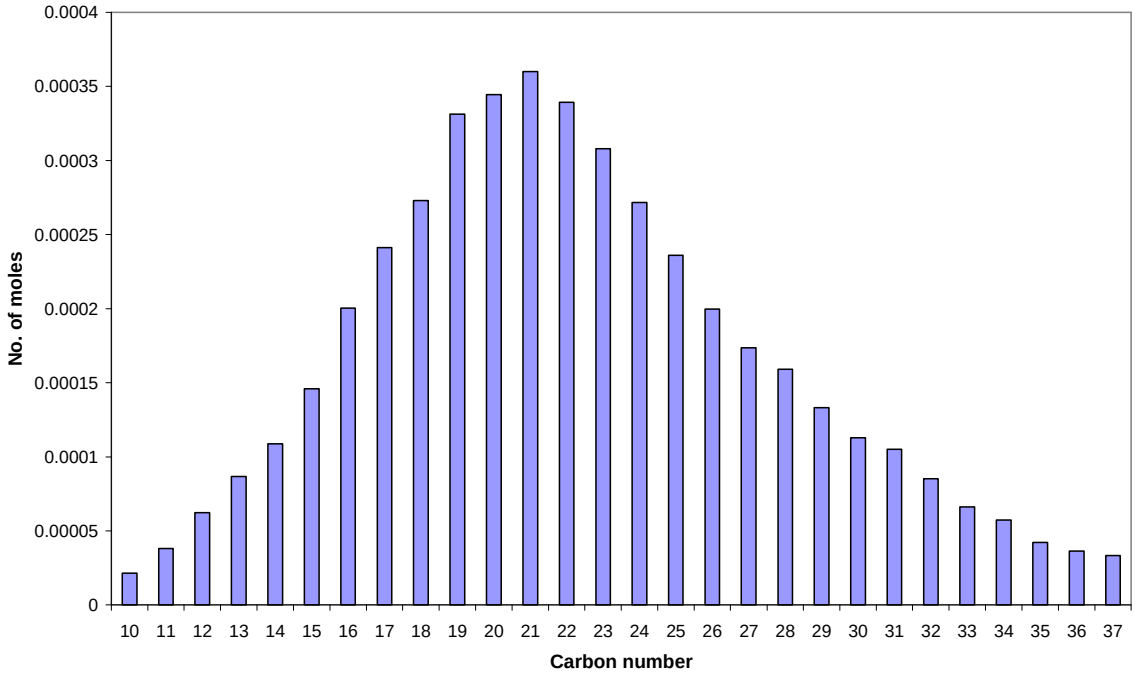

Figure 3-159: Hydrocarbon product distribution as a function of carbon number for uncalcined CoNZ catalyst wax sample at 317 hours TOS (T=220 ^{o}C)

3.9.2.4.3 605 hours TOS

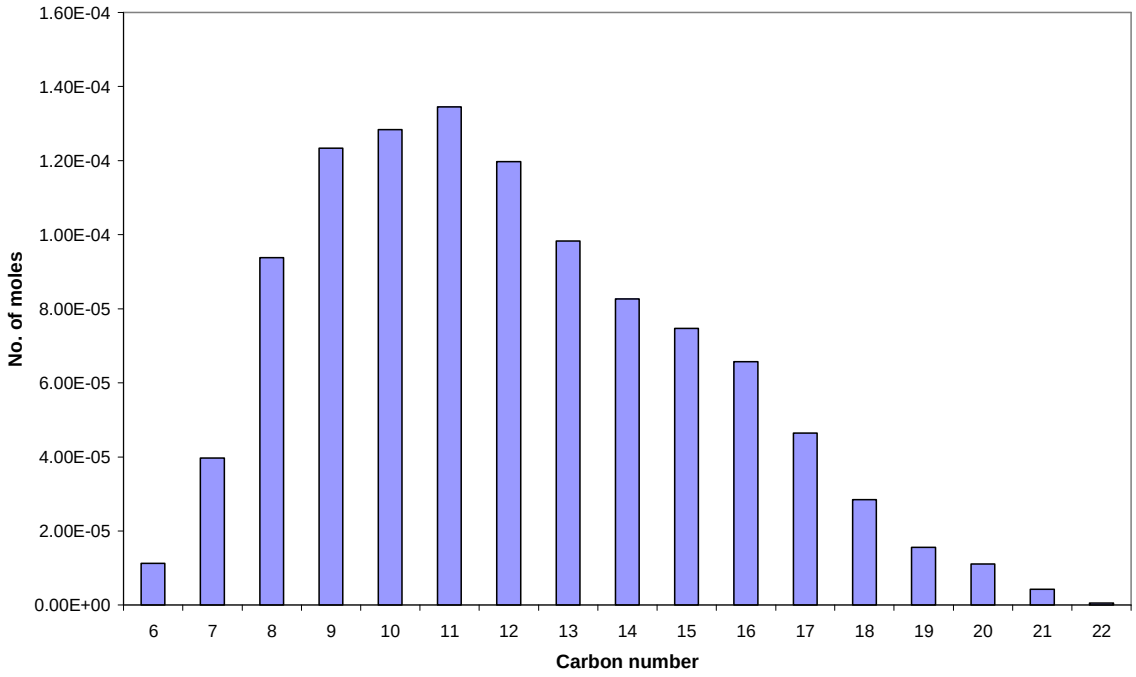

Figure 3-160: Hydrocarbon product distribution as a function of carbon number for uncalcined CoNZ catalyst liquid hydrocarbon sample at 605 hours TOS (T=220 ^{o}C)

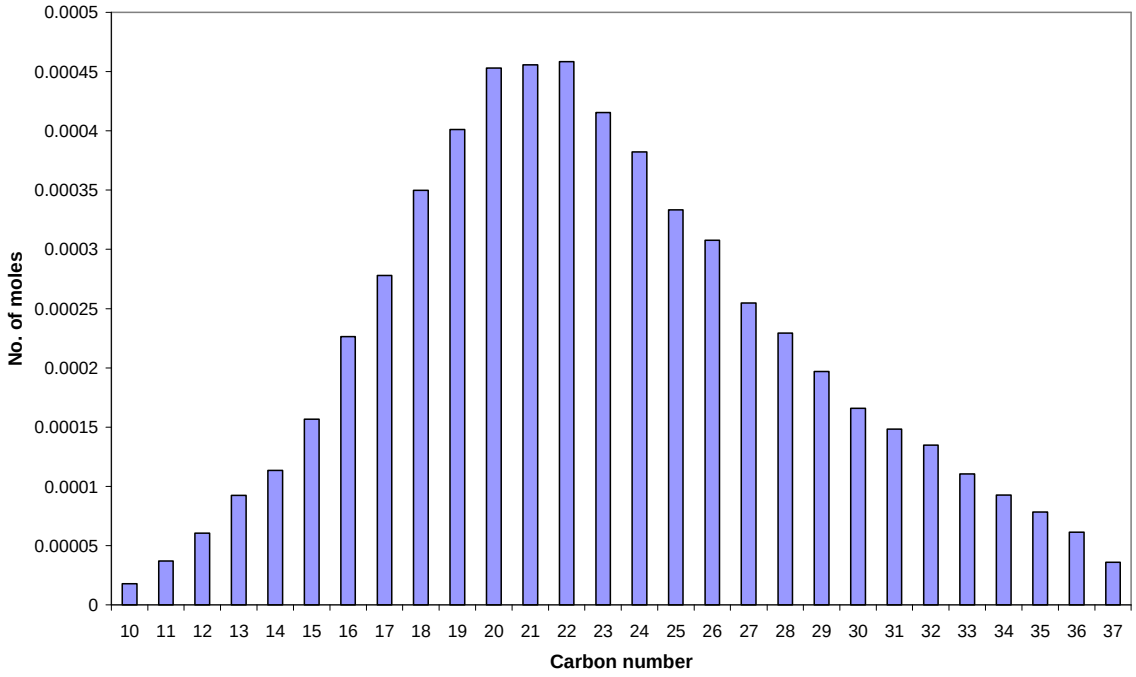

Figure 3-161: Hydrocarbon product distribution as a function of carbon number for uncalcined CoNZ catalyst wax sample at 605 hours TOS (T=220 ^{o}C)

3.9.2.4.4 702 hours TOS

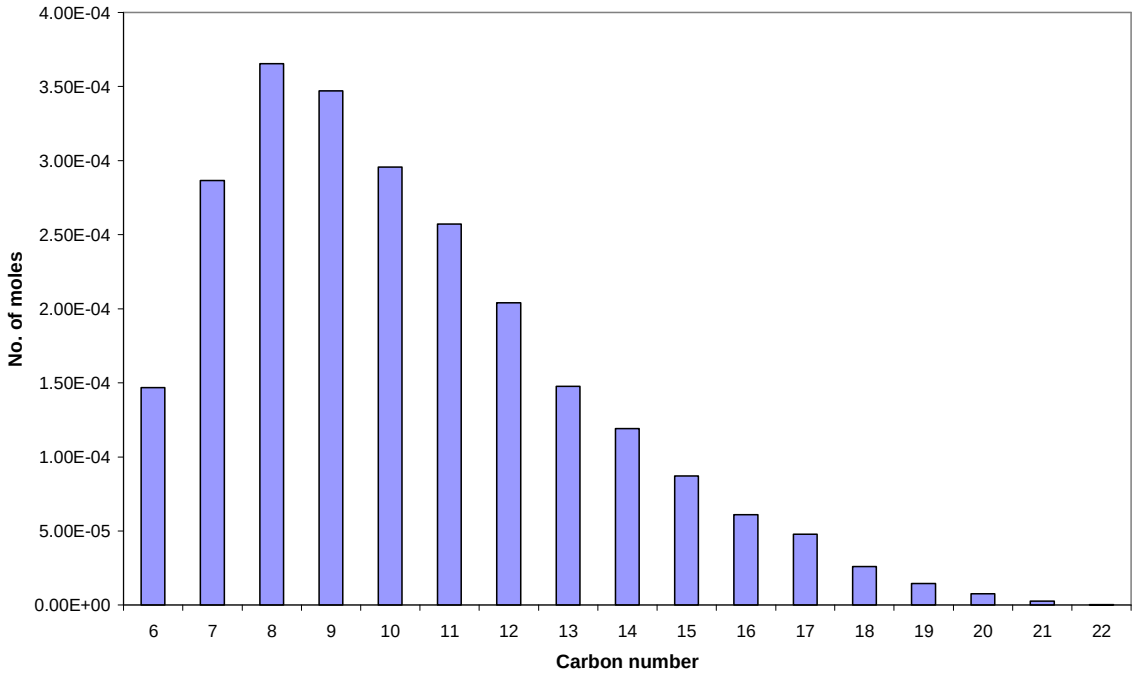

Figure 3-162: Hydrocarbon product distribution as a function of carbon number for uncalcined CoNZ catalyst liquid hydrocarbon sample at 702 hours TOS (T=220 ^{o}C)

3.9.2.4.5 798 hours TOS

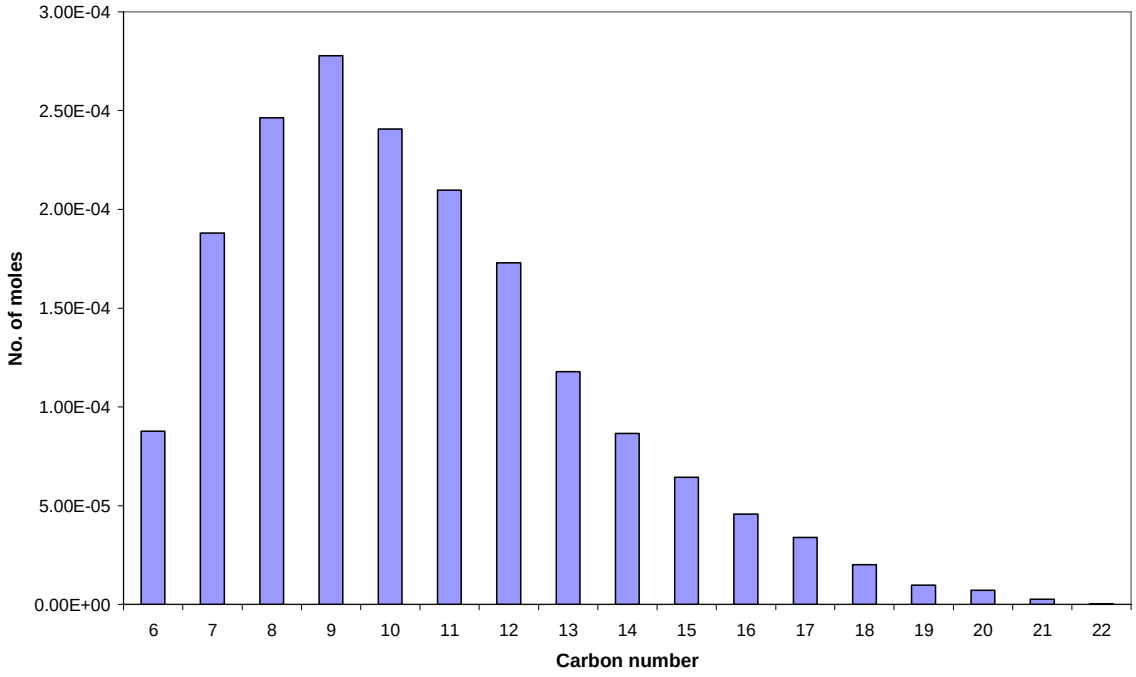

Figure 3-163: Hydrocarbon product distribution as a function of carbon number for uncalcined CoNZ catalyst liquid hydrocarbon sample at 798 hours TOS (T=220 ^{o}C)

3.9.2.4.6 894 hours TOS

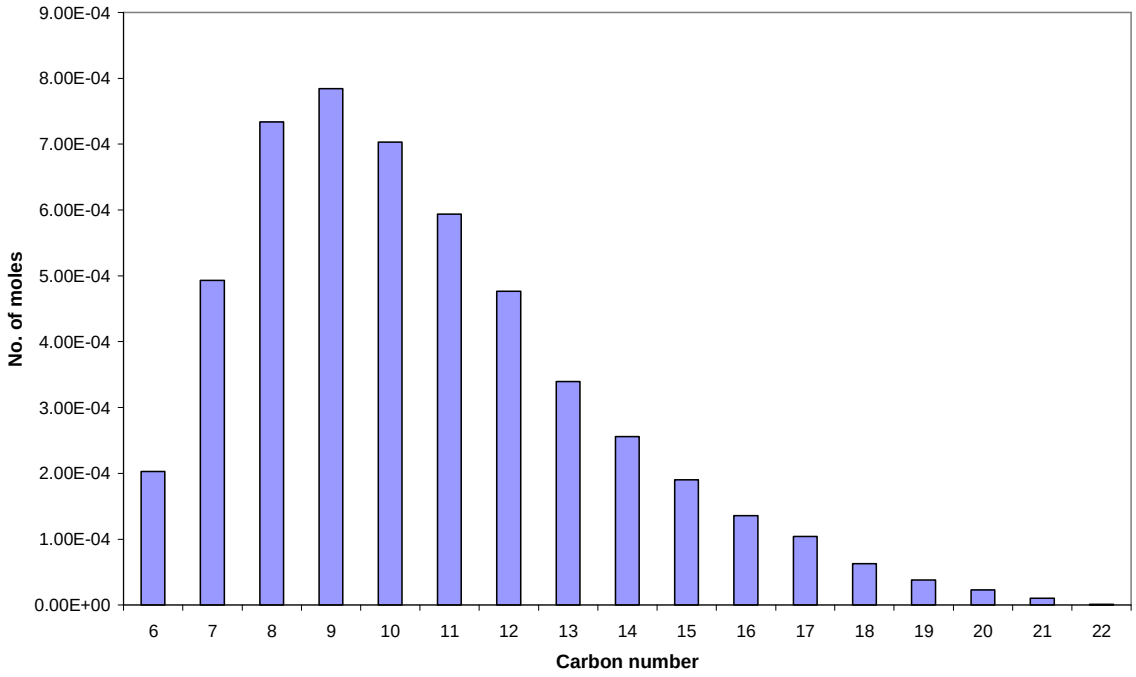

Figure 3-164: Hydrocarbon product distribution as a function of carbon number for uncalcined CoNZ catalyst liquid hydrocarbon sample at 894 hours TOS (T=220 ^{o}C)

3.9.3 FT post reaction analysis

3.9.3.1.1 Thermogravimetric analysis-Differential Scanning Calorimetry

The TGA-DSC profiles of the CoNZ catalyst obtained from heating the sample in oxygen post reaction are presented in figures 3-165 and 3-166. Overall, the derivative weight profile exhibits two main areas of weight loss. The first can be seen to have a maximum at 390 ^{o}C with a shoulder peak around 500 ^{o}C. The second is a relatively smaller, high temperature weight loss at 860 ^{o}C. There is also a weight gain most likely related to the re-oxidation of the catalyst in the region 85-235 ^{o}C. In figure 3-166, heat flow data shows that the main weight loss corresponds to an exotherm with a small endothermic inflection observed at 860 ^{o}C.

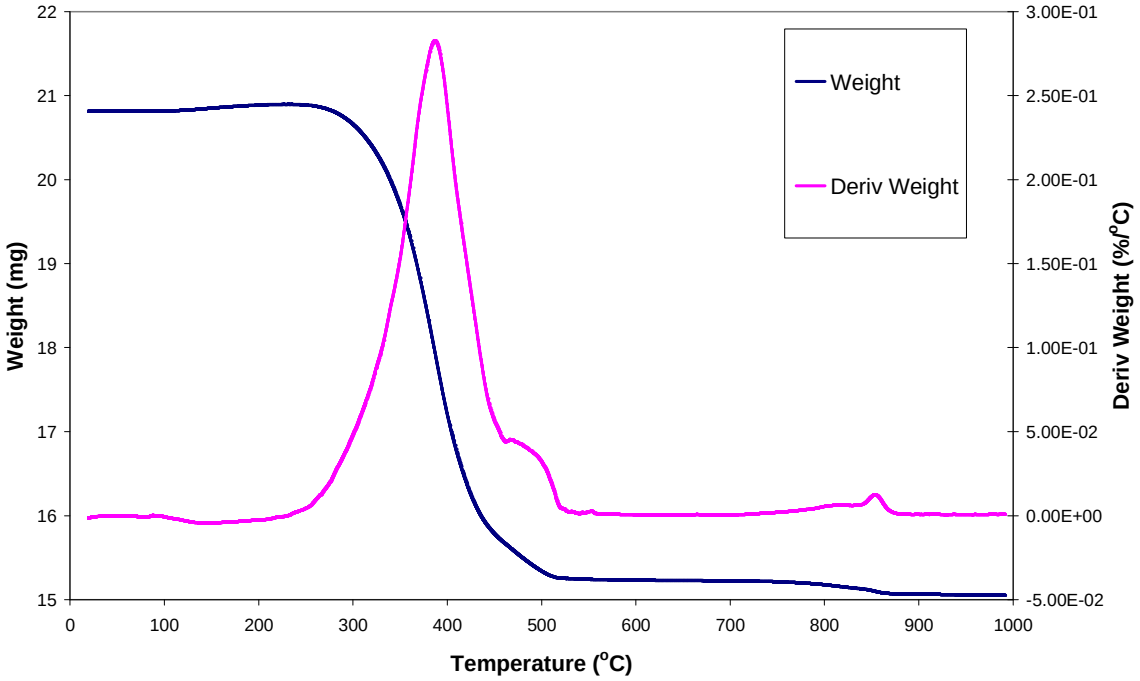

Figure 3-165: TGA weight and derivative weight profiles in oxygen for post FT reaction uncalcined cobalt nitrate on zinc oxide

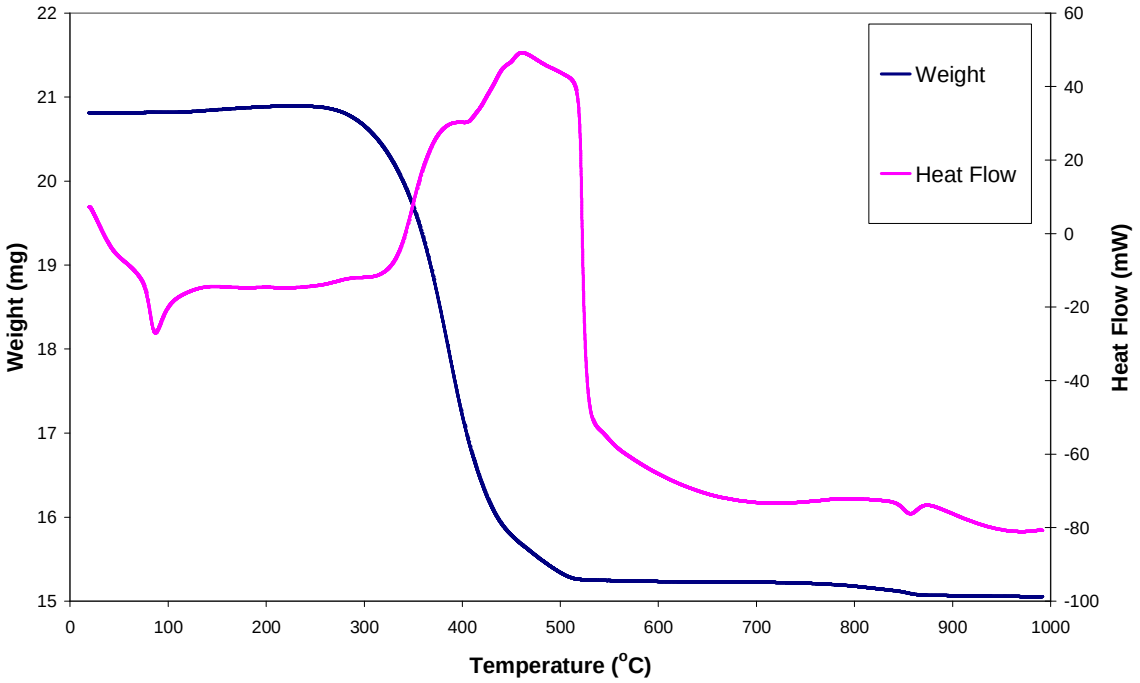

Figure 3-166: TGA-DSC weight and heat flow profiles in oxygen for post FT reaction uncalcined cobalt nitrate on zinc oxide

3.9.3.1.2 *Mass spectrometric analysis*

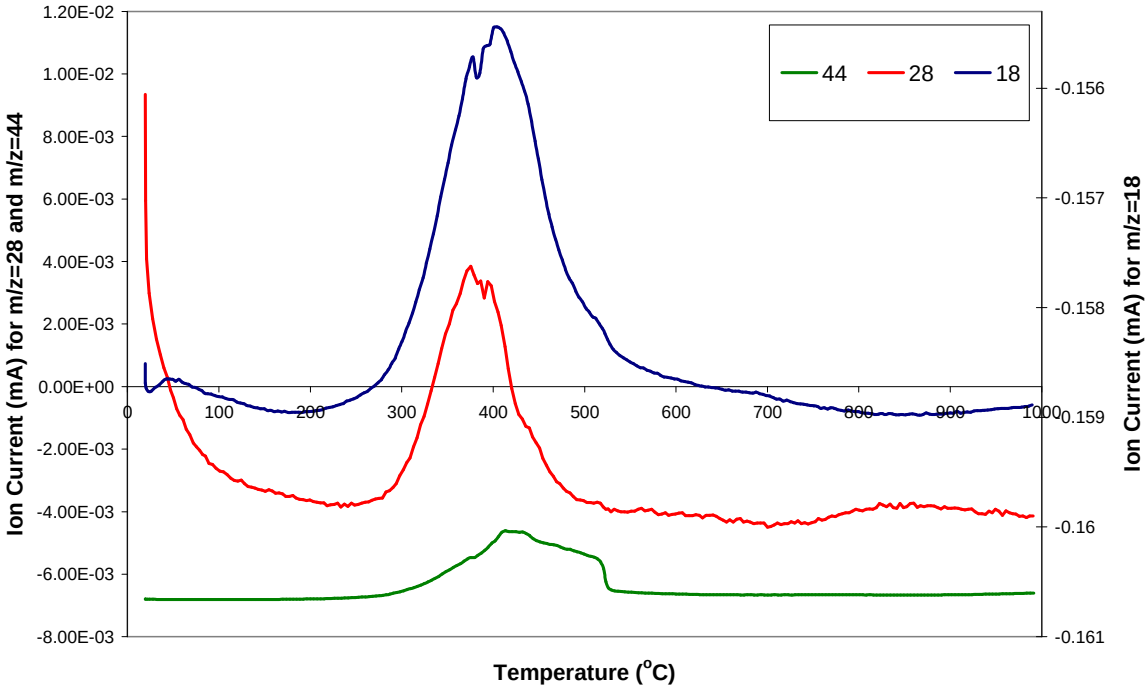

Figure 3-167: Mass spectrometric data of H_2O (m/z=18), CO (m/z-28) and CO_2 (m/z=44) in oxygen for post FT reaction uncalcined cobalt on zinc oxide

By comparing the mass spec data (figure 3-167) with the derivative weight profile in figure 3-165, it is clear that the main weight loss is accompanied by the evolution of water, carbon dioxide and carbon monoxide. The relative amount of these gases changes slightly as the temperature increases. No evolution of gas can be detected corresponding to the weight loss around 860 ^{o}C.

3.9.3.1.3 X-Ray Diffraction

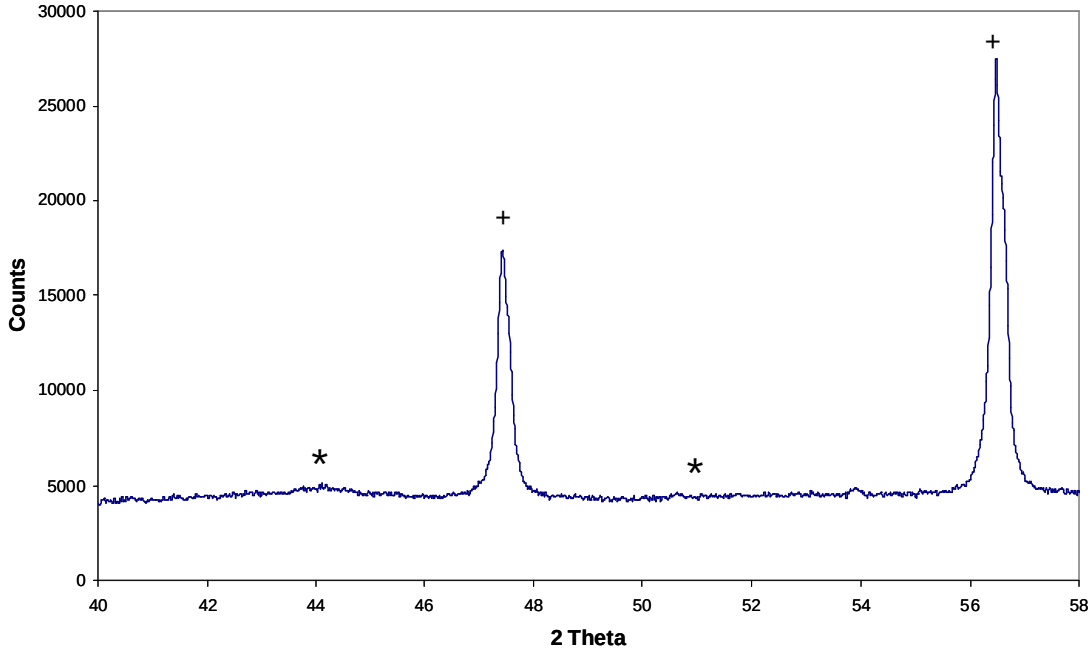

Figure 3-168: X-Ray diffraction pattern for uncalcined cobalt on zinc oxide catalyst post FT reaction.

X-ray diffraction analysis was carried out on the uncalcined cobalt on zinc oxide catalyst post FT reaction, with the results displayed in figure 3-168. The patterns show the presence of reflections corresponding to metallic cobalt. Due to broad nature of the reflections relating to metallic cobalt an estimation of the average crystallite size was not possible. Apart from the cobalt, the only other observed phase is the zinc oxide support.

4. DISCUSSION

4.1 Oxygen treatment

The effect of the nature of the support and cobalt precursor on catalyst calcination has been investigated. Using TGA-DSC with mass spectrometric analysis the decomposition of the precursor was followed as a function of temperature. XRD and TEM were used to investigate the species present on the catalyst after calcination. Results obtained for the unsupported and supported samples are compared in table 4-1. It can be seen from the results presented that both support and cobalt precursor, have a significant influence on the nature of the decomposition occurring on the supported catalyst.

Table 4--1: Decomposition temperatures and gases evolved for supported cobalt catalyst in oxygen.

Catalyst	Cobalt precursor decomposition temperature (^oC)	Gases evolved
Cobalt nitrate	242, 266	O_2, H_2O, NO, NO_2
Cobalt acetate	193, 276, 364	H_2O, CO, CO_2, O_2, H_2
CoNA	239, 340	H_2O, NO
CoAA	320	H_2O, CO, CO_2, O_2, H_2
CoNZ	204, 301	H_2O, NO, NO_2, N_2O

Cobalt nitrate has a complex decomposition occurring in two stages. Analysis of each stage suggests common processes even though they are occurring at different temperatures. The TGA-DSC and online mass spectrometric results from the cobalt nitrate on alumina catalyst have been discussed in previous work [92]. It was found that in comparison to the decomposition of the bulk nitrate, the alumina support stabilized the second stage of the nitrate decomposition, shifting it to

around 75 ^{o}C higher in temperature. From analysis of the gases evolved, the decomposition of the cobalt nitrate on alumina can be represented by the following equation:

$$3[Co(NO_3)_2.6H_2O] \rightarrow Co_3O_4 + 6NO + 18H_2O + 4O_2$$

In contrast to the bulk nitrate, no NO_2 was present during the decomposition on alumina. NO is known to react rapidly with molecular oxygen to give NO_2, however the reaction is unusual in having a negative temperature coefficient, where the rate of production of NO_2 becomes progressively slower at higher temperatures [93]. It is therefore possible that, due to complete decomposition of the nitrate requiring a higher temperature on the alumina support, no evolution of NO_2 occurs. However this is only true for the second decomposition event as the first occurs at the same temperature as the unsupported cobalt nitrate. Therefore the reason for the lack of NO_2 evolved during the first decomposition is unclear.

From the TGA-DSC and mass spectrometric data obtained for the cobalt nitrate on zinc oxide catalyst, it was found that all the weight losses were endothermic events and the decomposition of the nitrate was accompanied by the uptake of oxygen and evolution of H_2O, NO, N_2O and NO_2. The nitrate decomposition for the CoNZ is similar to that of the bulk cobalt nitrate in that the double event still occurs. However, the maximum temperatures of both nitrate decomposition events have changed. The weight loss event at 204 ^{o}C is decreased by around 40 ^{o}C in comparison to the bulk nitrate whereas the weight loss event at 301 ^{o}C has increased by around 30 ^{o}C. In addition, complete decomposition was delayed until around 400 ^{o}C. The profile of the gases evolved also changed as the temperature increased; with N_2O being the only gas evolved at the start of the decomposition and NO being the principal nitrogen oxide gas evolved at the end. This is due to the thermodynamic equilibrium of nitrogen oxides as discussed with the CoNA catalyst.

There is also a high temperature weight loss at 855 ^{o}C, which is likely to be due to the decomposition of the spinel oxide to the more stable CoO, accompanied by the evolution of oxygen, as seen with the bulk nitrate around the same temperature [94].

The decomposition on the CoNZ catalyst was also carried out in an inert atmosphere. Results showed that the decomposition is almost identical to that in oxygen, not only in terms of the temperatures of the weight losses but also in the nature of the gases evolved. The only difference was the evolution instead of uptake of oxygen, which occurred with a maximum at 234 ^{o}C. This suggests that the decomposition of the nitrate precursor is a thermal process, which occurs independently of the gas atmosphere employed.

A comparison of cobalt nitrate decomposition on the alumina and zinc oxide support surfaces showed differences in both the temperature of decomposition and the nature of the gases evolved. This indicates differences in the nature of the interaction between the nitrate complex and the alumina and zinc oxide supports and in turn differences in the properties of each support.

On both support surfaces, the decomposition of the nitrate precursor occurs as two distinct events, separated by around 100 ^{o}C. However, the temperature maxima at which these decomposition peaks occur is decreased by around 30 ^{o}C for the cobalt nitrate on zinc oxide catalyst. This difference in temperature of decomposition could be explained in terms of greater interaction of the cobalt nitrate with the alumina support. It is thought that this is due to the nitrate complex interacting with the support hydroxyls on the alumina, leading to an increase in the stability of the cobalt nitrate complex on the support and hence forcing the decomposition to higher temperatures.

In contrast to the cobalt nitrate on zinc oxide catalyst, there is no high temperature weight loss associated with the conversion of Co_3O_4 to CoO over the cobalt nitrate on alumina catalyst. This may be due to the stabilising effect of the alumina support which is seen to affect the decomposition events. It is thought the alumina support may stabilise the cobalt oxide spinel and consequently shift its conversion to CoO to a much higher temperature.

Results for the cobalt acetate on alumina catalysts have been briefly discussed previously and show that the decomposition is highly exothermic, occurring as a broad event, centred at 320 ^{o}C, which looks to consist of several overlapping peaks. Mass spectrometric data showed that the decomposition involved the evolution of water, carbon monoxide, carbon dioxide and hydrogen [92]. The

maximum of the decomposition events lies exactly between the main two decomposition events of the cobalt acetate. This suggests that the alumina has acted to combine these two separate events, stabilising one and catalysing the other.

This decomposition of the cobalt acetate on alumina is different to that observed for the cobalt nitrate on alumina. The most marked difference between the decomposition of the different precursors was observed in the DSC analysis, where the acetate decomposition was found to be highly exothermic in comparison to the nitrate precursor. With the cobalt nitrate on alumina, decomposition occurs as two events which have a greater temperature separation than the bulk nitrate; whereas the alumina has fused the partial processes of decomposition of the bulk metal acetate. In addition, the temperature at which decomposition is complete is around 100 ^{o}C lower for the CoAA catalyst. This behaviour may be related to the dispersion of the complexes on the support. If the nitrate was poorly dispersed on the alumina we may expect that the part less influenced by the support would retain the same decomposition as the unsupported cobalt nitrate, whereas the part in contact would be more strongly influenced. This would result in the two separate decomposition events observed in our study. However, if the acetate was well dispersed then the influence of the support may dominate and the result would be a single decomposition event, again as observed.

XRD patterns for the calcined CoNA catalyst confirm that as with the bulk nitrate, Co_3O_4 is the product of the decomposition. The average size of the Co_3O_4 crystallite determined by XRD was found to be 15 nm, which was similar to the average pore diameter of the support measured by B.E.T analysis. Previous studies have reported a direct correlation between average pore diameter and average size of the Co_3O_4 crystallite produced after calcination, indicating that the majority of the particles are located within the pores of the support. Our results are in keeping with these previous findings, in that the size of the Co_3O_4 crystallites are limited by the alumina pore size [46, 64, 71].

Transmission electron microscopy was carried out on the CoNA catalyst in its calcined state. Co_3O_4 appears as dark spherical clusters which show a variation in size from 150 to 300 nm. This contrasts with the mean Co_3O_4 crystallite size from the XRD data where cobalt oxide particles were calculated to be 15 nm. It is

therefore suggested that after calcination the cobalt oxide exists on the alumina surface as large agglomerates. Evidence of this can be observed from the higher magnification images where the Co_3O_4 clusters clearly consist of many smaller Co_3O_4 particles. However, the contrast is not sufficiently clear to allow for the measurement of exact crystallite sizes.

In contrast, XRD patterns obtained for the cobalt nitrate on zinc oxide catalyst post calcination only exhibit reflections relating to the zinc oxide support. This may be due to the cobalt species after calcination being below the detection limits for XRD and suggests that most of the cobalt species are highly dispersed on the zinc oxide support. The absence of cobalt oxide reflections could also be explained by the formation of non crystallized cobalt phases induced by a strong cobalt-support interaction. When using *in-situ* XRD analysis, however, peaks relating to the cobalt oxide phase are observed. This may be due to the heating rate used during treatment of the catalyst in oxygen. Several groups have found that a decrease in the heating rate leads to higher dispersed cobalt catalysts [60, 61]. Since calcination of the catalysts before XRD analysis was carried out at 1 $^{o}C\ min^{-1}$ compared to 10 $^{o}C\ min^{-1}$ for hot-stage *in-situ* XRD analysis, the effect of the different heating rates may explain the difference in crystallite sizes produced after decomposition.

XRD results for CoAA were similar to the CoNZ catalyst in that, apart from a very broad low intensity peak situated around 77^{o}, the XRD pattern only exhibited reflections attributed to the support. Similar XRD data has been published for cobalt acetate on alumina catalysts in the literature [33, 95]. Again these results point towards either amorphous or well dispersed cobalt species after decomposition. A strong cobalt-support interaction is more likely in the case of the acetate, given the change in decomposition temperature observed in the TGA.

From the XRD and TEM data obtained for the cobalt nitrate on zinc oxide catalyst, that was received already calcined, the average crystallite size was found to be 14 and 17-25 nm, respectively. This is much larger than the crystallite size observed from the analysis of the zinc oxide catalyst, calcined under the procedure outlined in section 3.7.2.4. Without knowledge of the precise calcination profile of the catalyst, as supplied by BP, it is difficult to ascertain the cause of this measured difference in the average crystallite sizes of the cobalt species. However, it is likely

that the calcination profile employed by BP, differed in terms of the heating rate and final calcination temperature from the procedure outlined previously. Changes in these parameters have a well documented effect on the size of the cobalt crystallite, where increased heating rate and increased calcination temperature have been found to result in larger crystallites being formed [28]. This would suggest that the calcination procedure employed by BP is likely to be more forcing in terms of the temperature or heating rate.

From the TEM data of the calcined catalysts, both the cobalt nitrate on zinc oxide catalysts exhibit cobalt oxides species which appear as discrete particles. This is in contrast with the alumina support where the cobalt oxide was located in large aggregates. It is thought that this difference in particle distribution after calcination is attributed to the surface area of the support. Several groups have found that cobalt has been found to exist as clusters on high surface area supports and as single, more evenly distributed particles on low surface area supports [52, 96, 97] . Given the different surface areas of the zinc oxide and alumina supports, these results would be in keeping with the literature.

Therefore we have shown that the support and the heating rate play a significant role in determining the dispersion of the cobalt oxide during calcination.

4.2 Hydrogen treatment

Reduction of the supported cobalt catalysts was followed by TGA-DSC coupled to online MS as well as hot-stage XRD. This was carried out in an attempt to provide insight into the cobalt reduction and elucidate the steps observed. From the results, table 4-2 below can be constructed:

Table 4-2: Reduction temperatures and gases evolved for supported cobalt catalyst in hydrogen.

Catalyst	Weight loss temperature (^oC)	Gas Evolved
CoNA	354, 607	H_2O
CoAA	317, 369 466-779 >779	H_2O
CoNZ	305, 450	H_2O
CoNZC	360, 558	H_2O
CoNZ no calc	203, 293	H_2O, NO, NO_2, N_2O, O_2
	585, >670	H_2O

For all the calcined cobalt catalysts, two reduction events are observed accompanied by the uptake of hydrogen and evolution of water. From the DSC data, the heat flow associated with the reduction is observed to be relatively featureless.

Reduction of the CoNA catalyst has been briefly reported before [92]. Two weight losses corresponding to the uptake of hydrogen and evolution of water were observed at 354 ^{o}C and 607 ^{o}C. It was found that the hydrogen consumption of the reduction events observed corresponded to the stoichiometry of the two steps thought to be involved. This two step reduction is outlined in equations 4.1 and 4.2 below:

$$Co_3O_4 + H_2 \rightarrow 3CoO + H_2O \qquad (4.1)$$

$$3CoO + 3H_2 \rightarrow 3Co + 3H_2O \qquad (4.2)$$

In-situ hot-stage XRD data is consistent with the idea of the reduction occurring in a step-wise manner. From the XRD pattern for the CoNA at 200 ^{o}C, before the first reduction peak, only Co_3O_4 was detected. Between 300-400 ^{o}C, during the first reduction event, CoO was also present. By 500 ^{o}C, during the second reduction event, metallic cobalt was detected.

Varying the heating rate for the reduction of the catalysts in the TGA resulted in a shift in the derivative weight peak maxima to lower temperatures with increasing heating rate. This was as expected and agrees with previous findings in the literature [98] . It should be noted however, that the overall weight loss remained constant regardless of the heating rate employed.

TGA in hydrogen of the calcined cobalt nitrate on alumina catalyst was used to calculate the amount of reducible cobalt. The degree of reduction was found to be 94%. This extent of reduction ties in with the reduction profile, where no high temperature weight losses, indicative of the presence of cobalt aluminates, were observed. Previous studies have shown that larger cobalt oxide particles, often formed when catalysts are prepared via cobalt nitrate, are much more easily reduced than smaller ones [28, 29]. With a calculated average Co_3O_4 crystallite

size of 15 nm, measured by XRD, this high extent of reduction observed for the cobalt catalysts prepared via the nitrate is expected.

The TGA in hydrogen for the calcined cobalt acetate on alumina catalyst is characterised by several weight loss events with a region of continuous weight loss after 800 ^{o}C. As discussed with the CoNA catalyst, the weight losses are due to the step wise reduction of cobalt oxide to metallic cobalt. Evidence from the hot-stage XRD suggests that cobalt metal phase is not present until 500 ^{o}C. This indicates that the weight loss events from 230 ^{o}C to 460 ^{o}C are most likely to be associated with the reduction of Co_3O_4 to CoO; with the reduction of CoO to metallic cobalt occurring from 470 ^{o}C to 800 ^{o}C. The presence of two weight loss events associated with the reduction of Co_3O_4 to CoO can be ascribed to either, Co_3O_4 particles having varying interactions with the alumina support or variation in the size of the Co_3O_4 particles. The continuing weight loss after 800 ^{o}C is assigned to the reduction of cobalt aluminate species, which are known to be reducible only at temperatures above 800 ^{o}C. Small cobalt oxide particles are more likely to have a stronger interaction with the support, resulting in partial replacement of Co^{3+} ions in the cobalt spinel with Al^{3+} ions, producing cobalt aluminates. This agrees well with XRD data which shows that the cobalt oxide was highly dispersed on the alumina support after calcination, which would encourage the formation of these, hard to reduce, cobalt aluminate species.

It can be observed that the reduction profile of the cobalt acetate on alumina catalyst and that prepared from the nitrate precursor show significant differences. Nevertheless, the first reduction event, of Co_3O_4 to CoO, occurred around the same temperature region of 230 ^{o}C to 440 ^{o}C, for both catalysts, with the weight loss calculated per gram of catalyst also similar. This indicates that the reduction of Co_3O_4 to CoO did not depend on the Co_3O_4 particle size but took place in the same temperature interval for both the catalysts despite evidence from XRD data that the size of the cobalt oxide particles after calcination differed significantly. This result is consistent with Caster *et al.* [64] who showed for a series of silica supported catalysts that the temperature at which the first reduction step occurred was independent of the particles size, pore size and surface area. This result is also in agreement with Borg *et al.* [99] who found for a series of cobalt catalysts, the initial reduction event occurred in the same temperature range. For conversion of CoO to metallic cobalt, the temperatures again are similar however the weight

loss was markedly different, with that for the calcined CoNA catalyst being significantly greater than the catalyst prepared via the acetate. This is clearly apparent from the intensity of the peaks in the derivative weight profiles for each catalyst. This difference in weight loss suggests the presence of difficult to reduce cobalt species, formed during the calcination step, in the catalyst prepared via the cobalt acetate. This implies that using an acetate precursor increases the salt-support interaction on the alumina support. Such a strong interaction is likely to be favoured by the high dispersion of the cobalt phase, which is confirmed by XRD analysis and the highly exothermic nature of the decomposition of the acetate salt as observed during DSC analysis.

In addition to evidence from the reduction profiles, the degree of reduction calculated from the weight loss also indicates a relationship between the cobalt oxide particle size and the ease of reduction. For the cobalt acetate catalyst the extent of reduction was found to be only 15 %, which is substantially lower than that of the cobalt on alumina catalyst prepared via the nitrate precursor (94 %). It has been reported in the literature that hydrogen reduction properties of supported cobalt oxide particles depend upon the size of the Co_3O_4 crystallites with larger particles being much more easily reduced [29]. Thus comparing the cobalt catalyst prepared from the acetate with the cobalt catalysts prepared via the nitrate, our findings are in agreement with the observed increase of reducibility with increasing Co_3O_4 particle size. The much lower extent of reduction in the cobalt acetate catalysts is also related to the more extensive formation of cobalt aluminate, which was only seen to reduce at temperatures in excess of 800 ^oC.

TGA analysis in hydrogen of the calcined CoNZ catalyst exhibited two weight loss events, centred at 305 ^oC and 450 ^oC, corresponding to the uptake of hydrogen and evolution of water. There is a further weight loss above 600 ^oC that can be ascribed to the reduction of the zinc oxide support, which is known to start at above 550 ^oC. These reduction events are consistent with previous TPR studies with cobalt on zinc oxide where it was reported that reduction occurs in two stages [100-102]. Similar temperatures of reduction have also been reported, with reduction peaks reported at 290 ^oC and 430 ^oC for the first and second reduction events, respectively [103]. These reduction events with the CoNZ catalyst were similar to that of the CoNA catalyst in that the reduction still occurred as two

events, however the maximum temperatures were approximately 50 and 150 ^{o}C lower for the first and second reduction events respectively.

As stated above it has been well documented in the literature that reduction of cobalt oxide to metallic cobalt on a support usually occurs in two steps via equations 4.1 and 4.2. Such a process gives a weight loss ratio of 1:3. However integration of the derivative weight peaks for the calcined CoNZ catalyst gave a ratio of 1:1.6. This suggests that the reduction on the zinc oxide surface is different from that which was found on the cobalt nitrate supported on alumina catalyst. One proposition is that after calcination the cobalt has interacted strongly with the support to form cobalt zincate. Van Loon *et al*. [103] came to a similar conclusion when examining the preparation of cobalt on zinc oxide catalyst.

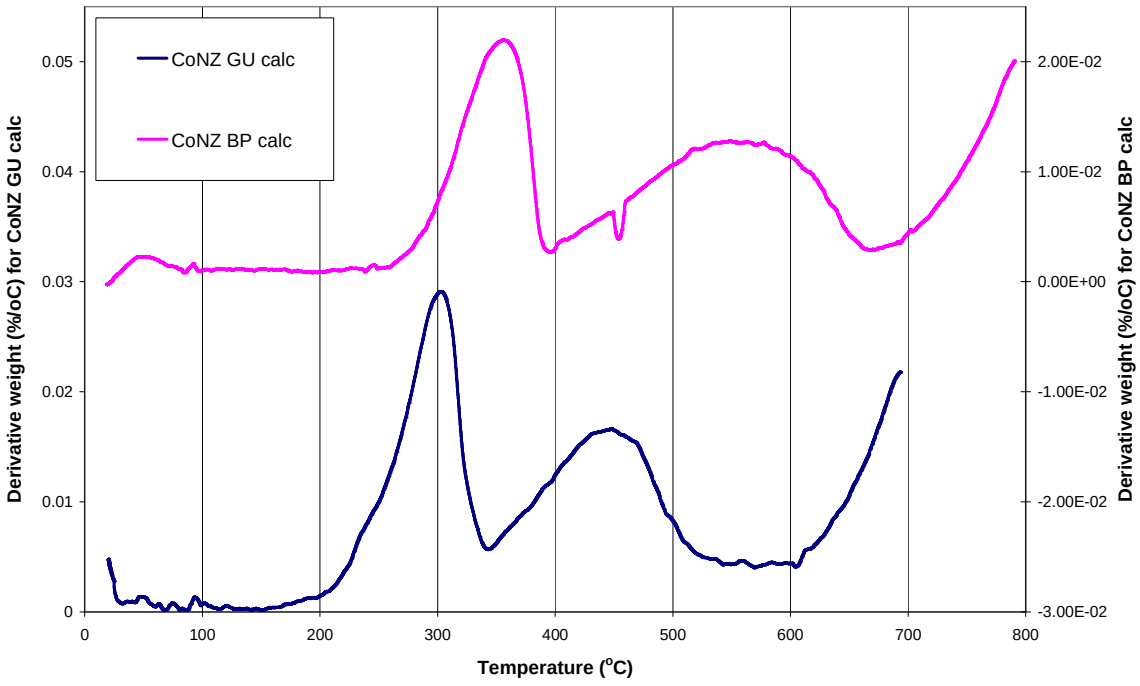

Figure 4-1: Derivative weight profile comparing reduction of cobalt nitrate on zinc oxide catalysts with different calcination procedures

It was found by use of extended TEM analysis in combination with elemental analysis that after drying and calcination a Co_3O_4/ZnO mixed oxide composition was obtained as a result of a chemical reaction between precipitated Co-ions and ZnO. If this was the case in the current system then the reduction to metallic cobalt from cobalt zincate could then be interpreted by the following equations:

$$ZnCo_2O_4 + H_2 \rightarrow 2CoO + H_2O + ZnO \quad (4.3)$$

$$2CoO + 2H_2 \rightarrow 2Co + 2H_2O \quad (4.4)$$

Such a process would give a weight loss ratio of 1:2 for first to second reduction events, which is more in keeping with our calculated ratio of 1:1.6, suggesting that the reduction proceeds in a step-wise manner involving the conversion of cobalt zincate to CoO prior to subsequent reduction to metallic cobalt. Hence, although it was initially thought that the cobalt was present on the catalyst surface after calcination as the cobalt oxide spinel Co_3O_4, evidence from the TGA analysis in hydrogen now suggests that the phase present is more likely to be cobalt zincate. Due to the similarities in the structure of these two cobalt species neither the XRD nor T.E.M analysis, initially employed to examine the cobalt phases present were able to clearly differentiate between them. The *in-situ* XRD results are in keeping with this suggested reduction. At 300 ^oC, during the first reduction event, only peaks corresponding to CoO are evident. It is not until 400 ^oC that peaks corresponding to metallic cobalt are present, by which temperature the second reduction event has begun. This postulation of the cobalt species being present as the cobalt zincate after calcination is further reinforced when examining the extent of reduction of the zinc oxide supported catalyst. The extent of reduction was found to be, 20.3 %, much lower than that of the alumina supported catalysts made from the same cobalt nitrate precursor. This low extent of reduction is in keeping with the CoAA sample and reinforces the view that cobalt species that have interacted with the support, in this instance to form cobalt zincate, will be much harder to reduce than their cobalt oxide counterparts.

For the cobalt on zinc oxide catalysts calcined at BP, the TGA in hydrogen exhibits two weight losses which can again be attributed to a two-stage reduction. Both reduction events, at 360 and 558 ^oC, occur at a higher temperature than those observed with the cobalt on zinc oxide calcined as outlined in section 3.7.2.4. From the TGA derivative weight profiles it was calculated that the ratio of the peaks for the two reduction events is 1:1.7. This is similar to that found for the Glasgow University calcined cobalt on zinc oxide catalyst. These results again indicate that the reduction differs from that observed with the alumina support and

reduction of the cobalt species after calcination is likely to occur as described in equations 4.3 and 4.4.

Further insight into the effect on the cobalt on zinc oxide catalysts of varying the calcination procedure is gained through comparing the TGA in hydrogen data (Figure 4-1). Analysis of the results suggested that cobalt reducibility is influenced by the calcination procedure employed. A difference in temperature of reduction is not unexpected since it is clear from XRD analysis, that the size of the cobalt species after calcination was markedly different for each of the cobalt on zinc oxide catalysts. Cobalt reducibility is usually known to depend on the cobalt particle size with smaller particles tending to be more difficult to reduce than larger ones. The high temperature of the reduction events for the BP calcined catalyst would suggest the presence of smaller, more difficult to reduce, cobalt species. The evidence from the XRD data showed that the cobalt zincate species after calcination were larger on this catalyst. However, XRD limitations relating to small or amorphous particles could cause problems with correlating the particle size to ease of reduction. Small or amorphous particles, that are harder to reduce, may be present on the BP calcined cobalt on zinc oxide catalyst explaining the shift in reduction events to lower temperatures. Further evidence for this postulation is to be found in data relating to the extent of reduction of the cobalt on zinc oxide catalysts. For the CoNZC catalyst the extent of reduction was 15%, which was less than that calculated for the calcined CoNZ catalyst. A lower extent of reduction in the BP calcined cobalt on zinc oxide catalyst, would again suggest the presence of harder to reduce smaller cobalt oxide species or amorphous cobalt zincate that are undetected by XRD analysis.

For the cobalt on zinc oxide catalyst that was not calcined, a more complicated derivative weight profile from the TGA in hydrogen was produced. It can be seen from table 4-2 that the weight losses are likely to be attributed to the decomposition of the nitrate precursor followed by reduction of the cobalt species. Decomposition of the nitrate precursor occurs as two main events, at temperatures identical for those observed for the decomposition in oxygen and argon. Indeed the derivative weight profiles for the decomposition are almost identical for all three gas atmospheres (Figure 4-2). In hydrogen, the profile varies slightly above 250 ^{o}C, in that it exhibits an increased weight loss compared with the argon and oxygen. This is thought to be due to reduction of cobalt species, which is known

from the *in-situ* hot-stage XRD data to have commenced by this point. This reinforces the postulate, discussed previously, that the decomposition is a thermal process and occurs independent of the atmosphere employed. Several weight losses from around 475 ^{o}C, accompanied by the uptake of hydrogen and the evolution of water can most likely be attributed to the reduction of the cobalt oxide species.

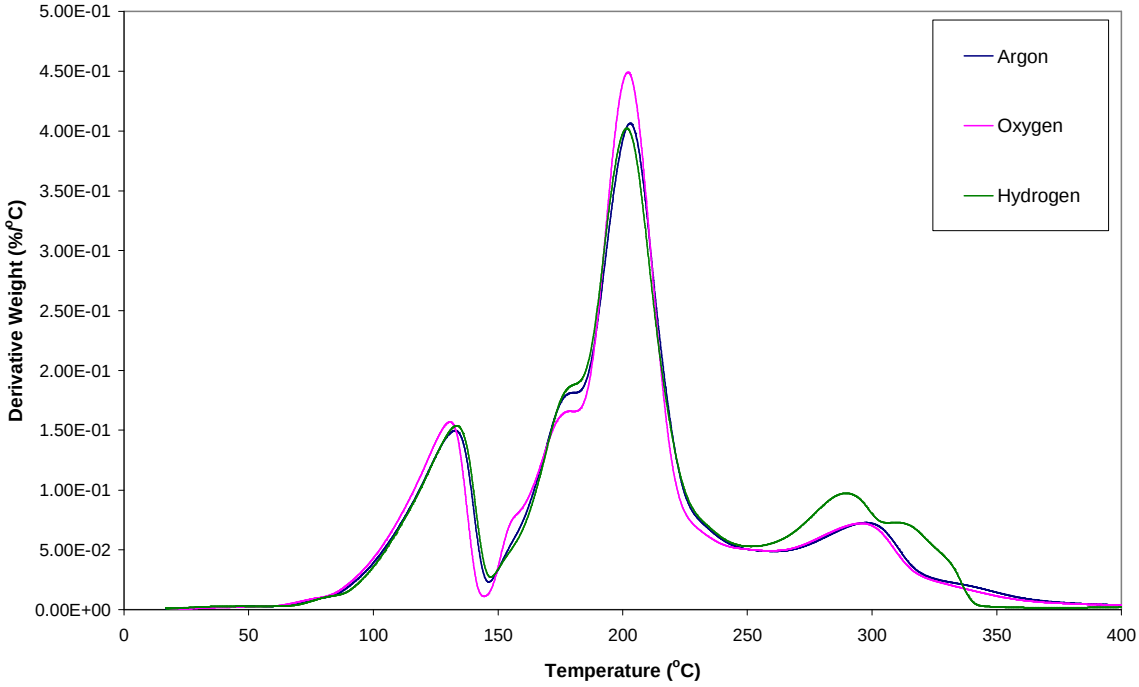

Figure 4-2: Derivative weight profile comparing decomposition of nitrate precursor on CoNZ catalyst in three different gas atmospheres

The presence of CoO is observed in the XRD data at 300 ^{o}C, slightly after the nitrate decomposition. This suggests that reduction of the cobalt species has begun before decomposition of the nitrate precursor is complete. Further evidence for this comes from the DSC data where towards the end of the endothermic decomposition of the nitrate precursor, a clear exothermic event is apparent. The peak maximum of this exotherm, at 325 ^{o}C, corresponds to the point of highest hydrogen uptake observed from the mass spectrometric data. It is known that the reduction of cobalt nitrate is highly exothermic compared to the reduction of cobalt oxide, which provides a DSC profile that is relatively featureless [59]. By 500 ^{o}C, as well as CoO, peaks indicating the presence of metallic cobalt are present. This

suggests that the weight loss centered at 585 ^{o}C could be attributed to the second stage of the reduction, that of CoO to metallic cobalt. The final weight loss from 670 ^{o}C onwards can be ascribed to the reduction of the zinc oxide support.

Similar to the calcined cobalt on zinc oxide catalysts, the reduction still occurs in two-stages, however, the temperature of the second reduction event is higher than that observed for both calcined cobalt on zinc oxide catalysts.

4.3 FT reaction

4.3.1 Activity

The catalytic activity of the different supported cobalt catalysts was studied in a fixed-bed reactor under typical FTS conditions which are outlined in section 2.4. Under these conditions the following table 4-3 can be constructed. The conversions and TOF were calculated after pseudo steady state operation was reached. The surface-specific activities (TOF) were calculated using the dispersion obtained from CO chemisorption.

Table 4-3: CO conversion and calculated TOF for supported cobalt catalyst.

Catalyst	CO Conversion (%)	TOF (s^{-1})
CoNA	6	$9.47x10^{-4}$
CoAA	11	$4.99x10^{-1}$
CoNZ	5	$1.11x10^{-1}$
CoNZC	6	$3.08x10^{-1}$
CoNZnc	6	-

During the first 48 hours on-stream, an increase in CO conversion is observed during the first 48 hours. This initial increase in conversion is seen for all the supported cobalt catalysts studied. One possible explanation for this initial increase in activity may be the occurrence of further reduction of the catalysts under the syngas atmosphere, which is known to have more reducing power than hydrogen. This has been reported in several studies where it was found that slight, further reduction of the catalyst occurred during the first hours under syngas [82, 104]. However this theory is contradicted by the TGA data for some of the catalysts, for example the cobalt nitrate on alumina, where the extent of reduction was calculated at 94%, allowing limited scope for further reduction. An alternative explanation could be surface redistribution of the cobalt. A study using STM has

shown changes in the morphology of cobalt particles when introduced into a more reducing syngas atmosphere [105]. This effect has been also observed by Grundwaldt *et al.* [106] for copper catalysts, where it was found that a more reducing atmosphere led to a change in the morphology of the copper particles, increasing the surface area and as a result having a positive effect on the activity of the catalyst.

The conversion for the cobalt nitrate on alumina catalyst reached a maximum after around 48 hours. The conversion then decreased rapidly with time on stream before undergoing a more gradual decrease. This initial rapid deactivation followed by a period of slower deactivation has been reported previously by others [107-109]. This two stage deactivation argues in favour of two mechanisms being responsible for the loss of activity. Similar to the initial increase in conversion, the two stage deactivation was also observed for all the catalysts tested. The overall deactivation behaviour for the catalysts can be described by a first-order deactivation model with the deactivation constants calculated for each of the catalysts summarised in table 4-4.

For the cobalt acetate on alumina catalyst, after achieving steady state operation, the temperature was increased from 220 ^{o}C to 240 ^{o}C to ascertain what effect this would have on the activity of the reaction. The observed increase in conversion on increasing the temperature is a well documented effect [110, 111]. A higher temperature promotes CO dissociation and hence provides more surface C atoms leading to the release of hydrocarbons [112, 113].

When comparing the rates of deactivation at the different temperatures, the deactivation constant was smaller at 240 ^{o}C than that obtained at 220 ^{o}C. This is unexpected as for most modes of deactivation during FTS, such as sintering, carbon deposition and cobalt oxidation, an increase in temperature would result in an enhancement in deactivation. However it is likely that this higher rate of deactivation at 220 ^{o}C may be due to the initial high activity after around 48 hours TOS.

Table 4-4: Calculated deactivation constants for supported cobalt catalyst.

Catalyst	Temperature (^{o}C)	Deactivation constant (hr^{-1})
CoNA	220	0.0051
CoAA	220 240	0.1685 0.0025
CoNZ	220 240	0.0019 0.0017
CoNZC	220 240 230	0.0015 0.001 -
CoNZnc	220 240	0.0018 0.0018

When comparing the activity of the cobalt acetate catalyst to that prepared from the nitrate a difference in activity between the catalysts is clearly seen. The starting precursor clearly plays a large part in determining the activity of the catalyst, however this is not unexpected as the XRD results indicate that the metal precursor is an important factor in determining the cobalt crystallite size. Conversion data shows that the catalyst prepared from the cobalt acetate was much more active than that of the cobalt nitrate.

This result is in contrast to much of the literature where catalysts prepared from cobalt acetate are found to be much less active than those prepared from cobalt nitrate at similar cobalt loading [29] . This low activity is thought to be related to the

formation of cobalt aluminates in the cobalt acetate catalysts, which are not active for FTS.

Cobalt time yields are known to increase linearly with increasing dispersion of cobalt crystallites. The higher activity observed with the cobalt acetate catalyst could be explained, at least in part, by the greatly increased dispersion of the active metal when compared to that of the cobalt nitrate catalyst. Thus despite the higher extent of reduction present in the catalyst prepared via the nitrate precursor, there may be a greater number of cobalt metal active sites available resulting in a higher FT activity in the cobalt acetate on alumina catalyst.

The turnover frequency can be seen from the summarised results to vary significantly for the cobalt on alumina catalysts. It has been reported that the turnover frequency should be independent of the cobalt crystallite size, therefore the variation could be ascribed to different degrees of deactivation of the different catalysts since the amounts of active surface metal were determined on the freshly reduced catalysts. Therefore, changes in Co dispersion during FTS would lead to deviations in the calculated turnover frequencies.

An increased rate of deactivation is observed with the cobalt acetate catalysts when compared with the cobalt nitrate on alumina catalyst. This is likely to be due to the higher activity of the catalyst, resulting in an increased partial pressure of water. This in turn will increase the re-oxidation of cobalt active sites to form FT inactive cobalt oxides as well as accelerating sintering, both of which would lead to a higher rate of deactivation. In addition, these effects will be more pronounced for the smaller cobalt crystallites present on the cobalt acetate catalyst which deviate more from the bulk-like cobalt of the nitrate prepared catalysts; making them more unstable and susceptible to both sintering and re-oxidation. Similar results have been reported in the literature with more active catalysts showing a higher rate of deactivation [29, 78].

Conversion data for the cobalt on zinc oxide catalyst is similar to that of the cobalt on alumina catalysts, in that there is an initial increase in conversion to a maximum of 10% after 51 hours TOS. Again, the deactivation occurs as two stages; however, the first stage of deactivation occurs over a far greater time period than the rapid deactivation observed with the alumina supported catalysts.

Van Berg *et al.* [108] also observed a two stage deactivation when using a cobalt supported catalyst. They proposed that the initial loss in conversion was associated with reversible deactivation caused by the build up of high molecular weight hydrocarbons inside the catalyst pores. Taking this postulation into account, the difference in rates of deactivation observed in our study could be related to the variation in pore size between the alumina and zinc oxide supports. From B.E.T analysis, the average pore diameter of the zinc oxide was found to be twice that of the alumina support. These larger pores may allow for the freer transport of large molecular weight molecules out of the pores, in turn increasing the period of time for pore blockage to occur. Therefore, support pore size may play a role in the rate of initial deactivation.

Comparison of the CO conversion data for the cobalt on zinc oxide catalysts indicates that the BP calcined catalyst gave a slightly higher CO conversion. Both catalysts exhibited similar rates of deactivation at 220 ^{o}C, 0.0015 hr^{-1} and 0.0019 hr^{-1} for the BP calcined and GU calcined catalyst, respectively. Steady state was achieved at around 450 hours TOS for both catalysts, at a similar CO conversion of 5%. However, a major difference is observed upon increasing the reaction temperature to 240 ^{o}C. For the BP calcined catalyst, this resulted in a four fold increase in percentage conversion from that observed at steady state. This effect was significantly greater than that observed for the GU calcined catalysts where CO conversion doubled. Again however, despite the difference in CO conversion at 240 ^{o}C, the rates of deactivation remain similar. For both cobalt on zinc oxide catalysts, after exposure to higher temperatures the reaction rate returned to the same level as expected from the reaction at 220 ^{o}C, implying that no permanent deactivation of the catalyst occurred at the higher temperature.

For the uncalcined cobalt on zinc oxide, an initial high activity in comparison to the calcined cobalt on zinc oxide catalysts was observed. Similar results have been observed by Bian *et al.* [114] investigating cobalt on silica catalysts; it was shown that the catalyst prepared by direct reduction exhibited higher FT activity than that which was pre-calcined in air. This was followed however by a more rapid 1st stage deactivation, suggesting that the mode of deactivation occurring is made worse by not calcining the catalyst. The second stage of deactivation showed continuous loss of activity with the catalyst failing to reach steady state operation. Following an increase in the temperature to 240 ^{o}C, the expected increase in conversion

occurred, however, upon returning the temperature to the initial 220^{o}C, the rate fell below that observed prior to the temperature increase and continued on the same downward trajectory. Both this rapid first stage deactivation and the continuing loss of activity throughout time on stream of reaction are in contrast to the calcined cobalt on zinc oxide supported catalysts. This suggests that calcination of the catalyst prior to reduction plays an important role in the stability of the catalyst. This instability from failure to precalcine the catalyst could be due to incomplete decomposition of the nitrate precursor which would then occur during the initial stage of the FT reaction. Lack of pre-calcination could also result in poor metal support interaction, which would cause the cobalt to slowly sinter leading to non-recoverable deactivation. It has been previously reported for a Co/SiO_2 catalyst that particles on a directly reduced catalyst aggregate more significantly than on a pre-calcined catalyst [114]. If this was the case, it would be expected that the rate of deactivation would increase with the extra water produced as a result of higher conversion at elevated temperatures, however this effect is not observed.

4.3.2 Selectivity

The selectivity of the Fischer-Tropsch synthesis over supported cobalt catalysts has also been investigated.

For all catalysts tested, the observed decrease in CO conversion with time on stream, described in the previous section, was concomitant with an increase in the production of heavier hydrocarbons with time on stream. This is illustrated in figure 4-3 which compares the selectivity with time on stream for the wax products of CoNA catalyst. This effect was also apparent in the light hydrocarbon products as well as the chain growth probability, α, obtained from the gradient of the Anderson-Shultz-Flory (ASF) plots in the C_{25}-C_{35} hydrocarbon range which increased from 0.87 at 48 hours TOS to 0.9 after 360 hours TOS. Given the known relationship between CO conversion and selectivity, a lower CO conversion would be expected to result in a decrease in the selectivity to higher hydrocarbon products. However, similar results have been found by Borg *et al.* [71], using a cobalt on alumina catalyst, who found that despite a decrease in CO conversion with time on stream, the catalysts gave similar C5+ selectivity. They postulated that these results could be possibly explained by an increase in the average particle size due to deactivation. Both sintering and reoxidation of small cobalt particles would lead to

an increase in the average cobalt particle size. Since a positive correlation has been reported between cobalt particle size and C5+ selectivity [71, 115], this increased particle size with time on stream could lead to an increase in selectivity towards higher hydrocarbons which could counteract the effect of decrease in selectivity because of lower CO conversion.

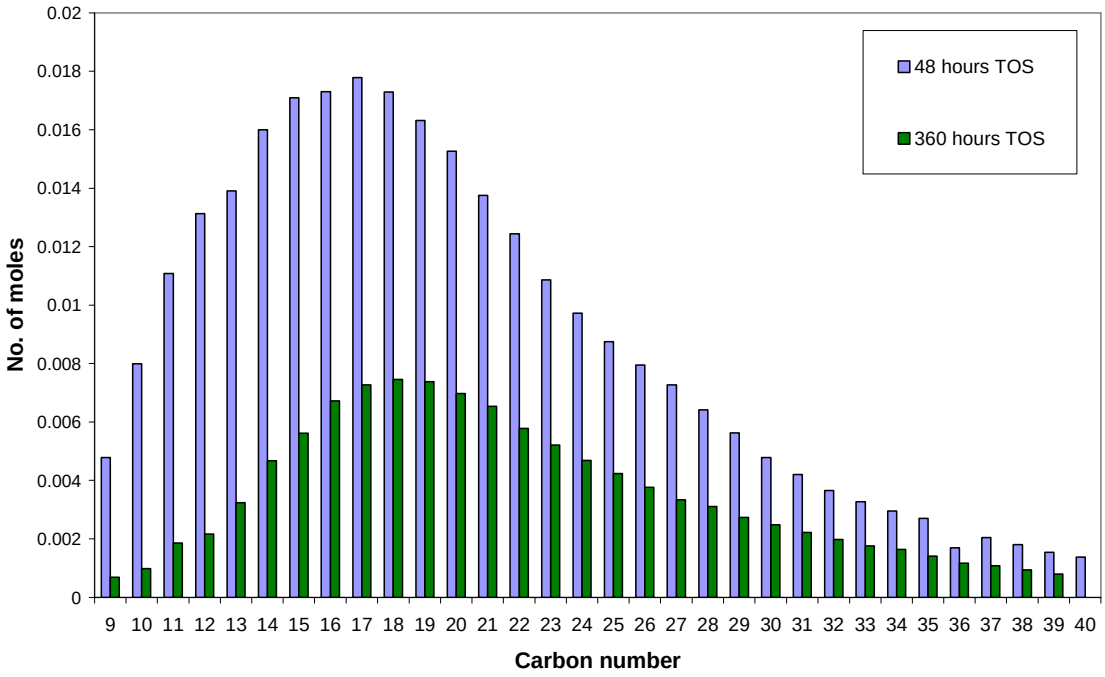

Figure 4-3: Comparison of hydrocarbon selectivities for CoNA catalyst at 48 and 360 hours TOS

The selectivity to the different FTS products obtained for the supported cobalt catalysts at 220 ^{o}C is summarised in table 4-5, with the values reported here corresponding to the catalysts during the period of pseudo steady state operation.

Table 4-5: Calculated CO conversion and alpha values for supported cobalt catalysts.

Catalyst	CO conversion (%)	α
CoNA	6	0.9
CoAA	11	0.82
CoNZ	5	0.92
CoNZC	6	0.9
CoNZnc	6	0.86

For the cobalt nitrate on alumina catalyst, selectivity at steady state operation showed a hydrocarbon product distribution centered around C_{20} and an alpha value of 0.90. For the CoAA hydrocarbon product distribution, it can be observed from figure 4-4 that the product selectivity differs significantly from the cobalt on alumina catalyst prepared via the nitrate precursor. It can be seen that the catalysts prepared from the acetate show a product distribution that is shifted towards lighter hydrocarbons. This is true for both the wax and liquid hydrocarbon fractions and is also reflected in the alpha values. This is in keeping with the literature, where an enhanced formation of heavier hydrocarbons for cobalt catalysts prepared from a nitrate has been generally reported. This difference in selectivity is likely to be due to the effect of the cobalt particle size, which can be seen from the XRD of the calcined catalysts to vary considerably for the two catalysts prepared via different cobalt precursors. The effect of the particle size has been shown to have an effect on the selectivity, with C5+ selectivity shown to increase with increasing cobalt particle size [69, 71, 115]. Therefore a product distribution that was shifted towards lower hydrocarbons produced from the cobalt acetate catalyst would be in keeping with these findings. This difference in

hydrocarbon product distribution could also be attributed to the extent of reduction, which was found by thermogravimetric analysis to be significantly different for each of these catalysts. Previous studies have suggested that lower hydrocarbon product distributions are due to the presence of unreduced cobalt oxides, likely to be found in highly dispersed cobalt catalysts such as those produced via acetate precursor. These cobalt oxides catalyse the WGS reaction increasing the ratio of H_2/CO which in turn increases the rate of hydrogenation. This will result in a decrease in the carbon chain length of the hydrocarbons being produced [29].

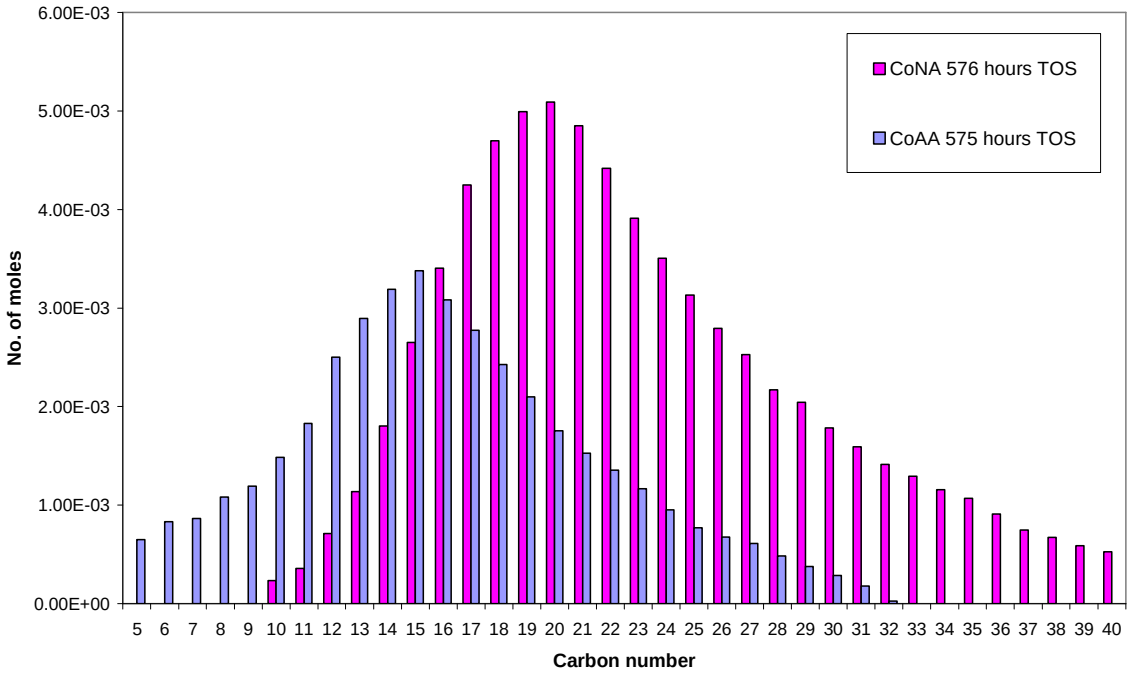

Figure 4-4: Comparison of hydrocarbon product distribution for CoNA and CoAA catalysts at similar TOS

Once steady state operation was reached for the CoAA catalyst, the temperature was increased from 220 ^{o}C to 240 ^{o}C. In addition to the previously discussed increase in conversion, this was found to result in a shift towards products with a lower carbon number. The same effect was apparent in both the wax and liquid product distribution, and was reflected in the chain growth probability which decreased noticeably, from 0.82 to 0.77, with an increase in temperature from 220 ^{o}C to 240 ^{o}C, respectively. These results are in agreement with the literature where the effect of process variables on the carbon number distribution has been well documented. An increase in temperature results in a change in the H_2/CO ratio, leading to higher surface coverage of hydrogen. This provides increased

opportunity for species present on the catalyst surface to undergo further hydrogenation to produce more light hydrocarbons. From these results it can be concluded that higher temperature is preferential for chain termination and therefore production of hydrocarbons of lower molecular weight [112, 113, 116] . Results have been reported for a variety of catalysts showing that this effect of temperature on product selectivity is irrespective of the catalyst type, or of the feed gas composition [117-122].

Similar to the cobalt on alumina catalysts, the selectivity for the cobalt on zinc oxide catalyst exhibits a shift towards production of higher molecular weight hydrocarbons with time on stream at 220 ^{o}C. Again, the increase in temperature to 240 ^{o}C resulted in an expected increase in CO conversion and a shift in the hydrocarbon product distribution towards lighter hydrocarbons.

From the table 4-5, at steady state, a comparison of the alpha values for the cobalt nitrate catalysts on different supports showed a distribution that was shifted towards heavier hydrocarbons for the zinc oxide support. The calculated alpha values which were 0.9 and 0.92 at 220 ^{o}C at steady state for the CoNA and CoNZ catalysts, respectively. Indicating again that the hydrocarbon product distribution was shifted towards higher molecular weight products for the zinc oxide supported catalyst. The effect of cobalt particle size on selectivity has been previously discussed, where it was stated that larger cobalt crystallites produce higher molecular weight products. From the XRD data, it was found that the cobalt crystallites were smaller on the zinc oxide support. Hence, this result cannot be explained in terms of the correlation between crystallite size and hydrocarbon product distribution. As the hydrocarbon production distribution was compared at the same CO conversion, the influence of levels of conversion can be discounted as a possible explanation for these findings. This leaves the identity of the support as the most likely reason for the shift towards heavier hydrocarbons.

The support effect observed could be attributed to the variation in pore size of the supports. However previous studies have found that product distributions cannot be explained in terms of pore diffusion effects [75, 123]. Therefore it is likely that the change in product distribution is due to the chemical properties of the surface of the supports. Previous studies have found marked differences in the product

distribution even when comparing different alumina supports with a range of cobalt particles sizes. This reinforces the postulation that selectivity is influenced by the nature of the support as well as the size of cobalt crystallites. A possible reason for this effect may be the decoration of the active cobalt sites with zinc metal from the reducible zinc oxide support. Several studies have shown that decoration of the active sites can led to a change in both the activity and the selectivity of catalysts. Mo et al. [124] showed using Co/CuZnO catalyst that decoration of the active cobalt metal with zinc, lead to a change in the selectivity, brought about by coverage of a significant portion of the hydrocarbon synthesis sites. A similar effect may be in evidence here through zinc decoration of the cobalt active sites. This could be concentrated on the hydrogenation sites, resulting in an increase in the relative amount of hydrocarbon propagation sites and in turn shifting selectivity towards higher chain hydrocarbons.

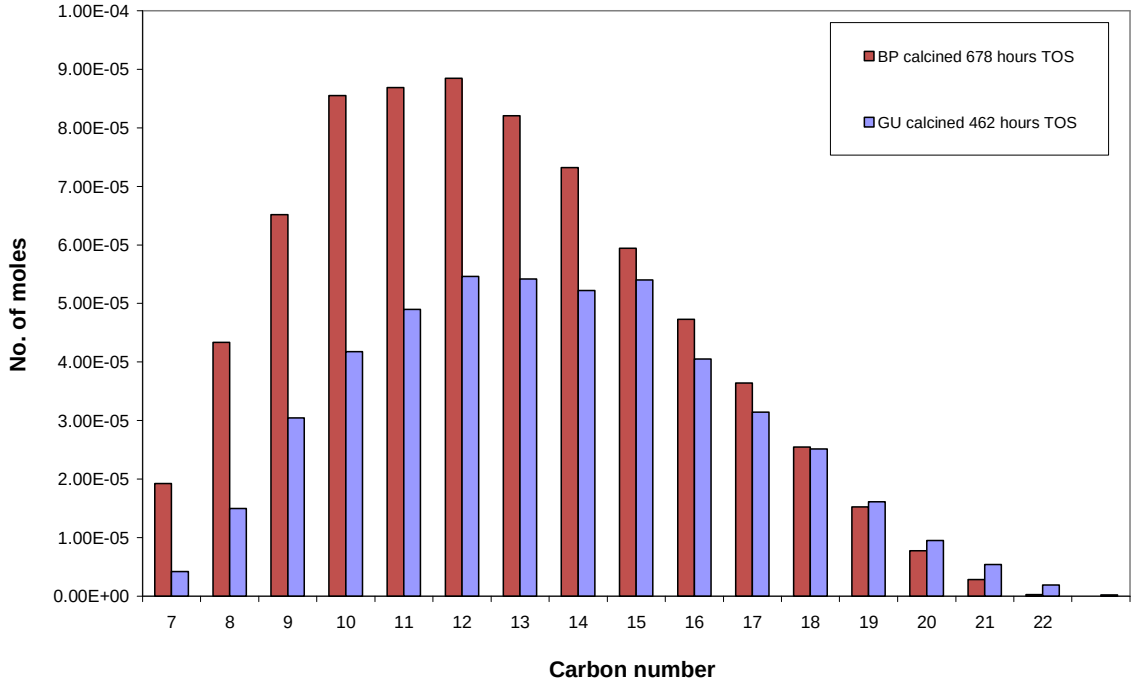

Figure 4-5: Comparison of hydrocarbon product distribution for cobalt nitrate on zinc oxide catalysts

At steady state at 220 ^{o}C, when compared with GU calcined catalyst, the BP calcined catalyst had a lower calculated alpha value (0.9 compared to 0.92), which means it was more inclined to produce lower molecular weight hydrocarbons. This is apparent in the light hydrocarbon product distribution shown in figure 4-5.

Despite these catalysts being similar in terms of nature of support and cobalt precursor, the calcination procedures differed resulting in a difference in average cobalt crystallite size after calcination. As mentioned previously, correlations between the cobalt particle size and product selectivity have been reported in the literature, with larger particles producing higher selectivities. By contrast, in our study we observed a larger average cobalt crystallite size on the cobalt on zinc oxide catalyst that was calcined using the procedure carried out at BP, which resulted in products shifted towards lighter hydrocarbons compared with the CoNZ catalyst. The difference in the selectivities may be explained, at least in part, by the lower extent of reduction exhibited in the BP calcined catalyst. This would result in a higher amount of cobalt-support interactions, which are thought in some cases to catalyse WGS reaction, leading to an increase in the amount of lower molecular weight hydrocarbons produced.

For the uncalcined cobalt on zinc oxide catalyst, product selectivities and the chain growth probability showed that the alpha value calculated for the uncalcined catalyst (0.86) is significantly lower than that for the calcined catalysts (0.90-0.92). This selectivity towards lower molecular weight hydrocarbons can be explained in terms of the exothermic nature of the reductive decomposition. The resultant increase in temperature is likely to lead to an increased interaction between cobalt species and the support. This in turn would lead to a higher percentage of cobalt zincates remaining unreduced. As with cobalt aluminates, these are likely to catalyse WGS reaction, increasing surface hydrogen coverage and hence increasing the formation of lower molecular weight hydrocarbons. This is in keeping with the effect seen with the cobalt acetate on alumina catalyst which also exhibited a highly exothermic decomposition and a lower alpha value.

4.4 Post reaction

The post reaction cobalt catalysts were analysed using XRD and TGA-DSC with an online mass spectrometer, in order to provide insight into both the cobalt phases present after, and the nature of species deposited on the catalyst surface during, FT reaction. The data acquired from this analysis was used to provide further information into the possible mechanisms of deactivation occurring during Fischer-Tropsch synthesis. From the XRD results, the following table 4-6 can be constructed, summarising the cobalt crystallite size before and after FT reaction for each of the cobalt catalysts:

Table 4-6: Comparison of cobalt oxide and cobalt crystallite size for supported cobalt catalysts. The experimental error for cobalt sizes calculated from X-ray diffraction is less than +/- 1 nm.

Catalyst	Co_3O_4 crystallite size [a] (nm)	Co crystallite size [b] – pre FT reaction (nm)	Co crystallite size [c] – post FT reaction (nm)
CoNA	15	11	12
CoAA	-	-	12
CoNZ	-	-	9
CoNZC	14	10.5	10
CoNZnc	-	-	-

[a] **Cobalt oxide partile size calculated from XRD data of calcined catalyst**

[b] **Cobalt metal particle size calculated from XRD data of calcined catalyst using using equation 4.5**

[c] **Cobalt metal particle size calculated from XRD data of post reaction catalyst**

The cobalt metal crystallite sizes before FT reaction are an estimate calculated by the following equation (4.5), where the measured Co_3O_4 crystallite size is converted according to the relative molar volumes of metallic cobalt and Co_3O_4 [125].

$$d(Co^0) = 0.75d(Co_3O_4) \quad (4.5)$$

Examination by XRD of the catalyst post FT reaction confirms the cobalt to be present in the reduced phase in all catalysts. It is thought that a build up of wax, produced during the reaction, on the catalyst surface prevents the re-oxidation of the cobalt metal. No peaks indicating the presence of CoO or Co_2C, which are thought to be causes of deactivation during FTS, were detected. These cobalt phases have been observed from XRD analysis performed during similar studies [126]. This could then rule out re-oxidation of the bulk cobalt as a major cause of deactivation, which would be in line with bulk thermodynamics which state that re-oxidation of cobalt will only occur on small particles since these deviate from bulk like behaviour under realistic FT conditions. Within the literature however it is proposed that re-oxidation of the cobalt will only occur where the crystallite size is less than 6 nm, suggesting that even if re-oxidisation of the cobalt takes place it would be difficult to detect by XRD.

For the cobalt nitrate on alumina catalyst, comparison of the XRD patterns after 24 hours and 768 hours in figure 4-6 below show that narrowing of the reflections related to the cobalt metal occurred, suggesting an increase in the size of the metal particles of cobalt with time on stream. The cobalt metal crystallite size increased to 12 nm. Sintering of cobalt metal as a cause of deactivation has been reported by several groups using a variety of techniques including *in-situ* XRD as well as EXAFS techniques and it is clear from these results that sintering of the active cobalt metal phases is occurring [78, 82, 87, 88, 126].

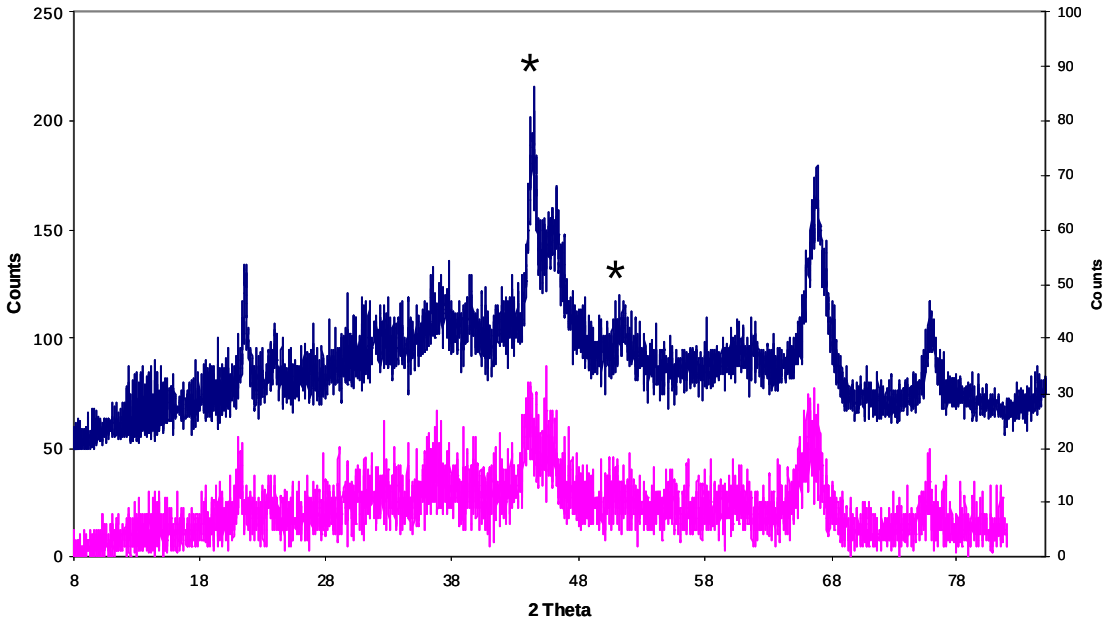

Figure 4-6: Comparison of XRD patterns for cobalt nitrate on alumina catalysts after 24 and 768 hours TOS. The experimental error for cobalt sizes calculated from X-ray diffraction is less than +/- 1 nm.

The TGA results from the CoNA catalyst post FT reaction show desorption of the adsorbed water on the sample below 160 ^{o}C. There is a slight weight increase between 170 and 235 ^{o}C which can be related to re-oxidation of the cobalt metal phase, corresponding to the beginning of the uptake of oxygen, to form cobalt oxide. The major weight loss is exhibited between 240 and 570 ^{o}C, which can be assigned to the exothermic burn off of carbonaceous material and corresponds to the evolution of water, carbon monoxide and carbon dioxide. Although it is not clear from the weight loss profile, this event can be seen clearly in the derivative weight profile to consist of three separate overlapping events. From the mass spectrometric data it can be observed that the maximum of the water evolution, at 370 ^{o}C, is lower than that of the carbon dioxide at 415 ^{o}C. As a consequence, the ratio of hydrogen, carbon dioxide as well as carbon monoxide gas evolved changes as the temperature increases. This change in gas ratios demonstrates that different types of carbonaceous material exist on the catalyst surface; at the lower temperature evolution of carbon monoxide and carbon dioxide are accompanied by the evolution of water, suggesting the species being removed are predominantly hydrocarbons; as the temperature increases the evolution of water drops off indicating that the species being removed contain comparatively less hydrogen, for example, graphitic carbon or aromatics.

Deactivation of the cobalt active phase by carbonaceous species has been postulated as a possible cause of loss of activity during FTS in a number of studies. It is difficult however from these results alone to ascertain the exact nature of the carbon species involved due to the presence of heavy hydrocarbon wax product on the catalyst.

Table 4-7: Comparison of weight loss during TGA in oxygen for supported cobalt catalysts post FT reaction

Catalyst	Weight loss (g/g of catalyst)
CoNA	0.21
CoAA	0.28
CoNZ	0.04
CoNZC	0.11
CoNZnc	0.27

For all the post reaction catalysts, the weight loss associated with the removal of this carbonaceous material was calculated. Table 4-7 shows these results, expressed in terms of weight loss of deposited material per gram of catalyst. It is seen that for the CoNA catalyst, the weight loss was similar to that exhibited by both the CoAA catalyst and the uncalcined CoNZ catalyst whilst being considerably greater than both calcined cobalt on zinc oxide catalysts.

XRD analysis performed on the cobalt acetate on alumina catalyst post FT catalyst, also confirmed the presence of cobalt metal on the catalyst after the reaction. If we presume that the absence of cobalt oxide peaks in the calcined catalyst suggests that the cobalt oxide particles are too small to be detected by XRD then the cobalt crystallite size calculated post reaction (12 nm) must be much greater than the Co_3O_4 particle size after calcination. This would then confirm that sintering of the active metal phase has occurred.

Comparing this result to the sintering occurring on the cobalt on alumina catalyst prepared via the nitrate precursor, it is clear that there has been a greater degree of sintering associated with the cobalt acetate on alumina catalyst. This would tie in with the deactivation results where it was seen that the initial loss of activity was much greater on the catalysts produced via the acetate. This however conflicts with the data relating to deactivation, where the increase in temperature did not lead to an increase in rate of deactivation. A possible explanation for this is that sintering of the cobalt occurs as a mechanism for deactivation only in the initial stages of the FT reaction. Therefore an increase in temperature after a considerable time on stream will not necessarily equate to an increase in the rate of deactivation as sintering is no longer occurring. This would agree with findings in the literature where it is suggested that sintering occurs only in the initial stages of the reaction [78, 88] .

TGA results for the cobalt acetate on alumina catalyst are superficially similar to those seen with the cobalt nitrate on alumina catalyst, with the bulk of the weight loss occurring over the same temperature range from 200-600 ^{o}C. However, weight loss on the catalyst prepared via the acetate continued until around 780 ^{o}C, which was 200 ^{o}C higher than that observed with the cobalt nitrate on alumina. The total weight lost due to the removal of carbonaceous material was also slightly greater at 0.28 g/g_{cat} compared to 0.21g/g_{cat} on the CoNA. These findings would be expected as the cobalt acetate on alumina catalyst was on stream for a longer time as well as being subjected to higher temperatures. In addition no initial weight gain associated with the re-oxidation of active cobalt metal was observed, suggesting the presence of carbon species deposited on the cobalt crystallites. Analysis of the deactivation data in table 4-4 shows that the rate of loss of activity was greatest for this catalyst, which was the only one of all the catalysts studied not to exhibit this initial weight increase.

There is a small high temperature weight loss observed with the acetate prepared catalyst that is not observed with the nitrate. This weight loss around 975 ^{o}C is endothermic and can be seen from the mass spec data to correspond to the evolution of oxygen. This is most likely to be associated with the decomposition of the spinel oxide to the more thermodynamically stable CoO.

For the cobalt on zinc oxide catalyst, post reaction XRD analysis confirmed the cobalt to be present in the reduced state post FT reaction, with the crystallite size calculated to be 9 nm. Similar to the cobalt acetate on alumina catalysts, no reflections indicating the presence of cobalt oxide species were detected after calcination. This might suggest that the cobalt oxide species were present as small, very highly dispersed particles. If this is indeed the case, then the measured cobalt size after reaction indicates the possibility of sintering, of the cobalt metal active phase being at least partly responsible for the observed deactivation of the cobalt on zinc oxide catalysts during the FT reaction. However as previously discussed, it is thought that there is a possibility that the cobalt species present after calcination is cobalt zincate. As a consequence, the absence of XRD peaks may not indicate the presence of highly dispersed cobalt oxide but instead signal that the cobalt oxide exists in an amorphous form. In this instance, the occurrence of sintering could not be proven.

The TGA results for the cobalt nitrate on zinc oxide catalyst differ considerably when compared to the cobalt on alumina catalysts. As with the CoNA catalyst, an initial weight gain was observed in the TGA of the post reaction catalyst prior to removal of carbonaceous material. Although both weight gain events occur at similar temperatures, the weight increase observed with the zinc oxide catalyst was considerably greater. We propose that this weight increase is again likely to be caused by re-oxidation of cobalt metal. The availability of these cobalt metal sites for re-oxidation post FT reaction may show some correlation to the rate of catalyst deactivation. Data in table 4-4 shows that there is a significantly smaller loss of activity for this catalyst when compared to the alumina supported catalysts both of which exhibited either no or relatively smaller initial weight gains.

This larger initial increase in weight for the zinc oxide catalysts compared with the catalysts prepared using an alumina support could also be explained in terms of zinc decoration of the cobalt metal. This theory was put forward previously to explain changes in the catalysts selectivity. If this was the case, this increased weight gain for the catalyst supported on zinc oxide could be due to re-oxidation of zinc as well as cobalt, resulting in an increased weight gain for the zinc oxide catalysts.

As with the alumina supported catalysts, the major weight loss is accompanied by the evolution of water, carbon monoxide and carbon dioxide and can be attributed to the removal of carbonaceous material. All three weight losses commence around 280 ^{o}C, however, complete removal of carbonaceous material on the CoNZ catalyst occurred around 80 ^{o}C below that of the CoNA catalyst and 300 ^{o}C lower than the CoAA catalyst. Again, however, it is difficult to identify the exact nature of the carbon species due to large amounts of hydrocarbons that are present on the catalyst.

From table 4-7, the calculated weight loss for the CoNZ catalyst is significantly smaller than that observed with the alumina supported catalysts. Indicating that, considerably less carbonaceous material is present on the catalyst surface after FT reaction.

From the XRD data for the BP calcined cobalt nitrate on zinc oxide catalyst (CoNZC) it was possible to measure the cobalt crystallite size for both pre and post FT reaction. It can be observed from the calculated values in table 4-6 that despite the catalyst being tested for an extended period of time and at elevated temperatures, there is no change in the crystallite size. This therefore excludes sintering as a mode of deactivation during FTS. This agrees with our earlier findings where an increase in temperature does not lead to an increase in the rate of deactivation as would be expected with classic metal sintering.

The results from the post reaction TGA for the CoNZC catalyst exhibited a similar profile to that of the CoNZ catalyst, although the initial weight gain was slightly less. One possible explanation for this is the fact that the CoNZC catalyst was run for a considerably longer period of time which may have resulted in increased levels of carbon laydown and in turn less exposed cobalt metal to be re-oxidised. The observed weight loss associated with the removal of carbonaceous material was similar to that of the CoNZ catalyst. Again, the slightly higher value may be attributed to the extended run time that this catalyst was subjected to allowing for increased build up of carbon based deposits on the catalyst surface. Both cobalt on zinc oxide catalysts, however exhibited appreciably less weight loss when compared with the alumina supported catalysts.

This substantial difference in the comparative levels of carbonaceous build up between the alumina and zinc oxide based catalyst could be explained in terms of the nature of the support. It is proposed that the acid sites on the alumina support may promote the cracking of the hydrocarbons, leading to an increase in carbon laydown. This difference in weight loss could also be explained by zinc decoration of the cobalt. If reoxidation of the zinc is occurring for the cobalt on zinc oxide catalysts, this may mask the contribution of weight loss from carbon burn off and hence the weight loss appears comparatively less.

Post reaction XRD data for the uncalcined cobalt on zinc oxide catalyst again showed cobalt to be present as metallic cobalt. However, due to the broad nature of these peaks, data relating to crystallite size could not be accurately obtained, although it is clear that the cobalt is highly dispersed. As a consequence it can be postulated, that as with the calcined cobalt on zinc oxide, sintering of the active metal phase is not likely to be a major contributor to loss of activity.

Comparison of the uncalcined CoNZ catalyst with the calcined cobalt on zinc oxide catalysts shows a broadly similar TGA profile with an initial weight gain followed by burn off of carbonaceous material and a high temperature weight loss. A number of noticeable differences are present however. The major weight loss observed occurs over a much smaller temperature range. Despite this it can be observed from table 4-7 that a considerable amount of carbonaceous material is removed during the post reaction analysis. The quantity was similar to that observed for the cobalt on alumina catalyst but much greater than for the calcined cobalt on zinc oxide catalysts. Although deactivation rates are similar to that of the calcined cobalt on zinc oxide catalysts, the nature of the deactivation differs significantly in that it takes the form of a continuous loss of activity. The initial weight gain associated with the re-oxidation of the active cobalt phase is less marked than in the calcined zinc oxide catalysts which might indicate less available cobalt to be present post FTS. As sintering is not thought to be the major cause of loss of activity, it is likely that the elevated levels of carbonaceous material present when compared to the calcined cobalt on zinc oxide catalysts are playing an important role in the nature of deactivation.

The increased initial weight gain, for the calcined catalysts, might also be explained in terms of zinc decoration of the cobalt. It is possible that due to the

difference in activation of this cobalt on zinc oxide catalyst, no decoration of the cobalt metal with zinc occurs. If this was the case, this cobalt on zinc oxide catalyst, which has been reduced directly, will not benefit from the increased weight gain due to reoxidation of zinc and therefore the initial weight gain will be comparably much smaller.

5. CONCLUSIONS

The main scientific objective of this thesis was to investigate the role of the support, cobalt precursor and calcination procedure on the activation processes and their subsequent impact on the properties of the final catalyst. It is widely accepted that all these variables have a significant effect on the catalyst properties and final Fischer-Tropsch performance; however, the precise nature of this impact has proved to be a complex process to understand. By employing a multiple characterisation technique approach, a greater understanding of the chemical and physical properties of the studied cobalt supported catalysts has been obtained.

Data obtained from TGA, XRD and TEM analysis proved effective in determining that the interaction between the support and cobalt nitrate complex varied significantly depending on the nature of the support. The cobalt species were found to be less well dispersed on the alumina when compared with the zinc oxide support. The nature of the decomposition of the cobalt nitrate on alumina was more closely related to that of the bulk nitrate, indicating less interaction between support and nitrate complex. This was reflected in the measured crystallite size after calcination, where the average cobalt oxide crystallite was found to be relatively larger. The size and distribution of the cobalt species was found to be determined by the pore structure of the alumina support. Zinc oxide support facilitated greater dispersion of the cobalt nitrate complex. The cobalt oxide particles were found to have greater interaction with the support, resulting in a higher dispersion of the cobalt species on the zinc oxide support.

Precursor effects were examined using cobalt nitrate and cobalt acetate salts on an alumina support. Decomposition on the catalyst prepared via the acetate precursor occurred as a single event, in contrast to the bulk acetate decomposition, suggesting a significant interaction between support and cobalt acetate complex. The cobalt nitrate however, exhibited a decomposition profile that was closer in nature to that of its bulk salt. The highly exothermic nature of the cobalt acetate decomposition, observed from the DSC data, is likely to be responsible for this increased salt-support interaction. Absence of cobalt oxide peaks from the XRD data suggest small or amorphous particles present after calcination on the catalyst prepared from the acetate. The measured cobalt oxide

particle size was found to correlate with the extent of cobalt reduction. Large particles, as observed on the cobalt nitrate on alumina catalyst, exhibited a much greater extent of reduction, 94%, when compared to that of the cobalt acetate on alumina (15%).

The effect of the calcination procedure was examined using differently calcined but otherwise identical cobalt on zinc oxide catalysts; exposing a difference in the measured cobalt oxide crystallite size, and subsequently, a measurable effect on the extent of reduction. The reduction profiles for the cobalt on zinc oxide catalyst did not exhibit the expected ratio for reduction of cobalt spinel oxide to metallic cobalt, seen with the cobalt nitrate on alumina catalyst; instead it was found that reduction profile was more closely linked to reduction of cobalt zincate. This suggests strong cobalt species-support interaction, with cobalt zincate being the predominant species present after calcination.

All cobalt supported catalysts were tested under industrially relevant FT conditions to obtain comparative data on the activity, selectivity and mechanisms of deactivation for each catalyst. All catalysts exhibited typical reaction profiles for supported cobalt catalysts. It was found that both FT activity and selectivity were influenced by the nature of the cobalt precursor. Catalysts prepared from the cobalt acetate exhibited higher activity than those prepared from the cobalt nitrate; a result of the highly dispersed cobalt present on the cobalt acetate; brought about by greater interaction between the cobalt acetate species and the support during the exothermic cobalt acetate decomposition. The formation of higher molecular weight hydrocarbons was favoured over cobalt nitrate on alumina exhibiting high reducibility, while the product distribution shifted towards the formation of lighter hydrocarbons for the less reducible cobalt acetate catalyst. The presence of unreducable cobalt species on the acetate catalyst lead to an increase in the amount of lower molecular weight hydrocarbons produced. The cobalt particle size can also be correlated to selectivity, with the larger cobalt particles found on the cobalt nitrate catalyst producing higher molecular weight hydrocarbons.

Comparison between the zinc oxide and alumina supported catalysts showed little effect on FTS activity. However, cobalt supported on zinc oxide exhibited a shift towards products with higher molecular weight hydrocarbons. It has been postulated that this increased C5+ selectivity is due to decoration of the active

cobalt sites with zinc. Evidence for this decoration effect is evident in the low CO chemisorption values but high catalyst activity.

Calcination of zinc oxide supported catalysts was shown to play an important role in influencing both activity and selectivity. Direct reduction of the cobalt on zinc oxide supported catalyst resulted in a higher dispersion of cobalt, and as a result an initial higher activity. This however was followed by a significantly greater rate of initial deactivation than that observed on the calcined cobalt on zinc oxide catalysts. It is clear that calcination of the catalyst prior to reduction plays an important role in stabilising the active cobalt component, and in turn inhibits deactivation brought about through sintering. Selectivities were found to favour lower molecular weight hydrocarbons on the uncalcined zinc oxide catalysts. This is likely to be due to unreduced cobalt zincate species catalysing WGS reaction, producing more hydrogen and in turn increasing the rate of chain termination.

All catalysts exhibited a two stage deactivation suggesting several modes of deactivation are occurring during time on stream. The nature of the support plays a role in the cause of deactivation. Of the calcined catalysts, the alumina supported catalysts exhibited the highest rates of initial deactivation. Sintering for the cobalt active phases has been put forward as the likely mechanism responsible for this, however this is only thought to occur during the initial stages of the reaction. It is proposed that no significant sintering occurs on the calcined cobalt on zinc oxide catalyst. Once pseudo steady state operation had been reached, an increase in reaction temperature did not result in an increased rate of deactivation. Therefore the mechanism for loss in activity at this stage of reaction is unlikely to be sintering. This was not the case for the cobalt nitrate on zinc oxide catalysts that was directly reduced without prior calcination. Post FT analysis by TGA showed varying degrees of carbonaceous material present on all catalysts. However, the levels were significantly higher on the alumina supported. This is likely to be related to the more acidic sites on the alumina support enhancing carbon formation.

6. REFERENCES

[1] F. Fischer, H. Tropsch, Brennstoff-Chem. 7 (1926) 97-104.

[2] British Petroleum. Statistical Review of Worl Energy 2011. *BP.com*, 16 July 2011

[3] L.P. Dancuart, A.P. Steynberg, Studies in Surface Science and Catalysis. 163 (2007) 379-399.

[4] H. Schulz, Applied Catalysis A: General. 186 (1999) 3-12.

[5] A.C. Vosloo, Fuel Processing Technology. 71 (2001) 149-155.

[6] M.E. Dry, Journal of Chemical Technology and Biotechnology. 77 (2001) 43-50.

[7] T.H. Fleisch, R.A. Sills, M.D. Briscoe, Journal of Natural Gas Chemistry 11 (2002) 1-14.

[8] Sasol GTL Brochure. *www.sasol.com*, 21 February 2011.

[9] Chemistry and Industry. Go faster FT catalysts. *www.soci.org*, Issue 9, 2011.

[10] F. Morlaes, B. Weckhuysen, Catalysis. 19 (2006) 1-40.

[11] M.E. Dry, Catalysis Today. 71 (2002) 227-241.

[12] Foster Wheeler. Oryx GTL - a case study. *www.fwc.com*, July 2006.

[13] G.P. Van Der Laan, A.A.C.M. Beenackers, Catalysis Reviews. 41 (1999) 255-318.

[14] J.M. Thomas, W.J. Thomas, *Principles and Practice of Heterogeneous Catalysis*, VCH Publishers Inc., New York, 1997.

[15] A.A. Adesina, Applied Catalysis A: General. 138 (1996) 345-367.

[16] Anderson, (1984).

[17] S. Shetty, R.A. Van Santen, Catalysis Today. 171 (2011) 168-173.

[18] H.C. Long, M.L. Turner, P. Fornasiero, J. Kaspar, M. Graziani, P.M. Maitlis, Journal of Catalysis. 167 (1997) 172-179.

[19] B.H. Davis, Industrial and Engineering Chemistry Research. 46 (2007) 8938-8945.

[20] A. Raje, J.R. Inga, B.H. Davis, Fuel. 76 (1997) 273-280.

[21] R. Oukaci, A.H. Singleton, J.G. Goodwin, Applied Catalysis A:General. 186 (1999) 129-144.

[22] C.H. Bartholomew, R. J. Farrauto, *Fundamentals of Industrial Catalytic Processes, Wiley-Interscience*, New Jersey, 2006.

[23] H. Pichler, H. Schulz, Chemie Ingenieur Technik. 42 (1970) 1162-1174.

[24] V. Dijk, Topics in Catalysis. 26 (2003) 111-119.

[25] Bell, Rev. Sci. Eng. 23 (1981) 203-232.

[26] P. Biloen, J.N. Helle, W.M.H. Sachtler, Journal of Catalysis. 58 (1979) 95-107.

[27] J. van de Loosdrecht, M. van der Haar, A.M. van der Kraan, A.J. van Dillen, J.W. Gens, Applied Catalysis A: General 365-376.

[28] J.S. Girardon, A.S. Lermontov, L. Gengembre, P.A. Chernavskii, A. Griboval-Constant, A.Y. Khodakov, Journal of Catalysis. 230 (2005) 339-352.

[29] A. Martinez, C. Lopez, F. Marquez, I. Diaz, Journal of Catalysis. 220 (2003) 486-499.

[30] M. Kraum, M. Baerns, Applied Catalysis A:General. 186 (1999) 189-200.

[31] J. Panpranot, S. Kaewkun, P. Praserthdam, J.G. Goodwin, Catalysis Letters. 91 (2003) 95-102.

[32] Y. Okamoto, K. Nagata, T. Adachi, T. Imanaka, K. Inamura, T. Takyu, Journal of Physical Chemistry. 95 (1991) 310-319.

[33] S. Sun, K. Fujimoto, Y. Yoneyama, N. Tsubaki, Fuel. 81 (2002) 1583-1591.

[34] S.L. Sun, N. Tsubaki, K. Fujimoto, Applied Catalysis A:General. 202 (2000) 121-131.

[35] G. Bian, T. Mochizuki, N. Fujishita, H. Nomoto, M. Yamada, Energy & Fuels. 17 (2003) 799-803.

[36] Ming, Applied Catalysis A: General. 123 (1995) 23-36.

[37] E. van Steen, G.S. Sewell, R.A. Makhothe, C. Micklethwaite, H. Manstein, M. De Lange, C.T. O'Conner, Journal of Catalysis. 162 (1996) 220-229.

[38] M.C. Lok, Studies in Surface Science and Catalysis. 147 (2004) 283-288.

[39] P. Concepcion, C. Lopez, A. Martinez, V.E. Puntes, Journal of Catalysis. 228 (2004) 321-332.

[40] G. Calleja, A. Delucas, R. Vangrieken, Applied Catalysis. 68 (1991) 11-29.

[41] G. Yang, J. He, Y. Yoneyama, Y. Tan, Y. Han, N. Tsubaki, Applied Catalysis A:General. 329 (2007) 99-105.

[42] A. Tavasoli, R.M.M. Abbaslou, M. Trepanier, A.K. Dalai, Applied Catalysis A:General. 345 (2008) 134-142.

[43] H. Xiong, M.A.M. Motchelaho, M. Moyo, L.L. Jewell, N.J. Coville, Journal of Catalysis. 278 (2011) 26-40.

[44] M. VoB, D. Borgmann, G. Welder, Journal of Catalysis. 212 (2002) 10-21.

[45] G. Jacobs, T.K. Das, Y. Zhang, J. Li, G. Racoillet, B.H. Davis, Applied Catalysis A: General. 233 (2002) 263-281.

[46] A.M. Saib, M. Claeys, E. van Steen, Catalysis Today. 71 (2002) 395-402.

[47] A.Y. Khodakov, A. Griboval-Constant, R. Bechara, V.L. Zholobenko, Journal of Catalysis. 206 (2002) 230-241.

[48] A.Y. Khodakov, R. Bechara, A. Griboval-Constant, Applied Catalysis A: General. 254 (2003) 273-288.

[49] A.Y. Khodakov, A. Griboval-Constant, R. Bechara, F. Villain, Journal of Physical Chemistry B. 105 (2001) 9805-9811.

[50] H. Xiong, Y. Zhang, S. Wang, J. Li, Catalysis Communications. 6 (2005) 512-516.

[51] A.K. Dalai, T.K. Das, K.V. Chaudhari, G. Jacobs, B.H. Davis, Applied Catalysis A: General. 289 (2005) 135-142.

[52] S. Storsaeter, B. Totdal, J.C. Walmsley, B.S. Tanem, A. Holmen, Journal of Catalysis. 236 (2005) 139-152.

[53] J. Jablonski, J. Okal, D. Potoczna-Petru, L. Krajczyk, Journal of Catalysis. 220 (2003) 146-160.

[54] B.G. Johnson, C.H. Bartholomew, D.W. Goodman, Journal of Catalysis. 128 (1991) 231-247.

[55] M. Rameswaran, C.H. Bartholomew, Journal of Catalysis. 117 (1989) 218-236.

[56] J.L. Zhang, J.G. Chen, J. Ren, Y.H. Sun, Applied Catalysis A:General. 243 (2003) 121-133.

[57] L. Shi, D. Li, B. Hou, Y. Wang, Y. Sun, Fuel Processing Technology. 91 (2010) 394-398.

[58] P. Arnoldy, J.A. Moulijn, Journal of Catalysis. 93 (1985) 38-54.

[59] A. Lapidus, A. Krylova, V. Kazanskii, V. Borokov, A. Zaitsev, J. Rathousky, A. Zukal, M. Jancalkova, Applied Catalysis. 73 (1991) 65-82.

[60] J. van de Loosdrecht, S. Barradas, E.A. Caricato, N.G. Ngwenya, P.S. Nkwanyana, M.A.S. Rawat, B.H. Sigwebela, P.J. van Berge, L.J. Visagie, Topics in Catalysis. 26 (2003) 121-127.

[61] S.L. Soled, E. Iglesia, R.A. Fiato, J.E. Baumgartner, H. Vroman, S. Miseo, Topics in Catalysis. 26 (2003) 101-109.

[62] K.E. Coulter, A.G. Sault, Journal of Catalysis. 154 (1995) 56-64.

[63] A.Y. Khodakov, J. Lynch, D. Bazin, B. Rebours, N. Zanier, B. Moisson, P. Chaumette, Journal of Catalysis. 168 (1997) 16-25.

[64] D. G. Castner, P. R. Watson, I. Y. Chan, Journal of Physical Chemistry. 94 (1990) 819-828.

[65] R.C. Reuel, C.H. Bartholomew, Journal of Catalysis. 85 (1984) 78-88.

[66] M. A. Vannice, Journal of Catalysis. 50 (1977) 228.

[67] E. Iglesia, S.L. Soled, R.A. Fiato, Journal of Catalysis. 137 (1992) 212-224.

[68] S. Bessell, Applied Catalysis A: General. 96 (1993) 253-268.

[69] G.L. Bezemer, J.H. Bitter, H.P.C.E. Kuipers, H. Oosterbeek, J.E. Holewijn, X. Xu, F. Kapteijn, A.J. van Dillen, K.P. de Jong, Journal of American Chemistry Society. 128 (2006) 3956.

[70] N. Koizumi, S. Suzuki, S. Niiyama, T. Shindo, M. Yamada, Catalysis Letters. 141 (2011) 931-938.

[71] O. Borg, S. Erib, E.A. Blekkan, S. Storsaeter, H. Wigum, E. Rytter, A. Holmen, Journal of Catalysis. 248 (2007) 89-100.

[72] T. Witoon, M. Chareonpanich, J. Limtrakul, Fuel Processing Technology. 92 (2011) 1498-1505.

[73] P.B. Radstake, J.P. den Breejen, G.L. Bezemer, J.H. Bitter, K.P. De Jong, V. Froseth, A. Holmen, Studies in Surface Science and Catalysis. 167 (2007) 85-90.

[74] E. Iglesia, Applied Catalysis A-General. 161 (1997) 59-78.

[75] O. Borg, P.D.C. Dietzel, A.I. Spjelkavik, E.Z. Tveten, J.C. Walmsley, S. Diplas, S. Eri, A. Holmen, E. Ryttera, Journal of Catalysis. 259 (2008) 161-164.

[76] D. Song, J. Li, Journal of Molecular Catalysis A:Chemical. 247 (2006) 206-212.

[77] P.J.v. Berge, J.v.d. Loosdrecht, S. Barradas, A.M.v.d. Kraan, Catalysis Today. 58 (2002) 321-334.

[78] G. Jacobs, P.M. Patterson, Y. Zhang, T. Das, J. Li, B.H. Davis, Applied Catalysis. 233 (2002) 215-226.

[79] D. Schanke, A.M. Hilmen, E. Bergene, K. Kinnari, E. Rytter, E. Adnanes, A. Holmen, Catalysis Letters. 34 (1995) 269-284.

[80] E. van Steen, M. Claeys, M.E. Dry, J. van de Loosdrecht, E.L. Viljoen, J.L. Visagie, Journal of Physical Chemistry B. 109 (2005) 3575-3577.

[81] A.M. Saib, A. Borgna, J. van de Loosdrecht, P.J. van Berge, J.W. Niemantsverdriet, Applied Catalysis A:General. 312 (2006) 12-19.

[82] H. Karaca, O.V. Safonova, S. Chambrey, P. Fongarland, P. Roussel, A. Griboval-Constant, M. Lacroix, A.Y. Khodakov, Journal of Catalysis. 277 (2011) 14-26.

[83] A.M. Saib, D.J. Moodley, I.M. Ciobica, M.M. Hauman, B.H. Sigwebela, C.J. Weststrate, Catalysis Today. 154 (2010) 271-282.

[84] D. Schanke, A.M. Hilmen, E. Bergene, K. Kinnari, E. Rytter, E. Adnanes, A. Holmen, Energy & Fuels. 10 (1996) 867-872.

[85] J. Li, X. Zhan, Y. Zhang, G. Jacobs, T. Das, B.H. Davis, Applied Catalysis A-General. 228 (2002) 203-212.

[86] G. Jacobs, T.K. Das, P.M. Patterson, J. Li, L. Sanchez, B.H. Davis, Applied Catalysis A-General. 247 (2003) 335-343.

[87] A.M. Saib, D.J. Moodley, I.M. Ciobica, M.M. Hauman, B.H. Sigwebela, C.J. Weststrate, J.W. Niemantsverdriet, J. van de Loosdrecht, Catalysis Today. 154 (2010) 271-282.

[88] T.K. Das, G. Jacobs, P.M. Patterson, W.A. Conner, J. Li, B.H. Davis, Fuel. 82 (2003) 805-815.

[89] G. Kiss, C.E. Kliewer, G.J. DeMartin, C.C. Culross, J.E. Baumgartner, Journal of Catalysis. 217 (2003) 127-140.

[90] D.J. Moodley, A.M. Saib, J. van de Loosdrecht, C.A. Welker-Nieuwoudt, B.H. Sigwebela, J.W. Niemantsverdriet, Catalysis Today. 171 (2011) 192-200.

[91] J.T. Richardson, R. Scates, M.V. Twigg, Applied Catalysis A: General. 246 (2003) 137-150.

[92] F. Wigzell, 'The Characterisation of Supported Cobalt Catalysts', Masters Thesis, University of Glasgow, 2007.

[93] N. N. Greenwood, A. Earnshaw, *Chemistry of Elements*, Butterworth Heinmann, 1984.

[94] Handbook of Chemistry and Physics, CRC Press, Florida, 1986, p. B-87.

[95] Y. Wang, M. Noguchi, Y. Takahashi, Y. Ohtsuka, Catalysis Today. 68 (2001) 3-9.

[96] D.G. Castner, P.R. Watson, I.Y. Chan, Journal of Physical Chemistry. 93 (1989) 3188.

[97] J. M. Jablonski, J. Okal, D. Potoczna-Petru, L. Krajczyk, Journal of Catalysis. 220 (2003) 146-160.

[98] H.-Y. Lin, Y.-W. Chen, Materials Chemistry and Physics. 85 (2004) 171-175.

[99] O. Borg, M. Ronning, S. Storsaeter, W. Van Beek, A. Holmen, Studies in Surface Science and Catalysis. 163 (2007) 255-272.

[100] Z. Pan, D.B. Bukur, Applied Catalysis A: General. 404 (2011) 74-80.

[101] A. Casanovas, C. De Leitenburg, A. Trovarelli, J. Llorca, Chemical Engineering Journal 154 (2009) 267-273.

[102] M.A. Martin-Luengo, P.A. Sermon, Y. Wang, Journal of Catalysis. 135 (1992) 263-268.

[103] C.J.J. Van Loon, European Patent 2008714 (2008).

[104] A. Rochet, V. Moizan, C. Pichon, F. Diehl, A. Berliet, V. Briois, Catalysis Today. 171 (2011) 186-191.

[105] J. Wilson, C. De Groot, Journal of Physical Chemistry. 99 (1995) 7860-7866.

[106] J.-D. Grunwaldt, A.M. Molenbroek, N.-Y. Topsoe, H. Topsoe, B.S. Clausen, Journal of Catalysis. 194 (2000) 452-460.

[107] E. Iglesia, S.L. Soled, R.A. Fiato, G.H. Via, Journal of Catalysis. 143 (1993) 345-368.

[108] P.J. van Berge, Studies in Surface Science and Catalysis. 107 (1997) 207.

[109] K. F.Tan, J. Chang, A. Borgna, M. Saeys, Journal of Catalysis. 280 (2011) 50-59.

[110] M.E. Dry, Journal of Molecular Catalysis. 17 (1982) 133-144.

[111] A.R. de la Osa, A. De Lucas, A. Romero, V.J. L., P. Sanchez, Fuel. 90 (2011) 1935-1945.

[112] L. Tian, C.-F. Huo, D.-B. Cao, Y. Yang, J. Xu, B.-S. Wu, H.W. Xiang, Journal of Molecular Structure: THEOCHEM. 941 (2010) 30-35.

[113] F.E.M. Farias, F.G. Sales, F.A.N. Fernandes, Journal of Natural Gas Chemistry. 17 (2008) 175-178.

[114] G.-Z. Bian, N. Fujishita, T. Mochizuki, W.-S. Ning, M. Yamada, Applied Catalysis A-General. 252 (2003) 251-260.

[115] S. Storsaeter, O. Borg, E.A. Blekkan, A. Holmen, Journal of Catalysis. 231 (2005) 405-419.

[116] Y. Liu, B. Teng, X. Guo, Y. Li, J. Chang, L. Tian, X. Hao, Y. Wang, H.W. Xiang, Y.Y. Xu, Y.-W. Li, Journal of Molecular Catalysis A:Chemical. 272 (2007) 182-190.

[117] R.A. Dictor, A.T. Bell, Journal of Catalysis. 97 (1985) 121-136.

[118] T.J. Donnelly, C.N. Satterfield, Applied Catalysis. 52 (1989) 93-114.

[119] R.C. Everson, E.T. Woodburn, A.R.M. Kirk, Journal of Catalysis. 53 (1978) 186-197.

[120] E.S. Lox, G.F. Froment, Ind. Eng. Chem. Res. 32 (1993) 61-70.

[121] S.-H. Kang, K.-J. Woo, J.W. Bae, K.-W. Jun, Y. Kang, Korean J Chem Eng. 26 (2009) 1533-1538.

[122] H. Jung, J.-I. Yang, J.H. Yang, H.-T. Lee, D.-M. Chun, H.J. Kim, Fuel Processing Technology. 91 (2010) 1839-1844.

[123] E. Rytter, S. Eri, T.H. Skagseth, D. Schanke, E. Bergene, R. Myrstad, A. Lindvag, Industrial & Engineering Chemistry Research. 46 (2007) 9032-9036.

[124] X. Mo, Y.-T. Tsai, J. Gao, D. Mao, J.G. Goodwin, Journal of Catalysis. 285 (2012) 208-215.

[125] E.J. Baum, Chemical Property Estimation: Theory and Application, Lewis Publishers Boca Raton, 1998.

[126] H. Karaca, J. Hong, P. Fongarland, P. Roussel, A. Griboval-Constant, M. Lacroix, K. Hortmann, O.V. Safonova, A.Y. Khodakov, Chemical Communications. 46 (2010) 788-790.